University of Florida
Civil and Coastal Engineering

University of Florida
Civil and Coastal Engineering

Final Report **December 2011**

Damage Detection and Repair Methods for GFRP Bridge Decks

Principal investigator:
H. R. Hamilton

Subcontractor:
Jeff R. Brown, Hope College
Holland, MI

Research assistants:
Rafael Asencio, University of Florida
Terra Fox, Hope College
Philip Hallam, Hope College

Department of Civil and Coastal Engineering
University of Florida
P.O. Box 116580
Gainesville, Florida 32611

Sponsor:
Florida Department of Transportation (FDOT)
Rodney G. Chamberlain, P.E. – Project Manager

Contract:
UF Project No. 00079094
FDOT Contract No. BDK75 977-17

Disclaimer

The opinions, findings, and conclusions expressed in this publication are those of the authors and not necessarily those of the State of Florida Department of Transportation.

SI* (MODERN METRIC) CONVERSION FACTORS

*APPROXIMATE CONVERSIONS **TO** SI UNITS*

SYMBOL	WHEN YOU KNOW	MULTIPLY BY	TO FIND	SYMBOL
LENGTH				
in	inches	25.4	millimeters	mm
ft	feet	0.305	meters	m
yd	yards	0.914	meters	m
mi	miles	1.61	kilometers	km
AREA				
in^2	square inches	645.2	square millimeters	mm^2
ft^2	square feet	0.093	square meters	m^2
yd^2	square yard	0.836	square meters	m^2
ac	acres	0.405	hectares	ha
mi^2	square miles	2.59	square kilometers	km^2
VOLUME				
fl oz	fluid ounces	29.57	milliliters	mL
gal	gallons	3.785	liters	L
ft^3	cubic feet	0.028	cubic meters	m^3
yd^3	cubic yards	0.765	cubic meters	m^3
NOTE: volumes greater than 1000 L shall be shown in m^3				
MASS				
oz	ounces	28.35	grams	g
lb	pounds	0.454	kilograms	kg
T	short tons (2000 lb)	0.907	Megagrams	Mg (or "t")
TEMPERATURE (exact degrees)				
^oF	Fahrenheit	5(F-32)/9 or (F-32)/1.8	Celsius	^oC
ILLUMINATION				
fc	foot-candles	10.76	lux	lx
fl	foot-Lamberts	3.426	$candela/m^2$	cd/m^2
FORCE and PRESSURE or STRESS				
kip	1000 pound force	4.45	Kilonewtons	kN
lbf	pound force	4.45	newtons	N
lbf/in^2	pound force per square	6.89	kilopascals	kPa

*SI is the symbol for the International System of Units. Appropriate rounding should be made to comply with Section 4 of ASTM E380.

SI* (MODERN METRIC) CONVERSION FACTORS

*APPROXIMATE CONVERSIONS **FROM** SI UNITS*

SYMBOL	WHEN YOU KNOW	MULTIPLY BY	TO FIND	SYMBOL
LENGTH				
mm	millimeters	0.039	inches	in
m	meters	3.28	feet	ft
m	meters	1.09	yards	yd
km	kilometers	0.621	miles	mi
AREA				
mm^2	square millimeters	0.0016	square inches	in^2
m^2	square meters	10.764	square feet	ft^2
m^2	square meters	1.195	square yards	yd^2
ha	hectares	2.47	acres	ac
km^2	square kilometers	0.386	square miles	mi^2
VOLUME				
mL	milliliters	0.034	fluid ounces	fl oz
L	liters	0.264	gallons	gal
m^3	cubic meters	35.314	cubic feet	ft^3
m^3	cubic meters	1.307	cubic yards	yd^3
MASS				
g	grams	0.035	ounces	oz
kg	kilograms	2.202	pounds	lb
Mg (or "t")	megagrams (or "metric	1.103	short tons (2000 lb)	T
TEMPERATURE (exact degrees)				
^oC	Celsius	1.8C+32	Fahrenheit	^oF
ILLUMINATION				
lx	lux	0.0929	foot-candles	fc
cd/m^2	candela/m^2	0.2919	foot-Lamberts	fl
FORCE and PRESSURE or STRESS				
kN	Kilonewtons	0.225	1000 pound force	kip
N	newtons	0.225	pound force	lbf
kPa	kilopascals	0.145	pound force per square inch	lbf/in^2

*SI is the symbol for the International System of Units. Appropriate rounding should be made to comply with Section 4 of ASTM E380.

Technical Report Documentation Page

1. Report No.	2. Government Accession No.	3. Recipient's Catalog No.

4. Title and Subtitle	5. Report Date
Damage Detection and Repair Methods for FRP Bridge Decks	December 2011
	6. Performing Organization Code

7. Author(s)	8. Performing Organization Report No.
Rafael Asencio, J. R. Brown, and H. R. Hamilton	

9. Performing Organization Name and Address	10. Work Unit No. (TRAIS)
University of Florida Department of Civil & Coastal Engineering P.O. Box 116580 Gainesville, FL 32611-6580	11. Contract or Grant No. BDK75 977-17

12. Sponsoring Agency Name and Address	13. Type of Report and Period Covered
Florida Department of Transportation Research Management Center 605 Suwannee Street, MS 30 Tallahassee, FL 32301-8064	Final Report March 2009 – November 2011
	14. Sponsoring Agency Code

15. Supplementary Notes

16. Abstract

Glass fiber-reinforced polymer (GFRP) decks are being considered for use as a replacement for worn steel grid bridge decks due to their high strength-to-weight ratio and fast installation time. In this research, two nondestructive evaluation techniques were considered for use in evaluating in-service GFRP bridge decks for damage: acoustic emissions (AE) and infrared thermography (IRT).

Three different commercially available deck systems were tested in positive and negative bending test setups. The testing consisted of loading each specimen sequentially with service, then ultimate, then service level loads, which provided AE data for both undamaged and damaged deck specimens. Damage was induced on the specimens by loading them to their ultimate capacity. The specimens generally exhibited linear elastic behavior up to failure. AE feature data were evaluated using intensity analysis and recovery ratio analysis (RRA). The recovery ratio analysis was adapted from calm ratio analysis, which is based on the Kaiser effect. RRA provided clear distinction between damaged and undamaged decks in all three specimens. Evaluation criteria based on this method are proposed. A modified form of RRA was then used on data collected during a bridge load test of the Hillsboro canal bridge.

Initial IRT work required finite element simulation of the heat transfer process to determine optimal heating and data acquisition parameters that were used to inspect GFRP bridge decks in the laboratory. Experimental testing was performed in a laboratory setting on damaged and undamaged GFRP bridge deck specimens from three different manufacturers. IRT evaluation focused on identifying damage in the specimens that had been loaded to their ultimate flexural strength. It was demonstrated that IRT successfully identified features of two types of GFRP bridge decks and that severe delamination/debonding could be detected under ideal circumstances. Additional research is needed to improve detection of severe damage, including methods to reduce the interference of surface imperfections, such as non-uniform heating, which are inherent to the GFRP bridge decks examined in the current study.

G17. Key Word	18. Distribution Statement
acoustic emissions, glass fiber- reinforced polymer (GFRP), Intensity analysis, calm ratio, FRP repair, bridge testing.	No restrictions. This document is available to the public through the National Technical Information Service, Springfield, VA, 22161

19. Security Classif. (of this report)	20. Security Classif. (of this page)	21. No. of Pages	22. Price
Unclassified	Unclassified	193	

Form DOT F 1700.7 (8-72) Reproduction of completed page authorized

Acknowledgements

The authors would like to acknowledge and thank the Florida Department of Transportation (FDOT) for providing funding for this project. Much of the laboratory work for this project was conducted at the FDOT Marcus H. Ansley Structures Research Center, and the authors would like to express their appreciation to David Allen, Stephen Eudy, Sam Fallaha, Tony Hobbs, Will Potter, Paul Tighe, David Wagner, and Chris Weigly for their assistance and input.

The authors would also like to thank Hope College undergraduate students Jonathan Winne, Ryan Converse and Chris Ploch for the work completed on the lamp and IRT camera fixtures that were used in the current study. This work was completed as part of their senior design projects in engineering at Hope College. The assistance of David Daugherty of Hope College is also gratefully acknowledged.

Hughes Brothers, Inc., is thanked for the donation of GFRP bars used in the repair of the GFRP deck. Fyfe Co., LLC, is thanked for the donation of GFRP fabric and epoxy used in the repair of the GFRP deck.

Executive Summary

Glass fiber-reinforced polymer (GFRP) decks are being used as a replacement for deteriorated bridge decks due to their high strength-to-weight ratio and fast installation time. Several different types of deck systems are available for commercial use. GFRP bridge decks are relatively new to the bridge industry. One concern regarding GFRP deck systems is their durability and field performance. Developing non-destructive evaluation (NDE) methods that can be used to monitor the GFRP decks is important to ensure long-term performance is monitored and documented.

This report presents research focused on the use of acoustic emission (AE) and infrared thermography (IRT) to inspect GFRP decks. AE is used extensively in the pressure tank and vessel industries. IRT is a relatively well-established NDE tool with existing ASTM standards for detecting delaminations in reinforced concrete bridge decks and detecting defects in FRP composites used in aerospace structures.

Three commercially available GFRP bridge decks were tested in both positive and negative bending in a three-point loading setup. Each specimen was subjected to sequential load tests consisting of service, ultimate, then service. Both positive and negative bending specimens were tested using the same test procedures. In addition, load steps were separated by a brief load reduction to allow observation of Kaiser and felicity effects during reloading. Two AE analysis methods were used to evaluate the data. Intensity analysis, which is routinely used in the testing of pressure vessels and has been tested on GFRP decks, did not provide sufficient discrimination between the damaged and undamaged state. Relative ratio analysis (RRA) was performed and did provide sufficient discrimination to allow the development of evaluation criteria for the laboratory testing. A modified form of RRA was also used to analyze selected AE data from a bridge load test.

The first phase of the IRT study involved numerical modeling of the heat transfer through GFRP deck panels. Analysis parameters included heat flux intensity and duration, heat source modulation, and image recording requirements (frequency and duration). Key findings from this phase were: (1) the minimum required inspection time for evaluating the web and bottom plate interface is on the order of 15 minutes; (2) after applying a least-squares sinusoidal curve fit to

the temperature vs. time response for each pixel in a series of thermal images, the resulting phase response was used to identify subsurface features of undamaged Deck A GFRP panels.

Trial inspections of damaged and undamaged specimens demonstrated that the general procedure developed through the numerical modeling was successful in identifying subsurface features and distinguishing between undamaged and severely damaged GFRP panels. Additional experimental work was then conducted on full-scale deck panels, which were loaded to failure in a laboratory environment. Results from the full-scale testing suggest that the phase image technique provides significant improvement for identifying subsurface features, but non-uniform heating and heat source reflections still pose challenges for detecting load-induced damage. IRT detection of load-induced damage depends heavily on the actual failure mode; delaminations must occur in relatively close proximity to the surface that is being heated. Most failure modes in this study were not detectable using the IRT. Additional research is recommended to explore the potential for IRT to detect and characterize other types of damage, such as blistering or other near surface delaminations, which might provide an overall indication of how well a particular GFRP deck system is performing in a specific environment throughout its anticipated service life.

Three repair procedures were developed and applied to deck A. Repair A1 was to place GFRP bars in the cavities between the webs and then fill these cavities with concrete. Repair A2 was to apply wet layup GFRP to the damaged webs. Repair A3 was to fill the cavities with grout and apply GFRP to the deck soffit. A1, A2, and A3 reached 89%, 128%, and 164% of the original deck capacity.

Table of Contents

Part I – Structural Testing and Acoustic Emission Evaluation

Table of Contents

Part II – Infrared Thermography

List of Figures – Part I

List of Figures – Part II

List of Tables – Part I

List of Tables – Part II

1 Introduction

Florida has the largest inventory of moveable bridges in the nation, with a total of 148, of which 91% are bascule, 7% are swing and 2% are lift bridges. Most employ open grid steel decks as a riding surface for part of their span (National Bridge Inventory 2008). Compared to solid bridge decks, steel grid decks have several advantages: they can be assembled in the factory, they are lightweight, and they are easy to install. Unfortunately, worn steel grid decks have high maintenance costs and provide poor skid resistance, especially when wet. As a possible option to replace the worn steel grid decks, the Florida Department of Transportation (FDOT) is investigating the possibility of using glass-fiber reinforced polymer (GFRP) decks. GFRP deck panels can be designed and manufactured to meet weight and dimensional requirements of a bridge, allowing direct replacement of steel grid decks.

GFRP bridge decks are relatively new to the bridge industry. One concern regarding GFRP deck systems is their durability and field performance. Developing non-destructive evaluation (NDE) methods that can be used to monitor the GFRP decks is important to ensure that long-term performance is monitored and documented.

This report presents research focused on the use of acoustic emission (AE) and infrared thermography (IRT) to inspect GFRP decks. AE is used extensively in the pressure tank and vessel industries. The standards developed in that industry serve as a starting point and reference for the use of acoustic emissions for testing GFRP deck specimens. ASTM standards for FRP pressure vessel testing are currently available and are commonly applied during AE testing of such vessels. These standards were used as a starting point in the development of AE test methods and evaluation criteria for GFRP bridge decks. Infrared thermography is a relatively well-established NDE tool with existing ASTM standards for detecting delaminations in reinforced concrete bridge decks and detecting defects in FRP composites used in aerospace structures.

Three commercially available GFRP bridge decks were tested in flexure initially to service load levels and then their ultimate strength. Service level loads were used with AE inspection to determine if damage could be detected. IRT inspection was conducted on the specimens after they had been loaded to their ultimate strength.

In addition to the NDE inspections, repair procedures for the damaged deck systems were developed for one of the deck types that is installed on a bridge in Belle Glade, FL. These repaired decks were then tested to their ultimate strength to determine if the original capacity could be restored.

This report is divided into two parts. Part I covers the GFRP and AE literature review (Chapter 2) and the development of the test setup and test procedure for load testing and AE data collection (Chapters 2, 3, 4, and 8). Chapter 5, 6, and 7 cover the specimen design, repair design and test instrumentation. Structural behavior and results are discussed in Chapters 9 and 10 and the analysis of the AE test data and evaluation criteria development are covered in Chapter 11. Chapter 12 covers the use of the AE evaluation method on AE data gathered during a bridge test. Part II covers the IRT literature review, heating methods, data acquisition, and evaluation.

2 Literature Review

Over the past 15 years more than 100 bridges in the United States have been rehabilitated using FRP composites (Reeve 2010). The lightweight, corrosion resistance and fast installation time of this material are the main advantages over conventional deck systems. In 1996, the first Glass Fiber Reinforced Polymer (GFRP) bridge was installed over an unnamed creek in Kansas (O'Connor 2008). Since then, GFRP decks have been used in a variety of vehicular bridge decks. On the Bently Creek Bridge, in New York, the concrete deck was replaced with GFRP taking advantage of the reduced weight of the deck to raise the load rating of the bridge and extend the life of the bridge (Alampalli and Kunin 2002). A GFRP bridge deck was installed on New York State Route 36 in Troupsburg, NY. The bridge system was constructed of several sections of the honeycomb decking (studied in this report) spanning the length of the bridge (Cole et al. 2006). In 2001, the South Carolina Department of Transportation completed the first GFRP bridge deck installation in the state. This bridge consisted of steel girders and a pultruded deck; the bridge was simply supported and had a span of 60 ft. (Turner et al. 2004)

2.1 GFRP Deck Design and Fabrication

Although the American Association of State Highway and Transportation Officials (AASHTO) presently publishes design and construction specifications for GFRP pedestrian bridges, it does not publish recommendations regarding the use of GFRP deck for vehicular bridges. Liu et al. (2008), however, contains design recommendations made for the design using load distribution factors (LDF). In addition, they indicate that relative deflections were found to be similar to that of timber and concrete decks in the AASHTO code.

GFRP deck designs and fabrication processes are manufacturer specific. Consequently, the details of components and production are usually proprietary. In general, however, GFRP deck assembly methods usually include pultrusion, wet layup, and preform molds. The pultrusion process involves drawing flexible glass-fiber reinforcement in varying orientations and sequences with a manufacturer specific vinyl ester resin through a die to construct a continuous element of constant cross-section (Figure 1). Longitudinal reinforcement is provided by the glass fibers in the roving racks. Mats can have different fiber orientations as prescribed by the manufacturer.

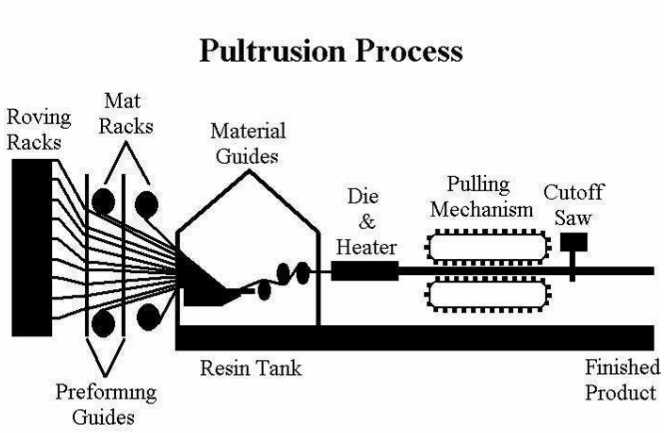

Figure 1 – Pultrusion process (Ultrafiberglass.com)

Wet layup is another fabrication technique that arranges layers of the glass fiber mats and resin in a prescribed sequence. The type of glass reinforcement and the orientation of the fibers are specified by the manufacturer in a schedule (Figure 2). One type of deck that is constructed using wet layup is the GFRP honeycomb sandwich deck. This deck consists of a honeycomb core placed between two flat sheets of GFRP and bonded together using vinyl ester resin (Figure 3). The honeycomb core is assembled from alternating sinusoidal-shaped sheets of GFRP, called flutes, and flat sheets designed to carry shear. The core is then placed between two outer faces which are designed to provide flexural rigidity. (Kalny et al. 2004)

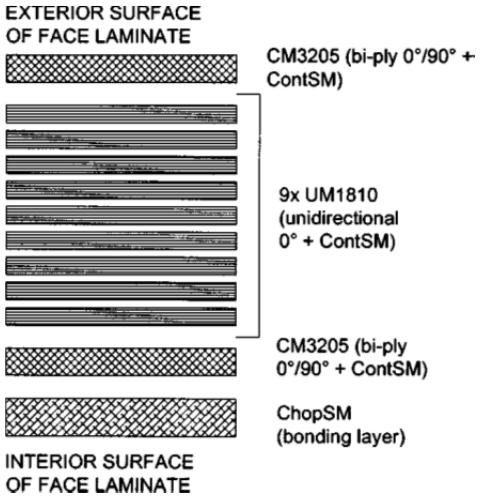

Figure 2 – Wet layup glass fiber schedule (Kalny et al. 2004)

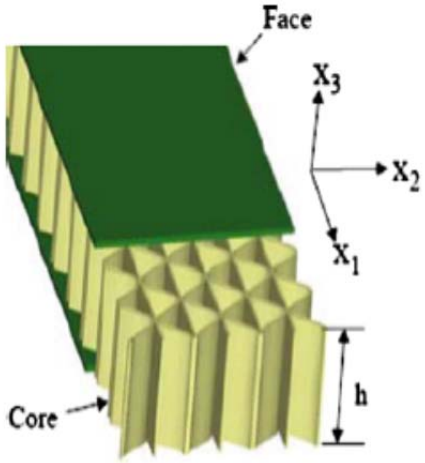

Figure 3 – GFRPH schematic

Stay-in-place preforms are made from polyurethane foam molded into the desired shape to create the cross-section. This method was developed for the boating industry and is now being used in the assembly of bridge decks (Figure 4). The assembly process is similar to the wet layup process but utilizes foam forms, which are made of 2 pcf floatation grade polyurethane foam, to hold the shape of the cross-section until the resin is cured.

Figure 4 – Prisma form sample beam (preforms.com)

2.2 GFRP Bridge Deck Structural Behavior

A number of GFRP deck systems have been tested for structural behavior. Prachasaree et al. (2009) investigated the in-plane and out-of-plane shear behavior of GFRP specimens and the load transfer efficiency of the joints between the specimens. Keller and Gurtler (2005) tested pultruded GFRP deck plate bending characteristics using a simply supported test setup. Alagusundaramoorthy et al. (2006) also tested deck systems in a simply supported system; deflection was the main interest of this investigation.

While testing different GFRP decks, Brown and Berman (2010), Cousins et al. (2009), and Vyas et al. (2009) reported similar behaviors when approaching the specimens' capacity. The Zellcomp (Durham, NC) deck failed as the top plate cracked. Damage was also observed in the web and the bottom panel (Vyas et al. 2009). GFRP Honeycomb (GFRPH) failed too quickly and catastrophically for the failure mode to be identified, though AE data indicated that the failure began at one end of the panel and spread throughout. Kalny et al. (2004) and Chen and Davos (2010) also investigated the design capacity of FRPH panels. Using small scale samples they investigated the strength of the fiber in tension and the flexural and compressive

strength of the specimens. The deck systems failed suddenly, which was usually preceded by loud audible cracking.

Several investigations have been conducted using test setups with several spans and deck-girder connections. This was done to capture the continuous beam behavior experienced by these deck systems as they span over several girders or stringers. Replicating the in-service conditions of the bridge deck was also the objective of Vyas et al. (2009) in the testing of a pultruded deck using the geometry of an actual bridge and connecting the deck to the girders using the stud in grout connections. Fatigue testing and capacity loading was performed in the setup. Two different setups were used with skew being the difference between the two. Camatta and Shing (2010) also tested GFRPH decks in fatigue and capacity loadings with the setup replicating the geometry of the bridge considered for installation. For the testing, the deck was simply supported with the deck resting on bearing pads placed on the girders.

2.3 GFRP Bridge Deck Connections

Connections between the GFRP decks and the steel superstructure have typically consisted of shear studs or bolts, which generally do not result in composite behavior (Alampalli and Kunin 2001). A new connection consisting of both a bolted connection and reinforcement added to the deck at the connection was compared to a simple bolted connection and was only found to improve the failure load by 16% in lab tests (Park et al. 2007). Keller and Schollmayer (2004) found that adhesive deck-to-girder connections have a smoother load transfer and better durability because the deck surface is not cut as in the case of bolted or shear stud connections.

Connections to steel girders contribute to the capacity and reduce long term deflections of these deck systems. Fatigue testing in the labshowed the connections have some composite action. Brown and Berman (2010) tested two deck to girder connections featuring bolts and plate shear studs welded to the girder and grouted into the GFRP deck. Keller and Schollmayer (2004) tested an adhesive connection between a GFRP pultruded deck and a steel girder and found the connection to hold after 10 million cycles of fatigue testing. Jeong et al. (2006) tested a deck system with both fatigue and static loading. The connection to the girder consisted of several through bolts and a steel plate and appeared to provide adequate performance.

2.4 GFRP Deck Damage

Hong et al. (2006) indicates that the main problems found in GFRP decks are debonding, delamination and cracking of the wearing surface. No specific inspection, repair or maintenance specifications or recommendations, however, are currently available. Telang et al. (2006) recommends the use of visual and tap-test methods as a suitable inspection method.

2.5 GFRP Bridge Deck Repair

Kalny el al. (2004) reported on a repair procedure for GFRP honeycomb members developed and implemented in the field by the manufacturer. Figure 5 shows a section view of the repair. During the repair process, the beam was first inverted so that the delaminated portion of the beam was on top. The next step was to completely remove the delaminated section. Three rebonding layers of 915 g/m^2 (3.0 oz/ft^2) ChopSM were placed on the core. Next, vinyl ester resin was applied to these and distributed evenly using a paint roller. The removed section was then placed on top of the wet resin to restore its connection with the core. Finally, dead weight was placed on top of the face to produce a near uniform pressure of roughly 3.6 kN/m^2 (75 psf) until the resin had cured. After removing the weight an additional wrap layer of 915 g/m^2 ChopSM was placed over each four exposed face laminate and core joints.

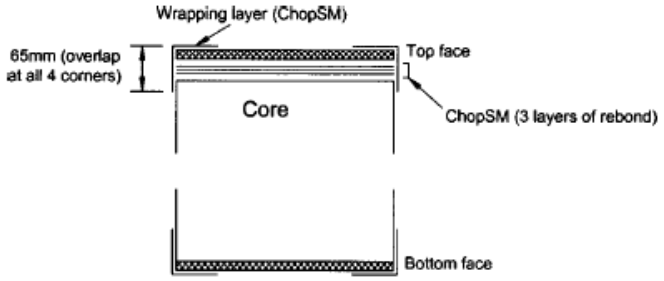

Figure 5 – Beam repair detail (Kalny et al. 2004)

The samples were tested to capacity and repaired as detailed in Figure 6. The original core and face laminates were in excellent condition; the face laminates were removed and reused. Three additional layers of 3.0 oz ChopSM were then placed on top of the core and a vinyl ester resin was applied. The face panels were then replaced on top of the wet resin for rebonding to the core. Then an external wrap of 3 layers of 3.0 oz ChopSM was applied over the four-core edges.

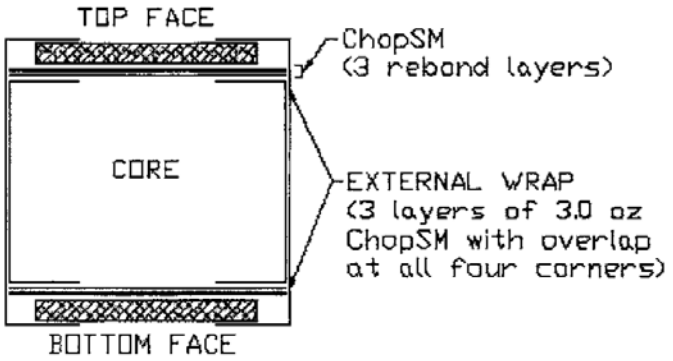

Figure 6 – Repair design for the specimens

2.6 Infrared Thermography

The present research is focused on the use of infrared thermography (IRT) and acoustic emission (AE) to detect overload damage in GFRP bridge decks. IRT is covered in volume two of this report and AE is covered in the following section.

2.7 Acoustic Emission

Acoustic emission (AE) is a widely used NDE method for detecting damage in FRP liquid storage tanks (Fowler et al. 1989). In addition, a number of researchers have begun to use AE to evaluate GFRP bridge decks. The principle behind AE is that fiber rupture and resin cracking, indicators of structural damage, emit stress waves in the structure that can be detected by sensors that are resonant in the frequency range in which these stress waves occur. Features of these stress waves can be used to distinguish them as genuine damage emissions rather than background noise or other spurious events. The following sections provide a brief description of AE fundamentals along with details of recent AE testing that has been conducted on GFRP bridge decks.

2.7.1 AE Fundamentals

Acoustic Emissions waves are elastic waves produced by the release of stored strain energy caused by fracture in the material. The release of energy causes an elastic wave in the material, detectable by a piezoelectric sensor, which converts the physical motion into an electrical signal. Figure 7 illustrates the AE detection process in which the wave is detected and analyzed by the sensor and instrument. The features of the wave shown in Figure 8 are recorded by the AE system. *Threshold* is the minimum amplitude that must be reached by the event for it to be analyzed. Events that do not exceed the threshold are ignored. Threshold values are

typically set based on the material and the testing conditions. *Energy* (also signal strength) refers to the area under the AE wave form. *Amplitude* is the peak voltage of the event and it is expressed in decibels rather than voltage (Grosse and Ohtsu 2008).

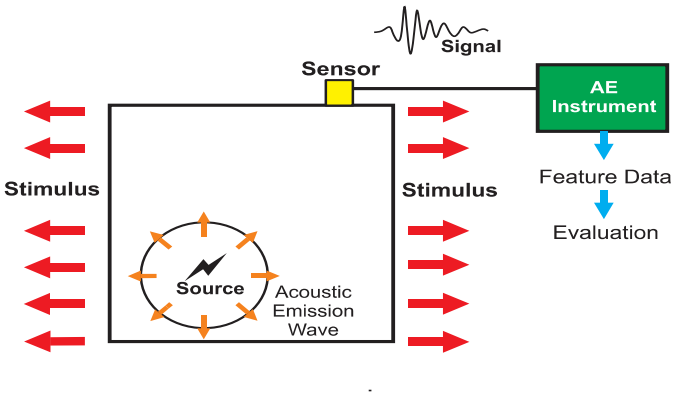

Figure 7 – Acoustic emission event

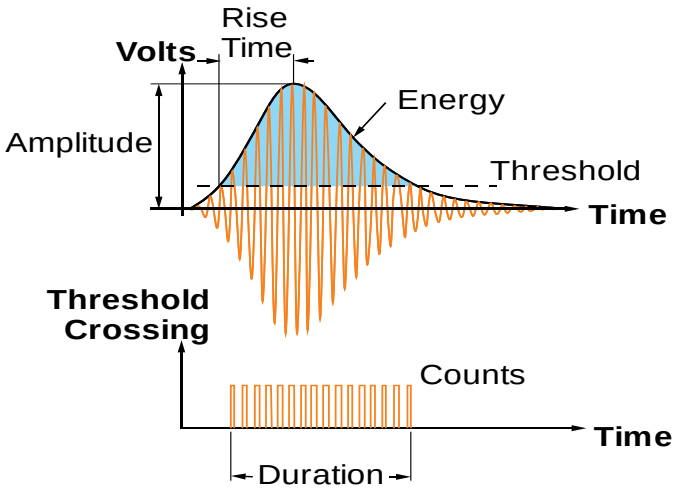

Figure 8 – Feature data gathered from a single AE waveform

AE are created by the release of strain caused by crack initiation and propagation. The Kaiser effect states that if a specimen is loaded, unloaded and then reloaded under the same conditions, AE events should not be detected until the previous load peak has been reached. This condition is satisfied if no permanent damage within the specimen has occurred. When there are emissions occurring at a lower load than a previous maximum it is known as the felicity effect. The felicity ratio (FR) quantifies the significance of this effect and its related damage; it is the ratio of load at the onset of AE activity to the previously achieved load. Therefore an event with

an FR of 1 or greater is viewed as causing no damage while an FR of less than 1 may be indicative of cumulative permanent damage (Gostautas et al. 2005).

2.7.2 Test Procedures

Figure 9 shows the AE data from an GFRPH specimen during loading (Kalny et al. (2004)). The specimen was simply supported in four point bending. Unfortunately, the test specimen was damaged before it could be loaded; the initial testing was performed on the damaged beam. One of the flat sheets was separated from the core for a length of approximately 10 ft on one side. The delaminated side was placed face down in the setup. Broadband and resonant AE sensors, optical fiber strain gages, and displacement transducers were used to instrument the specimen. The beam was loaded to a failure load of 40 kip in the test setup shown in Figure 10. An identical undamaged beam was tested in a similar setup and loading profile in a different laboratory to an ultimate capacity of 75 kip.

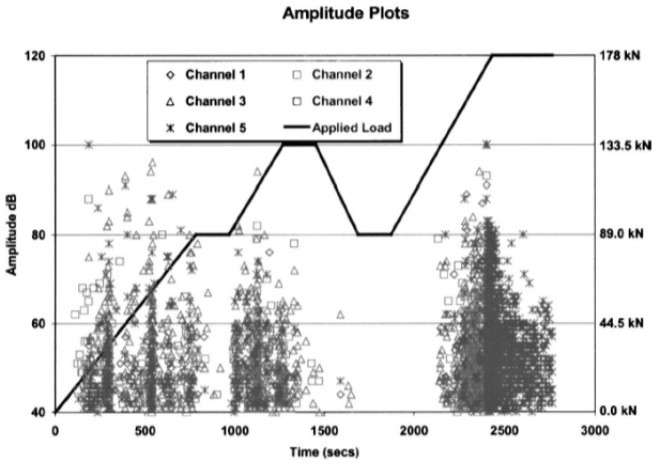

Figure 9 – Damaged beam loading to failure

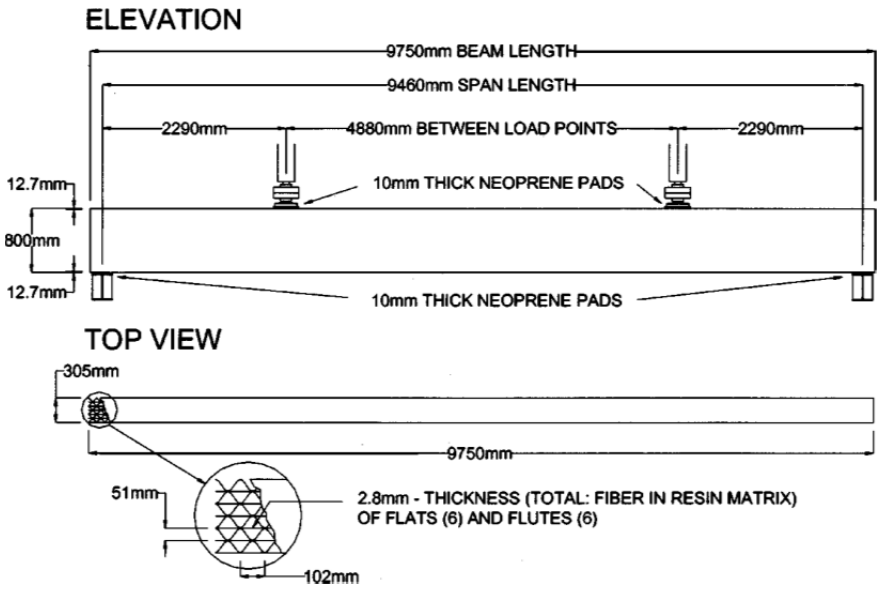

Figure 10 – Test setup and beam construction detail

Both resonant and broadband AE sensors were used as shown in Figure 11; sensors 1-3 were placed along the centerline of their respective surfaces.

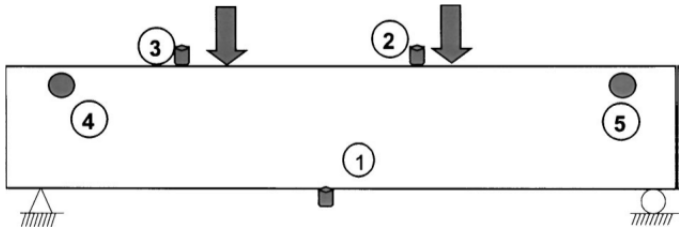

Figure 11 – AE sensor placement

Gostautas et al. (2005) also tested GFRPH specimens fabricated by KSCI and used AE to evaluate their structural integrity. Six different deck specimens were loaded using the profile in Figure 12; they were repaired and then retested using the same loading profile. This loading was designed to allow for the evaluation of Kaiser Effects and the determination of the felicity ratio for each step of the cycle. (Gostautas et al. (2005))

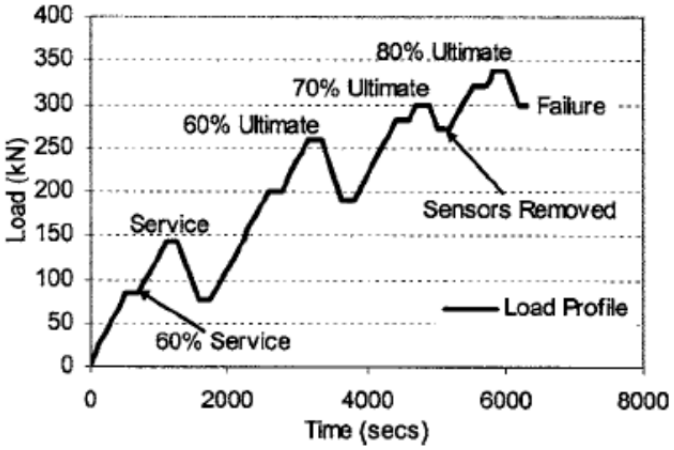

Figure 12 – Typical loading profile of all specimens

Cole et al. (2006) tested GFRPH decks using similar methods as Gostautas et al. (2005); Figure 13 shows the test setup and instrumentation. The specimen was first loaded in fatigue to two million cycles followed by static testing up to ultimate capacity. Strain and displacement were measured during the cyclic loading; following the cyclic loading the static testing was performed and evaluated using AE, strain and deflection. The cyclic loading, developed to simulate the maximum service loads according to the New York State Department of Transportation (NYSDOT), consisted of loads between 10 kN (2.2 kip) and 44 kN (9.9 kN) applied for 2 million cycles. After the cyclic loading of the specimen, it was tested in a static condition at increasing levels of load (Figure 19). The loads were held at each predetermined value and the AE emitted were monitored using modified American Society of Mechanical Engineers (ASME) 2004 guidelines for testing FRP pressure vessels. Significant emissions were said to have occurred when, in accordance with ASME guidelines,

- Emissions continue during a load hold, and
- More than 5 bursts of emissions during a 10% increase in stress, or
- More than Nc/25 counts during a 10% increase in stress; Nc is a specific count criterion

The first two criteria involve the recording of AE during the loading of the specimen and were not used for evaluation due to the possibility of non-genuine emissions during loading. The third criterion, however, was used for damage evaluation of the data in real time.

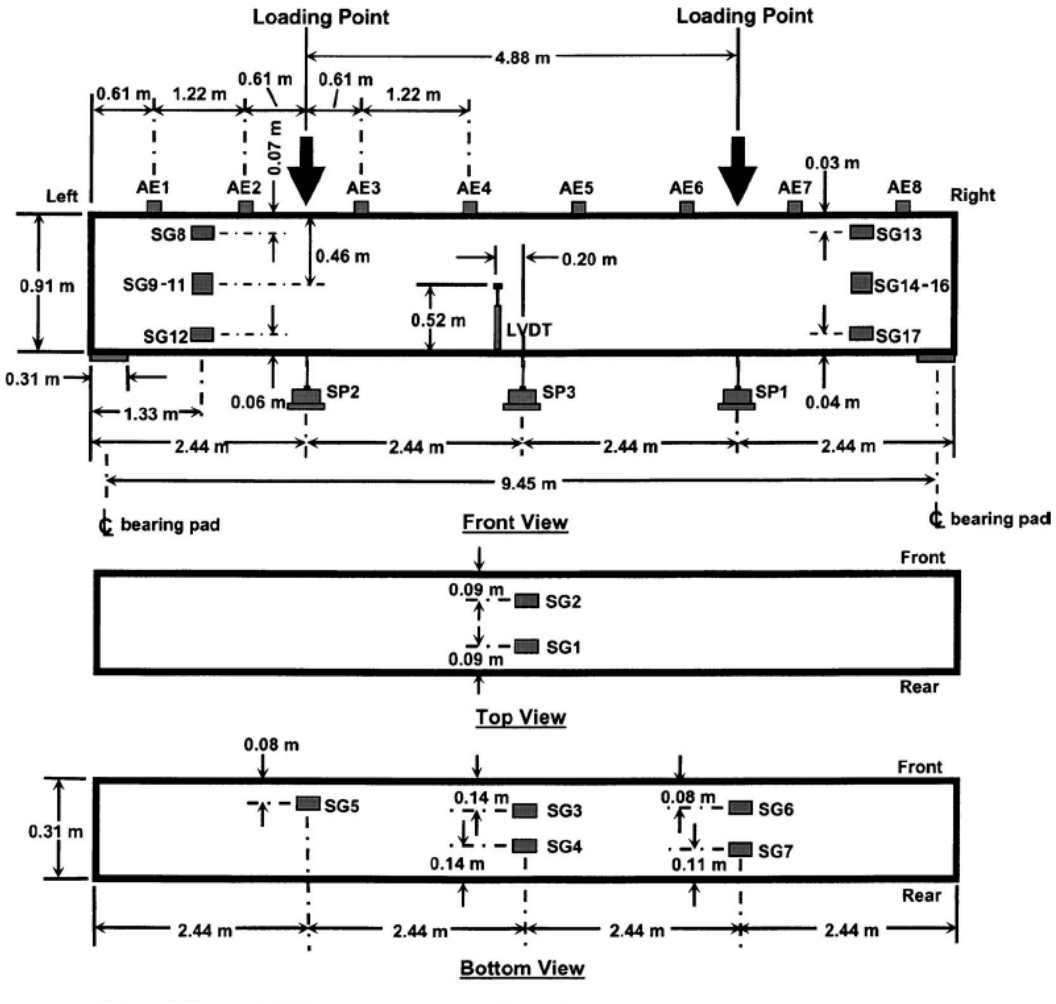

Figure 13 – Loading setup and sensor locations (Cole 2006)

2.7.3 Equipment and Settings

Cole et al. (2006), Gostautas et al. (2005), and Kalny et al. (2004) used 150 kHz sensors and broad band sensors with a response range of 100 to 2100 kHz; both were preamplified for a 40 dB gain. AE monitoring was conducted using a Physical Acoustic Corp. (PAC) system with the threshold set to 45 dB. A PAC data acquisition (DAQ) system with MISTRAS AE-DAQ software was used to collect and record the data. Each sensor was coupled to the beam using hot melt glue.

2.7.4 Evaluation Methods

Intensity, calm ratio, and comparison analysis have been used to process the AE data from different tests. Intensity analysis was developed for use in the FRP pressure tank industry by Fowler et al. (1989). Intensity analysis uses the AE signal strength on a per channel basis to calculate historic index and severity of the emissions, these values are then plotted to indicate the degree of damage in the structure under load. Comparison analysis evaluates the properties of AE events using duration-amplitude plots, event duration, event peak amplitude and the cumulative signal strength vs. time. The calm ratio is the ratio of AE activity during the loading of the structure to the AE activity during the unloading. The calm ratio is evaluated by plotting it against the load ratio, which is the ratio of load at the onset of AE activity to the maximum load experienced by the structure.

Kalny et al. (2004) used AE to monitor an GFRPH specimen during testing. Figure 14 is the loading of the damaged beam. Quiet episodes during load holds and unloading indicate that the type of damaged generated was likely associated with the opening of delaminations. Figure 15 is a plot of the cumulative signal strength of the damaged beam. It is notable that most of the energy was generated in channels 3 and 5, which is where the final failure occurred. Capacity was reached at 40 kip and was the result of the delamination of the damaged section.

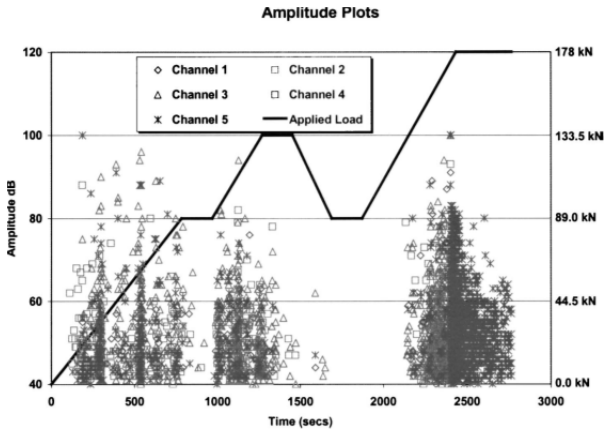

Figure 14 – Amplitude vs. Time of damaged beam (Kalny et al. 2004)

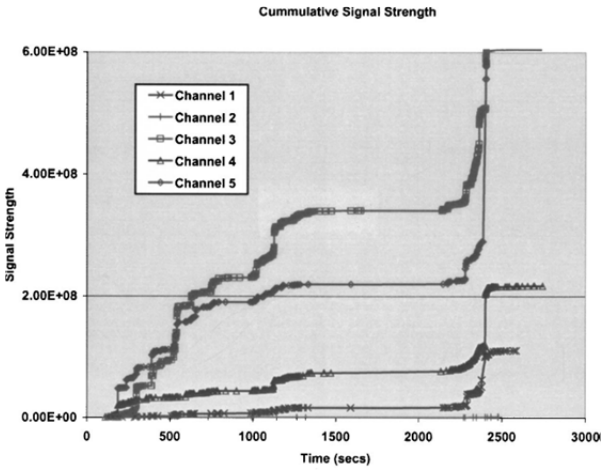

Figure 15 – Cumulative signal strength for damaged beam. (Kalny et al. 2004)

Kalny et al. (2004) reloaded the repaired beam using the same loading profile as for the damaged beam. Figure 16 shows the cumulative signal strength for both tests. The ultimate capacity of the repaired beam was found to be 125 kip. The cumulative signal strength

magnitude of the repaired beam was significantly less than that of the damaged beam, indicating that the Kaiser effect was present.

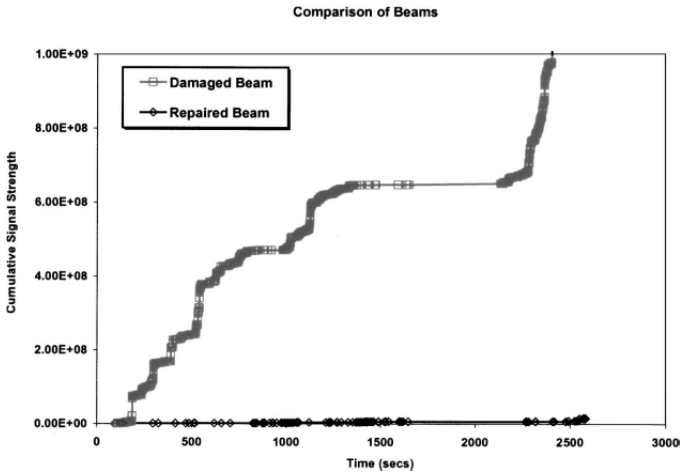

Figure 16 – Cumulative signal strength for both damaged and repaired beams

While comparison analysis compares the data to a previous loading and is based on the felicity ratio and Kaiser Effect, intensity analysis has been used in the pressure vessel industry and has been adapted to deck monitoring. (Gostautas et al. (2005))

Gostautas et al. (2005) used intensity analysis to evaluate AE data from the loading of GFRP deck specimens. Intensity analysis is a method of evaluating the structural significance of an event by calculating two values called historic index and severity from the signal strength and evaluating their change over time (Fowler et al. 1989). Historic index is an analytical method of estimating the changes of slope in the cumulative signal strength against time by comparing the signal strength of the most recent hits to all the hits of that channel and is calculated as follows:

$$H(t) = \frac{N}{N-K} \frac{\sum_{t=K+1}^{N} S_{Oi}}{\sum_{i=1}^{N} S_{Oi}} \qquad \text{Equation 1}$$

where N is the number of hits up to and including time t, S_{oi} is the signal strength of the i^{th} event, and K is an empirically derived constant based on material type (Table 1). The algorithm compares the signal strength of the most recent hits to all the hits of that channel. Past tests have shown a rapid change in historic-index values during the first 100 hits to be normally associated

with the cracking of excessive matrix material under initial loading. For that reason the historic index is only calculated after this number has been reached.

Table 1 – K values for FRP tanks

Number of hits	K
≤ 100	Not applicable
101 to 500	0.8N
>500	N-100

Severity is the average signal strength for a given number of events having the largest value of signal strength and is calculated as follows:

$$Sr = \frac{1}{J}\sum_{i=1}^{N} S_{Om} \qquad \text{Equation 2}$$

where S_{Om} is the signal strength of the m^{th} hit, with the ordering of m based on magnitude of signal strength, and J is an empirically derived constant based on material type. For $N \leq 20$, J is not applicable, and for $N \geq 20$, $J = 20$. Intensity plots are created by plotting severity and historic index on a log scale (Figure 17). Evaluation of the structure is facilitated by dividing the plot into intensity zones which indicate the structural significance of the emissions. The numbers plotted on the chart indicate intensity for an individual channel. Intensity values of high structural significance plot toward the top right hand corner while values with less significance plot toward the bottom left.

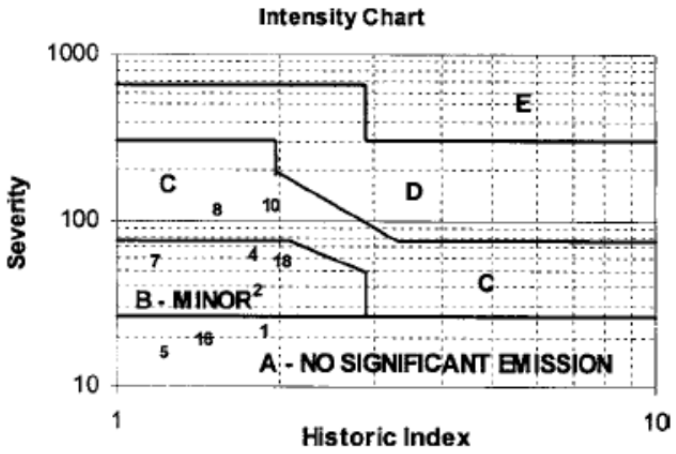

Figure 17 – Typical intensity chart from the metal piping system

Figure 18 shows the intensity plot for the GFRP deck testing by Gostautas et al. (2005). Only the maximum severity and historic index values for each channel are shown. Despite the difference in magnitude between the severity from the piping system and the magnitude of severity observed in Figure 18, the trends toward failure hold true. Channels two and five were near the damaged regions and experienced the largest intensity values. Damage zones were not established due to the small numbers of specimens.

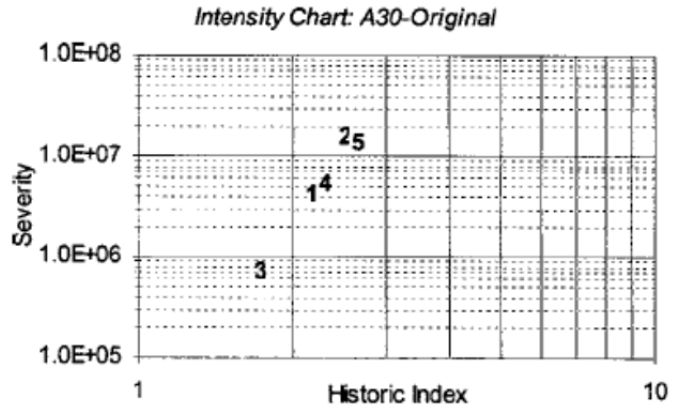

Figure 18 – Intensity results of an undamaged panel

Cole et al. (2006) loaded the specimen to the previous level of the maximum load and evaluated the AE of the test. The AE were evaluated in real time; the activity did not meet the criteria for "onset of significant" emissions previously defined as continuing emissions during load holds. The specimen was loaded in a stair step manner to 144 kN (32.4 kip). No significant

emissions were detected during these load holds (Figure 19a). Figure 19b is a plot of the results for loading number five. The first sign of continuous AE occurred during load hold number four. The following load holds all have the continuing AE during the load hold period. Significant damage occurred during load hold five at 267 kN (60.0 kip). The onset of damage was confirmed by the following load holds seven and eight. The load level was lowered during load hold seven and the AE stopped during the short hold; AE activity returned during load hold eight, indicating the onset of damage. The loading was continued up to 498 kN (112 kip). Figure 19c is a plot of loading number six and took place three days after loading five. The load holds indicate that the damage began again after load hold three; during load hold four, AE of significant amplitude was observed. No specific threshold for "high amplitude events" was defined.

The data were also analyzed using the felicity ratio. During load hold four, the felicity ratio was 0.71, indicating damage in the section. Looking at the felicity ratio during this loading indicates that the damage was not present below the load where damage first occurred.

Cole et al. (2006) also evaluated the location of the damage during the loadings. The sensors were located linearly along the top of the deck to cover the entire specimen and to facilitate locating the AE events (Figure 20). The general damage locations were observed during each load hold using the cumulative energy per sensor. Plots a and b correspond to loading number five. Plot a was prior to the damage and b was the reloading at 276 kN (62.0 kip) just after the suspected damage. Sensors four and six were observed to have the larger amount of energy during the first reloading. Plots c and d correspond to load holds number five and six of loading number six. The energy magnitudes were initially large at mid-span (plots a and b) and during subsequent loadings (plots c and d) were observed to migrate to the load points during loading number six. The damage was assumed to follow this same pattern.

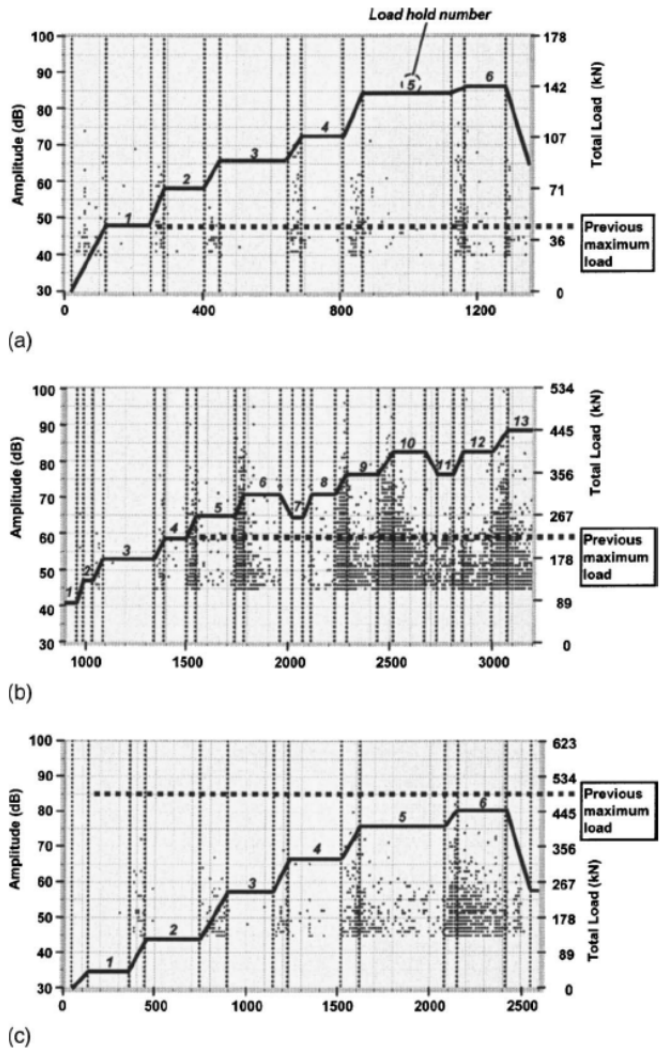

Figure 19 – Amplitude and load vs. time (Cole 2006)

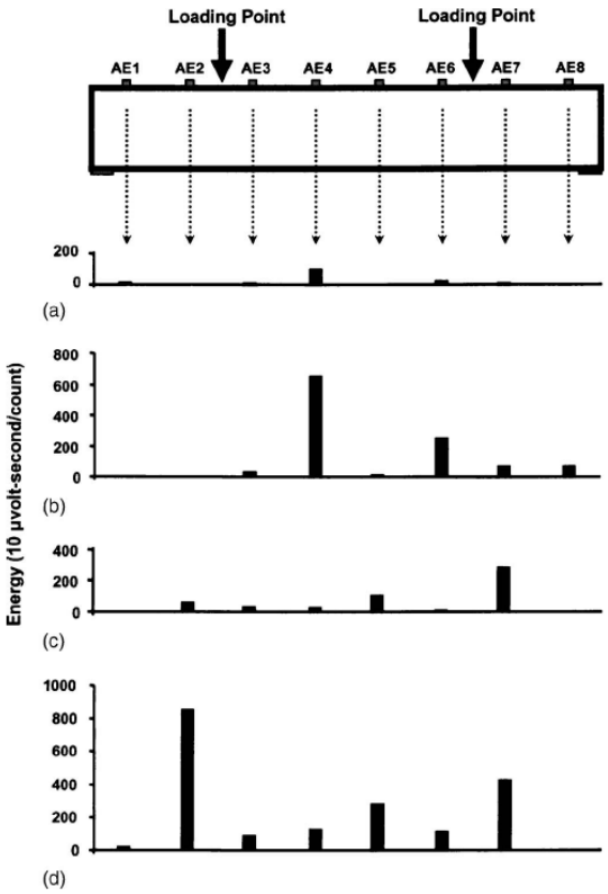

Figure 20 – AE results per sensor (Cole 2006)

Significant structural damage was assumed to occur when the load deflection curve began to deviate from linear. Using this criterion and the load deflection data, significant damage was found to occur at 223 kN (50.1 kip). AE monitoring was used to pinpoint the load which caused structural damage to the specimen, which was 267 kN (60.0 kip). The specimen held a maximum load of 747 kN (168 kip). AE sensors were not in place for the ultimate loading. Figure 21 is a picture of the damaged beam.

While AE testing on GFRP bridge components has been limited primarily to laboratory tests, a few AE tests have been conducted in the field on both GFRP and concrete structures. A field test of a GFRP deck was performed by Joeng et al. (2006). The deck was tested using a load truck with three axles and a total weight of 254 kN (57 kip). The deflection was 1.74 mm (0.0685 in.); considerably less than 2.5 mm (0.0984 in.) (L/800). The strain was only 13 % of the ultimate strain as measured in the lab. Turner et al. (2004) performed a load test on a GFRP

deck in South Carolina using load trucks near the HS 25 load level. Turner et al. evaluated the composite action of the deck and girders using service loads.

Figure 21 – Picture of the specimen after failure

2.7.5 Field Testing

Luo et al. (2004) used AE to evaluate the structural integrity of an in-service concrete bridge pier on a train bridge. Calm ratio was used in the analysis of the structure and a new index was developed to replace the load ratio, the ratio of the repeated train load at the onset of AE activity to the relative maximum load for inspection period (RTRI). Introducing this factor made it possible to use the calm ratio analysis when the historic maximum load on the structure is not known.

3 Research Approach and Specimen Selection

The primary focus of this research was on the development of NDE methods that can be used to evaluate GFRP bridge decks for structural damage. AE and IRT are the two selected NDE methods to be developed for this purpose and were applied to GFRP deck specimens that had been loaded beyond their structural capacity. The motivation was to determine if the NDE methods could distinguish structurally damaged decks from non-damaged decks.

Three different commercially available GFRP deck systems were selected for this research. They were designed and fabricated by Zellcomp, Structural Composites, Inc., and Kansas Structural Composites Inc. Each deck was tested independently in positive and negative bending test setups to capture the individual behavior of each action. The details of the test setup are presented in Chapter 4.

The Zellcomp (designated as "Deck A") system is pultruded in two separate pieces and is available in 5, 7, and 9 in. depths (Figure 22). The 5-in. deep section was chosen for this research. The bottom panel is composed of a bottom plate and four I-shaped sections (hereinafter referred to as "webs") that are pultruded as a single unit. The top plate is a pultruded sheet that provides support for the wearing surface and transferred wheel loads to the webs. Top plates are attached to the bottom panel using self-tapping countersunk screws; this is typically done in the field during erection.

Figure 22 – Zellcomp deck panel (Deck A)

The Structural Composites, Inc. (designated as "Deck B") system is a foam-filled GFRP trapezoidal deck (Figure 23). This deck type is manufactured with threaded sleeves that are used to attach the deck to the bridge superstructure with clips. Urethane preforms are used to form this deck. The preform is used to hold the wet layup fiber in place until it has cured. The depth of the deck used for this investigation was 5 in.

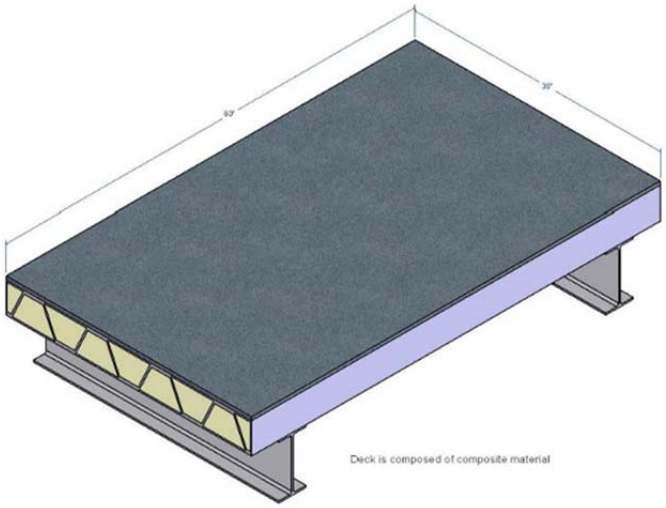

Figure 23 – Structural Composites Inc. deck panel (Deck B)

The glass fiber-reinforced polymer honeycomb panel (GFRPH) system is manufactured by Kansas Structural Composites, Inc. GFRPH panels are made by sandwiching a honeycomb core of chopped E-glass between two facesheets composed of unidirectional and bidirectional layers of E-glass (Figure 24). Both the facesheets and the honeycomb core are manufactured using vinyl ester resin. The corrugated core varies in depth as required by design conditions. The honeycomb core provides shear resistance and is configurable as needed by the design requirements. Deck panels are typically manufactured with pockets to accommodate stud connectors.

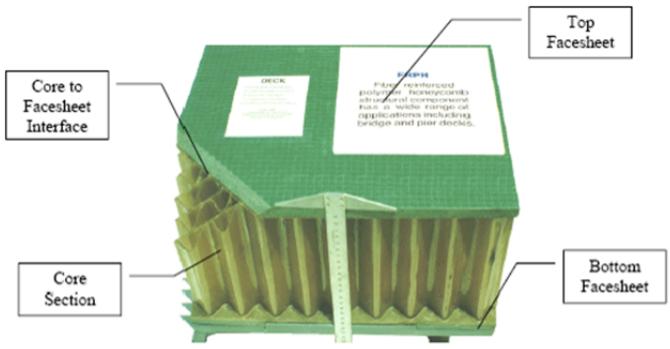

Figure 24 – GFRP honeycomb deck panel

4 Test Setup

Because GFRP deck panels are typically designed to span continuously over several supports, capturing both the positive and negative bending behavior of each deck type during structural testing was necessary to ensure that the damaged deck condition was as close to actual field conditions as possible. In addition, concentrated loading was used to simulate wheel loading that typically controls the design of a bridge deck.

This chapter describes the test setup used to impose damage on the GFRP deck systems for the purposes of applying acoustic emission or infrared thermography. Bridge deck sections were subject to concentrated loads to simulate wheel loads. Unique loading configurations were used to isolate positive and negative bending, which was important to the evaluation of AE and IRT NDE.

4.1 Wheel Load Simulation

AASHTO load and resistance factor design (LRFD) requires wheel loads to be distributed over a tire contact area 20 in wide and 10 in. long. Structural testing has traditionally used a steel plate to simulate the tire patch.

Distribution of load over the tire contact area on an GFRP bridge deck was explored in detail in Majumdar et al. (2009). Majumdar compares the truck tire actual pressure distribution with that of a steel plate (Figure 25). Majumdar found that the steel plate caused higher pressures along its perimeter; these pressures, however, were not present in the actual tire pressure profile (Figure 26). In addition, use of the steel plate caused localized punching around the plate edge that is not likely to occur under a tire.

Vyas et al. (2009) used neoprene pads to test a Zellcomp deck and found that this approach avoided the punching shear failure mode associated with steel bearing plates. Based on the recommendations of Majumdar and Vyas, neoprene bearing pads were adopted in the present experimental program.

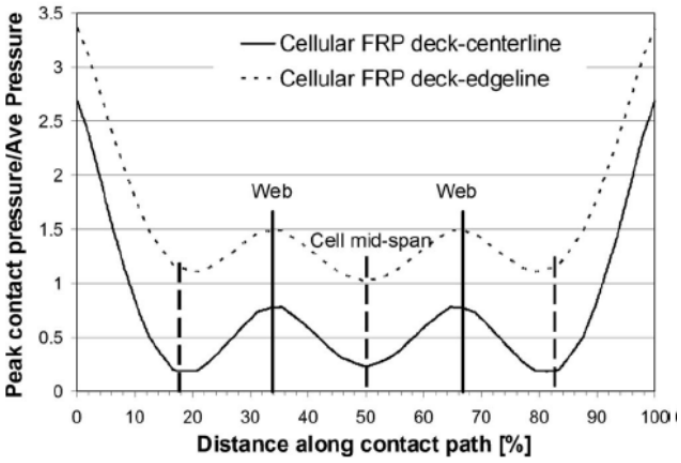

Figure 25 – Steel bearing plate pressure profile (Majumdar 2009)

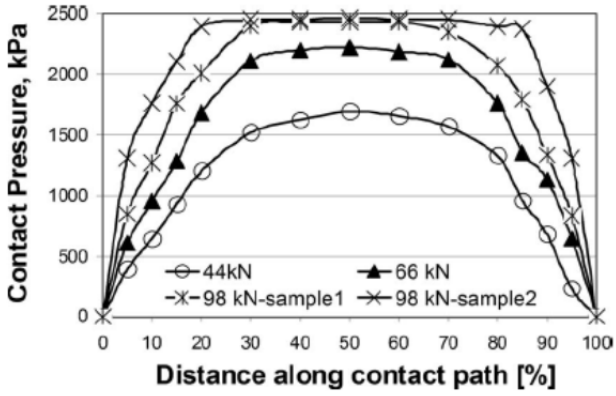

Figure 26 – Actual tire pressure profile (Majumdar 2009)

4.2 Span and Support Configuration

The test setup was designed to simulate the actions caused by wheel loads on a GFRP deck such as that of the bridge crossing the Hillsboro canal in Belle Glade, FL (Figure 27). The Hillsboro deck system was composed of 5-in. deep Zellcomp deck on W 24 x 68 steel girders that were spaced at approximately 4 ft (Figure 27) center-to-center. The girders were oriented in the direction of traffic while the GFRP deck was aligned with the abutment, resulting in a skew angle of approximately 62 deg. The deck panels spanned approximately 54-in. center-to-center and were continuous over multiple supports.

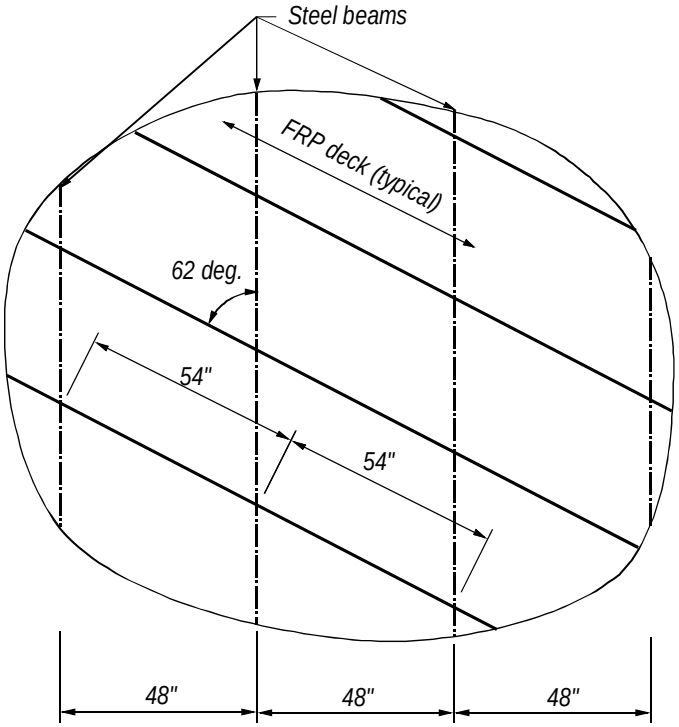

Figure 27 – Belle Glade bridge deck layout

To avoid testing an indeterminate system, it was necessary to design two different test setups to evaluate the positive and negative bending behavior (Figure 28) independently. The prototype model shown in Figure 29 was designed to duplicate the conditions experienced by in-service decks. The model was analyzed using wheel load configurations that produce the maximum positive and negative moments, as shown in Figure 28. It was the aim of the test that AE data be collected and evaluated at all load levels. Consequently the test procedure included cycles at the working load level.

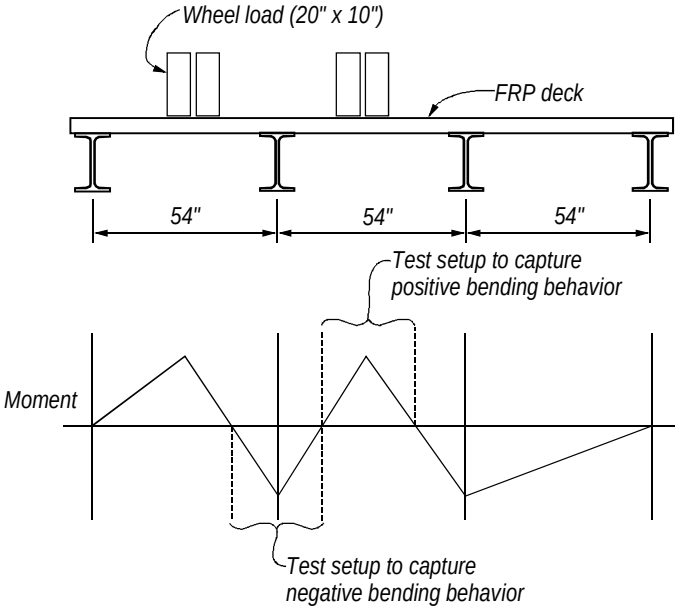

Figure 28 – Belle Glade deck configuration

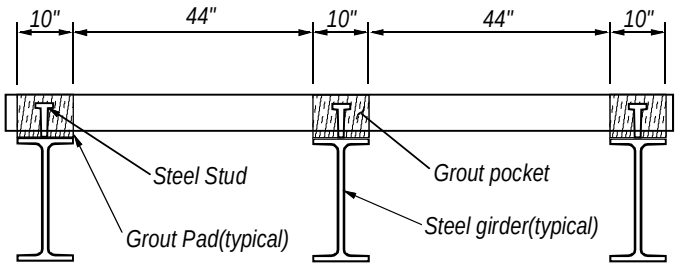

Figure 29 – Test prototype geometry

Figure 30 shows the positive bending setup. In this configuration the panels were tested in the upright position to simulate positive bending in the typical installation with load applied thru the 10-in. by 20-in. bearing pad.

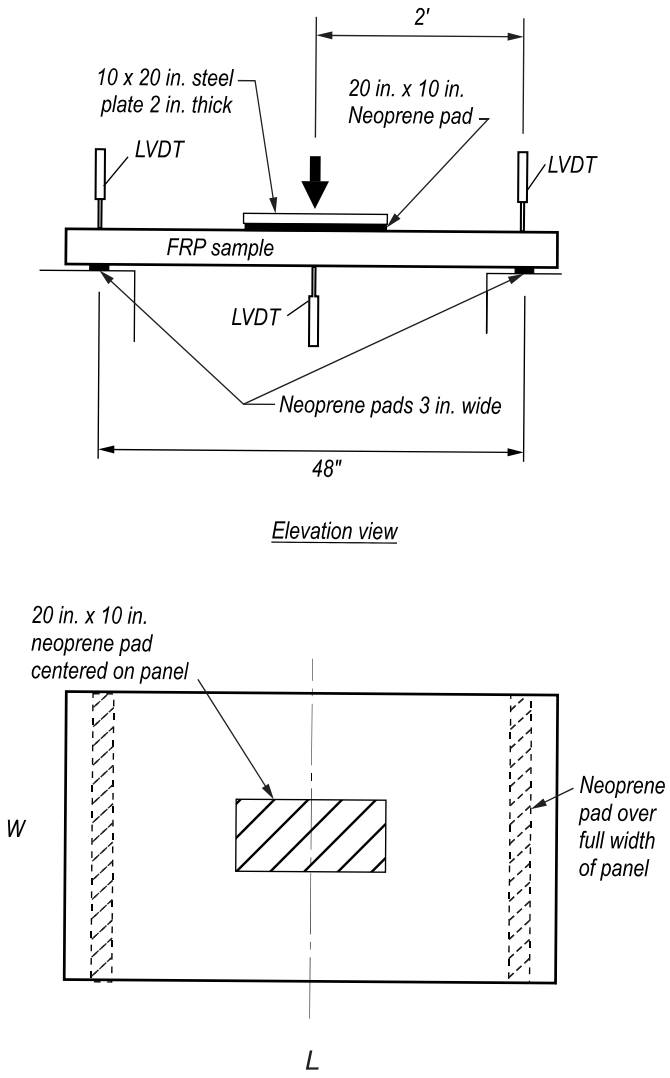

Figure 30 – Positive bending setup

Figure 31 shows the negative bending setup. The panels were inverted before placement in the test setup to simulate negative bending. Before testing, the deck to girder connection was constructed according to manufacturer's recommendations to simulate field support conditions for that particular deck type. Wheel loads on this setup were simulated by placing two 10-in. by 10 in. bearing pads between the deck and supports. Neoprene bearing pads were used for load application and support to reduce ambient and mechanical noises from the supports and the hydraulic actuator; this reduced spurious AE activity.

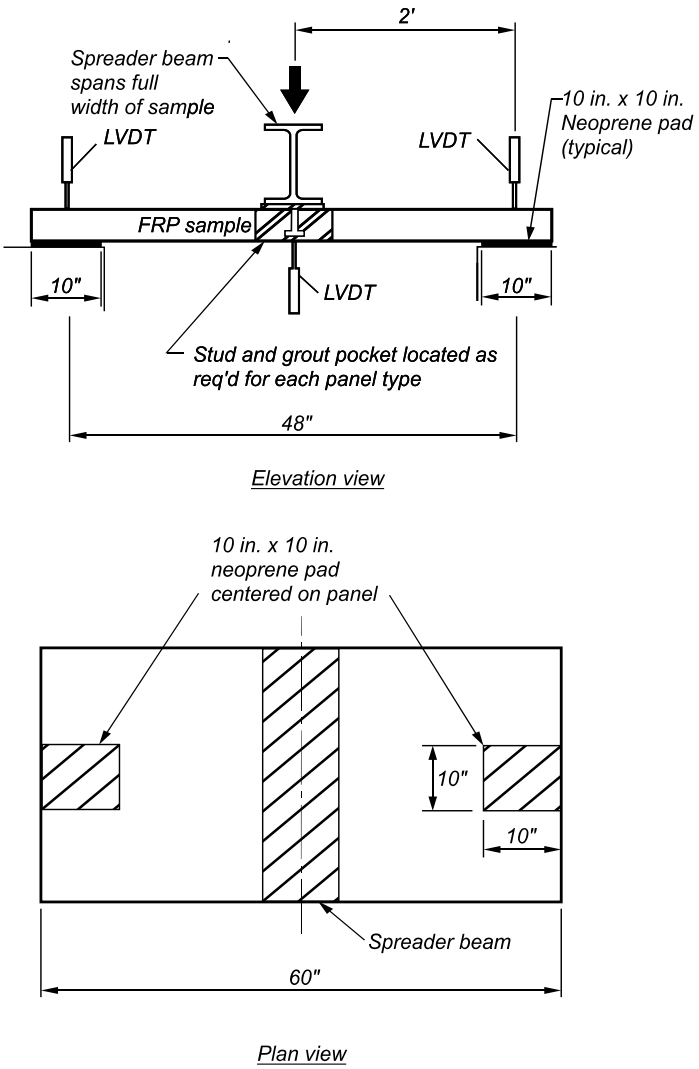

Figure 31 – Negative bending setup.

4.3 Service Load Development

AASHTO LRFD specifies that a deck system should be designed for 16 kip wheel loads based on a 32 kip axle from the HL-93 notional truck load. In addition, a dynamic load amplification factor of 33% increased the load to approximately 22 kip. For the AE testing, the specimens were first loaded stepwise up to the selected service load to condition the deck. This is referred to as the undamaged service test (UST). The ultimate load test (ULT) was then conducted in which the specimen was loaded to its ultimate capacity to cause damage without completely destroying the specimen. Finally, stepwise service loads were again imposed on the damaged deck to determine how well AE could detect the damage that had been imposed by the

ultimate strength test. These are referred to as damaged service testing (DST). Load steps were separated by a brief load reduction to allow observation of Kaiser and felicity effects during reloading.

GFRP material is subject to felicity effects; therefore, a series of loadings must be monitored in order to achieve the behavior of an in-service deck system. The specimens were tested repeatedly at the service load level both before and after the ultimate loading. These testing procedures are outlined in the following sections.

Because load is required to generate acoustic emissions cyclic loading in the service load range was necessary both before and after the ultimate load test. For deck A, the load levels were calibrated using the load distribution strain data obtained from the October 2009 test of the GFRP deck in Belle Glade. To determine the appropriate level of loads for Decks B and C, an analytical model of the two-span prototype was developed and analyzed for the service level moment.

4.3.1 Deck A Test Load

To calibrate the analytical model of the prototype, the results from the bridge load test performed on the Hillsboro canal crossing in Belle Glade in October 2009 were analyzed. The soffit of the GFRP deck was instrumented in several locations with 5-mm strain gages to measure flexural stresses. The gages were generally placed at the midspan of the deck just under one of the panel webs (Figure 32). The measured strains were taken at locations of maximum positive moment and typically indicated tension.

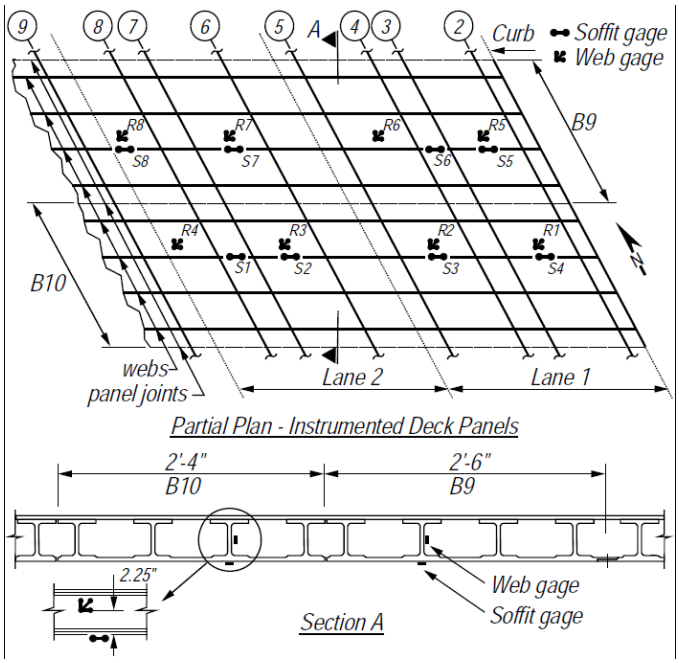

Figure 32 – Belle Glade instrumentation

The truck was loaded in four increasing increments that resulted in rear wheel loads of 9.5, 12.5, 15 and 17.5 kip. Figure 33 shows the load-strain relationship for soffit gage S7, which was located in the middle of the span between girder 6 and 7. The measured strains came from a truck position in which the wheel passed directly over the S7 gage, thus creating the maximum moment at that location. Figure 33 shows that the service loads remained in the linear elastic range.

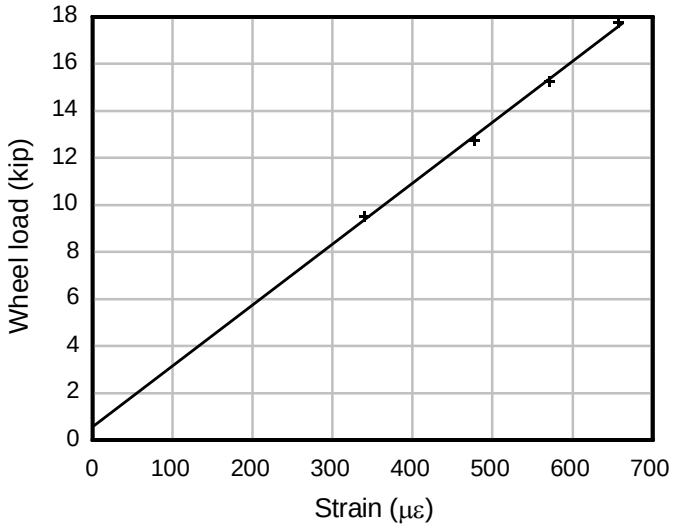

Figure 33 – Belle Glade load test results

To relate the results of the bridge load test to those of the analytical model, the percentage of the wheel load carried by each web must be known. This was accomplished by tracking the truck position (and wheel position) using global positioning system (GPS) positioning during the Belle Glade load test. Figure 34 shows the strain in S7 plotted against the wheel position. The plot indicates that the strain peaks when the wheel is directly over the gage and quickly decays as the wheel moves away from the gage. A cross-section of the deck is shown in the figure to show graphically the web positions relative to the wheel load. The web spacing shown in the figure is nine inches because the GFRP panels are placed at an angle to the truck's path (Figure 35).

The strain values registered at the strain gage when the wheel load was over each web was summed. Assuming that the system remained linear during the bridge test and that the Maxwell-Betti reciprocal work theorem holds, this sum is the total effect of the wheel load when it is positioned directly over the strain gage. The distribution factor can then be calculated by dividing the peak strain by the sum of the strains, which was found to be 0.37. This indicates that a single web will carry 37% of the wheel load when it is directly over that web.

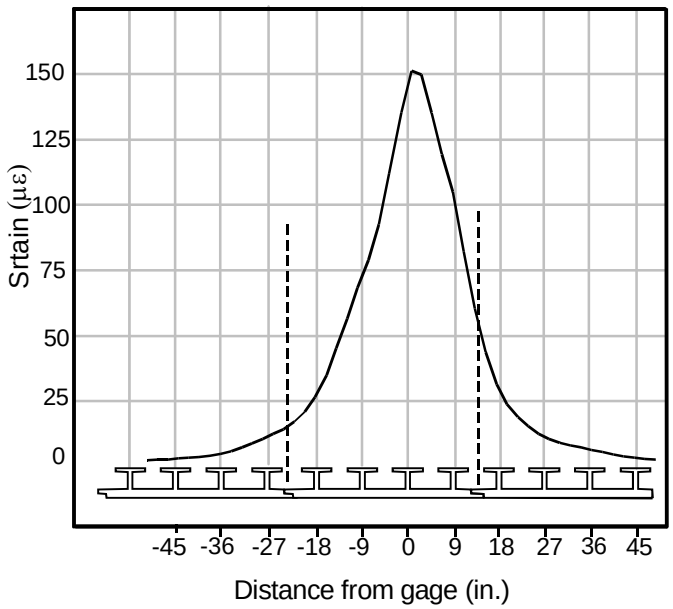

Figure 34 – Strain distribution profile

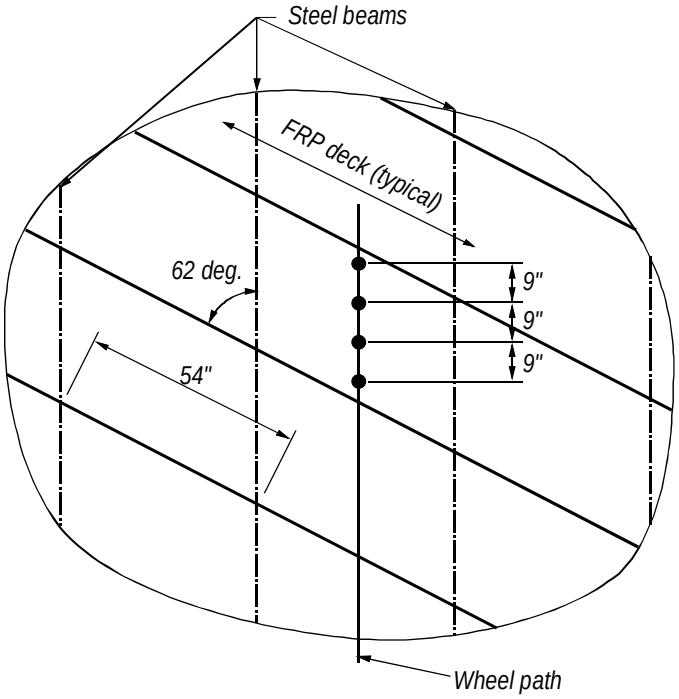

Figure 35 – Wheel path web intersection

4.3.2 Pilot Test Results

The moment-strain relationship for each web in the GFRP deck was obtained from a three-point bending test conducted in the laboratory (Figure 36). Although the top plate is fastened to the bottom panel with self-tapping screws, Cousins et al. (2009) found no significant composite action between the two sections. For this reason, the pilot test setup included only the bottom panel and was simply supported to facilitate the calculation of the moment corresponding to the measured strain. Strain gages similar to those used in the bridge load test were attached to the soffit of the test section.

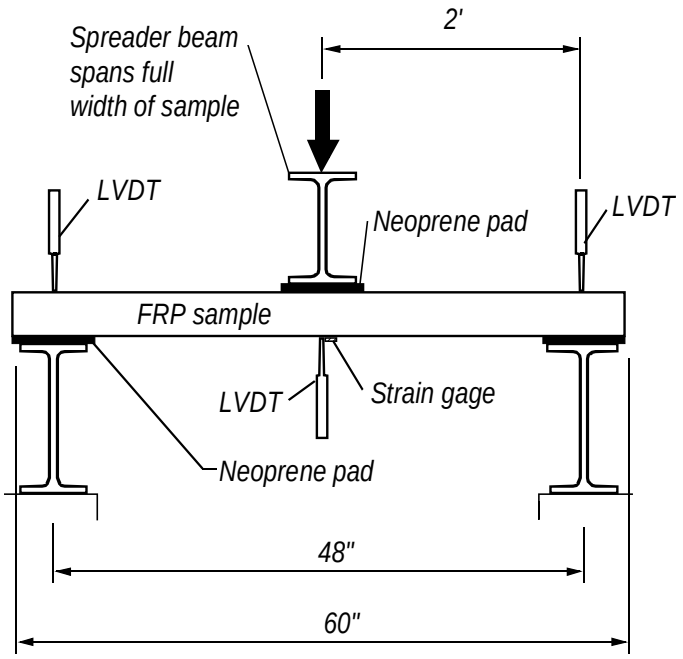

Figure 36 – Pilot load test setup

The moment-strain relationship measured during the pilot test was combined with the Belle Glade bridge test data (Figure 33) to develop the wheel load-moment relationship shown in Figure 37. The moment carried by the deck is in terms of moment per web. Because a relatively stiff steel cross beam was used to load the deck in the pilot test, the distribution factor was assumed to be 0.25, indicating that each web carried one quarter of the total applied load. This plot will be used to validate the analytical results presented in the next section.

4.3.3 Test Setup Model

The positive bending test setup was designed to use the AASHTO LRFD load patch placed at midspan and was analytically modeled as shown in Figure 38. The model shows the patch load and associated moment diagram. The total load shown is that necessary to produce a maximum moment of 73.4 kip-in. Using a web distribution factor of 0.37 gives a maximum web moment of 27.2 kip-in. Entering the plot in Figure 37 with this moment gives an equivalent wheel load of 16 kips, which is one of the target service loads. Consequently, the load required to generate a web moment in the test specimen that is equivalent to that obtained from the bridge test is 8.4 kip.

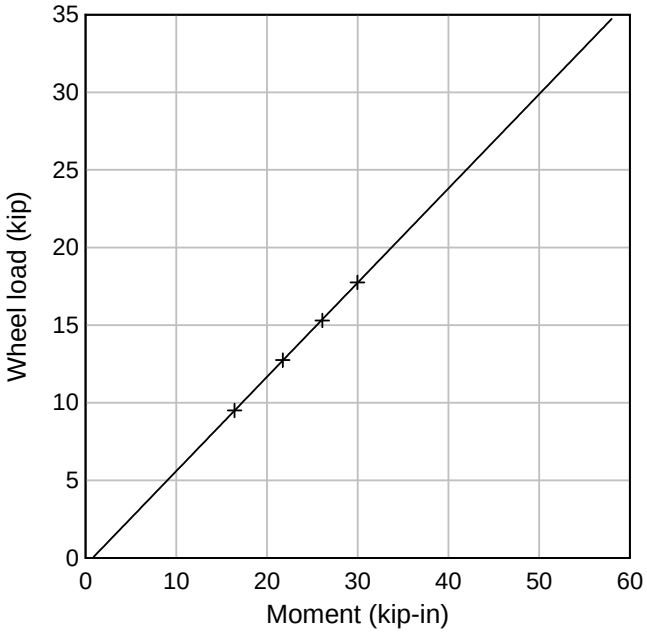

Figure 37 – Wheel load vs. moment in each web

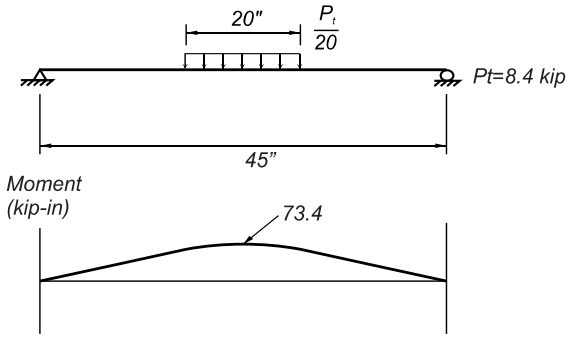

Figure 38 – Test setup to simulate positive bending

The negative bending setup was designed to simulate the actual support conditions with a single grouted stud at the mid-span (Figure 39). This location was also used to apply load. To ensure negative bending, the specimen was inverted in the test setup. Using the same approach as for the positive bending, the required applied load to simulate the moment caused by a 16 kip wheel load was 7.25 kip.

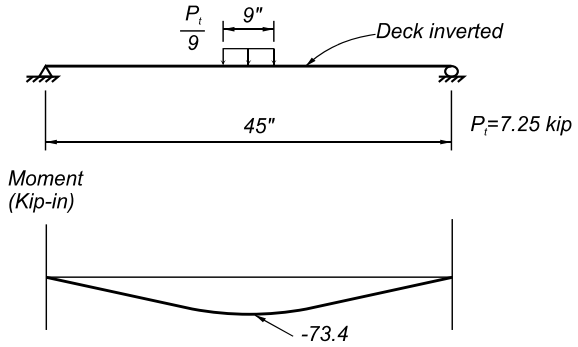

Figure 39 – Test setup to simulate negative bending

To provide a reasonable range of AE load cycles, two service load steps in addition to the design load of 16 kip were chosen. An 8 kip load step was arbitrarily chosen to provide 50% of the design load. The design wheel load of 16 kip was amplified by 33% to give a load of 22 kip to account for the dynamic load allowance required by AASHTO LRFD. The test loads corresponding to 8 kip and 22 kip wheel loads were calculated assuming linear elastic behavior; each load was calculated for both loading patterns. The resulting maximum moments from each load and each pattern are summarized in Table 2 along with the equivalent load required to generate the same moment in the test setup as in the prototype. These resulting values provide a range of moments-per-loading pattern. To obtain a more realistic set of moments, the data from a load test performed on the Belle Glade Hillsboro canal bridge were compared to the data from a pilot lab test of deck A. To simplify the load step procedures the load steps were rounded to 5, 9, and 12 kip for both positive and negative bending tests.

Table 2 – Summary of load steps for deck A

Wheel Load (kip)	Load test Moments (kip-in)	Equivalent test setup loads(kip)	
	Positive and Negative	Positive	Negative
8	37.7	4.2	3.6
16	73.4	8.4	7.25
22	100	11.6	10.0

4.3.4 Service Loads for Decks B and C

Field and laboratory structural data were unavailable for decks B and C. In addition, Decks B and C had transverse stiffnesses that appeared to be significantly higher than that of deck A. Consequently, unlike in deck A, nearly the full wheel service load was assumed to be

carried by the section tested in the laboratory. The maximum service load was chosen as 20 kip, which is slightly less than the full service load. Two additional load steps of 50% and 75% were incorporated into the service loading. The purpose of intermediate load holds was intended to check for Kaiser and Felicity effects, as prescribed in ASTM 1067.

5 Specimen Construction

This chapter describes the construction details used to fabricate the specimens for both the positive and negative bending test setups. The negative bending setup required that the fastener system for the particular deck system be used to fasten the deck to the steel support member, which was then used to load the deck in flexure (see Chapter 4 for details).

The specimens are designated by their system name (A, B, or C) and whether they were tested in negative (N) or positive (P) bending . For instance, specimen B-N was constructed from Deck B and was tested in negative bending.

The deck fabrication details are given in Chapter 3.

5.1 Deck A

The positive bending specimen, A_P, consisted of a single 31 in. wide x 55 in. long panel with a top plate attached using mechanical fasteners per manufacturer's recommendations. To simulate negative bending (flexural tension in the top plate), the loading frame was fitted with a shear stud. This stud was grouted into specimen A_N as shown in Figure 40.

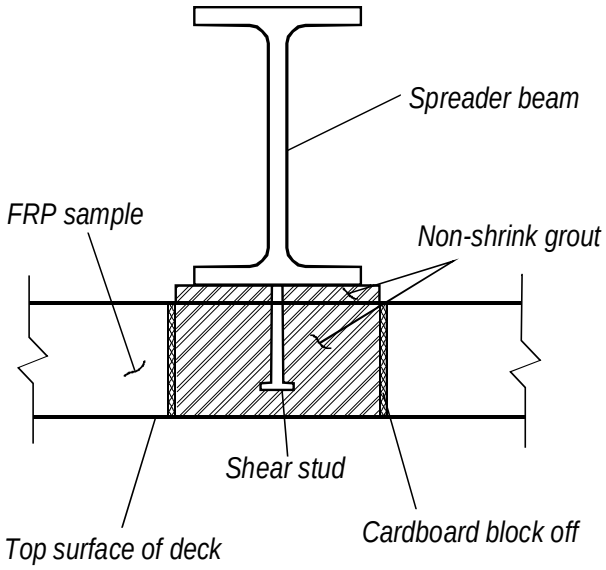

Figure 40 – Stud-in-grout connection detail

Figure 41(a) shows the shear stud and grout pocket detail used to connect the loading beam to the specimen for the negative bending test. Although a stud welding gun is typically

used in the field for attaching shear studs, the single 7/8-in. diameter stud was attached to the loading beam with a fillet weld. A 3-in. diameter hole was drilled through the bottom panel and shims were used to provide a 0.5-in. gap between the loading beam and deck into which the grout could flow. A non-shrink grout (Sikagrout 300) was then poured into the stud pocket of the bottom panel until the space under the panel and the grout pocket was filled (Figure 41b). Mechanical fasteners were used to connect the top plate to the bottom panel before the grout set.

(a)

(b)

Figure 41 – Specimen A_N (a) stud and beam assembly and (b) grout pour into pocket

5.2 Deck B

The positive bending specimen (B_P) was 36 in. wide and 55 in. long and had a wearing surface applied by the manufacturer. The negative bending specimen (B_N) had a significant amount of cracking on the wearing surface; this was present prior to testing as shown in Figure 42. The wearing surface was applied to the top of the deck specimen and was not a structural component of the deck according to the manufacturer. Due to the small number of specimens tested the effects of the cracked wearing surface could not be quantified in this investigation.

Figure 42 – Specimen B_N wearing surface cracking

For B_N, the mechanism for attachment to the girder was a series of bolts and clips which secured the girder to the deck (Figure 43). These were placed away from the girder connection as shown in Figure 44, however. The test setup used the spreader beam but the attachment was not in place because it would not have affected the AE data.

(a) (b)

Figure 43 – Specimen B-N (a) girder connection and (b) bolt size

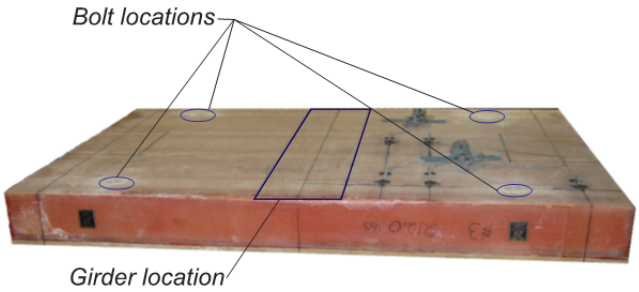

Figure 44 – B_N girder connection locations

5.3 Deck C

The positive bending specimen (C_P) was a solid section that was 36 in. wide, 60 in. long and 5 in. thick. The negative bending specimen (C_N) used a single attachment point composed of steel plate and pipe (Figure 45(a)). GFRP was cut to form a recess into which the connection was placed (Figure 45(c)). A threaded stud was welded to the loading beam (Figure 45(b)) and was inserted through the deck and into the recessed portion of the steel fixture to secure the deck to the loading beam. Neoprene was placed between the loading beam and deck to provide acoustic isolation. This is the typical manner in which the deck is secured to the superstructure in the field; following deck installation sand would be used to fill the cavity and the wearing surface would be applied.

(a)

(b)

(c)

Figure 45 – B_N (a) attachment flange, stud and nut (b) beam with stud and (c) soffit view of the assembly

6 Repair Design and Construction

Specimens were tested to failure during the damage detection phase of the project and were then repaired to evaluate proposed repairs to the damaged sections of the decks. None of the deck manufacturers had formal repair recommendations available for their particular deck system. Informal discussions with the manufacturers indicated that it is usually more cost effective and expeditious to replace damaged deck than to repair it. One exception is deck C, which is currently in service in the state of New York and has been repaired by the New York State DOT.

Given the lack of repair techniques available, the research team focused on developing repair techniques for deck A, which is currently in service in Belle Glade, FL. Three repair techniques were developed and applied to specimens that had been previously loaded beyond their ultimate capacity. This chapter describes the repair techniques and their application to the damaged specimens. In general, deck A failed due to partial rupture of some portion of the bottom panel. Consequently, the repair techniques were focused on strengthening the bottom panels.

6.1 Concrete Beam Repair (A1)

Repair technique A1 used the existing bottom panel as formwork for the placement of concrete beams spanning parallel to the webs. To ensure that the noncorrosive nature of the system was preserved, GFRP reinforcement was used in the bottom of each beam. Beams were placed on each side of the webs that were damaged during the initial ultimate load test. GFRP reinforcement and foam dams were placed as shown in Figure 46; reinforcing bars were placed one bar diameter clear from the bottom of the GFRP panel.

Quickrete prepackaged structural concrete was used to form the beams; concrete was mixed according to the instructions and poured into the cavities (Figure 47). Concrete was vibrated to ensure adequate consolidation. Four cylinders were formed for compression testing at the time of deck testing. All three cavities were filled with concrete up to the top flanges. The top plate was installed before the concrete had set, which allowed the fasteners to penetrate into the concrete without resistance.

Figure 46 – Bars and foam dams ready for concrete placement

(a) (b)

Figure 47 – Deck repair A1 (a) concrete placement and consolidation (b) concrete placement completed and awaiting installation of top plate

6.2 Wet-layup Repair (A2)

Wet-layup glass fiber sheets were used to restore strength to the damaged webs. The combination of TyfoSE II-51A glass fabric and Tyfo S epoxy constituted the repair system used. Strength and continuity were restored to the damaged webs by applying two layers glass fiber reinforcing sheets, orthogonal to one another, over the damaged sections (Figure 48). The fiber and resin composite properties of the system are listed in Table 3.

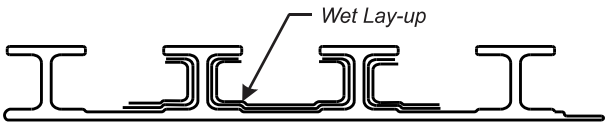

Figure 48 – Wet layup repair

Table 3 – TyfoSE II-51A fiber properties provided by manufacturer

Typical Dry Fiber Properties			
Tensile Strength			470,000 psi (3.24 GPa)
Tensile Modulus			10.5×10^6 psi (72.4 GPa)
Ultimate Elongation			4.5%
Density			0.092 lbs./in.^{3} (2.55 g/cm^3)
Weight per sq. yd.			34 oz. (1,153 g/m^2)
Composite Gross Laminate Properties			
Property	**ASTM Method**	**Typical test Value**	**Design Value**
Ultimate tensile strength in primary fiber direction	D-3039	83,400 psi (4.17 kip/in. width)	66,720 psi (460 MPa) (3.3 kip/in. width)
Elongation at break	D-3039	2.2%	1.76%
Tensile Modulus, psi	D-3039	3.79×10^6 psi (26.1 GPa)	3.03×10^6 psi (20.9 GPa)

To access the webs for the repair, the top plate was removed (Figure 49). Figure 50 shows the web damage immediately below the fillet under the top flange, which was caused by local crushing from the concentrated load.

Figure 49 – Specimen A1 with top plate removed

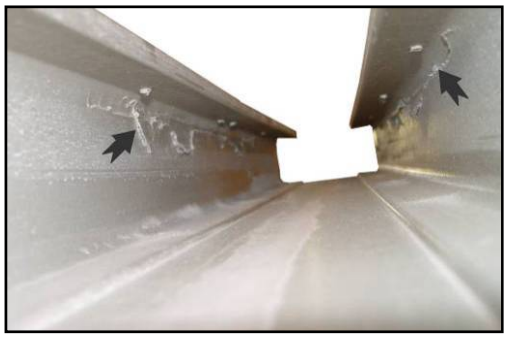

Figure 50 – Specimen A1 web damage before repair

To ensure the best possible bond between the wet layup and the pultruded surfaces, the rough edges of the fracture surface were removed and the surrounding surface was sanded using coarse sand paper.

Resin was mixed using an electric drill with a mixing blade bit. Figure 51(a) shows the consistency of the resin after mixing. To increase the resin's viscosity and its ability to hold fibers in placed until setting, silica fume (CAB-O-SIL TS-20) was added (Figure 51(b)).

(a) (b)

Figure 51 – Resin blending (a) resin only (b) resin with fume silica

Scissors were used to cut the glass fabric to the dimensions needed with the fibers oriented in the long direction (Figure 52). The cut pieces were laid out and impregnated with the resin. Figure 53 shows the fabric being saturated with resin, which did not contain silica fume to allow better saturation of the fibers.

Figure 52 – Glass mat cut to size

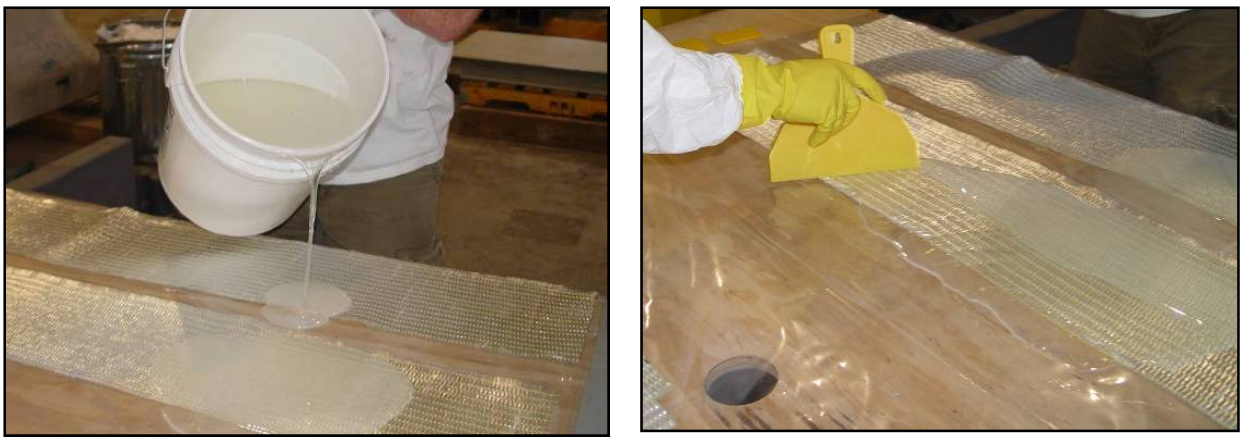

(a) (b)

Figure 53 – Saturating GFRP sheets with resin (a) pouring resin on mats and (b) spreading resin to saturate fibers

Surfaces of the GFRP deck receiving the reinforcement were coated with the silica fume imbued resin (Figure 54). Glass fabric was then placed into the cavities and rolled to smooth and remove bubbles (Figure 55). This procedure was repeated for all the surfaces being wrapped. A second layer of glass reinforcement was preceded by the application of another layer of resin containing silica fume. The second layer mat was then rolled in the direction of its fibers which were orthogonal to the first layer.

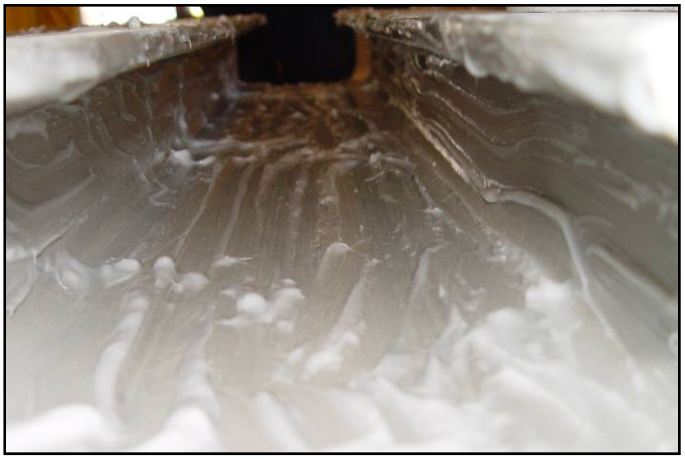

Figure 54 – Resin applied to deck

(a) (b)

Figure 55 – Saturated glass fabric (a) placement into cavities and (b) rolling to remove air pockets and further saturate fibers

Figure 56 shows the damaged specimen with the repair partially completed. The deck was allowed one week to cure before it was tested.

Figure 56 – Partially complete wet layup repair

6.3 Grout and Wet Layup Repair (A3).

Figure 57 shows the third repair option used on the damaged deck system, which consisted of reinforcing of the bottom panel soffit using the wet layup GFRP system used on A2 and filling the cavities on both sides of damaged webs with pourable non-shrink grout.

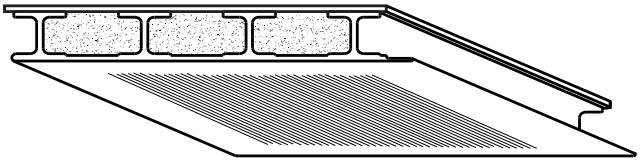

Figure 57 – A3 repair

The glass-fiber reinforcement was placed on the soffit of the specimen before the grout was poured into the deck to allow the deck to be inverted; thereby simplifying the wet layup repair. The soffit was cleaned and power sanded prior to wet layup application. A generous layer of thickened resin was applied to the soffit of the specimen (Figure 58(a)) prior to the application of the saturated glass mat. The saturated glass fabric was then placed on the surface and a roller was used to remove the excess resin and air bubbles (Figure 58(b)). The resin was allowed one day to set before the deck system was inverted in order to perform the grout repair.

(a)

(b)

Figure 58 – GFRP wrap (a) resin application to the soffit (b) the mat was rolled to ensure a proper bond to the soffit.

Quickcrete non-shrink grout was placed one day after the wet layup application. The top plate remained in place and access holes were drilled into the top plate to create a barrier using expandable foam and to allow access for grout placement (Figure 59a). Grout was mixed according to the manufacturer's recommendation to create a flowable consistency, which facilitated pouring it into the cavities of the deck using the access holes drilled into the top plate of the deck (Figure 59b). Grout flowed down the length of the cavity with the trapped air vented through the gap at the end of the specimen. All three cavities were filled completely with grout as shown in Figure 60.

(a) (b)

Figure 59 – Preparing specimen for the grout (a) barrier used to contain grout (b) drilling access holes for grout pour.

Figure 60 – Grout repair

The grout strength was tested using three two-inch cubes. The cubes were taken from three different batches during the grout mixing process. The cubes were allowed to cure and were tested during the strength testing of the repaired specimen.

7 Instrumentation

GFRP deck specimens were instrumented with strain gages, displacement gages, and load cells to measure the deck response to service and ultimate loads. Acoustic emission (AE) testing was conducted during loading while infrared thermography (IRT) was conducted after loading. Consequently, AE specimens had sensors in place during the loading and unloading process while the IRT specimens were inspected after each loading sequence.

7.1 Strain Gages

Strain was measured using quarter-bridge, 120-ohm resistance, 5 mm long gages. This gage size had been used successfully on recent tests of similar GFRP deck systems and on recent bridge load tests of a GFRP bridge deck. Using the same gages in the lab tests helped maintain more consistency between the bridge and the lab tests results.

Strain measurement was focused on measuring flexural tensile strains on the extreme fiber of the section. Because the decks were tested in either positive or negative bending, tensile strains occurred on opposite faces of the deck depending on the setup used. Positive bending test setup and strain gage locations are presented in Figure 61 and Table 4. Gages were arranged to capture the variation in strain over the width of the section that was expected to occur due to the concentrated nature of the load.

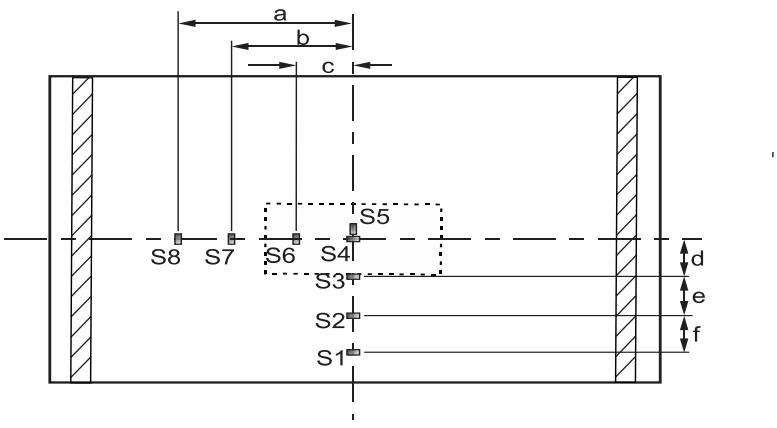

Figure 61 – Strain gage locations for positive bending test – soffit view

Table 4 – Strain gage locations (in.)

Specimen	a	b	c	d	e	f
A	12	8	4	4	4	4
B	13	9.5	5	5	4.5	4.5
C	13	9	5	5	6.5	7

In the negative bending test setup the strain gages were placed on the wearing surface face of the specimens. Deck A has been shown to have very little composite action between the top plate and bottom panel (Cousins et al. 2005), therefore the strain gages S1-S3 for deck A were placed on the flanges of the bottom panel as shown in Figure 62 in order to measure tensile strains under negative bending.

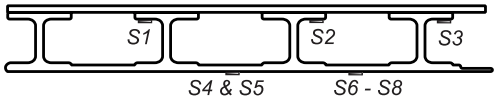

Figure 62 – Strain gage locations for negative bending

The top surface strain gage locations for decks B and C are shown in Figure 63. Different strain gage locations were used due to the different configuration of the webs in each of these deck systems. Gages S1, S2, and S3 were placed on the top surface of the specimen, what would be the road surface when installed. The other five gages were placed on the soffit of the deck; these locations are shown in Figure 64 with associated dimensions listed in Table 5.

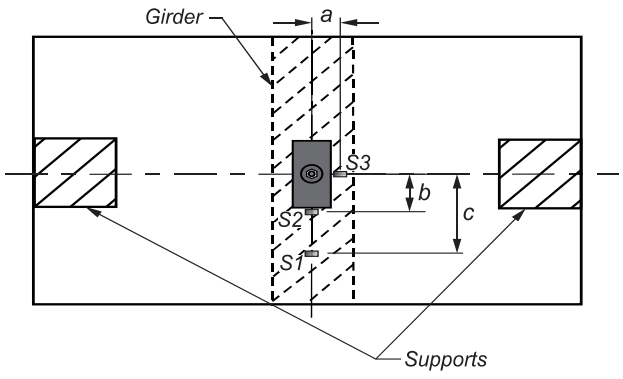

Figure 63 – Strain gage locations negative bending tests – wearing surface view

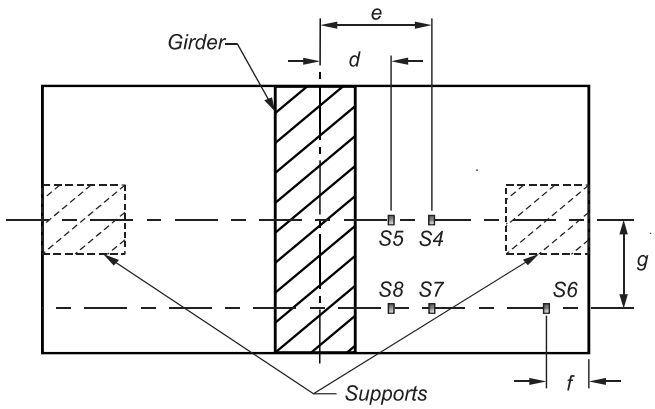

Figure 64 – Strain gage locations negative bending tests – soffit view.

Table 5 – Strain gage location dimensions for negative bending test (in.).

Deck Type	*a*	*b*	*c*	*c*	*e*	*f*	*g*
A	N/A	N/A	N/A	3.2	9.5	3.5	12
B	0.0	4.5	9.0	7.0	10.25	3.5	11
C	4.0	9.0	13	3.5	7.0	6.0	3.5

7.2 Load and Displacement

Displacement gages were arranged for the positive bending setup as shown in Figure 65. For Decks B and C, the gages were placed along the center line of the specimens; the gages were offset from the center line for deck A because the top plates had been observed to separate slightly from the bottom panel under high loads. The offset displacement gage location allows for the measurements to be based only on the bottom panel deflections. The load in the configuration is measured with an inline load cell placed between the load actuator and the specimen.

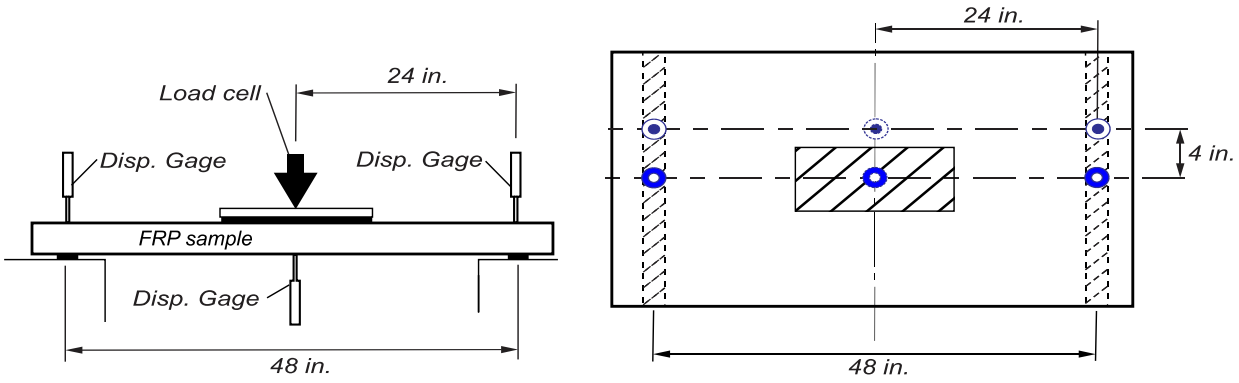

(a) (b)

Figure 65 – Displacement gage locations positive bending setup (a) elevation and (b) plan view

7.3 AE Sensors

Acoustic emission sensors were placed only in locations that would typically be accessible in a field application. For positive bending, damage was expected to be most severe under the load point. Sensors were placed on the soffit of the specimens under and away from the load and under the different features of each specimen (Figure 66 and Table 6). Placement of the sensors both under and away from the load point allowed the collection of data similar to that which might occur in a field load test with a truck tire traversing the deck either over a sensor location or away from it. Sensors away from the load (AE5-AE8) were placed with the intention

of observing and comparing the AE activity with that of the sensors under the load. The placement of these four sensors was chosen to be in line with the sensors placed along the mid-span of the specimen to better compare their response.

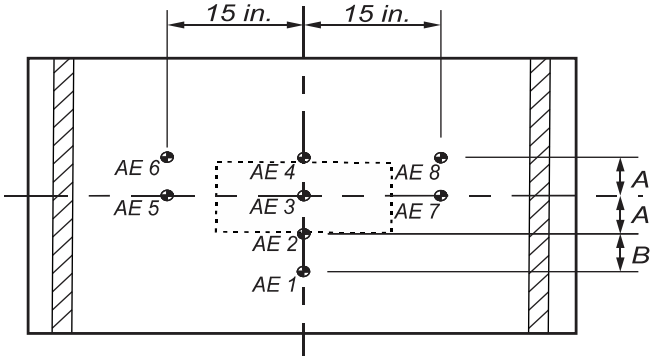

Figure 66 – AE sensor locations for positive bending tests – soffit view

Table 6 – Positive bending test AE sensor location dimensions (in.)

Deck	*A*	*B*
A	4	4
B	5	6
C	5	6.5

Damage was expected to occur at the load point in the negative bending test setup. Consequently, AE sensor locations for the negative bending test were similar to those of the positive bending test, but adjusted to accommodate the placement of the girder. As in the positive test setup, the sensor locations were chosen to capture the AE activity between the loading pad and the supports while being attentive to different features in each deck design. Figure 67 is a diagram of the negative bending setup and the specific locations relating to the different decks are listed in Table 7.

Using hot glue as the couplant, the sensors were attached in accordance with ASTM E 650-97. Prior to loading, as per ASTM E 976-99, the sensor placement and data acquisition were evaluated using the pencil lead break method.

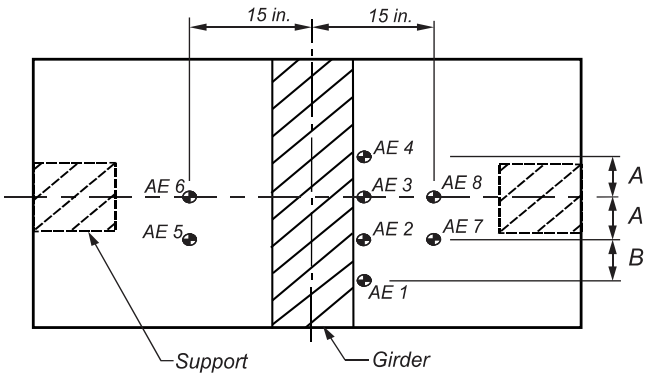

Figure 67 – Negative bending AE sensor locations

Table 7 – Negative bending AE sensor locations (in.)

Deck	*A*	*B*
A	4	4
B	5	9
C	5	6.5

7.4 Disp 16 System

The AE data acquisition system used was the DISP-16BT, manufactured by Physical Acoustics Corporation (Figure 68a). This system uses the software AEWin E3.11 to acquire, record, and replay 8-channels of feature data.

The system uses integral preamp piezoelectric sensors as shown in Figure 68b. The sensors have the capability to drive long cables without the need of a separate preamplifier. The sensors were designed for circumstances where background noise can be high and the distance between sensors may be less than 10 ft. (Mistras)

(a)

(b)

Figure 68 – AE system (a)16 channel DAQ (b) R15I-AST piezoelectric sensor

The AE system can be used on a variety of materials which all have unique wave timing parameters. Peak Definition Time (PDT) ensures the correct identification of the signal peak for risetime and peak amplitude measurement; Hit Definition Time (HDT) ensures that each AE signal corresponds to only one hit; and Hit Lockout Time (HLT) avoids recording spurious measurements during the signal decay (AE win 2004). Table 8 list the adjustable parameter values used in this investigation. The threshold was selected after several lab tests measured ambient noise. The sample rate was set to the maximum allowed by the machine. The PDT, HDT, HLT, and Max duration were recommended by the AE win manual for GFRP materials.

Table 8 – AE recording parameters

Threshold	45 dB
Analog filter	10 kHz-2MHz
Sample rate	10MSPS
Peak Definition Time (PDT)	35 μs
Hit Definition Time (HDT)	150 μs
Hit Lockout Time (HLT)	300 μs
Max duration	1000 ms

8 Test Procedure

Three load tests were conducted on each specimen in the sequence shown in Table 9. First, the specimen was subjected to two undamaged service tests (UST) composed of three load holds. The specimen was then subjected to an ultimate load test (ULT) in which the specimen was loaded to its ultimate capacity to cause damage without completely destroying the specimen. Finally, stepwise service loads were again imposed on the damaged deck to determine how well AE could detect the damage that had been imposed by the ultimate strength test. This test is referred to as the damaged service test (DST). Both positive and negative bending specimens were tested using the same procedures and load steps were separated by a brief load reduction to allow observation of Kaiser and felicity effects during reloading. Details of the loading profile are provided in the next section.

The loading rest time requirements for each loading were designed to duplicate the field conditions experienced by the deck. The initial UST was followed by a rest period of 24 hours, which allowed the GFRP to rest. A second UST was performed to ensure that Kaiser effects were considered in the testing.

Table 9 – Testing sequence and rest time

Load Profile	**Post-Test Rest time**
Initial UST	24 hr min
UST	30 min.
ULT	30 min.
DST	30 min.

8.1 Service Loading (UST and DST)

Figure 69 shows the profile used for service loading, which was similar to the step-loading procedure for AE tests of pressure vessels specified in ASTM E 1067-96; this profile was used for both UST and DST. Load hold magnitudes and duration are given in Table 10. Before loading, AE readings were taken during a 30 second period to identify spurious AE signals. To detect either Kaiser or felicity effects and to develop undamaged AE data of the specimens, two UST were performed on each specimen before the ultimate loading. The specimens were then tested to capacity, ensuring that the specimens sustain damage as defined

by loss of load. Following the ultimate loading test, the damaged specimens were then retested twice (DST) using same load profile as was used for UST.

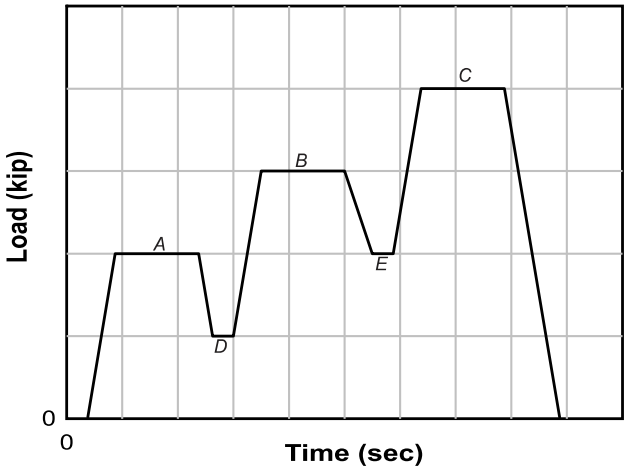

Figure 69 – UST and DST load profile

Table 10 – Load profile characteristics

Load Hold	Load (kip)		Minimum Duration (sec.)
	Deck A	Deck B&C	
A	5	10	120
B	9	15	120
C	12	20	120
D	2.5	5	30
E	5	10	30

8.2 Ultimate Loading (ULT)

The ultimate load test (ULT) was designed to provide AE data for each type of deck tested up to failure and to take the specimen to ultimate capacity to ensure significant damage had been imposed on the specimen before the follow-up DST. Figure 70 shows the load profile used in the ULT. The duration of each load hold was a minimum of 2 min. and was adjusted based on the live AE data observed during the loading (ASTM 1067-96). Load hold levels started at 45 kip and increased by 15 kip until capacity was reached.

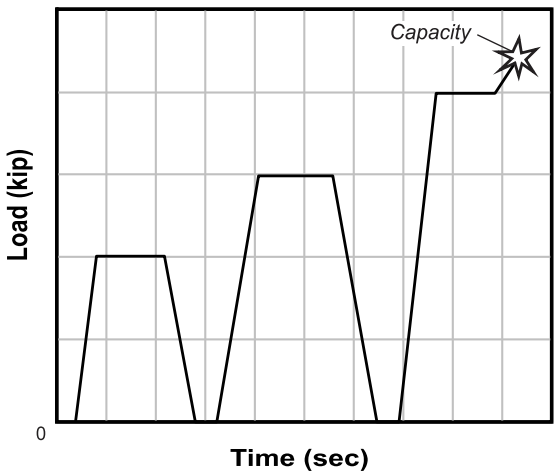

Figure 70 – Ultimate loading profile

9 Ultimate Strength Test–Results and Discussion

Positive and negative bending tests were conducted on each deck type. The focus of the tests was to load the specimens beyond their ultimate capacity and cause damage that might be associated with an overload in the field. This was done primarily to evaluate the effectiveness of AE and IRT in detecting the damage caused by overload. Recall that service loadings were applied both before and after each ultimate load test to assist in evaluating damage detection procedures.

In general, failure modes differed between positive and negative bending tests. The following sections describe the behavior and observations of the positive and negative bending tests conducted on the respective deck type.

Initially the specimens were loaded using the service load profile to establish the behavior of the undamaged specimens; these were referred to as undamaged service-load tests (UST). The ultimate loading test (ULT) was then used to impose damage and determine the ultimate load capacity. Damaged specimens were then reloaded using service level loads; these tests were referred to as damaged service load test (DST). The following sections describe the behavior during each of the three load tests including the failure mode noted during ULT. Strain data are also presented and evaluated.

9.1 Deck A Positive Bending (A_P)

Figure 71 shows the load-displacement response of Deck A for the positive bending test and includes UST, ULT and DST plots. Two UST's were initially performed on the specimen. During the first test, sharp audible cracking was noted as the load increased. During the service load hold, however, the deck remained quiet. Audible cracking was less notable during the second UST and there was quiet during the load hold. The second load cycle is shown in the plot and is linear, indicating that the deck remained linear elastic during this test.

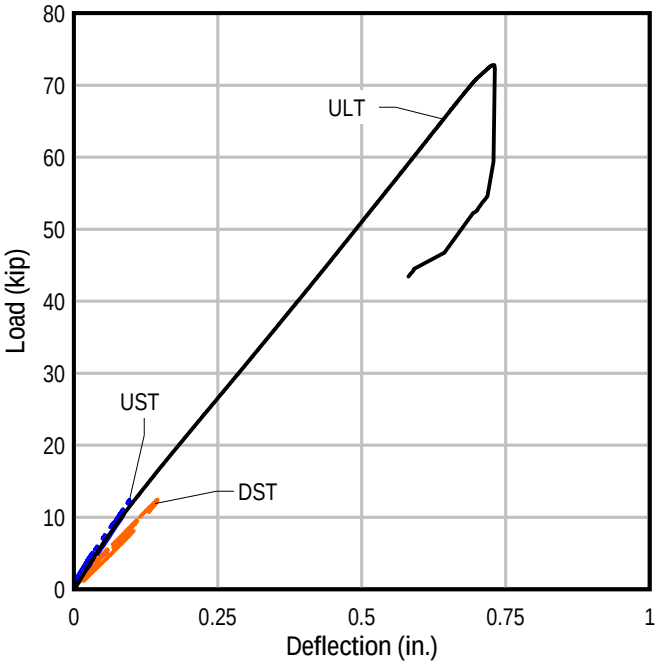

Figure 71 – Load-displacement plot specimen A_P

ULT load-deflection was linear up to a peak load of 72 kip. Audible cracking was noted as load was increased. In addition, when service load levels were exceeded, the top plate of the deck system was observed to deform out-of-plane between fasteners (Figure 72); this was an indication that the deck system was not acting compositely. Ultimate capacity was signified by both a sharp audible crack and partial loss of load but not complete collapse. A residual capacity of 43 kip remained after the specimen load reached its ultimate limit state. The unloading portion of the ultimate loading plot is not shown below the 43 kip mark to more clearly show the service load level loadings. Visual inspection indicated that the loss of load was caused by the crushing and buckling of the webs adjacent to the loading pad (Figure 73).

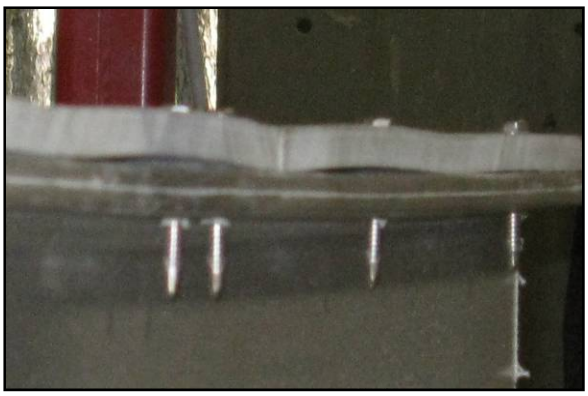

Figure 72 – A_P top plate buckling under load

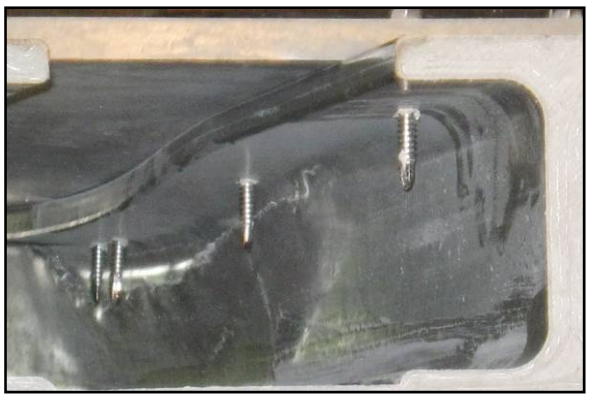

Figure 73 – A_P web failure

DST shown in Figure 71 indicates that the web damage reduced the overall deck stiffness. Table 11 shows the stiffness of the specimen for each test regime as determined by linear regression of the last curve of each test. As indicated in Table 11, the measured stiffness was reduced by 27% from the undamaged state.

Table 11 – A_P stiffness

Load Profile	Stiffness (kip/in)	Stiffness Ratio
UST	114	1
ULT	111	0.97
DST	83	0.73

Figure 74 shows the ULT strain values for A_P. The relative magnitude of the strain values at any given load indicates transverse distribution of the concentrated load. The strain under the load point (S3) was approximately twice that of the strains under the outside web (S1) which indicates that the interior webs are carrying about twice the load of the outside web. This significant difference in load is indicative of the relative flexibility of the panels connecting the webs and the marginal amount of load distributed to adjacent webs. Linearity of the strains in S1 and S2 indicates that the system remained linear elastic up to ultimate capacity. Abrupt loss in load with little indication of softening demonstrates the brittle nature of the material.

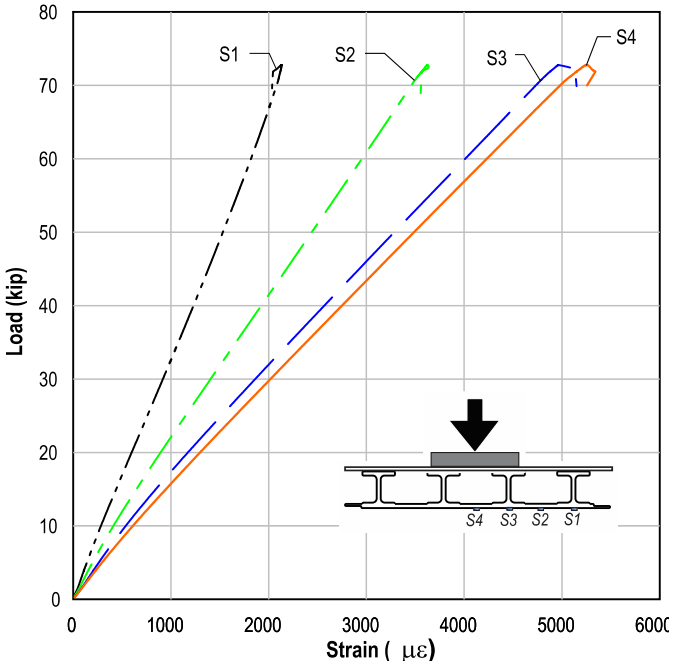

Figure 74 – Load-strain plot A_P ULT

9.2 Deck A Negative Bending (A_N)

Figure 75 shows the load-deflection curves for the UST, ULT, and DST load test. It was anticipated that the grout pocket might have exhibited additional audible cracking during UST. No increase in audible cracking, however, was noted over that of the positive bending test.

ULT load-deflection was initially linear with audible cracking noted at about 50 kip, which was thought to be the grout cracking. The grout was thought to provide some support due to the large deformations noted in other tests. At approximately 65 kip the ULT load-deflection curve changes slope, which suggests the specimen sustained a large amount of damage at that time, but the specimen supported additional load up to 76 kip when the sudden failure occurred. The residual load after reaching ultimate strength was 63 kip.

A post ULT inspection was performed which indicated that a single web directly above the supports was found to be damaged (Figure 76). Figure 77 shows the location of the damaged web in relation to the test setup. This localized failure is similar in nature and location to the failure encountered in the positive bending ULT. In this test setup, however, the failure resulted in very little loss of global stiffness due to its localized nature. Consequently, the specimen retained its original stiffness at the lower service load levels, as indicated by the slope of the DST load-displacement curve.

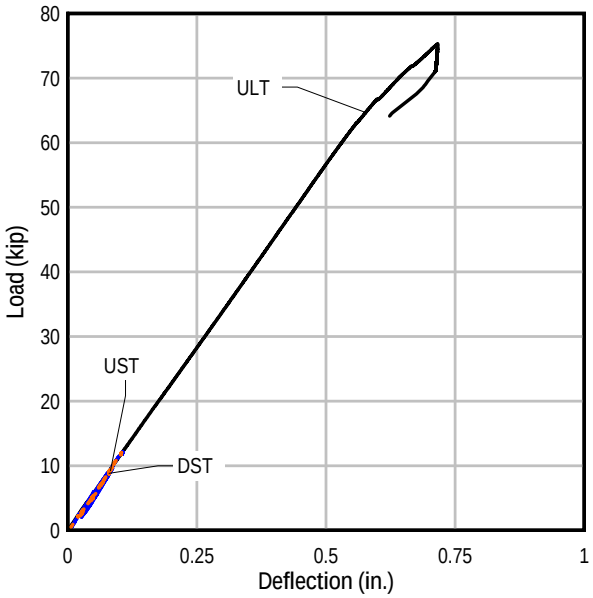

Figure 75 – Load-deflection A_N

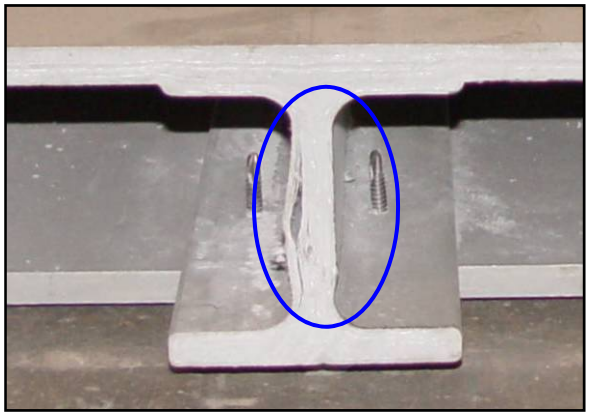

Figure 76 – A_N damaged web

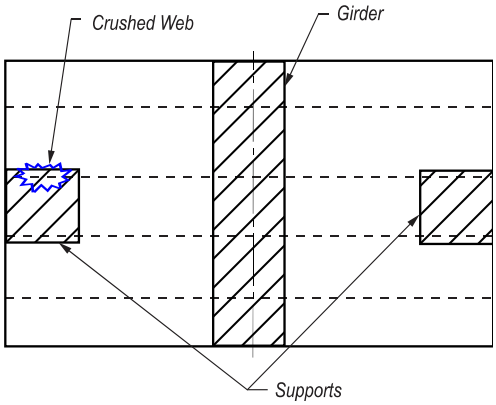

Figure 77 – Damaged web location

Table 12 shows the calculated deck stiffness for each test. As previously mentioned, only two of the webs were directly in contact with the supports (Figure 77), one of which was crushed during ULT. The strain differential of the two webs directly under the load could not be confirmed with the strain data since one of the strain gages was damaged during assembly. In contrast, the positive bending specimen lost 24% of its original stiffness after ULT and had damage to both webs under the applied load.

Figure 78 shows the load-strain data. The specimen initially had three strain gages, but S3, which was mounted under the web that failed, was damaged when the top plate was being

replaced. S1 strain values were 35% of the S2 strains, confirming transverse flexibility. The strain curves remained linear up to capacity.

Table 12 – A_N stiffness

Load Profile	Stiffness (kip/in.)	Stiffness Ratio
UST	114	1
ULT	113	0.99
DST	110	0.96

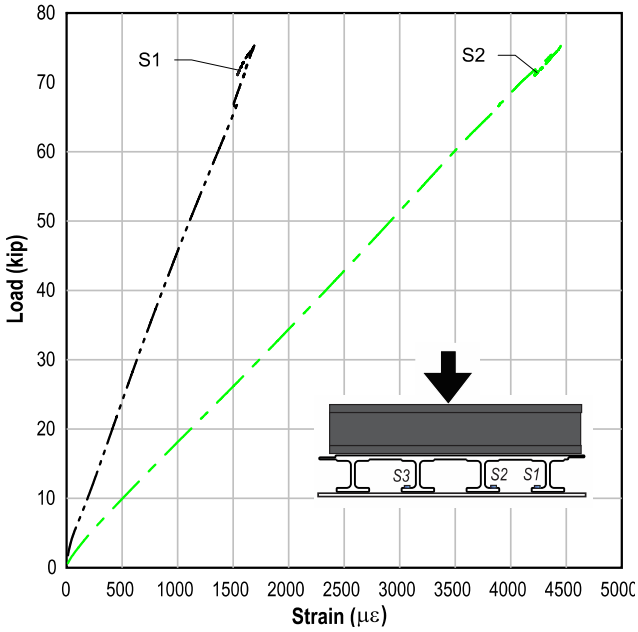

Figure 78 – A_N ULT load-strain curve

9.3 Deck B Positive Bending (B_P)

Figure 79 shows the load displacement response of specimen B_P and includes UST, ULT, and DST plots. Specimen B_P was qualitatively noted to have significantly less audible cracking than A_P, which was thought to be due to damping effects of the foam core.

ULT of the specimen reached an ultimate capacity of 112 kip, which was accompanied by a sharp audible cracking. A residual load of 92 kip was observed prior to the unloading of the specimen.

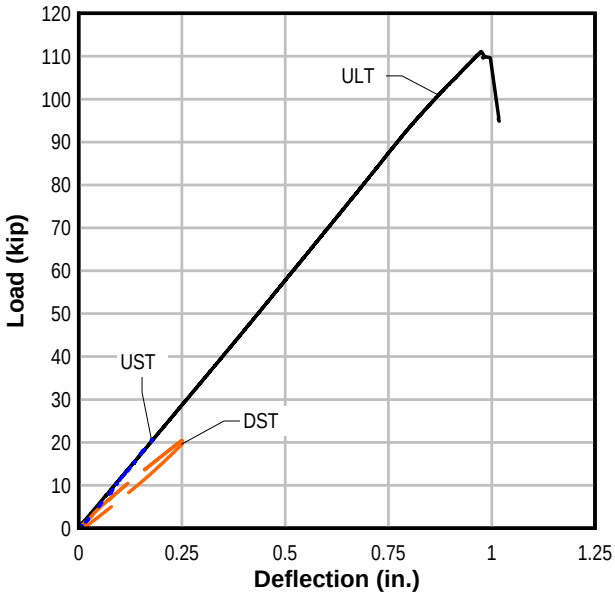

Figure 79 – Load-deflection plot B_P test

During the ultimate strength test, cracks formed around the load point in the top panel (highlighted in Figure 80). As load was increased, the cracks grew parallel to the span and eventually merged over the supports when the ultimate capacity was reached (Figure 81). Post ULT inspection of the specimen indicated that the bottom soffit of the specimen was intact and that the top surface retained a bowl-shaped permanent deformation, indicating that the interior webs were also permanently deformed.

The difference in slope between the UST and the DST curves demonstrates the loss of stiffness after the ULT. The stiffness and stiffness ratios were calculated using linear regression for the three loadings and are presented in Table 13. The stiffness of the section decreased by 30% after ULT procedure.

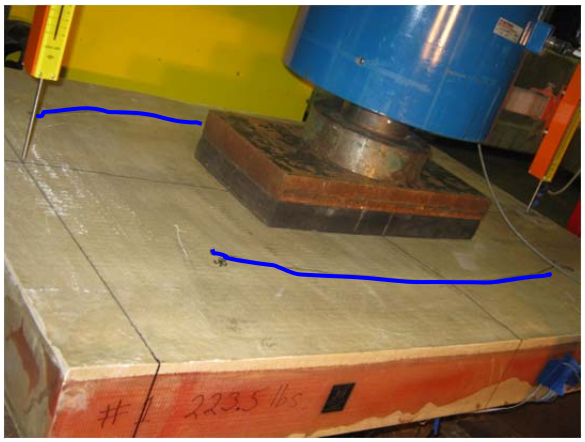

Figure 80 –Deck B positive bending crack pattern

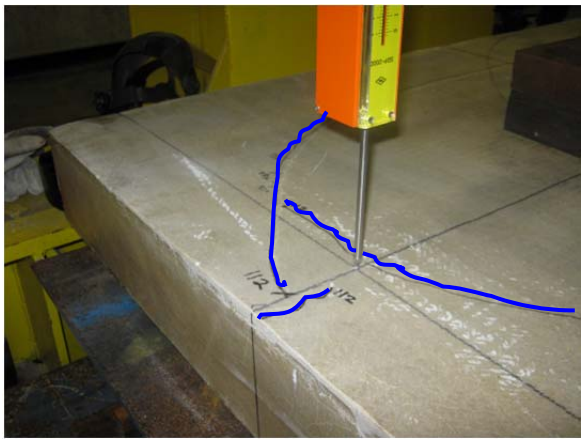

Figure 81 – Deck B positive bending cracks at failure

Table 13 – B_P stiffness

Load Profile	Stiffness (kip/in.)	Stiffness Ratio
UST	117	1
ULT	116	0.99
DST	82	0.70

Figure 82 shows the strain values for the ULT of specimen B_P. Strain gage plots were grouped by their respective positions in relation to the load pad. S1 and S2, the gages positioned away from the load, reported values 50% that of the gages directly under the pad, S3 and S4. The transverse stiffness of the deck is small and similar to deck A.

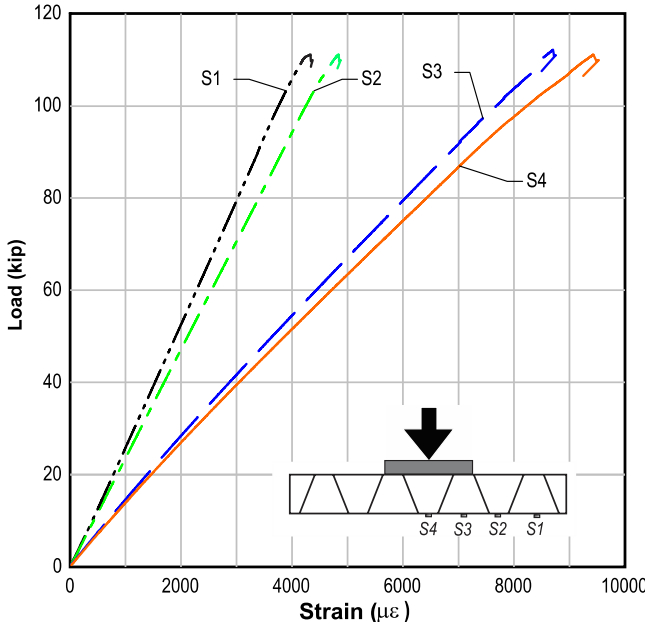

Figure 82 – Load-strain B_P ULT

9.4 Deck B Negative Bending (B_N)

Figure 83 shows B_N results of UST, ULT and DST load-deflection plots. The specimen B_N setup had no mechanical connection to the girder, the deck was insulated by a ½ in. neoprene pad; this contributed to the lack of audible cracking emitted by the specimen. A large crack formed over one of the supports at approximately 112 kip as indicated by the discontinuity in the ULT plot. The specimen did not lose load however and the loading continued to an ultimate capacity of 134 kip. The specimen failed abruptly and violently with a residual load of 69 kip.

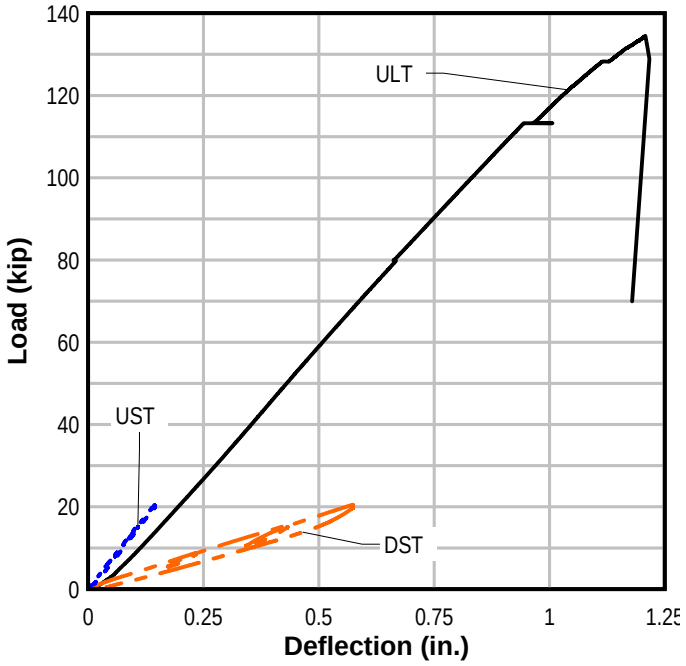

Figure 83 – B_N load-deflection plot

Figure 84 shows punching shear failure over the support. The crack followed the edge of the interior web and extended past the support into the deck. Figure 85 highlights the approximate location of the failure plane. The deck wearing surface delaminated from the deck surface and pieces can be seen on the steel support beam in Figure 84.

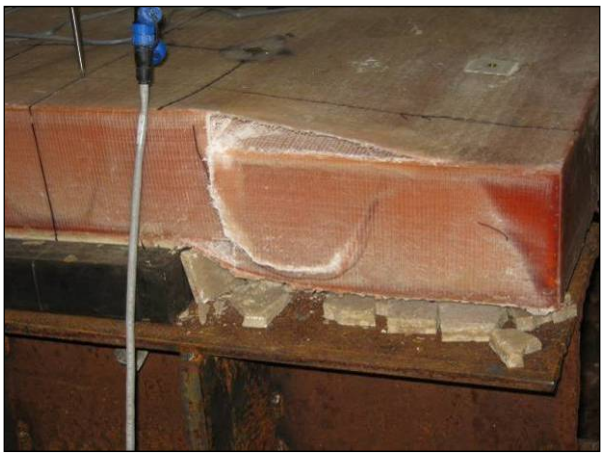

Figure 84 – B_N shear failure over support

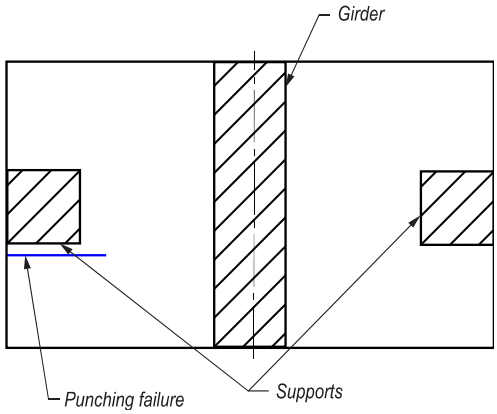

Figure 85 – B_N punching shear location

Table 14 shows the stiffness and the stiffness ratio for the negative bending test. The difference in stiffness between the UST and ULT was 14%; this was the only deck system to lose significant stiffness between after ULT. The DST stiffness was 76% less than the UST and 62% less than the ULT. The punching shear failure caused a large loss of stiffness relative to the other deck tests.

Table 14 – B_N stiffness

Load Profile	Stiffness (kip/in.)	Stiffness Ratio
UST	140	1
ULT	120	0.86
DST	34	0.24

Strain gages were placed on the road surface of the specimen to capture the largest magnitude of strain during loading. During ULT, however, the road wearing surface applied by the manufacturer debonded from the deck, damaging two of the strain gages. The ULT load-strain plot for the remaining undamaged strain gages is presented in Figure 86. The strain magnitudes were significantly less than those of the positive bending test of the same deck type, which were nearly 10000 (με) at 112 kip. The reported strain of the negative bending test was expected to be similar in magnitude to the positive bending strains. Recorded strain values, however, were only 1200 (με) at 135 kip. This suggests that the debonded wearing surface affected the remaining strain gages and the data are not accurate.

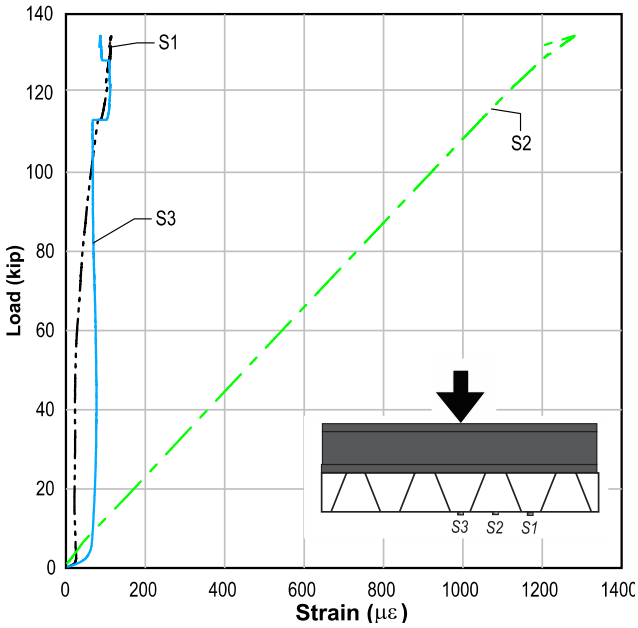

Figure 86 – B_N ULT load-strain plot

9.5 Deck C Positive Bending (C_P)

UST, ULT and the DST results for C_P are presented in Figure 87. Initially two UST's were performed on specimen C_P followed by the ULT. During the service loading audible emissions were notably less than those from the other two deck types. During the ULT, sharp audible cracking began at the 70 kip load level and continued up to the ultimate capacity of 100 kip. A residual load of 80 kip was supported by the specimen; the unloading portion of the curve was not shown to avoid obscuring the UST and DST results. The failure mode of the deck system is designed such that the compression flange delaminates from the honeycomb core, which was the observed failure mode during ULT. Delamination, however, was not visible so coin tap testing was used to estimate extent of the delamination (outlined in blue in Figure 88).

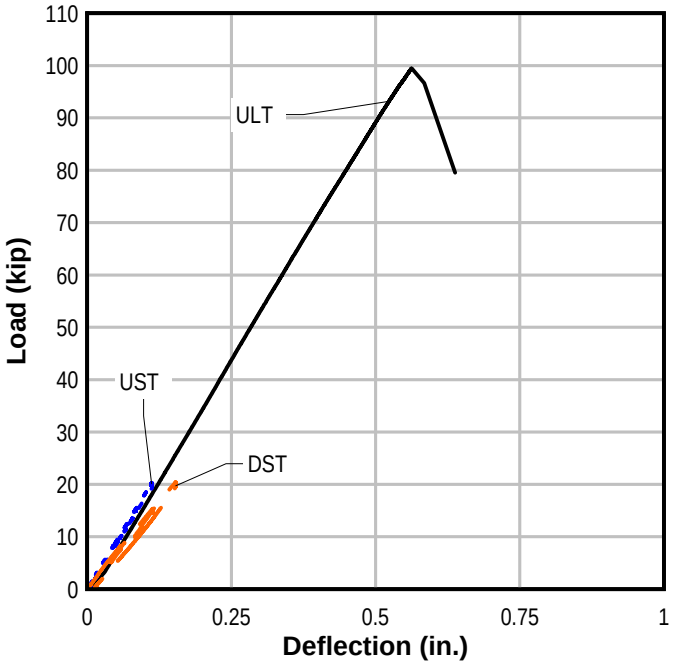

Figure 87 – C_P plot positive bending test

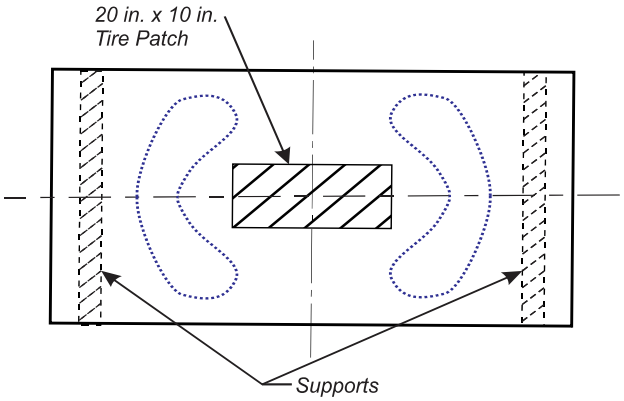

Figure 88 – C_P ULT failure zone

The stiffness of each loading was determined by linear regression (Table 15). The stiffness of this specimen was the greatest of the three tested. Stiffness was reduced by 30% after the ULT.

Table 15 – C_P stiffness

Load Profile	Stiffness (kip/in.)	Stiffness Ratio
UST	181	1
ULT	184	1.01
DST	128	0.70

Figure 89 shows the ULT strain values. The transverse stiffness of the specimen was very large in comparison with the other specimens. The strain value near the outside edge of the specimen (S1) had the smallest strain magnitude and it was 75% of the peak value under the concentrated load (S4).

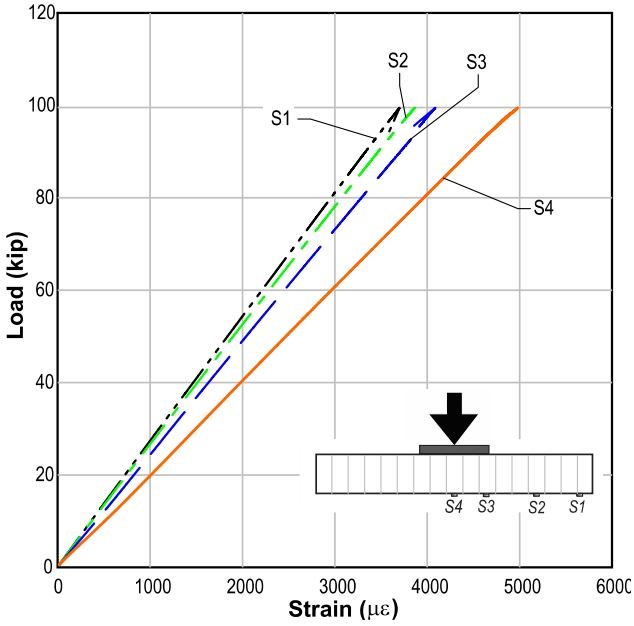

Figure 89 – C_P ULT load-strain plot

9.6 Deck C Negative Bending (C_N)

The load-deflection plots for UST, ULT, and DST are presented in Figure 90. During the initial UST no audible cracking was noticed. The ULT was also quiet up to the 65 kip level when audible cracking was noted, increasing up to the sudden and violent failure at 79 kip load level. Immediately after the ultimate load level was reached, the system lost almost all of its strength. Specimen damage was extensive with a residual load of only 14 kip.

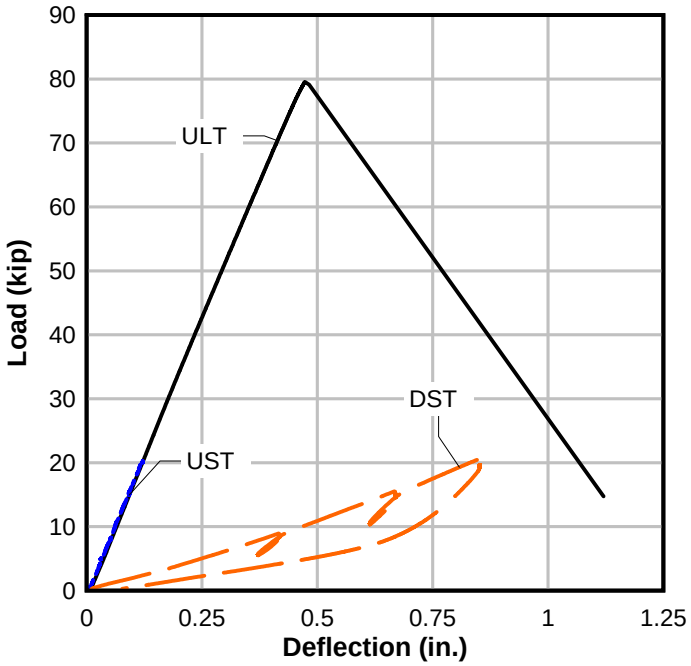

Figure 90 – C_N load-displacement plot

The specimen failed by separation of the top plate from the honeycomb core as seen in Figure 91. The specimen was designed to fail by delamination of the compression zone of the deck; in this case, however, the large load combined with the short span resulted in complete separation of the plate.

Figure 91 – C_N failure

The stiffness and stiffness ratio of each load case were determined by linear regression and are shown in Table 16. This deck was very stiff in comparison to the other decks tested, but

because the plate was nearly completely separated from the core, it had the largest decrease in stiffness (86%) after ULT.

Table 16 – C_N stiffness

Load Profile	Stiffness (kip/in.)	Stiffness Ratio
UST	169	1
ULT	172	1.01
DST	24	0.14

The strain gage data along the top of the girder is presented in Figure 92. In this configuration the lateral stiffness of the deck was not as large as in the positive bending setup. S1 only had 20% of the peak strain recorded during the ULT near the center of the specimen (S2).

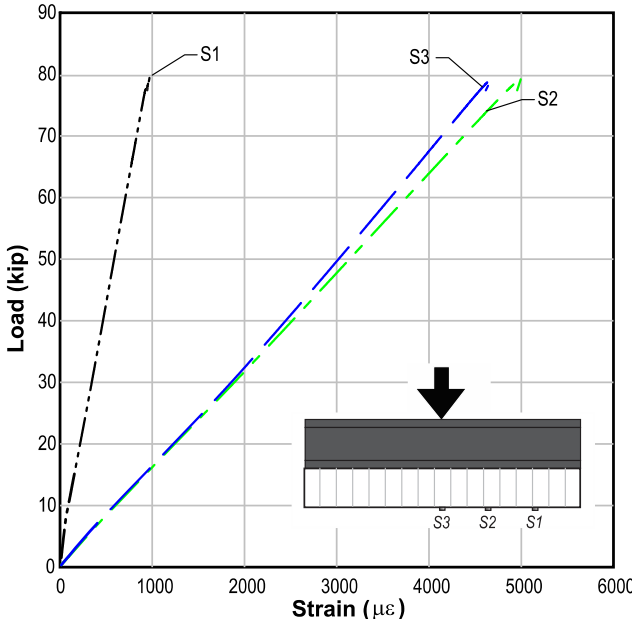

Figure 92 – C_N ULT load-strain plot

10 Ultimate Strength Test of Repaired Deck–Results and Discussion

After deck A specimens were tested to ultimate capacity, the damaged specimens were repaired. One approach was to place GFRP bars in the cavities between the webs and then fill this cavity with concrete. Another approach was to apply wet layup GFRP to the damaged webs. The last approach was to fill the cavities with grout and apply GFRP to the soffit of the deck. The goal was to evaluate the structural efficacy and construction practicality of procedures that could be used to repair this system in the case of an overload or other similar damage. All three specimens were tested to their ultimate strength (ULT) in the positive bending test setup described previously.

10.1 Concrete and GFRP Bars (A1)

Figure 93 is a diagram of the concrete repair which consisted of using the cavities as stay-in-place molds for concrete beams reinforced with GFRP bars.

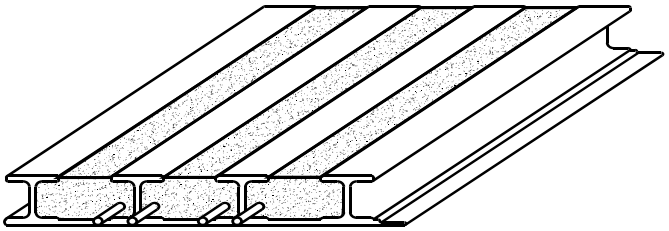

Figure 93 – Concrete repair (A1)

Figure 94 shows the load deflection results for specimen A1. The bi-linear nature of the plot indicates that the concrete fill cracked at a load of approximately 10 kip. As indicated by the change in slope, cracking significantly reduced the stiffness of the system. Beyond a load of 10 kip, however, the stiffness remained relatively constant up to ultimate capacity of 63 kip. The specimen did not reach its original capacity of 74 kip. Residual capacity of the specimen was 45 kip.

Post-test inspection, in which the top plate was removed, revealed that the concrete fill had cracks throughout the length of the specimen. It is speculated that the cracking occurred just before the 10 kip load level due to the bilinear characteristic of the load deflection curve. Further inspection revealed that the two outer webs delaminated from the bottom sheet at midspan (Figure 95).

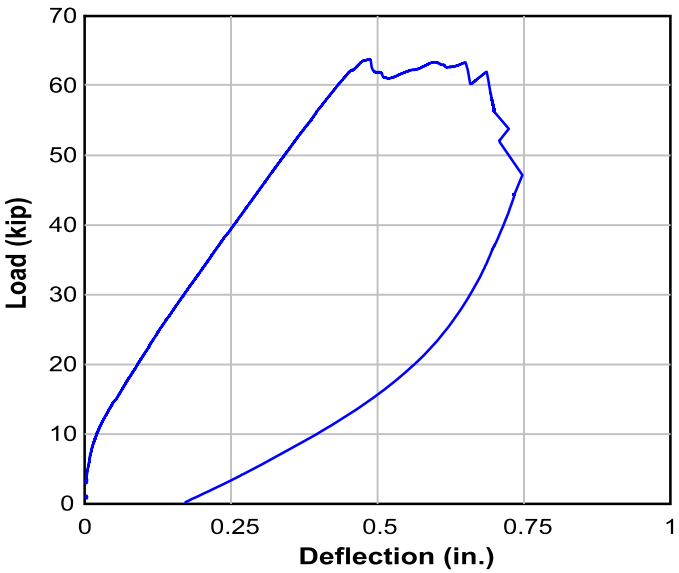

Figure 94 – A1 load-deflection curves

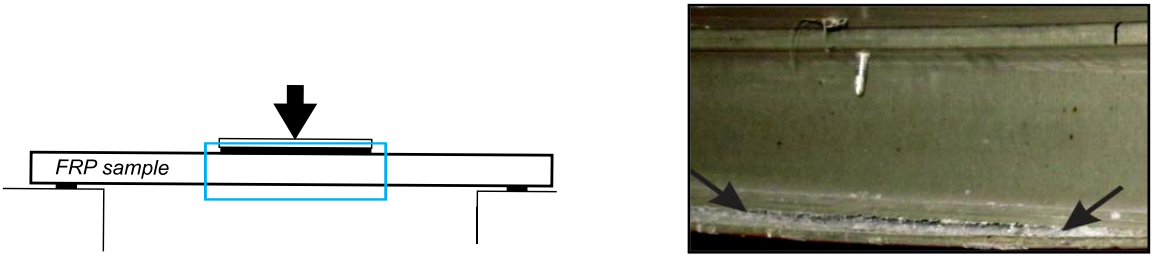

(a) (b)

Figure 95 – A1 failure (a) location and (b) detail

While placing the concrete, several 4 in. diameter concrete cylinders were cast. Compressive strength was expected to be at least 5000 psi at 7 days. Unfortunately the average cylinder strengths averaged at approximately 1800 psi. If the concrete strength had reached the design level, it is possible that the specimen would have had a somewhat higher flexural capacity and perhaps reached or exceeded the original strength.

Figure 96 shows the strain measured on the soffit of the test specimen. The bi-linear nature of the load-strain plots reflect that of the load-deflection plot, indicating that cracking occurred at approximately 10 kip. Beyond approximately 15 kip, post-cracking strain remained linear up to the specimen failure. The plot also indicates that the strain value was higher away from the load, suggesting that the concrete fill increased the transverse stiffness of the specimens considerably. A strain ratio between the value of S1, furthest from the load, and S4, directly

under the load, at a load of 60 kip for this specimen was 1.33. The relative magnitudes of the strains in the original specimens are the reverse. The interior gages (S3 and S4) have higher relative strains. Damage to the webs under the load caused a significant reduction in stiffness relative to that of the outside webs where damage was minimal. The addition of the concrete fill transferred the load transversely to the stiffer outside webs, thus causing higher strains.

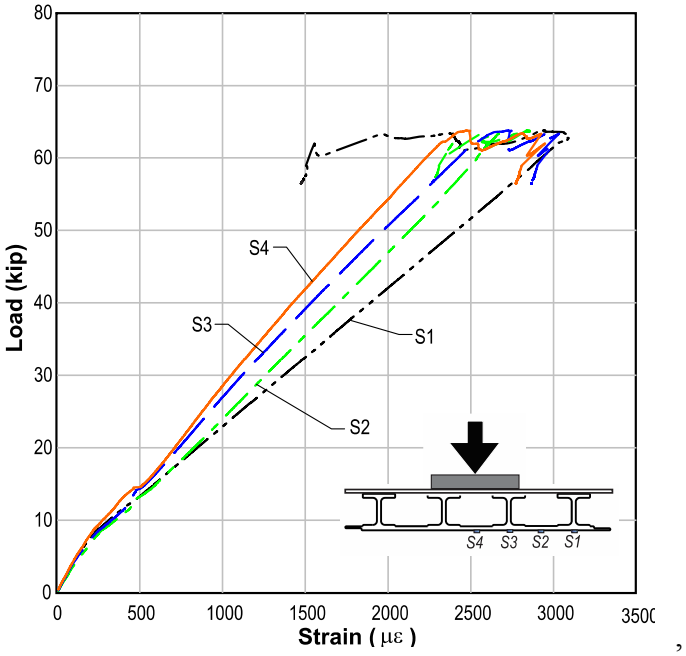

Figure 96 – A1 load-strain curve.

10.2 Glass Wrap Repair (A2)

Figure 97 shows the load-deflection results for specimen A2. At about the 60 kip load level the GFRP web repair debonded from the web surface as indicated by the change in slope. Figure 98 is a picture of the debonding of the repair at the previously cracked web. The specimen continued to hold load, however, beyond that point up to the 85 kip load level. At the 85 kip load level the specimen sustained further damage, detailed in the next paragraph, but was able to reach an ultimate capacity of 92 kip. Residual load was approximately 60 kip.

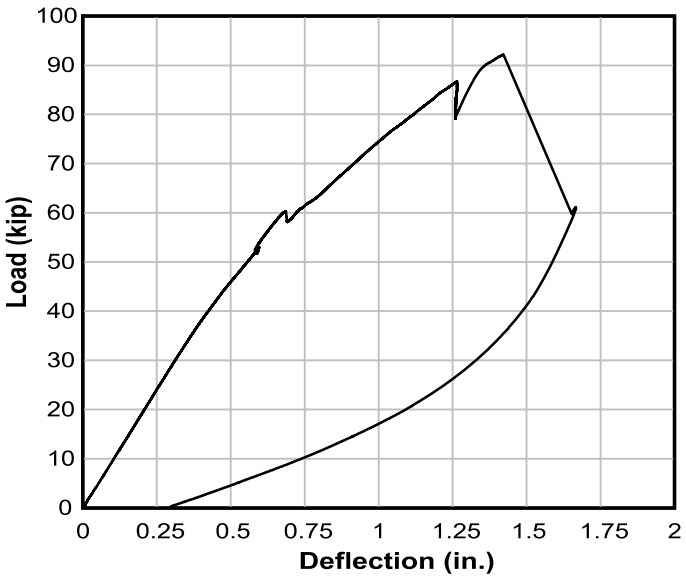

Figure 97 – A2 repair load-deflection plot

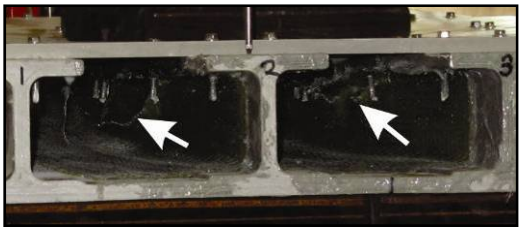

Figure 98 – A2 glass repair damage

Figure 99 shows that the bottom flange of the outside webs has separated from the bottom of the panel and that the bottom flange ruptured due to the flexural tension. Figure 100 shows that web 1 and the top flange of web 2 delaminated. It is suspected that the addition of the glass wrap to the interior webs strengthened the interior of the specimen causing the failure of the outer portions of the specimen.

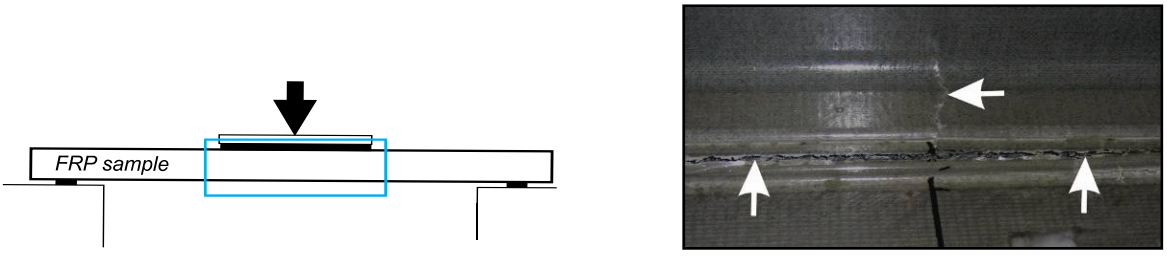

(a) (b)

Figure 99 – A2 web-flange failure at midspan (a) location and (b) detail

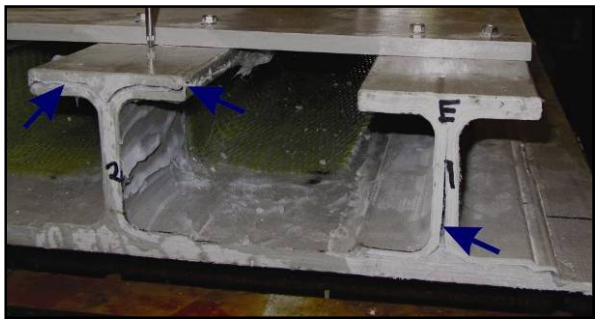

Figure 100 – A2 shear failure of the web

Figure 101 shows the load strain results for A2. The strain ratio of S1 to S4 is 0.61 suggesting that this repair had a greater transverse stiffness than that of the undamaged deck, which had a ratio of 0.45. At about the 52 kip level the wrap on one of the webs buckled, which explains the discontinuity in the plot. Beyond 60 kip S3 reported a larger strain than S4, suggesting that this web had lost stiffness due to either wet layup buckling or delamination of the deck flange, or both.

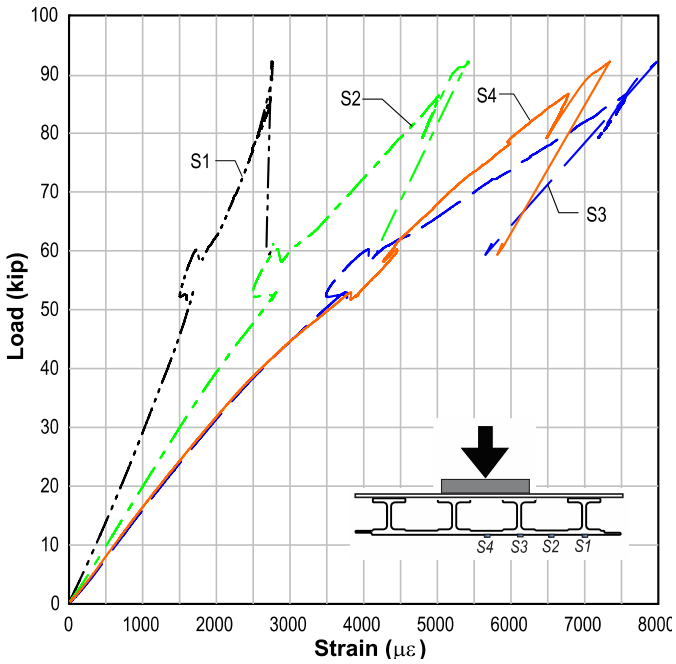

Figure 101 – A2 load-strain plot

10.3 Grout and Wrap Repair (A3)

Figure 102 shows the load deflection plot for A3. Early performance of A3 was similar to that of A1 including bilinear load-displacement with cracking occurring at approximately 10

kip. Audible cracking was noted as the load passed through 10 kip. Beyond this load the slope of the load-deflection curve remained constant up to the capacity of 117 kip, well above the original capacity of 74 kip. The loss of load was abrupt, with a residual load of 90 kip remaining before the test was terminated.

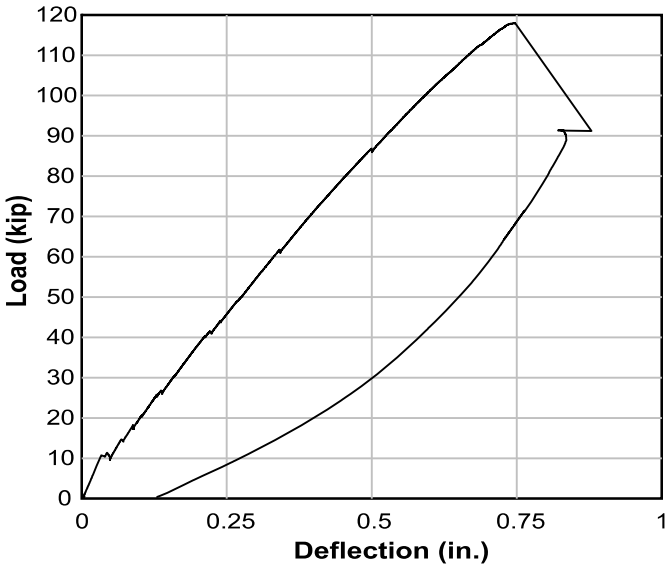

Figure 102 – A3 repair load-deflection plot

Figure 103 shows the location and the failure mode of the deck, which was delamination of the outer webs from the bottom panel. Because grout filled the cavities of the specimen, interior portions of the specimen were inaccessible for examination. Removal of the top plate after testing revealed multiple cracks in the grout in a pattern similar to that of A1.

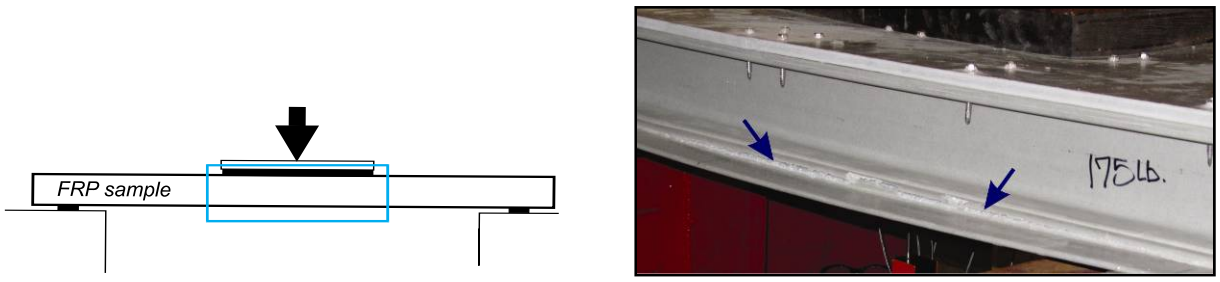

(a) (b)

Figure 103 – A3 failure (a) location and (b) detail

The stiffness of this specimen was the largest of the repaired specimens; this was the contribution of the stiff non-shrink grout. Grout strength was obtained from compressive tests

on 2-in. cubes prepared during the grout pour; the average strength was 9.8 ksi. These results exceeded the expected strength of 8 ksi and contributed to the added capacity of the section.

Figure 104 shows the load-strain plots for A3. Strains on the soffit were less than those of the unrepaired decks at the same load levels. Differences in strains magnitudes in relation to the load on the specimen suggest that the grout in the cavities was not bonded to the deck at failure and was carrying a small fraction of the load. The strain ratio of S1 to S4 at 60 kip is 1.17 compared to 0.45 in the original specimen, indicating that the transverse stiffness of the repairs is sufficient to transfer load away from the interior webs to the undamaged exterior webs.

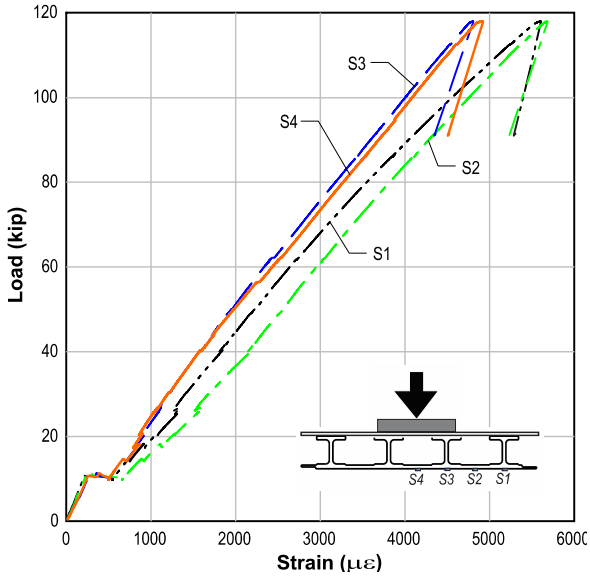

Figure 104 – A3 repair load-strain plot

10.4 Repair Evaluation

Three repair procedures applied to damaged specimens were evaluated. Figure 105 shows all the load-displacement curves from the test on the repaired specimens. For comparison, the curve from the original specimen (A_P) test is included.

Original and repaired capacities are compared in Table 17. The A1 repair fell short of the original capacity. This was likely due to the low compressive strength of the concrete fill. A2 and A3 both raised the capacity of the deck and provided significantly more strength by 28% and 64%, respectively.

Original and repaired stiffnesses are compared in Table 18. These stiffnesses were determined by linear regression on the second branch of the bi-linear load-deflection relationships to ensure that the effect of cracking is included in the comparison. Even after

cracking of the fill material, both A1 and A3 exceed the original stiffness. A2 stiffness decreased due to the partial delamination of the repaired web; for this reason both pre- and post-delamination stiffness were determined. Neither reached the original stiffness. A3 exceeded the original stiffness by more than 50%.

Based on both the strength and stiffness of these tests, repair scheme A3 appears to perform the best. In addition, repair A3 was relatively simple to implement, since removal of the top plate was not required. A1 might also perform well if the concrete used to fill the deck is of adequate strength.

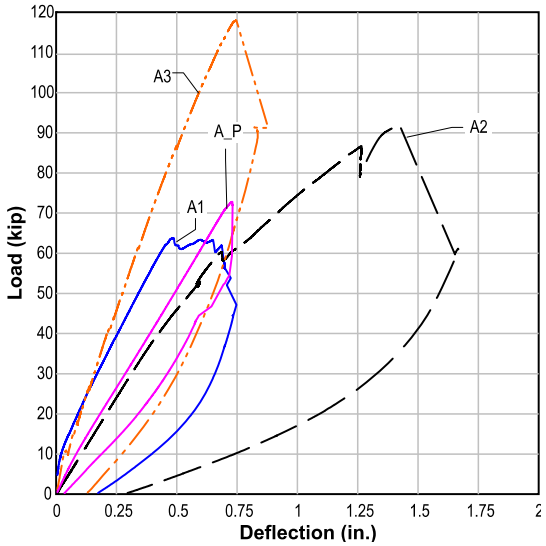

Figure 105 – Load-deflection ULT all A type specimens

Table 17 – Repaired specimen's load capacities

Repair	Capacity (kip)	Load Ratio
A1	64	0.89
A2	92	1.28
A3	118	1.64

Table 18 – Repaired specimen's stiffness

Repair	Stiffness (kip/in.)	Stiffness Ratio
A-1	120	1.08
A-2	91-51*	0.82-0.46
A-3	171	1.54

*Stiffness changed during testing (Figure 97)

11 Analysis of AE Test Data

This chapter covers the analysis of AE data gathered during structural testing of the deck specimens. The objective was to adapt an existing method or develop a new assessment procedure that uses the AE data to evaluate the structural integrity of the decks. Intensity analysis and Recovery Ratio (RR) were initially used to analyze the AE data. Intensity analysis was developed for and is still in use by the railroad tank industry for inspecting steel rail cars; it uses the cumulative signal strength and changes in signal strength to determine structural integrity. RR analysis is based on the calm ratio, which was developed for use in several materials including reinforced concrete and GFRP. It is a quantitative analysis that compares the AE data gathered during loading to the data gathered during unloading.

The differences in the deck materials and configurations resulted in varying failure modes. Consequently, the analyses first focused on the individual specimen types. Ultimately, a test methodology and evaluation criteria were developed that are applicable to all tested specimens.

11.1 Intensity Analysis

The AE data from the load tests were evaluated using an intensity analysis procedure that measured the structural significance of AE activity based on signal strength; the signal strength was evaluated on a per channel basis (Fowler 1989). Two parameters are typically determined for each channel: historic index and severity. Historic index (H(t)) compares the average signal strength of the last 20% or 200 events, whichever is less, to the average signal strength of all events (Fowler 1989). Further detail on this method is available in the literature review chapter. Historic index measures the change in signal strength magnitude relative to the loading cycle. The sudden increase in signal strength during a loading cycle will typically result in a significant historic index. Figure 106a is a specimen historic index plot corresponding to a DST for A_P. This is a hit based plot; the lack of hits during the 5 kip load hold is reflected by the lack of the load data on the plot. The historic index has several local maxima; each is related to an increase in load.

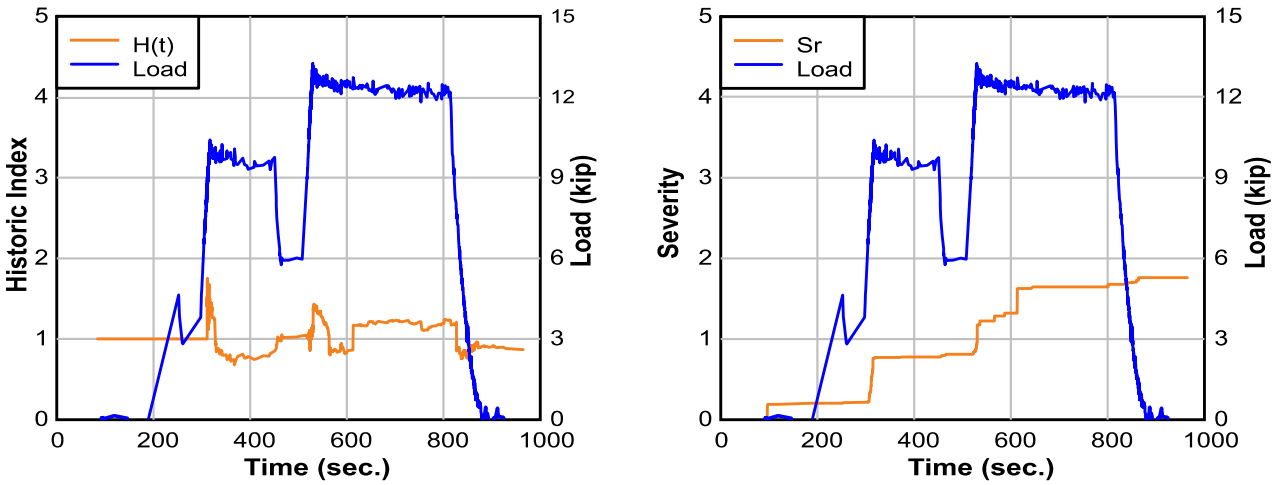

(a) (b)

Figure 106 – (a) Historic index and (b) severity specimen plots

Figure 107 shows a typical plot of the intensity analysis results. This example corresponds to channel four on specimen A_P. Intensity analysis did not provide clear distinction between loading of undamaged and damaged specimens. In general, the severity or HI, or both, would be expected to show an increase for an analysis on a damaged system. This example shows some distinction when considering HI, where the undamaged results are close to 1 and the damaged specimens hover below 2. These results, however, were not consistent. Consequently, effort was focused on developing the recovery ratio analysis.

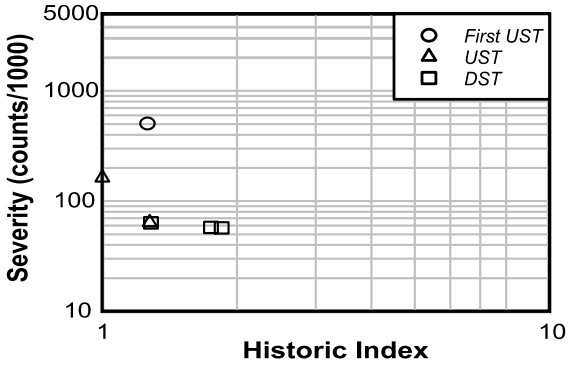

Figure 107 – Intensity plot specimen A_P channel 4

11.2 Recovery Ratio Analysis

Luo et al. (2004) and Ohtsu et al. (2002) both used the calm ratio to evaluate structural damage in the form of cracking in concrete beams. The calm ratio is the ratio of AE activity during the unloading to the AE activity during the loading for a selected feature. This approach

requires that the strain be measured at or near the AE sensor to ensure that the local peak strain is identified; loading and unloading AE data are then apportioned appropriately based on the peak strain. Ohtsu et al. used load in laboratory testing of prestressed concrete beams to index the key points needed for the analysis. Other strain related parameters such as load or displacement have also been used to index the data. Luo et al. applied the calm ratio to a load test on an in-situ bridge pier using displacement as the indexing factor.

Structural evaluation using the calm ratio also requires that the load ratio be determined, which is based on the felicity effect and is the ratio of the load at the onset of AE activity to the maximum load experienced by the specimen. Ohtsu et al. used the load ratio in their investigation because it is appropriate for laboratory settings where the load is known. Load history for in-service bridge components, however, is unknown. To circumvent load measurement, Luo et al. proposed using the RTRI ratio (ratio of the repeated train load at the onset of AE activity to relative maximum load for inspection period) be used in place of the load ratio; it uses the ratio of displacement at the onset of AE activity to the peak displacement seen in the current load cycle. This differs from the load ratio in that a relative value is used instead of the maximum load ever experienced.

To evaluate the structure, Ohtsu suggested plotting the calm and load ratios as shown in Figure 108 and using the four quadrants to rate the potential damage. A high calm ratio combined with a low load ratio is indicative of heavy damage. A large amount of AE data during unloading (high calm ratio) is typically indicative of significant damage; this combined with AE activity at low loads (low load ratio) is a strong indicator of damage.

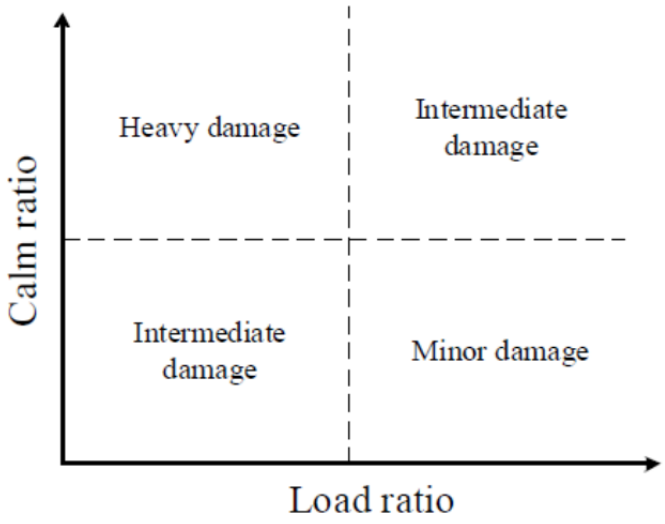

Figure 108 – Calm ratio plot (Grosse and Ohtsu 2008)

The goal of the present research was to determine if AE could be used to detect damage in GFRP deck panels in the laboratory and then eventually in the field during bridge load tests. Consequently, the preceding procedures by Ohtsu et al. (2002) and Luo et al. (2004) were adapted for use in laboratory deck testing and are referred to as recovery ratio analysis (RRA). The relative load ratio (RL) (Equation 3) is defined as the ratio of the load at onset of AE activity to the maximum load during each loading cycle:

$$RL = \frac{ILD}{MLD} \qquad \text{Equation 3}$$

where ILD is the load at which significant AE activity is detected and MLD is the maximum load level of the load cycle. The AE ratio (AEr) is a hit-based parameter and can be calculated as follows:

$$AEr = \frac{ULH}{LDH} \qquad \text{Equation 4}$$

where ULH is the number of hits during the unloading of the specimen and LDH is the number of hits during the loading.

Eight channels of AE data were collected during testing of both undamaged (UST) and damaged (DST) specimens. Recall that service loads were used, which simulate the type of loading that would be used to generate AE in the field. Figure 109(a) shows the hits recorded

during DST on specimen B_P. To remove spurious hits, the modified Swansong 2 filter was used (Figure 109b). This is typically used in the pressure tank industry to remove known mechanical noises from the data (Association of American Rail Roads). Any hit with a duration of greater than 3.5 milliseconds and amplitude within 10 dB of the threshold is extracted along with all hits occurring within ± ½ sec of the selected hit. This approach removes long-duration hits, which are typically indicative of rubbing and not resin cracking or fiber rupture. In this investigation, only the hits known to be the rubbing are removed and the one second window around the hit was not removed. All hits with zero energy were also removed from the data set. In the example shown in Figure 109 filtering removed approximately 60% of the hits. From the filtered data the AE ratio and the relative load ratio were then calculated for all the tests.

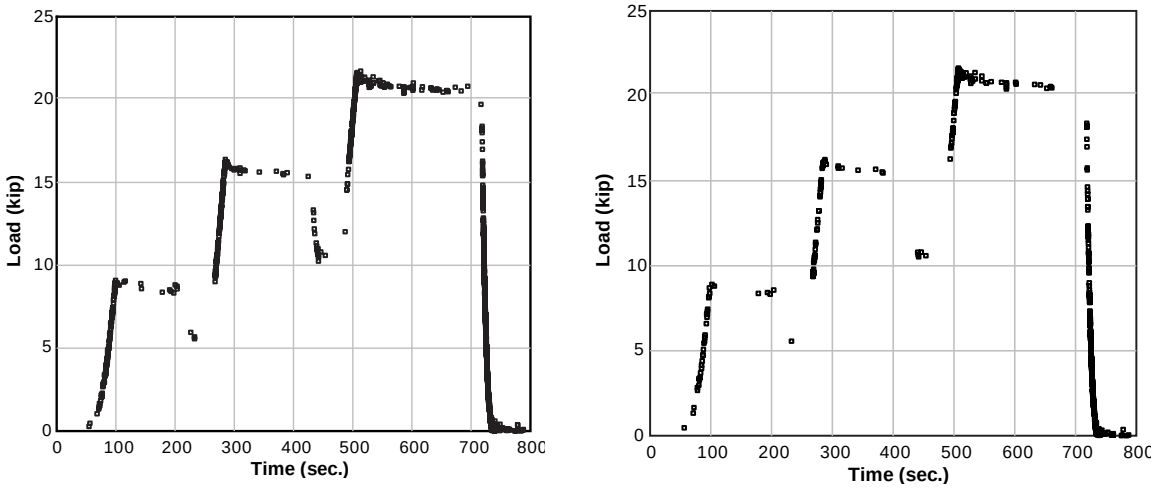

(a) (b)

Figure 109 – Specimen B_P AE data (a) unfiltered and (b) after Swansong filter 2

Figure 110 illustrates the parameters used in the RRA analysis and the method used to calculate AEr and RL. The analysis was conducted for each channel (sensor); each analysis produced a single set of values that can be used to evaluate whether damage has occurred. Not all channels produced sufficient AE to be considered in the analysis. This varied depending on the distance from the AE sensor to the damaged area and on the specimen type.

The AEr average results for DST positive and negative bending tests for all specimens are plotted in Figure 111(a) & (b). The UST AEr average values for most of the specimens were considerably less than the DST values; the analysis was successful in separating the damaged and the undamaged data. Only one specimen (B_N UST) did not have the same trend as all the

other specimens. It is not clear why the undamaged specimen generated more AE than the damaged specimen. That particular specimen only had one test which was useable in the analysis. In general, however, the method provides excellent discrimination between damaged and undamaged laboratory specimens.

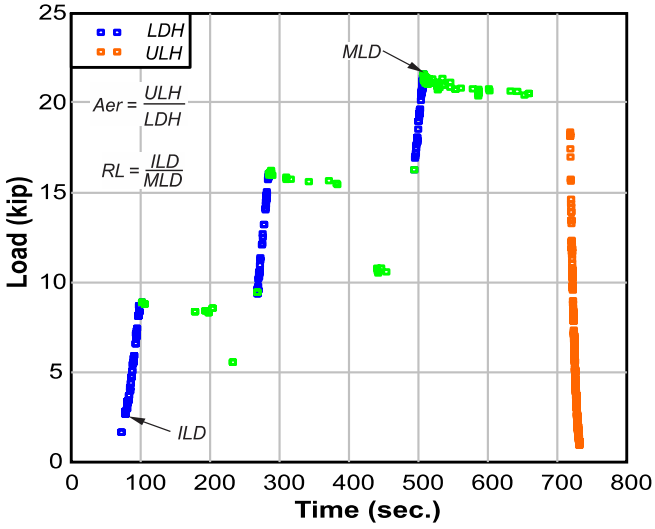

Figure 110 – Filtered data used in AE ratio analysis

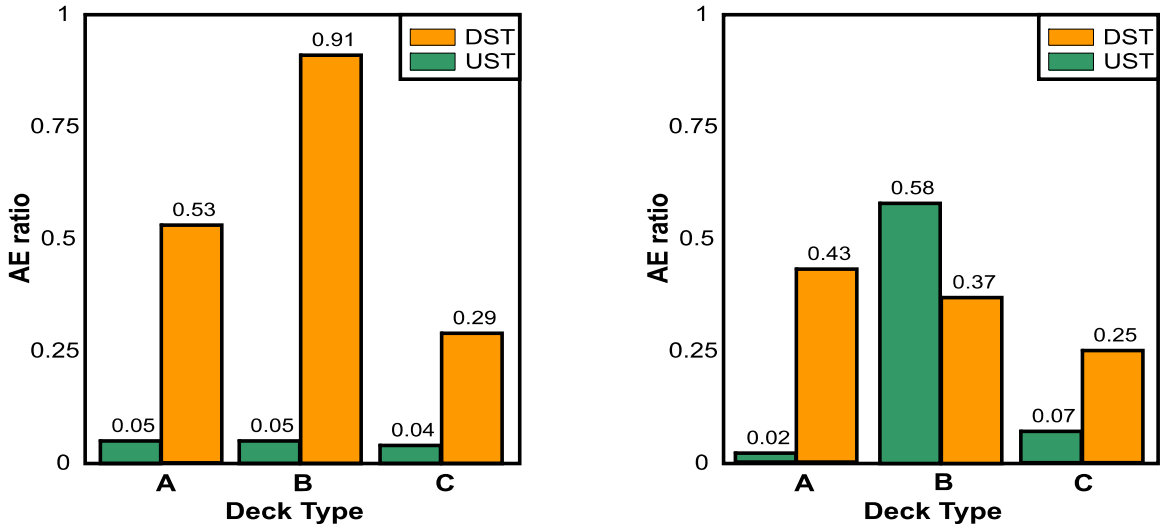

(a) (b)

Figure 111 – Average DST and UST values for (a) positive and (b) negative bending

Figure 112 shows the results of the RRA for positive bending results. Each point represents an AE sensor with sufficient data to generate the plotted values. Respective damaged (hollow markers) and undamaged (solid markers) values are plotted. As noted previously, all

three decks have distinctive differences between results from damaged and undamaged decks. The various failure mechanisms and the varying severity of damage explain the large range of DST results. The UST AEr results were exclusively grouped in the lower range of the plot; this was the pattern used to develop the proposed pass-fail line, highlighted in blue in Figure 112. Decks A and B appear to have some difference in the relative loading ratio, but Deck C does not. More testing should be performed in the varying damage levels for the development of a pass fail criterion.

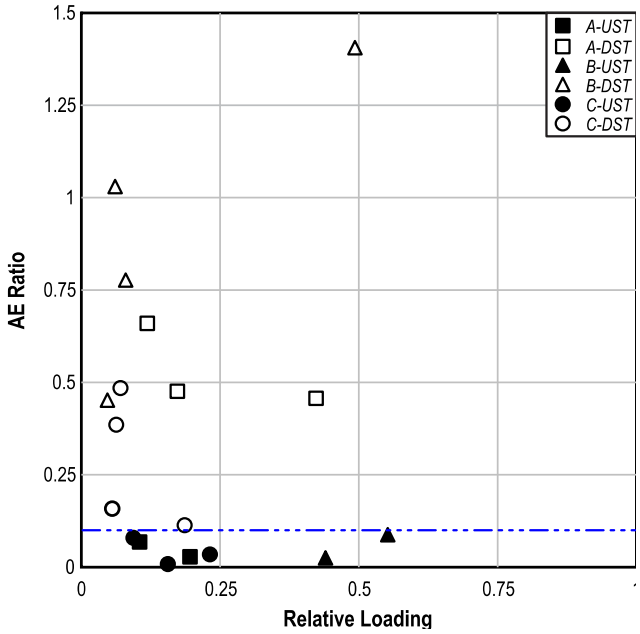

Figure 112 – RRA plot for positive bending-all specimens

Figure 113 shows the negative bending UST and DST results. The negative bending appeared to have good discrimination for both positive and negative bending. Consequently, two sets of damage regions were proposed based on the results and are depicted by the blue lines. UST RRA results were grouped below an AEr of 0.2 with one outlier at 0.6 for Deck A. This configuration did present a pattern in relation to the relative load axis. The DST results all plotted below 0.1 relative loads. A larger specimen group will need to be considered in order to confirm these findings.

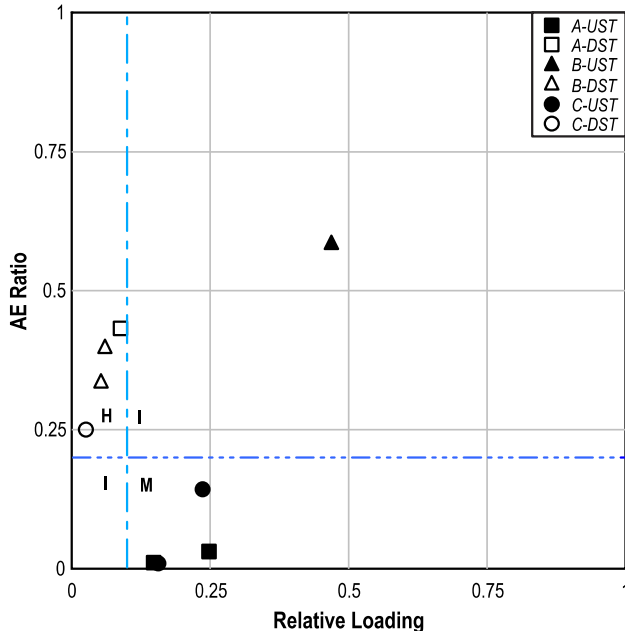

Figure 113 – RRA plot-negative bending test

Table 19 shows the average AE evaluation results along with the stiffness and strength ratios. These ratios provide a metric for comparing the damage levels sustained by each of the decks; lower ratios indicate more severe damage. The damage data do not appear to be correlated with the AE evaluation results.

Table 19 - Average values from RRA and stiffness and strength ratio

Specimen	AEr (avg.)		RL (avg.)		Stiffness	Strength
	UST	DST	UST	DST	ratio	Ratio
A_P	0.05	0.53	0.15	0.24	0.73	0.60
A_N	0.02	0.43	0.20	0.09	0.96	0.83
B_P	0.05	0.91	0.50	0.17	0.70	0.82
B_N	0.58	0.37	0.47	0.06	0.24	0.51
C_P	0.04	0.29	0.16.	0.09	0.70	0.80
C_N	0.07	0.25	0.20	0.03	0.14	0.18

12 Belle Glade Test

In a related FDOT research project, the steel deck of a bridge over the Hillsboro Canal in Belle Glade Florida was replaced with deck A. (McCall et al. 2011) The deck was load tested using strain and displacement gages; during one of the load tests AE data were also recorded. Trucks typically use lanes 1 and 2 to deliver sugarcane to the refineries north of the bridge during the harvest (Figure 114). These lanes were tested during the load test because of the large loads experienced compared to the south-bound lanes. Strain and displacement gages were placed along the north-bound lanes. AE sensors were located near strain gages. Details of the test procedures can be found in McCall et al. (2011).

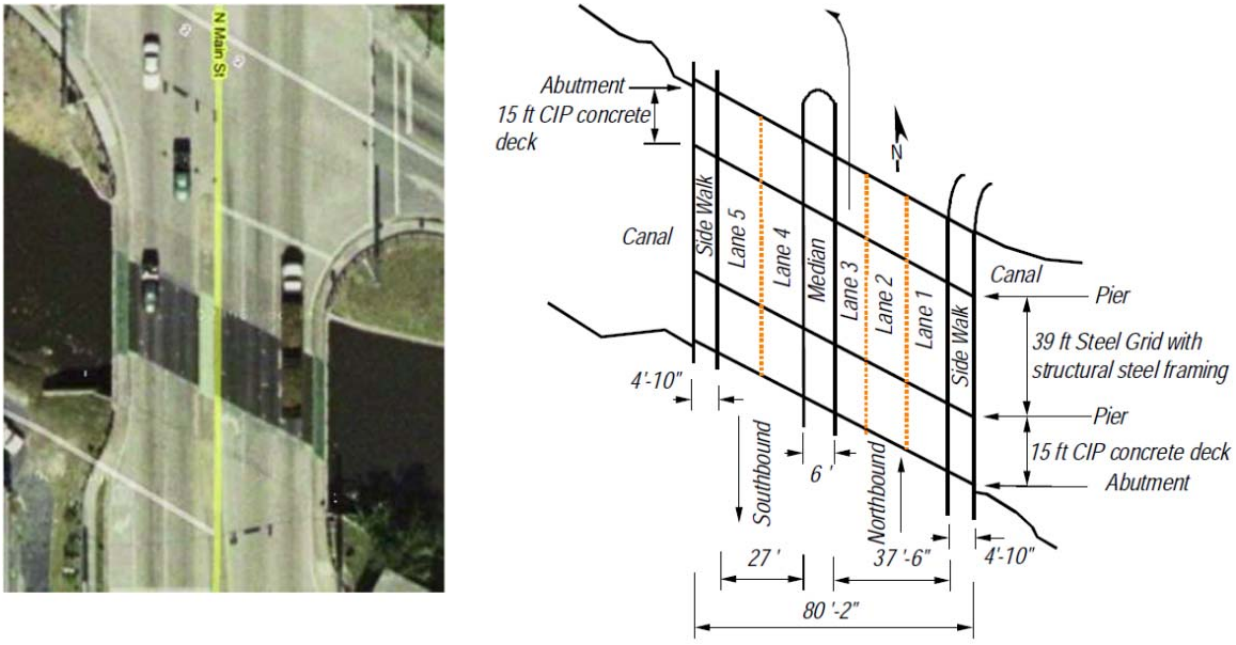

(a) (b)

Figure 114 – Bridge site (a) aerial photo and (b) detailed site plan

12.1 Sensor Locations

Figure 115 is a diagram of the bridge deck placement and the location of the AE sensors on the bridge relative to the deck panels. B9 and B10 are the panels monitored during the load test. The numbered lines running along the direction of travel represent the steel girders of the

bridge. Table 20 lists the AE sensors identifications and the coordinates corresponding to the location of each sensor on the soffit of the deck.

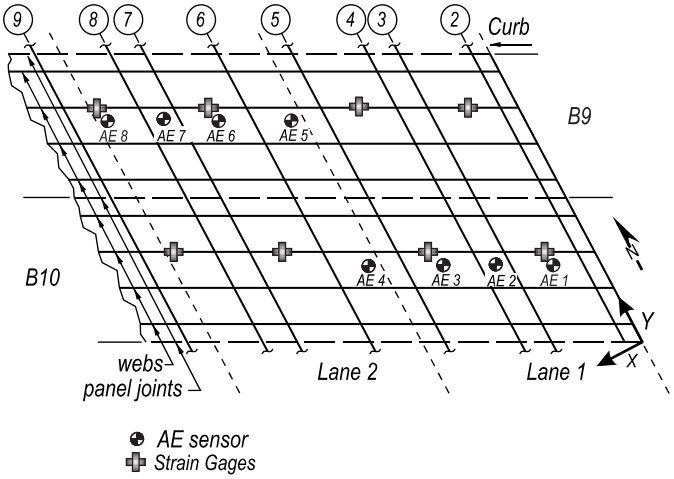

Figure 115 – AE Sensor locations on the deck panels

Table 20 – AE sensor identification and coordinates

Sensor	Sensor part number	Panel ID	Coordinate (in.)	
			X-coordinate	Y-coordinate
AE 1	BD 45	B10	36	188
AE 2	BD 32	B10	70	206
AE 3	BD 36	B10	104	224
AE 4	BD 48	B10	152	250
AE 5	BD 34	B9	152	282
AE 6	BD 42	B9	200	307
AE 7	DM 09	B9	234	325
AE 8	BD 43	B9	268	344

12.2 Relative Ratio Analysis on Belle Glade Bridge Data

The Relative Ratio analysis procedure developed to analyze the AE results from the laboratory testing requires that the peak load be known so that RL can be calculated, which may not be known during a bridge test. Another parameter that may be used to mark peak load is wheel position. The influence of the load on the area of interest can be obtained from the combination of GPS and strain gage data at the AE sensor location. This approach is particularly suited to bridge testing using GPS truck positioning in which the position of the wheel relative to the sensor is known.

The best approach would be to use the wheel position to calculate the Relative Load ratio. Unfortunately, the wheel location relative to the AE sensor position was not recorded. Figure 116 illustrates the adjustment made to the relative ratio analysis procedure to accommodate the constraints of the bridge test. RR analysis was adjusted so that the strain at the sensor caused by the rolling load rather than the position of the rolling load was used. The influence ratio is defined as the ratio of the strain at the onset of AE activity to the relative maximum strain of the loading.

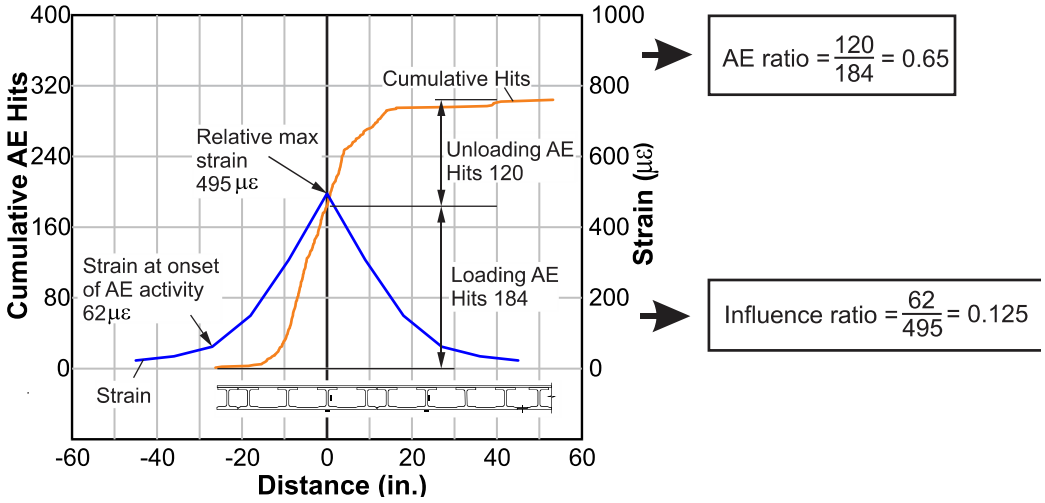

Figure 116 – AE ratio calculation for LC 4

Each wheel load passing the AE sensors could be used in the RR analysis because each represents the loading and unloading of the deck. Figure 117 shows the hits recorded during the load test for one pass of the truck over a single AE sensor. Each grouping represents the load imposed by one of the five truck axles. Although RR analysis could be used for any of the wheel loads, only the front and rear axles were selected for analysis. The front wheel was chosen because the data for this load was not influenced by any adjacent loads. The rear axle was also chosen because it transmits the largest wheel load.

Figure 118 shows a summary of the RR analysis results for the sampled loadings for truck position one; the AE ratio was calculated estimating the point of peak load from the AE data. Even though all the channels were used in the collection of the data, only channels 1-4 registered hits during the loading due to the attenuation of the emissions across the deck.

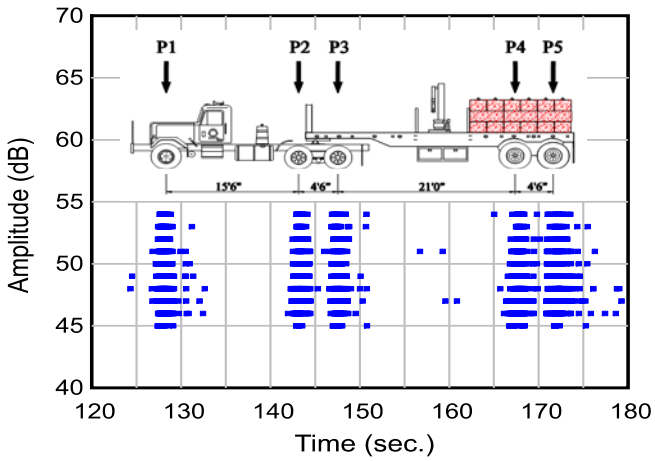

Figure 117 – AE data from bridge test LC4

AE results for the various load cases considered ranged from 0.3 to 0.8. If the evaluation criteria developed for the laboratory test are used, then these values indicate potential deck damage. Based on visual observation, however, it is unlikely that the bridge had sustained structural damage. The exact wheel position with reference to the sensor was not known for the load test; the ratios may have shifted due to the large number of hits near what was believed to be the peak of the load. The front axle results were above 0.5 and all the rear axle results were less than 0.5. This also suggests that the proximity of other wheels may have an effect on the calculated AE ratio. Another possible reason for the high ratio is that grout cracking may have influenced the AE recorded during the bridge test.

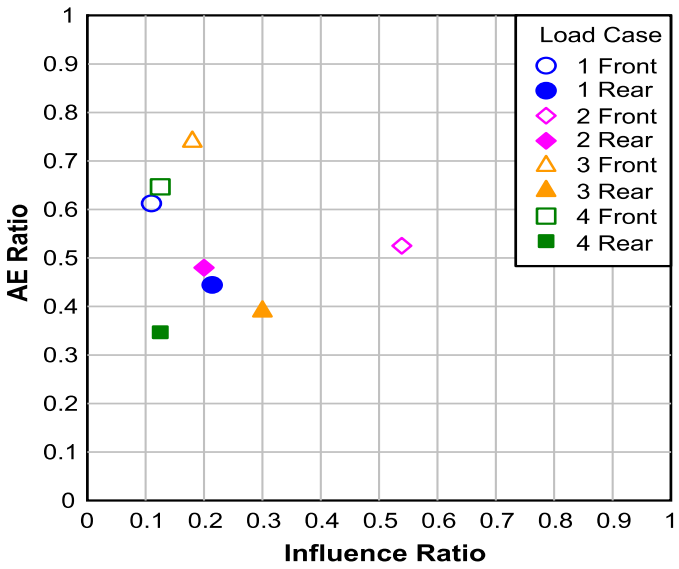

Figure 118 – Sample RR analysis results for bridge load test

13 Summary and Conclusions

Three commercially available GFRP bridge deck systems were tested in both positive and negative bending in a three-point loading setup. Each specimen was subjected to sequential load tests having the following characteristics. First, the specimen was subjected to two undamaged service tests (UST) composed of three load holds. The specimen was then subjected to an ultimate load test (ULT) in which the specimen was loaded to its ultimate capacity to cause damage without completely destroying the specimen. Finally, stepwise service loads were again imposed on the damaged deck to determine how well AE could detect the damage that had been imposed by the ultimate strength test. This test is referred to as the damaged service test (DST). Both positive and negative bending specimens were tested using the same procedures. Load steps were separated by a brief load reduction to allow observation of Kaiser and felicity effects during reloading. During load testing, AE, load, strain, and displacement were monitored.

Two AE analysis methods were used to evaluate the data. Intensity analysis, which is routinely used in the testing of pressure vessels and has been tested on GFRP decks, was used initially to analyze the AE data from the load tests. In addition, relative ratio analysis (RRA) was developed and applied to the laboratory results. RRA was also used to analyze selected bridge load test data from Belle Glade.

Three repair procedures were developed and applied to deck A. Repair A1 was to place GFRP bars in the cavities between the webs and then fill this cavity with concrete. A2 was to apply wet layup GFRP to the damaged webs. A3 was to fill the cavities with grout and apply GFRP to the soffit of the deck.

From the previously described testing the following conclusions are drawn:

- Flexural capacity and damage characteristics of each specimen were determined for both positive and negative bending in each of the three deck types. The ultimate capacity was found to be well beyond the maximum service wheel loads and ranged from 3.8 to 6.7.
- Deck A retained 60% and 83% of its positive and negative bending capacity, respectively. Deck B retained 82% and 51% of its positive and negative bending capacity, respectively. Deck C retained 80% and 14% of its positive and negative bending capacity, respectively.

- A1, A2, and A3 reached 89%, 128%, and 164% of the original deck capacity. Based on the constructability and strength gain, A3 is the best repair method.
- Intensity analysis was found to be inadequate to discriminate between damaged and undamaged AE results.
- Recovery ratio analysis provided significant discrimination between AE data taken from undamaged and damaged decks. For positive bending, damaged decks generally exhibited an AE ratio of 0.1 or greater, while undamaged results were below 0.1. For negative bending, those specimens with an AE ratio greater than 0.2 and a Relative Loading less than 0.1 were damaged, while nearly all those with an AE ratio less than 0.2 were undamaged.
- Recovery ratio analysis was applied to AE data gathered from a bridge load test on a bridge with deck A. The results, when compared to the criteria developed for the laboratory tests, indicated damage. No deck damage was noted. Refinement in the method may be needed or cracking of the grout pad used to support the GFRP deck system may be leading to false positive readings.

14 References for Part I

Alagusundaramoorthy, P., Harik, I. E., & Choo, C. C. (2006). Structural Behavior of FRP Composite Bridge Deck Panels, *Journal of Bridge Engineering, 11*(4), 384-393.

Alampalli, S. & Kunin, J. (2001), Load testing of an FRP bridge deck on a truss bridge. Report FWHA/NY/SR-10/137.

Alampalli, S. & Kunin, J. (2002). Rehabilitation and field testing of an FRP bridge deck of a truss bridge, *Composite Structures* 57, 373-375.

Arnold, R. E, (2003). Acoustic Emission Evaluation of FRP Composite Specimens in Tension and Bending. Morgantown, W. Va.: West Virginia University *College of Engineering and Mineral Resources*. West Virginia University.

Association of American Railroads operations and maintenance department-mechanical division.(1998) Procedure for Acoustic emission evaluation of tank cars and IM101tanks.

Brown, D. L., & Berman, J. W. (2010). Fatigue and Strength Evaluation of Two Glass Fiber-Reinforced Polymer Bridge Decks. *Journal of Bridge Engineering, 15*(3), 290-301.

Camatta, G., &Shing, P. B. (2010). Static and fatigue load performance of a gfrp honeycomb bridge deck. Composites:Part B 41, 299-307

Chen, A., & Davalos, J. F. (2010). Strength evaluations of sinusoidal core for FRP sandwich bridge deck panels. Composite Structures, 92, 1561-1573.

Cole, T. A., Lopez, M., & Ziehl, P. H. (2006). Fatigue behavior and nondestructive evaluation of full-scale FRP honeycomb bridge specimen. *Journal of Bridge Engineering, 11*(4), 420-429.

Cousins, T. E., Lesko, J. J., Mjumdar, P. K., & Liu, Z. (2009). Rapid replacement of Tangier Island bridges including lightweight and durable fiber-reinforced polymer deck systems. FHWA/ VTRC 10-CR3

Fowler, T.J., Blessing, J.A. and Conlisk, P.J. (1989). New directions in testing. In: Proc. 3rd International Symposium on Acoustic Emission from Composite Materials, Paris, France

Gostautas, R., Ramirez, G., Peterman, R. J. & Meggers, D. (2005) Acoustic Emission Monitoring and Analysis of Glass Fiber-Reinforced Composites Bridge Decks. *Journal of Bridge Engineering*, 10 (6), 713-721.

Grosse, C. U., & Ohtsu, M. (2008). Acoustic Emissions Testing. *Springer-Verlag Berlin Heidelberg*.

Hong, T., & Hastak, M. (2006) Construction, Inspection, and Maintenance of FRP Deck Panels. *Journal of Composites for Construction*, 10 (6), 561-572.

Jeong, J., Lee, Y. H., Park, K. T., & Hwang, Y. K. (2006). Field and laboratory performance of a rectangular shaped glass fiber reinforced polymer deck. *Composite Structures* 81, 622–628

Kalny, O., Peterman, R. J.,& Ramirez, G., (2004). Performance evaluation for repair technique for damaged fiber-reinforced polymer honeycomb bridge deck panels, *Journal of Bridge Engineering,9*(1), 75-86.

Keller, T., & Gurtler, H. (2005). Quasi-static and fatigue performance of a cellular FRP bridge deck adhesively bonded to steel girders. *Composite Structures*, 70, 484–496.

Keller, T., & Schollmayer, M. (2004). Plate bending behavior of a pultruded GFRP bridge deck system. *Composite Structures, 64*(3-4), 285-295.

Liu, Z., Cousins, T. E; Lesko, J.J., & Sotelino, E. D.(2008). Design Recommendations for a FRP Bridge Deck Supported on Steel Superstructure. *Journal of Composites for Construction, 12*(4), 660-668.

Luo, X., Haya, H., Inaba, T., Shiotani, T., Nakanishi, Y. (2004). Damage evaluation of railway structures by using train-induced AE. *Construction and Building Materials* 18, 215–223.

Majumdar, P. K., Lesko, J. J., Cousins, T. E., & Liu, Z. (2009). Conformable tire patch loading for FRP composite bridge deck. *Journal of Composites for Construction, 13*(6), 575-581.

McCall, J. L., Peng, X., Singh, A. P., & Hamilton, H. R., (2011) *Hillsboro Canal Bridge Monitoring*, FDOT Research Report BDK75 977-16.

O'Connor, J. S. (2008), GRP bridge decks and superstructures in the USA. *Reinforced Plastics,* 26-31.

Ohtsu, M, Uchida, M; & Okamoto, T (2002). Damage assessment of reinforced concrete beams qualified by acoustic emission. *ACI Structural Journal,* 99, 411-417.

Park, K. T., Hwang, K. T., Lee, Y. H., & Kim, S. M (2007). Performance verification of a new pultruded GFRP bridge deck-to-girder connection system. *Composite Structures* 81 (2007) 114–124.

Prachasaree, W., Gangarao, H. V. S., & Shekar, V. (2009). Performance Evaluation of FRP Bridge Deck Under Shear Loads. *Journal of Composite Materials,* 43(4), 377-395.

Reeve, S., (January 2010), FRP bridges-14 years and counting. *Reinforced Plastics,* 40-44.

Telang, N. M., Dumlao, C., Mehrabi, A. B., Ciolko, A. T., & Gutierrez, J. (2006). *Field inspection on in-service FRP bridge decks* (No. 564). Transportation Research Board.

Turner, M. K., Harries K. A., Petrou, M. F., Rizos, D.,(2004). In situ structural evaluation of a GFRP bridge deck system. *Composite Structures*, 65, 157–165.

Vyas, J. S., Zhao, L., Ansley, M. H., & Xia, J. (2009). Characterization of a low-profile fiber-reinforced polymer deck system for moveable bridges. *Journal of Bridge Engineering, 14*(1), 55-65.

Zhou, A., Coleman, J. T., Temeles, A. B., Lesko, J. J., & Cousins, T. E. (2005). Laboratory and field performance of cellular fiber-reinforced polymer composite bridge deck systems. *Journal of Composites for Construction, 9*(5), 458-467.

Appendix A Load-Strain and Load-Deflection Plots

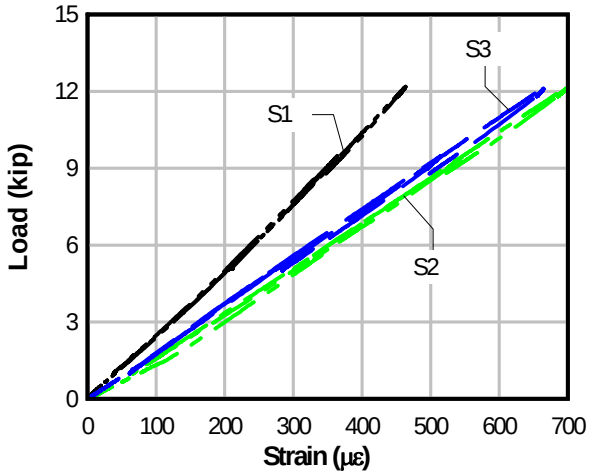

A_P_S_1 load-strain plot

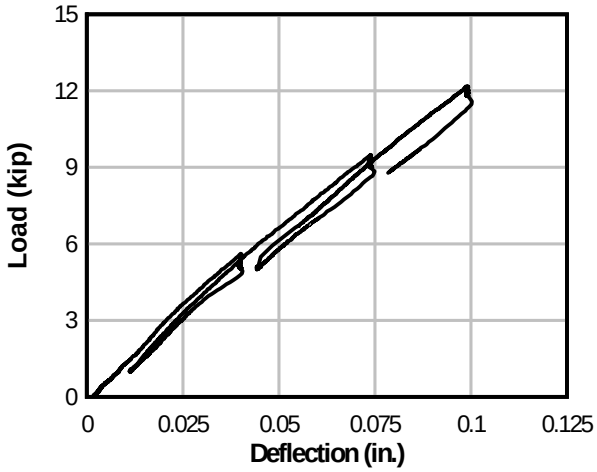

A_P_S_1 load-deflection plot

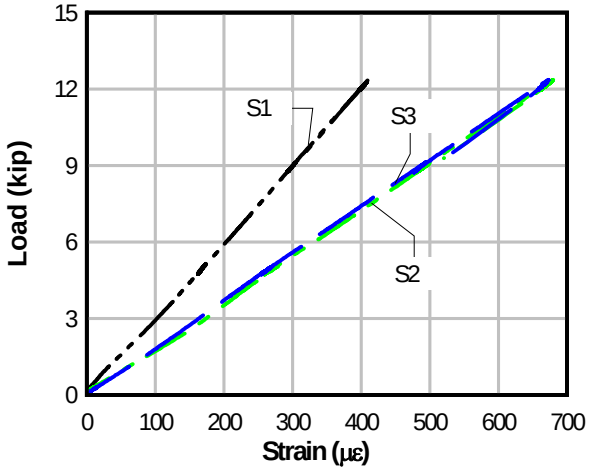

A_P_S_2 load-strain plot

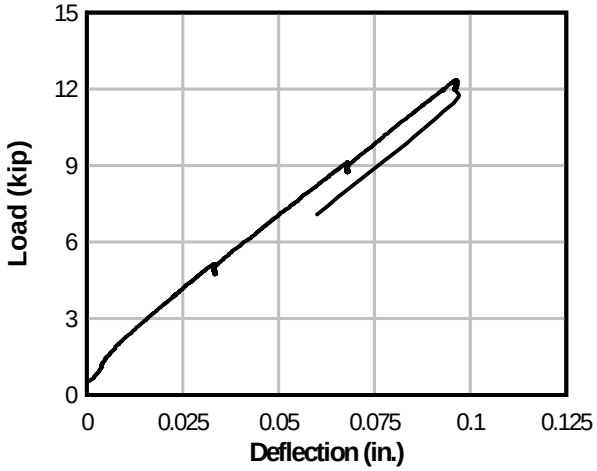

A_P_S_2 load-deflection plot

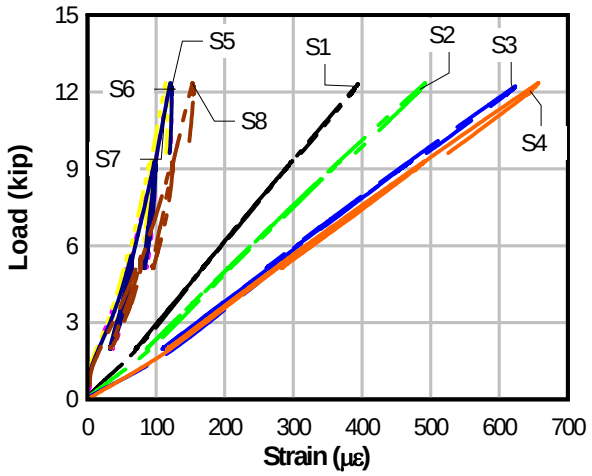

A_P_S_3 load-strain plot

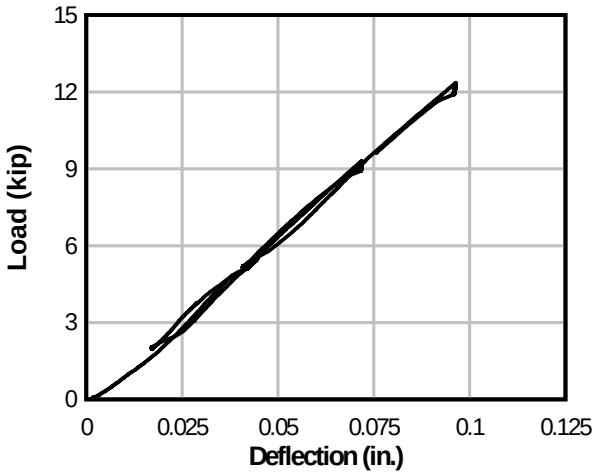

A_P_S_3 load-deflection plot

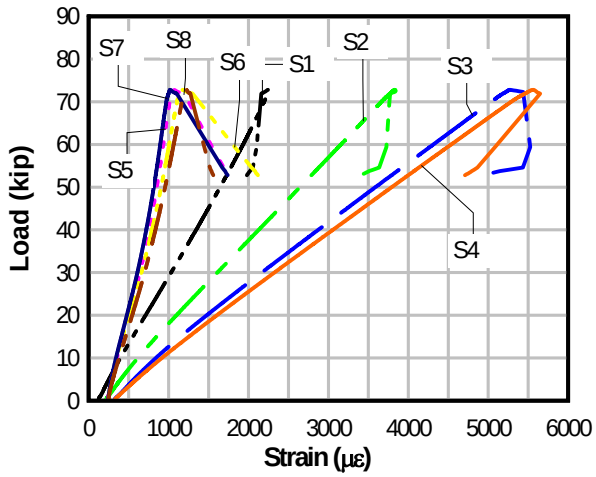

A_P_U load-dtrain plot

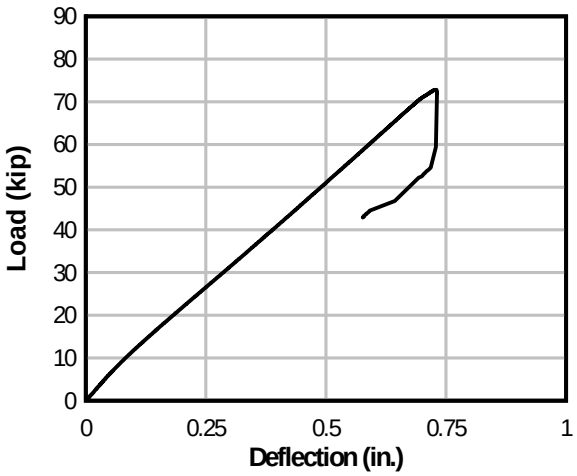

A_P_U load-deflection plot

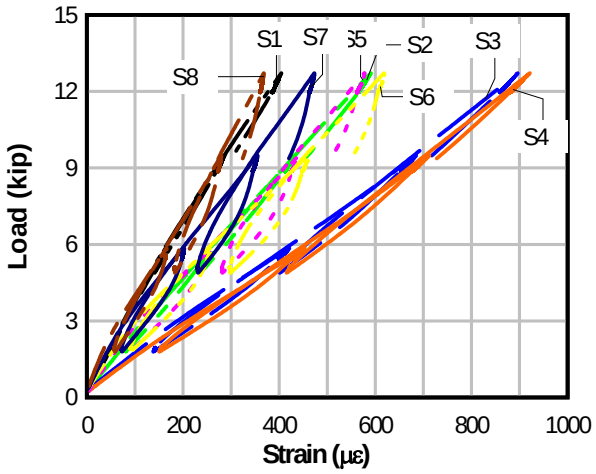

A_P_S_4 load-strain plot

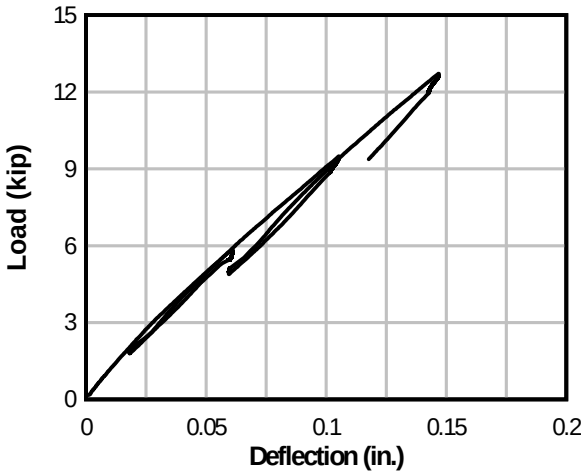

A_P_S_4 load-deflection plot

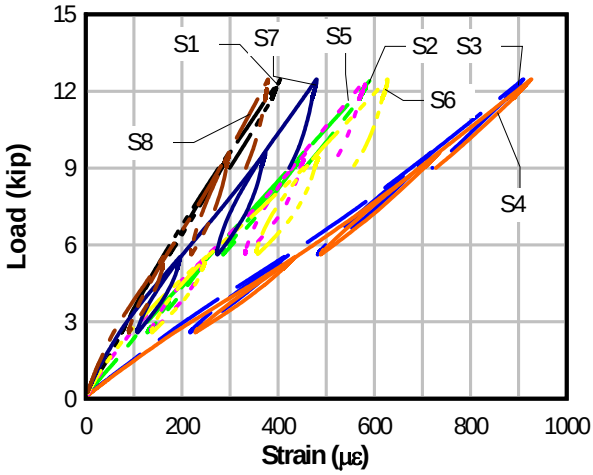

A_P_S_5 load-strain plot

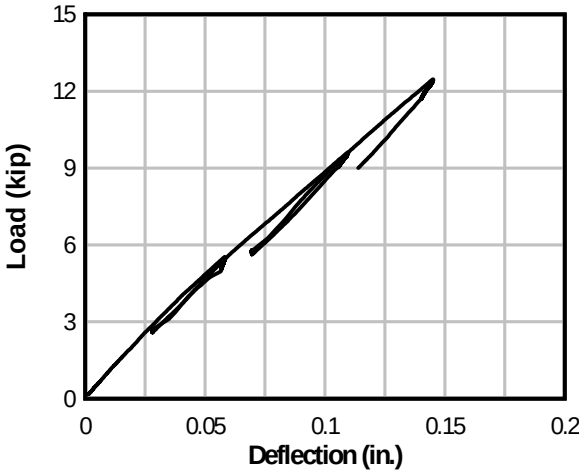

A_P_S_5 load-deflection plot

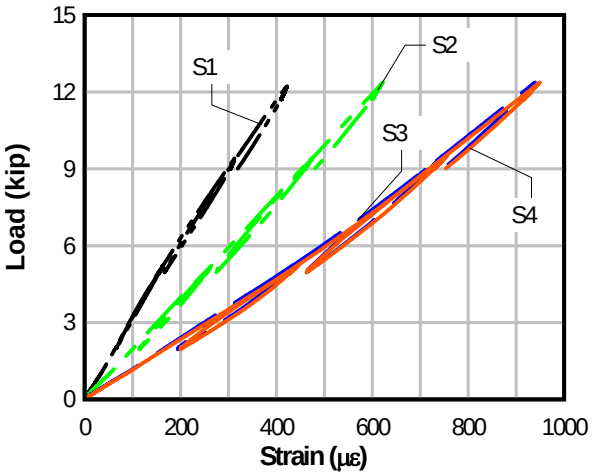

A_P_S_6 load-strain plot

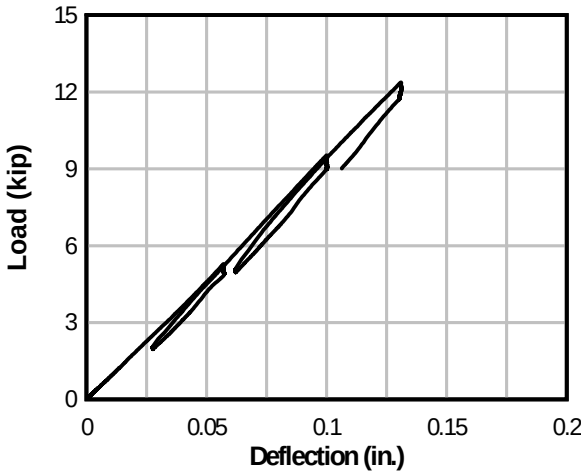

A_P_S_6 load-deflection plot

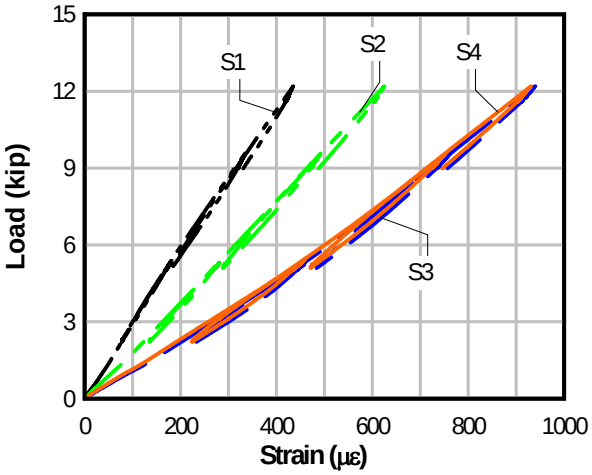

A_P_S_7 load-strain plot

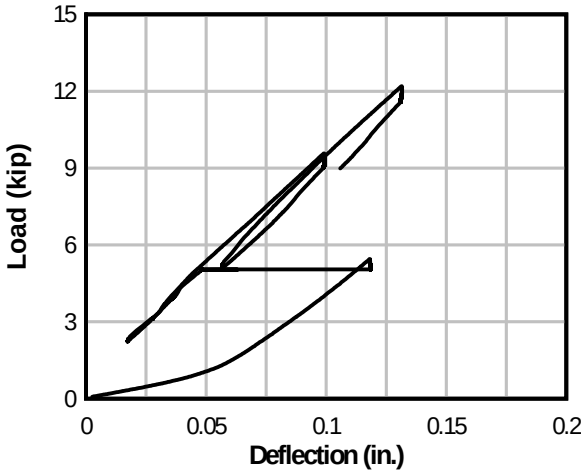

A_P_S_7 load-deflection plot

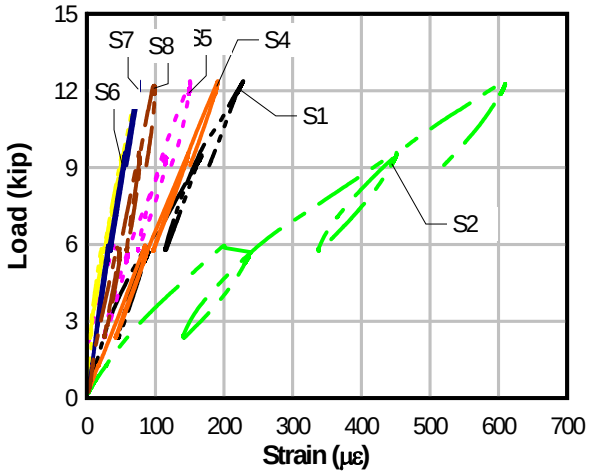

A_N_S_1 load-strain plot

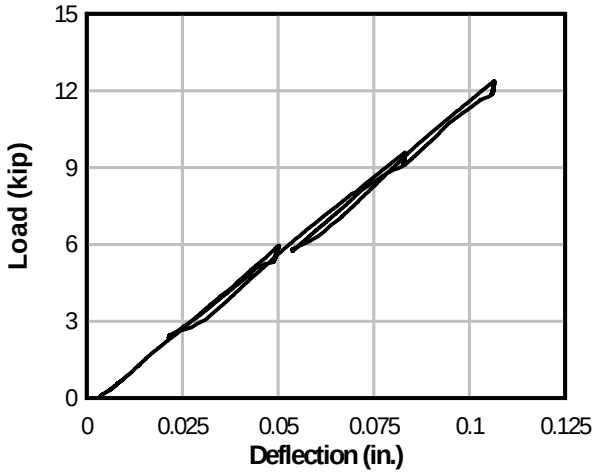

A_N_S_1 load-deflection plot

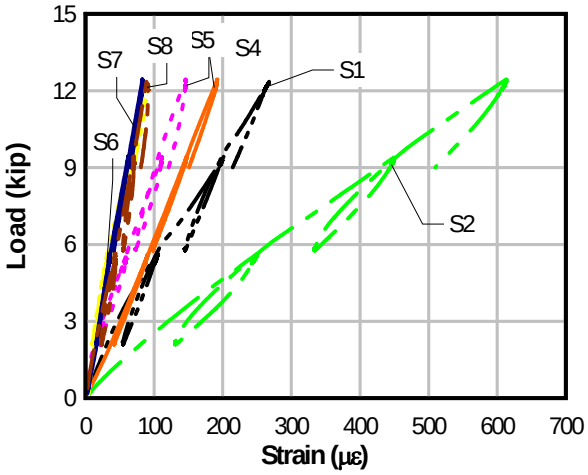

A_N_S_2 load-strain plot

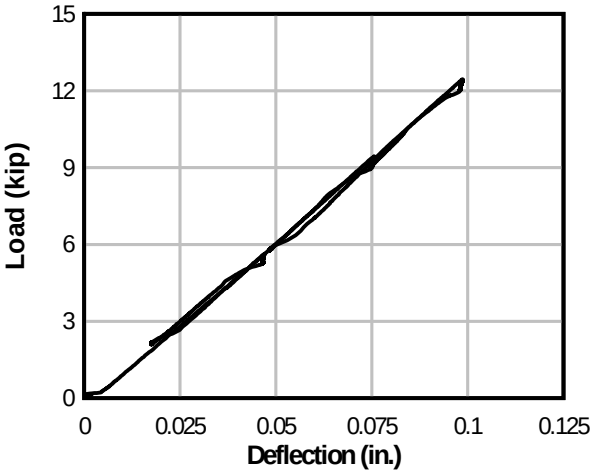

A_N_S_2 load-deflection plot

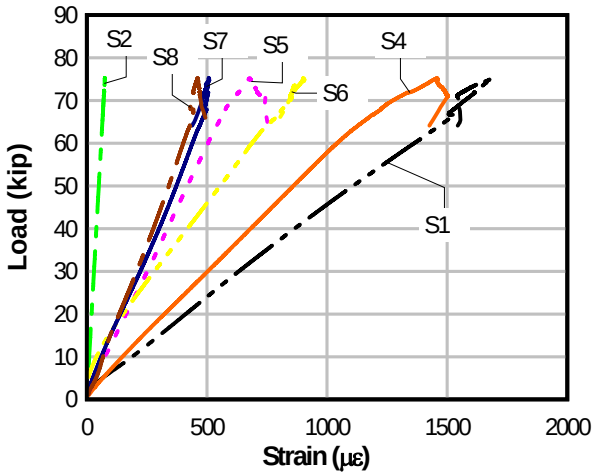

A_N_U load-strain plot

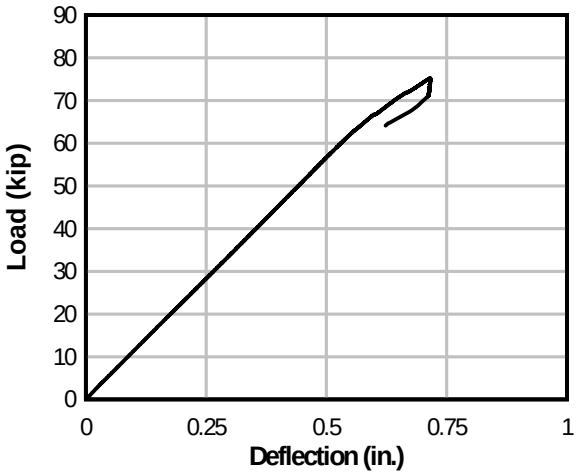

A_N_U load-deflection plot

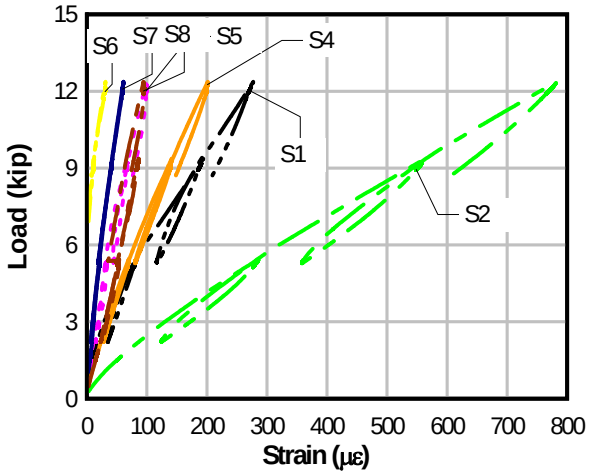

A_N_S_3 load-strain plot

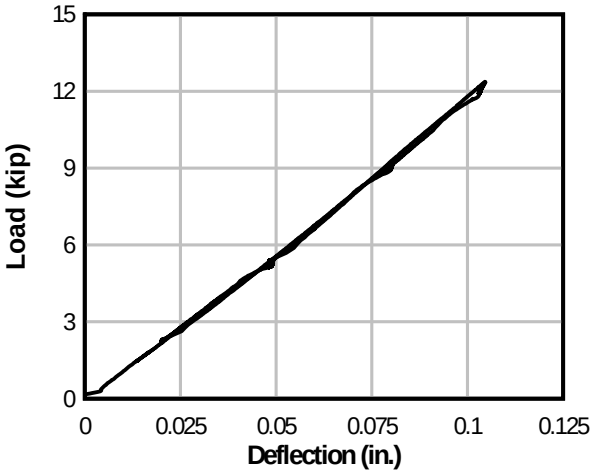

A_N_S_3 load-deflection plot

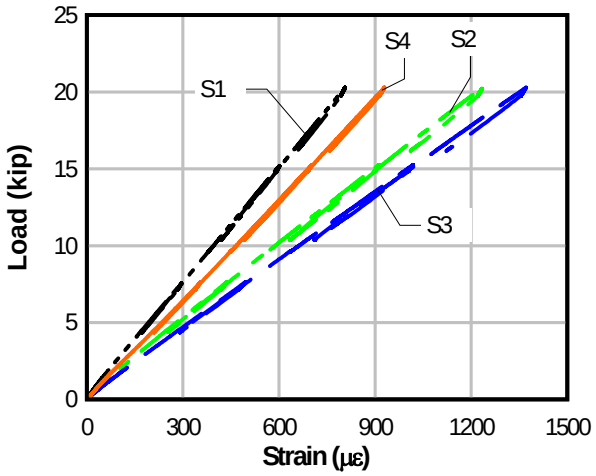

B_P_S_1 load-strain plot

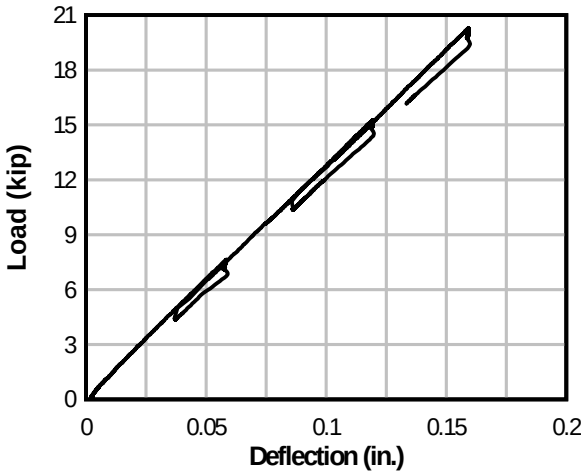

B_P_S_1 load-deflection plot

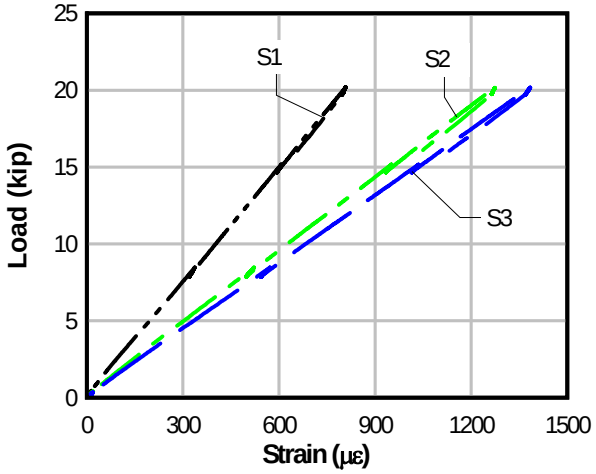

B_P_S_2 load-strain plot

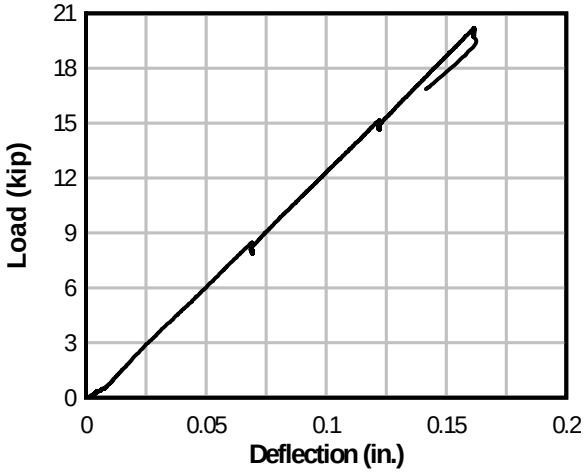

B_P_S_2 load-deflection plot

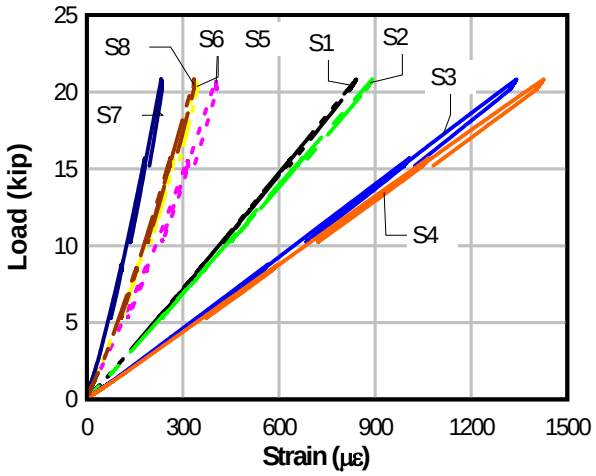

B_P_S_3 load-strain plot

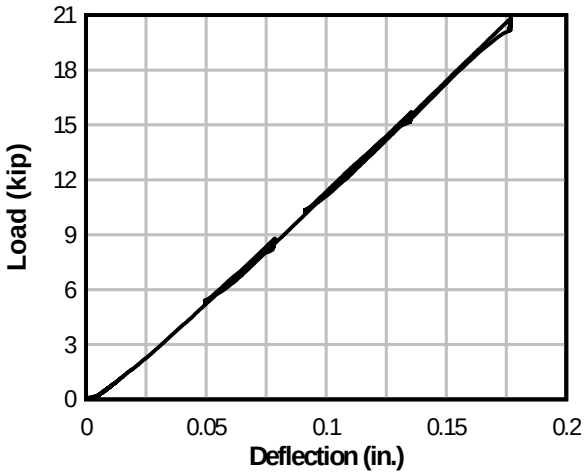

B_P_S_3 load-deflection plot

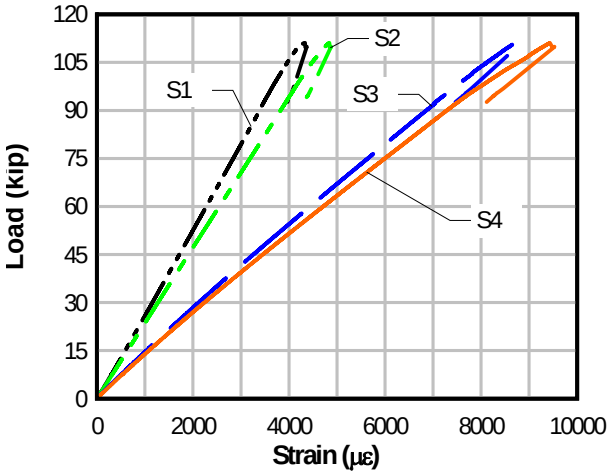

B_P_U load-strain plot

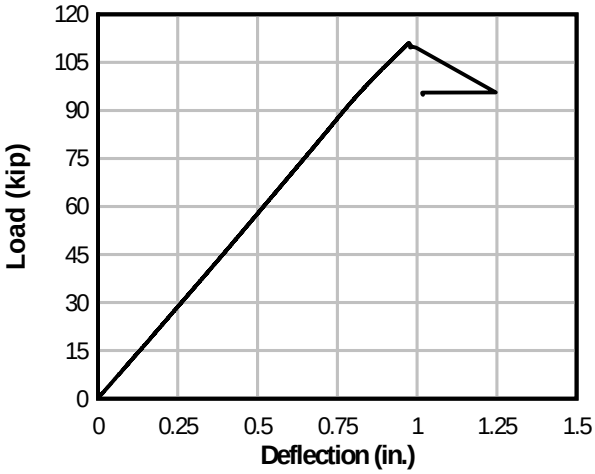

B_P_U load-deflection plot

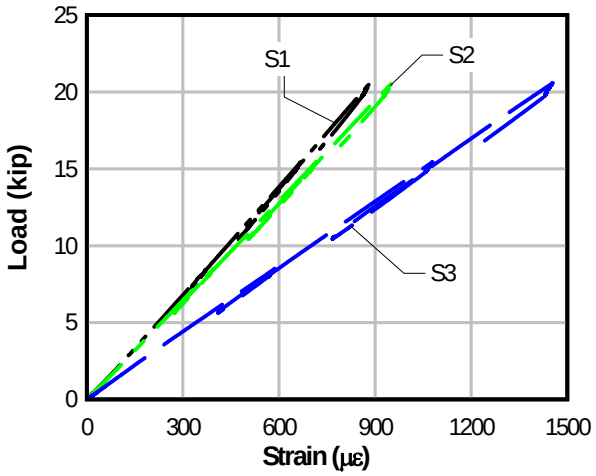

B_P_S_4 load-strain plot

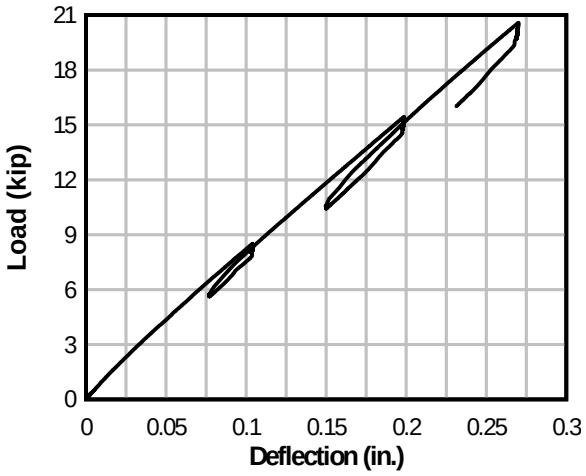

B_P_S_4 load-deflection plot

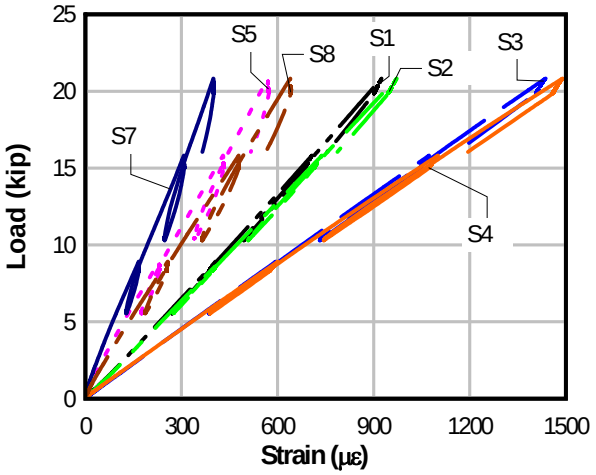

B_P_S_5 load-strain plot

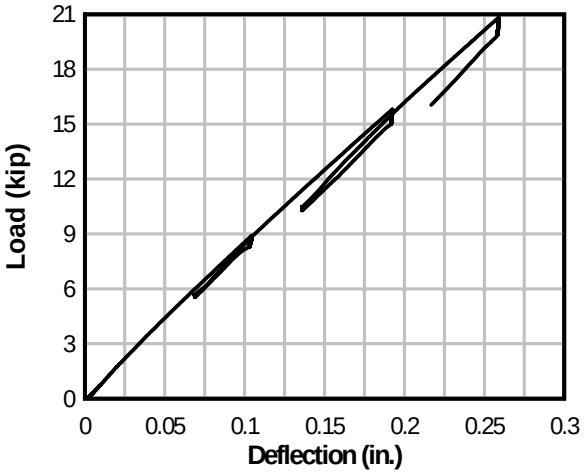

B_P_S_5 load-deflection plot

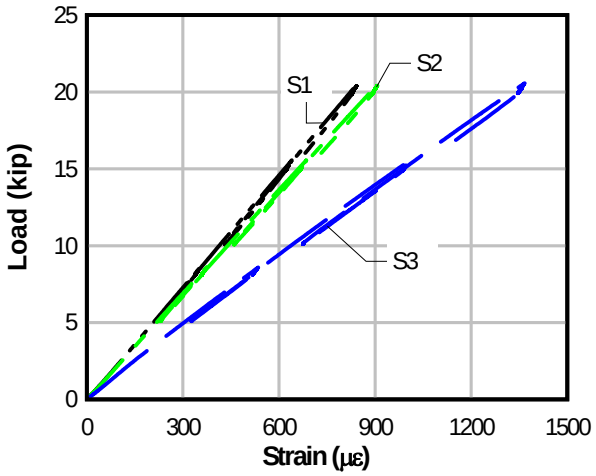

B_P_S_6 load-strain plot

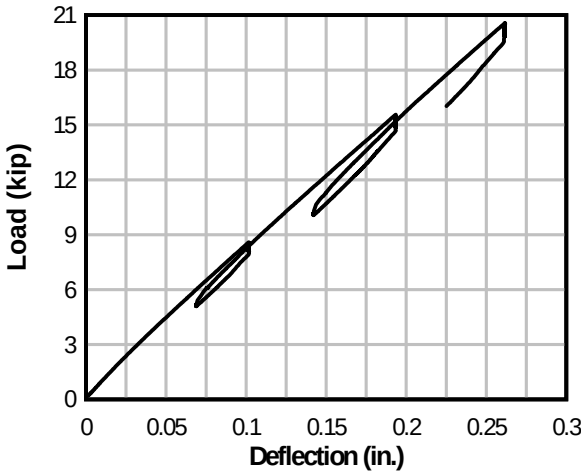

B_P_S_6 load-deflection plot

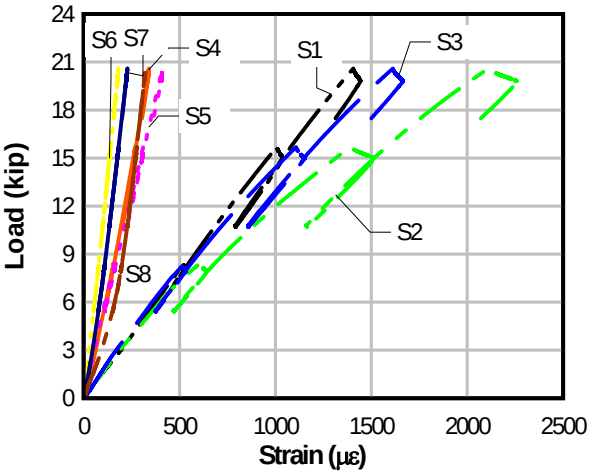

B_N_S_1 load-strain plot

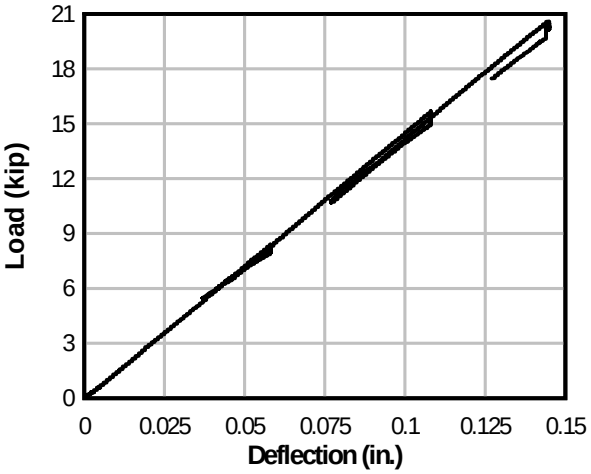

B_N_S_1 load-deflection plot

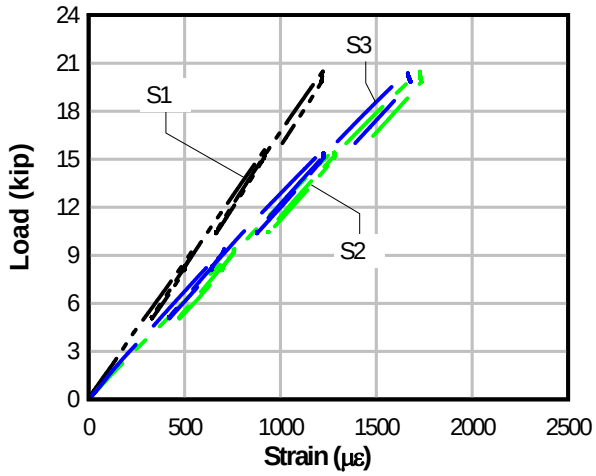

B_N_S_2 load-strain plot

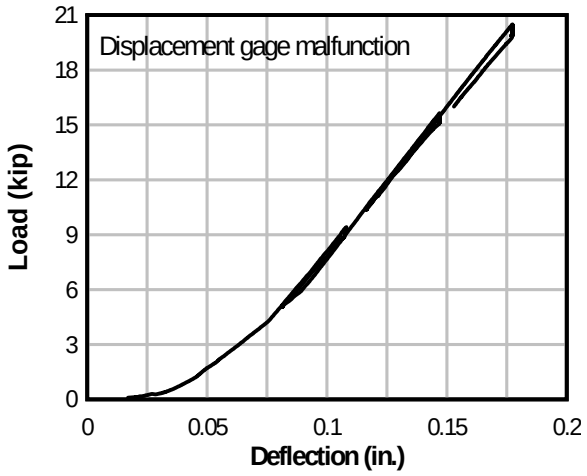

B_N_S_2 load-deflection plot

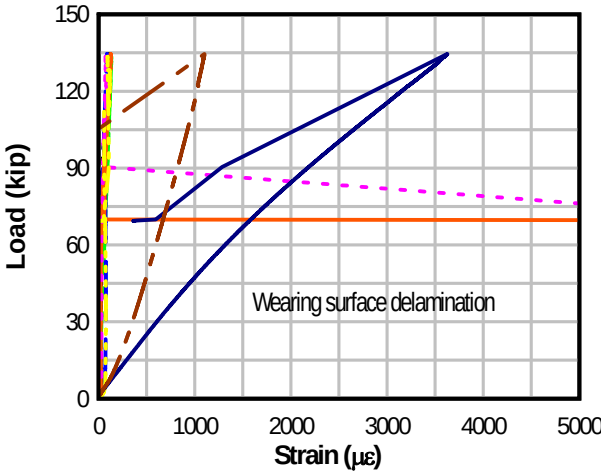

B_N_U load-strain plot

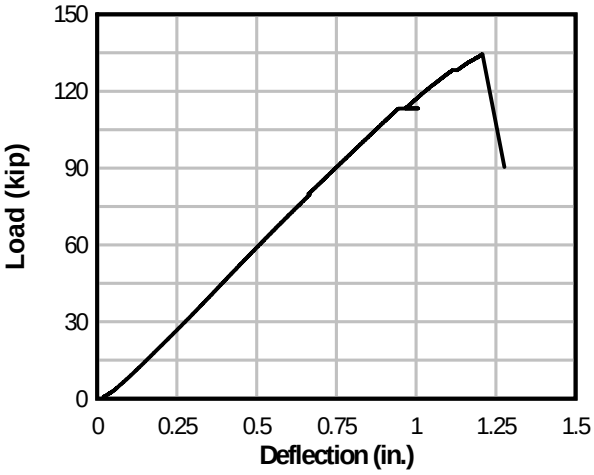

B_N_U load-deflection plot

Strain data not available for this test.

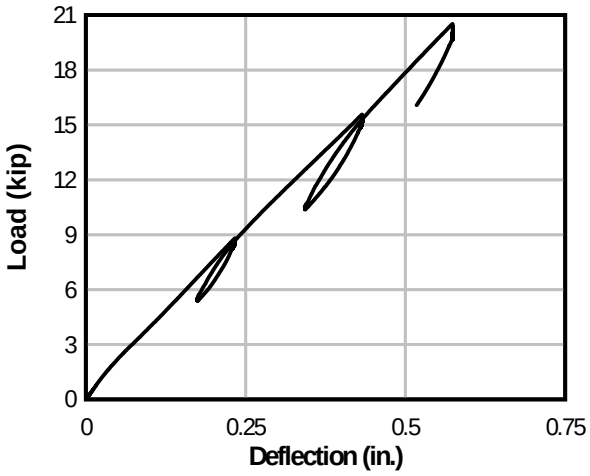

B_N_S_3 Load-Strain plot

B_N_S_3 load-deflection plot

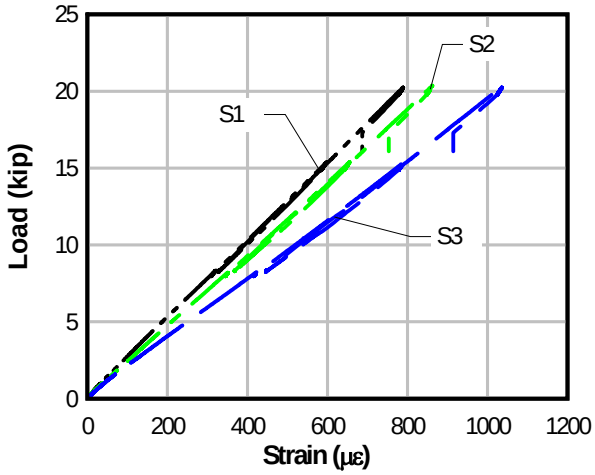

C_P_S_1 load-strain plot

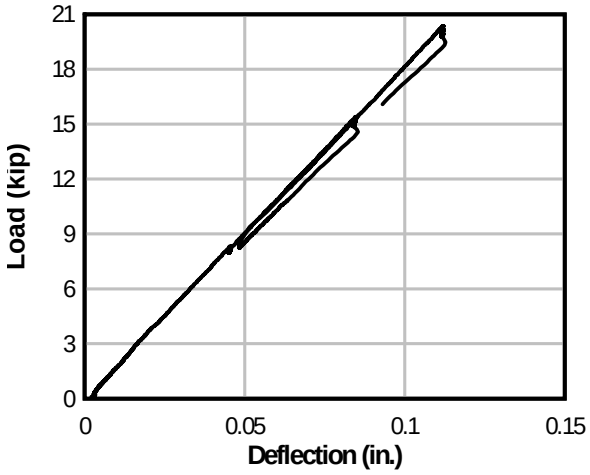

C_P_S_1 load-deflection plot

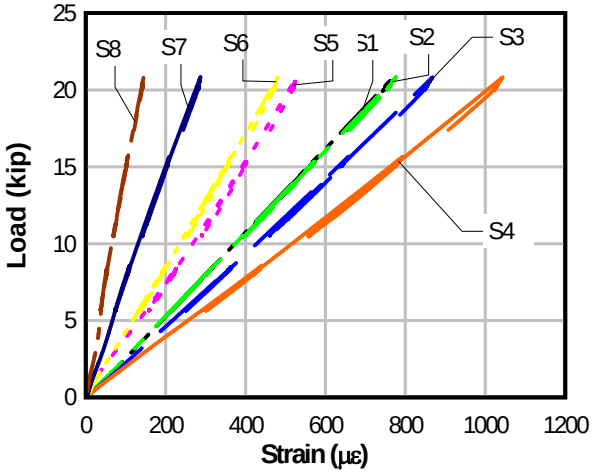

C_P_S_2 load-strain plot

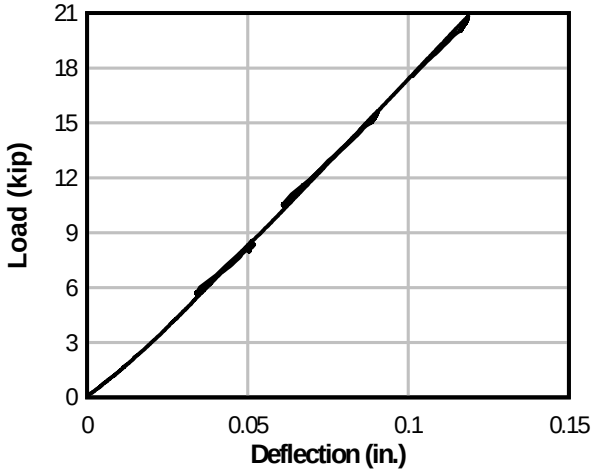

C_P_S_2 load-deflection plot

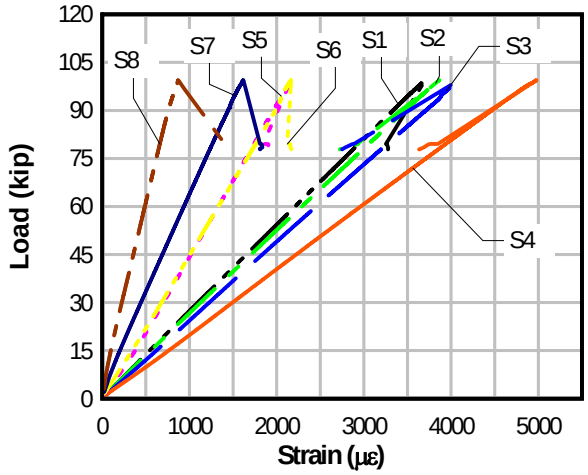

C_P_U load-strain plot

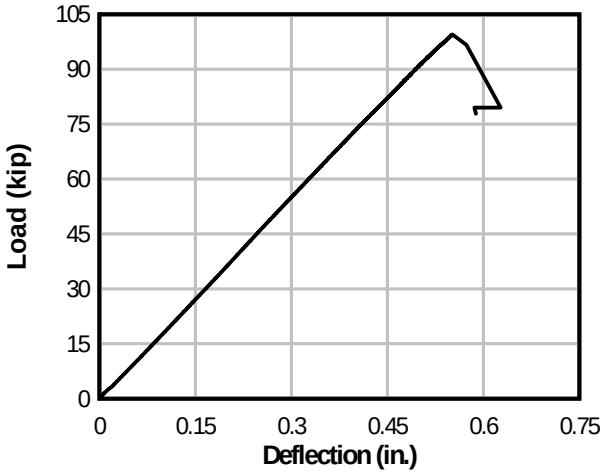

C_P_U load-deflection plot

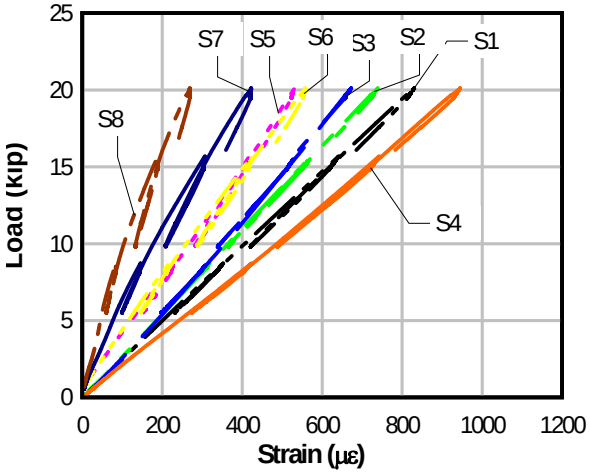

C_P_S_3 load-strain plot

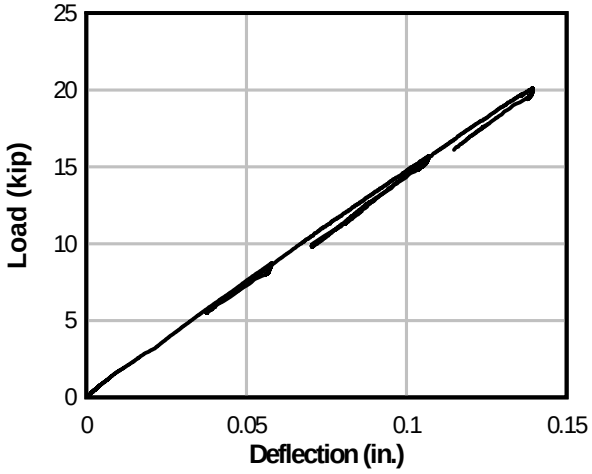

C_P_S_3 load-deflection plot

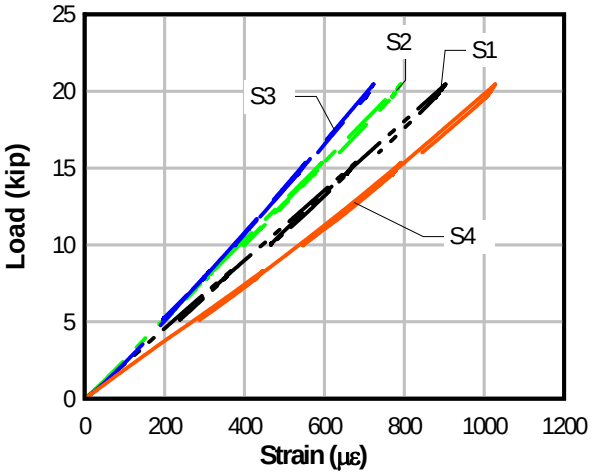

C_P_S_4 load-strain plot

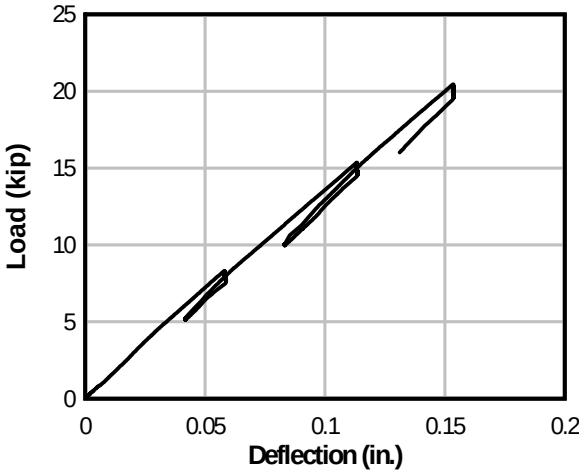

C_P_S_4 load-deflection plot

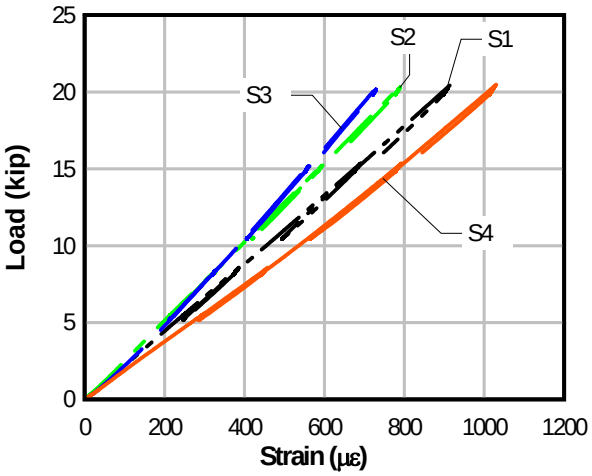

C_P_S_5 load-strain plot

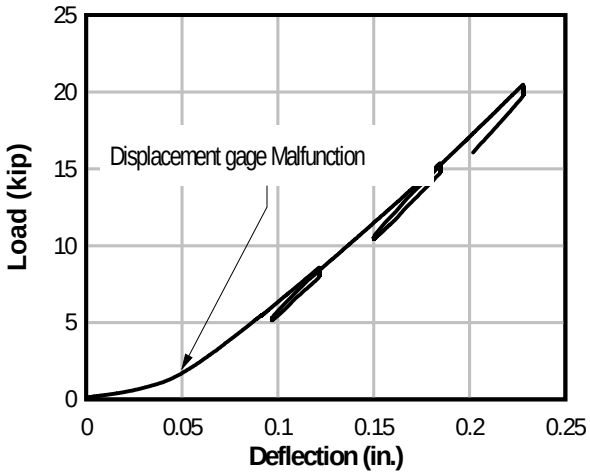

C_P_S_5 load-deflection plot

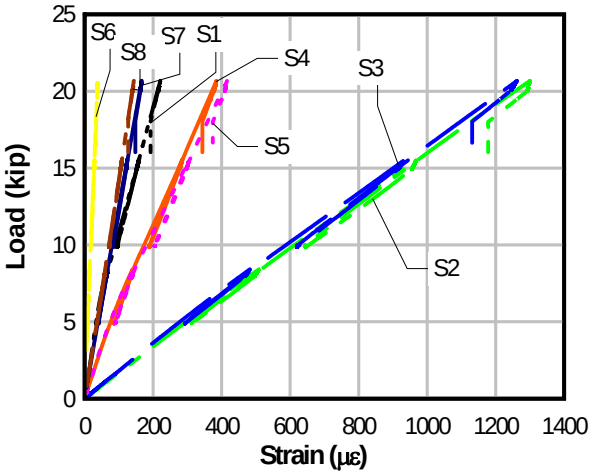

C_N_S_1 load-strain plot

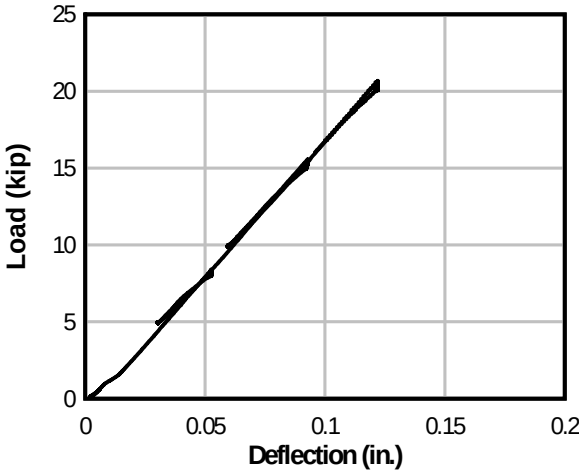

C_N_S_1 load-deflection plot

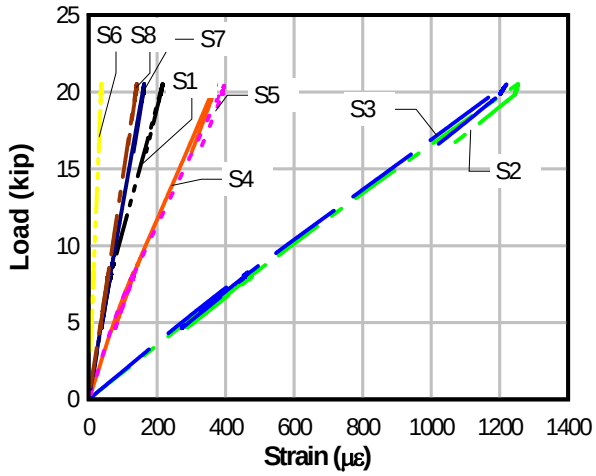

C_N_S_2 load-strain plot

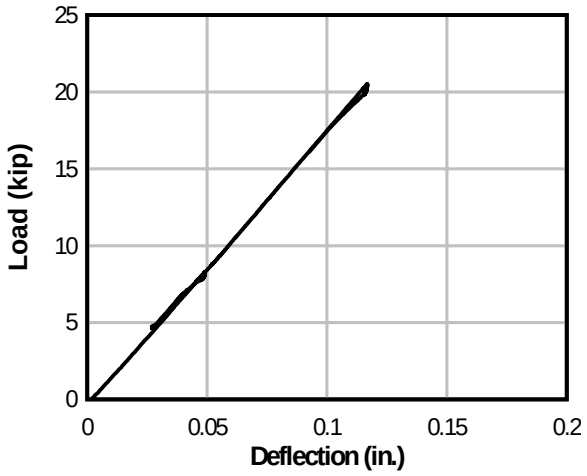

C_N_S_2 load-deflection plot

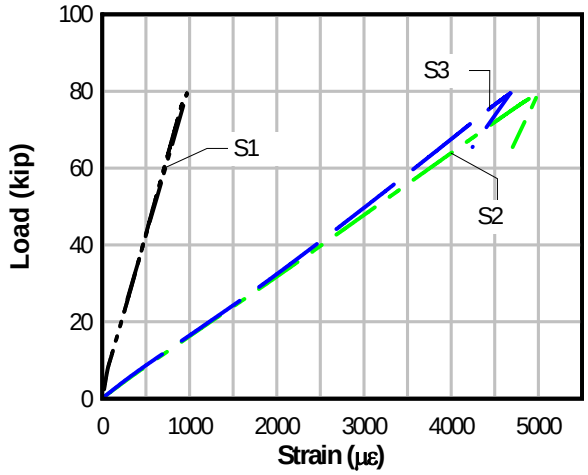

C_N_U load-strain plot

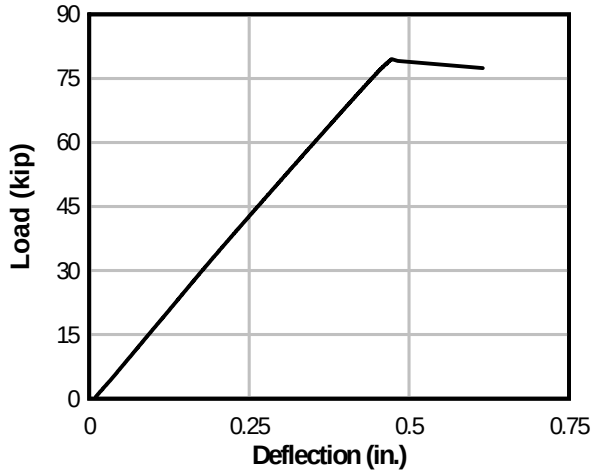

C_N_U load-deflection plot

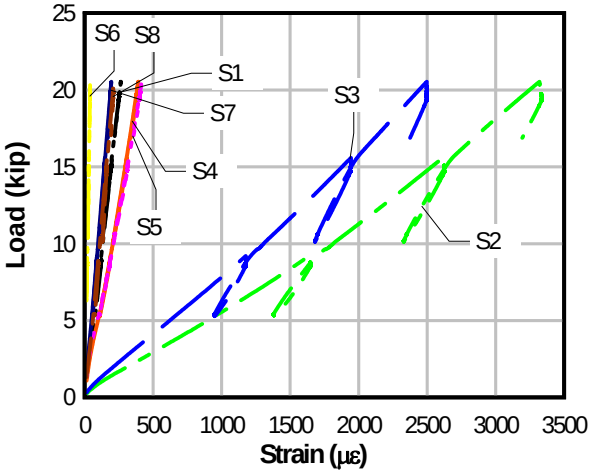

C_N_S_3 load-strain plot

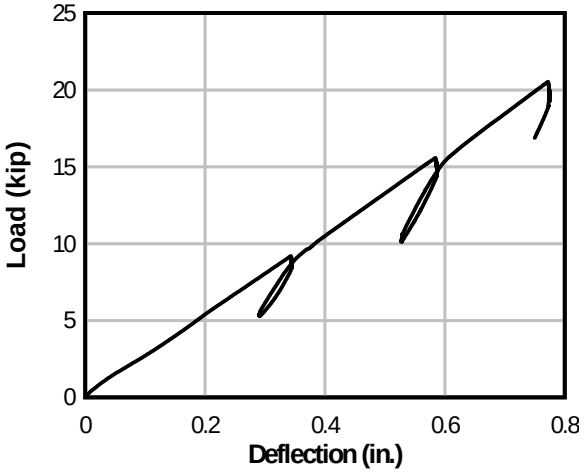

C_N_S_3 load-deflection plot

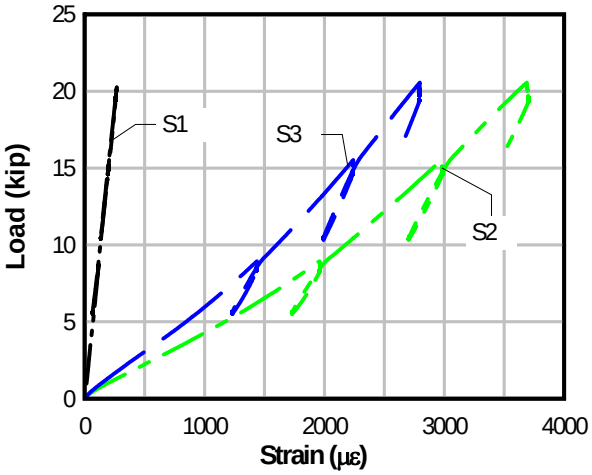

C_N_S_3 load-strain plot

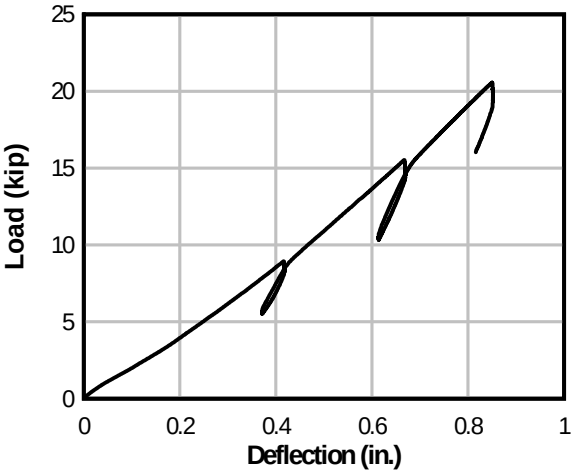

C_N_S_3 load-deflection plot

Appendix B Intensity Analysis Plots

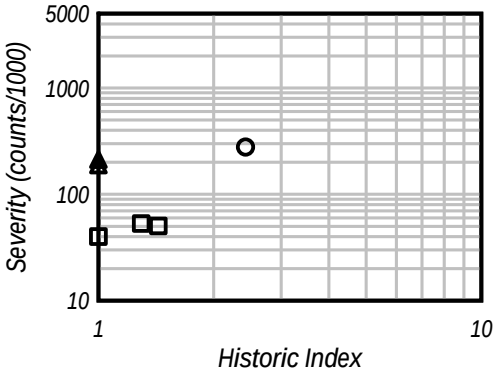

A_P service load level tests channel 1

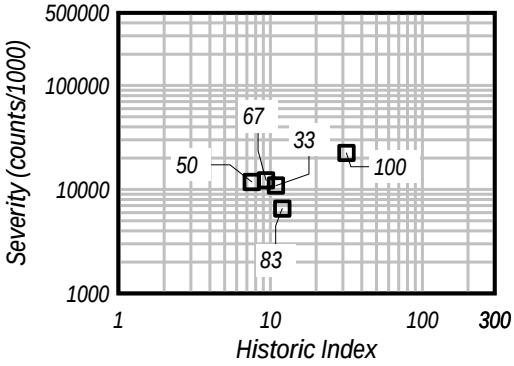

A_P ultimate load tests channel 1

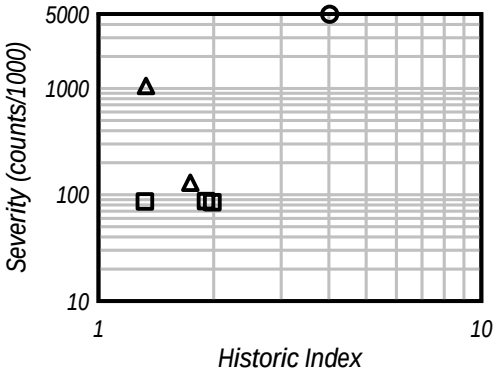

A_P service load level tests channel 2

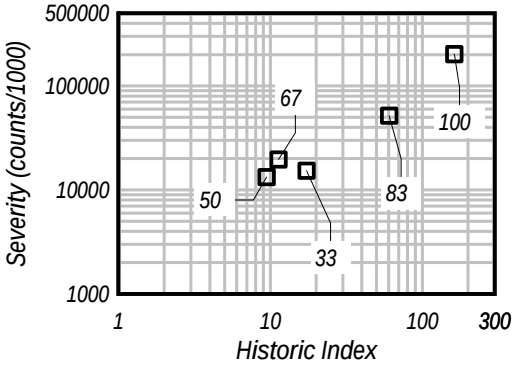

A_P ultimate load tests channel 2

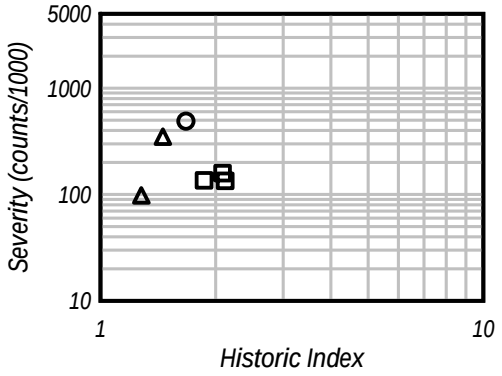

A_P service load level tests channel 3

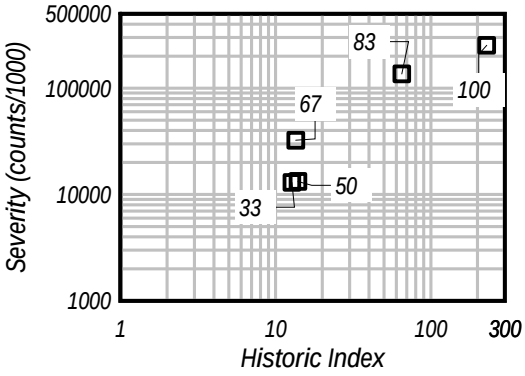

A_P ultimate load tests channel 3

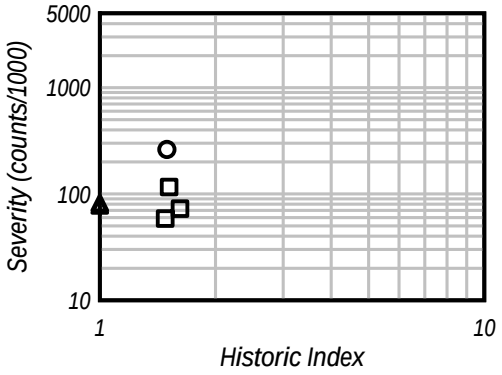

A_P service load level tests channel 4

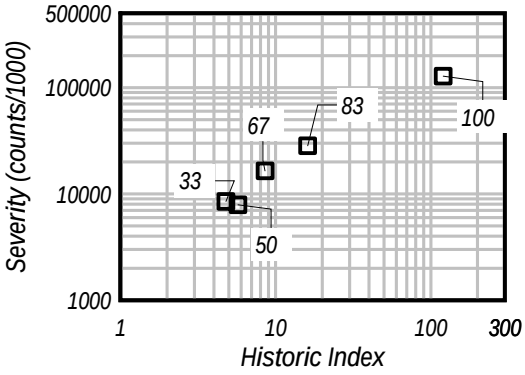

A_P ultimate load tests channel 4

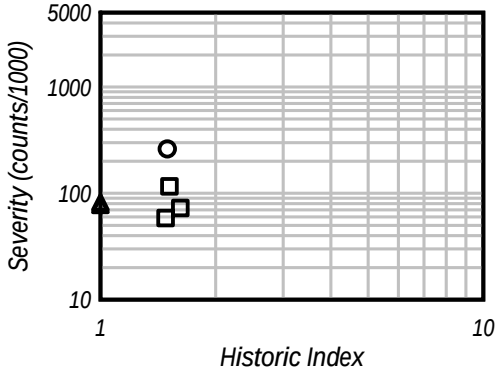

A_P service load level tests channel 5

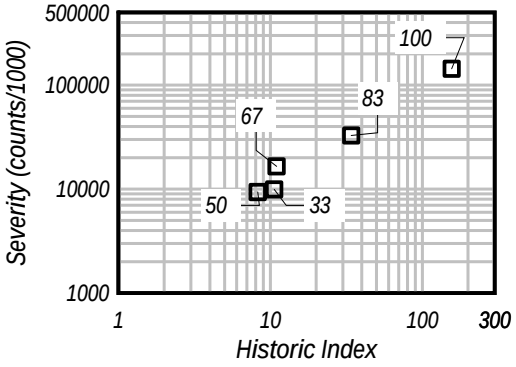

A_P ultimate load tests channel 5

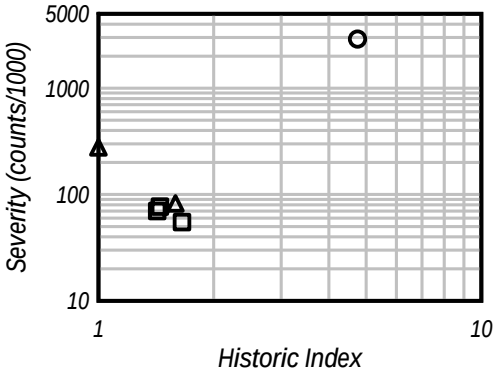

A_P service load level tests channel 6

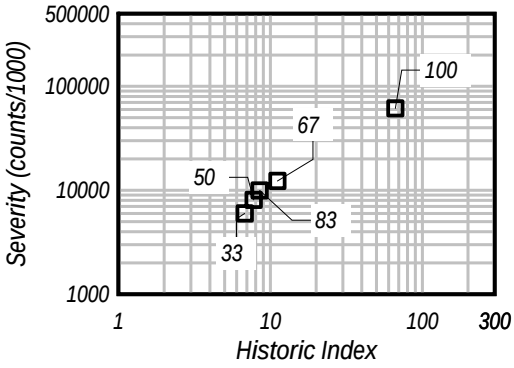

A_P ultimate load tests channel 6

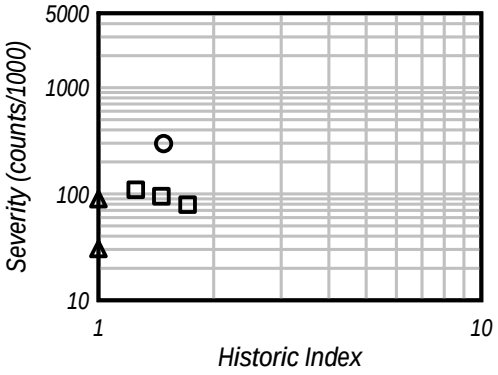

A_P service load level tests channel 7

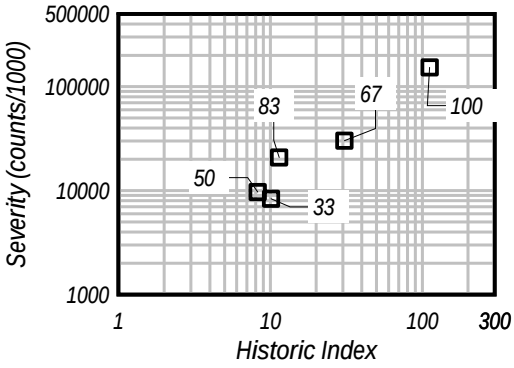

A_P ultimate load tests channel 7

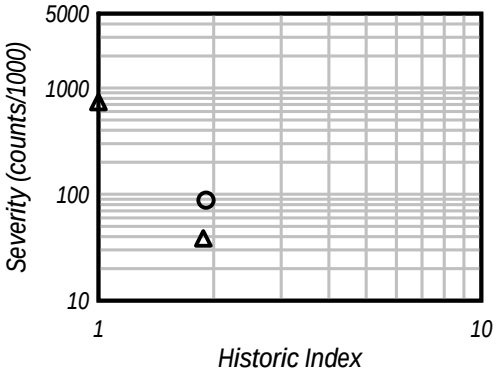

A_P service load level tests channel 8

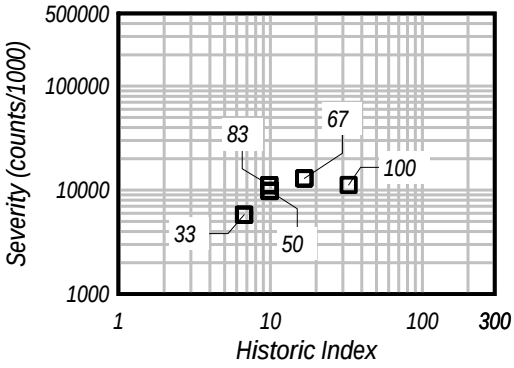

A_P ultimate load tests channel 8

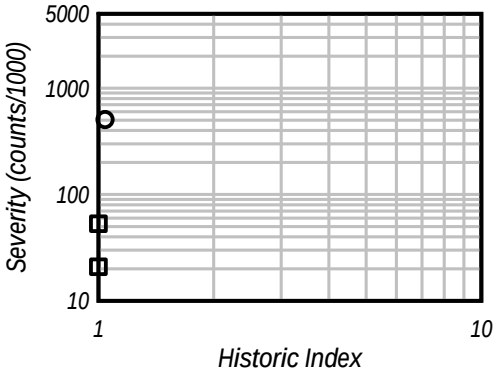

A_N service load level tests channel 1

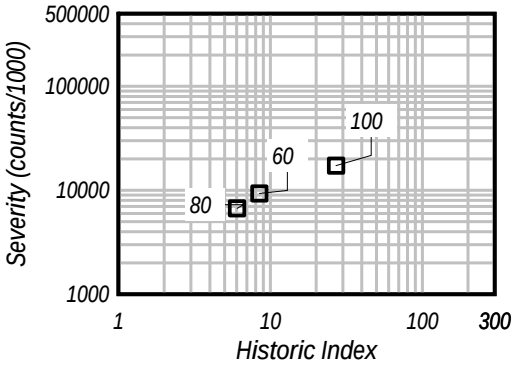

A_N ultimate load tests channel 1

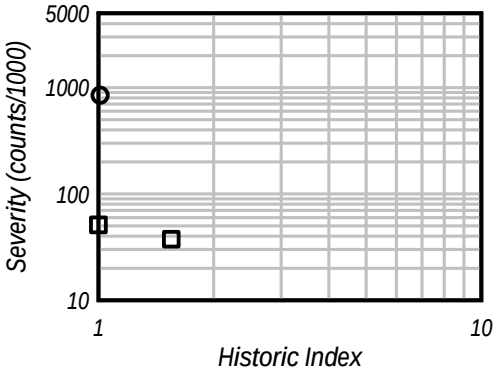

A_N service load level tests channel 2

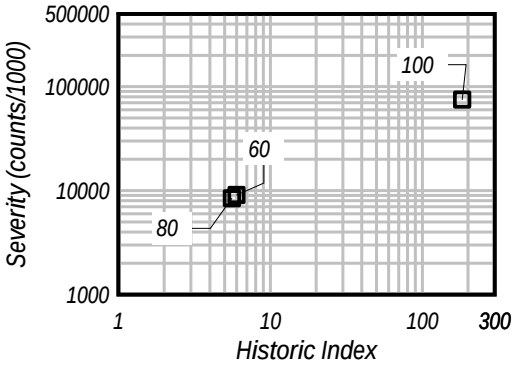

A_N ultimate load tests channel 2

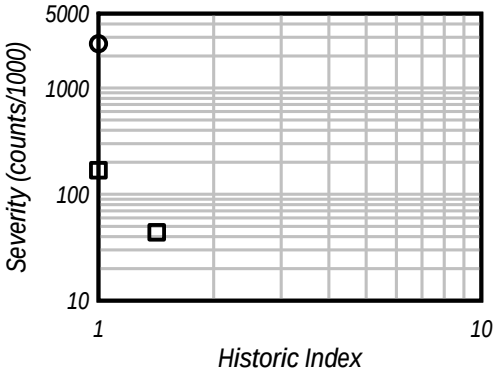

A_N service load level tests channel 3

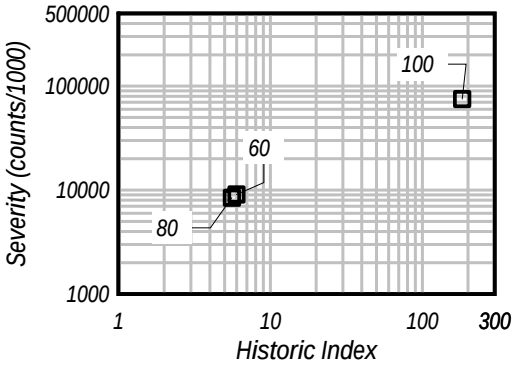

A_N ultimate load tests channel 3

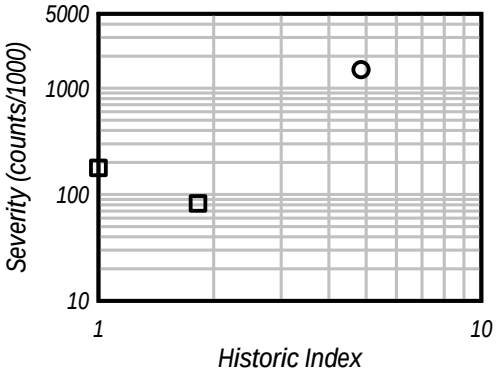

A_N service load level tests channel 4

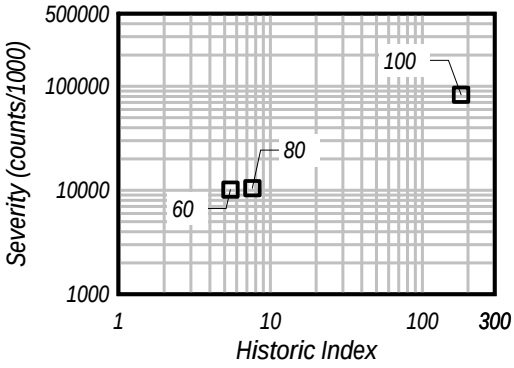

A_N ultimate load tests channel 4

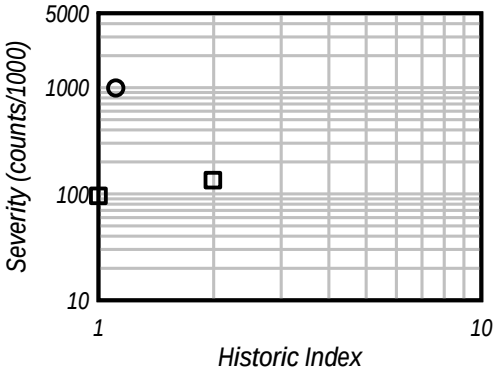

A_N service load level tests channel 5

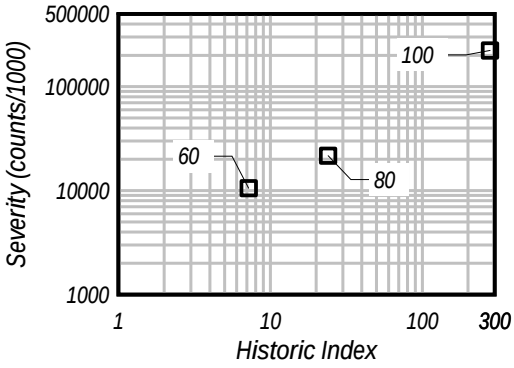

A_N ultimate load tests channel 5

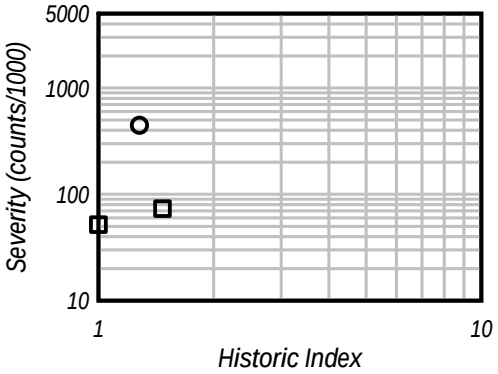

A_N service load level tests channel 6

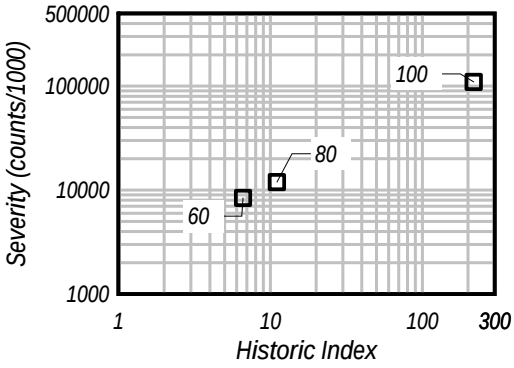

A_N ultimate load tests channel 6

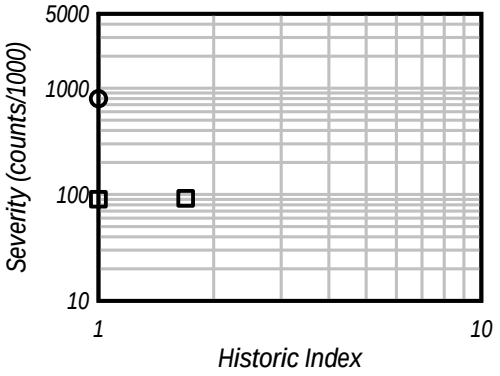

A_N service load level tests channel 7

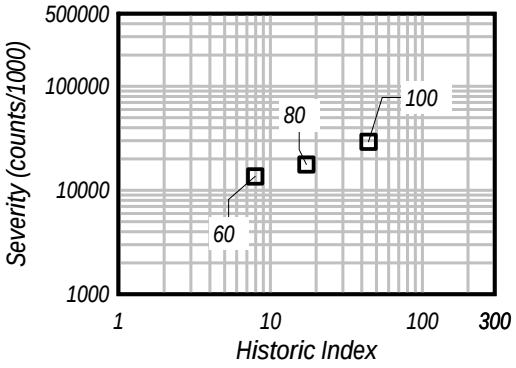

A_N ultimate load tests channel 7

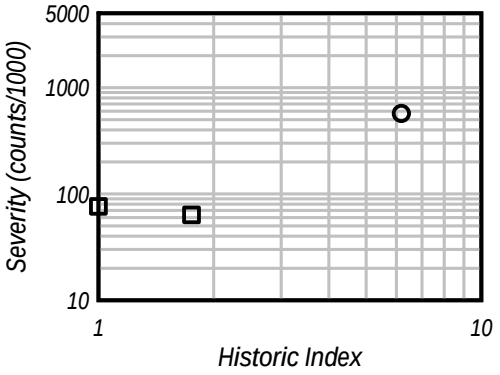

A_N service load level tests channel 8

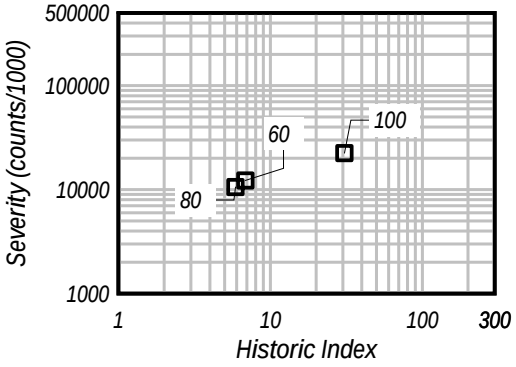

A_N ultimate load tests channel 8

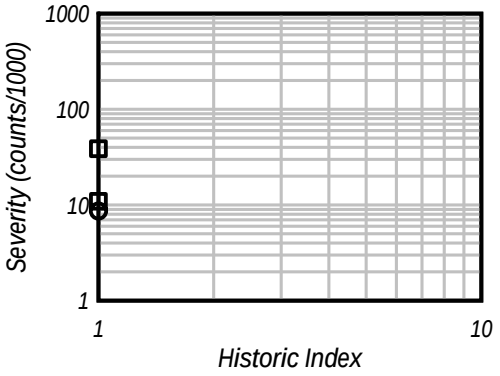

B_P service load level tests channel 1

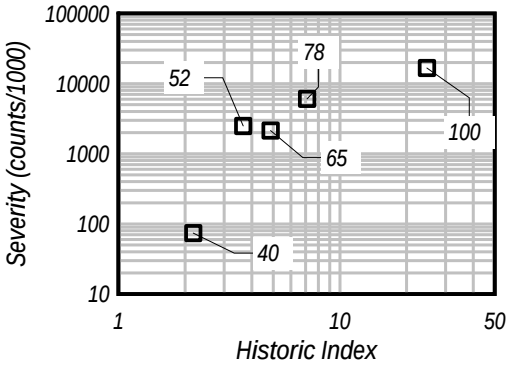

B_P ultimate load level tests channel 1

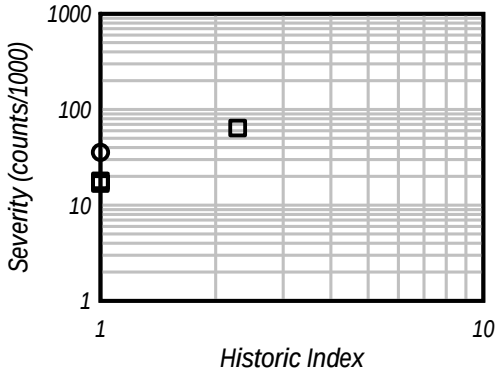

B_P service load level tests channel 2

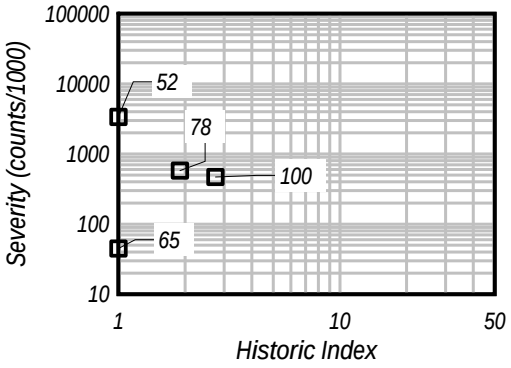

B_P ultimate load level tests channel 2

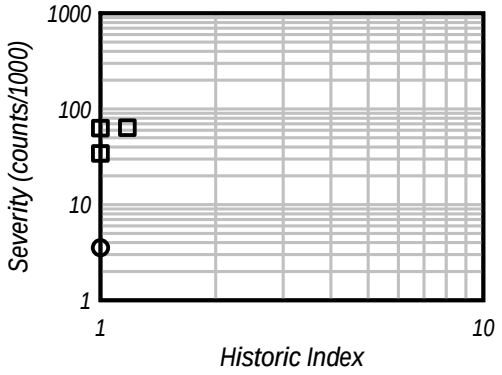

B_P service load level tests channel 3

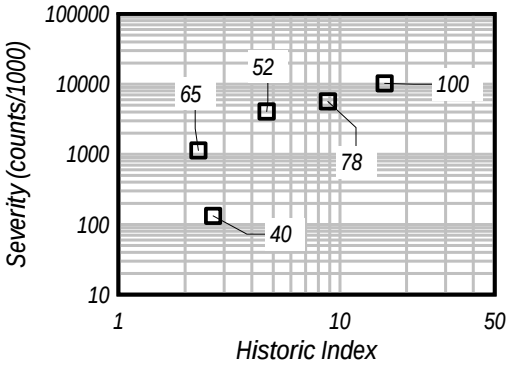

B_P ultimate load level tests channel 3

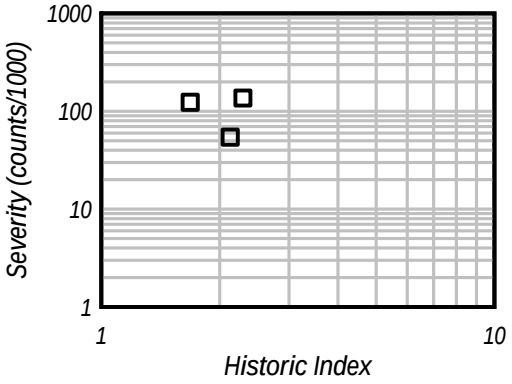

B_P service load level tests channel 4

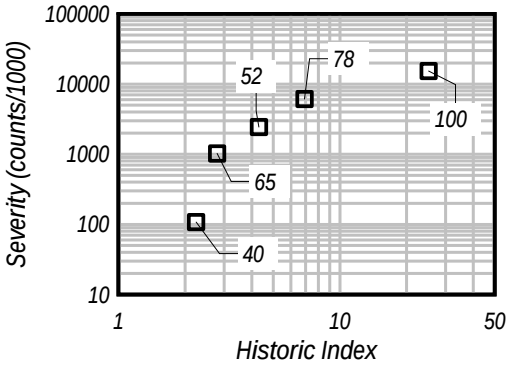

B_P ultimate load level tests channel 4

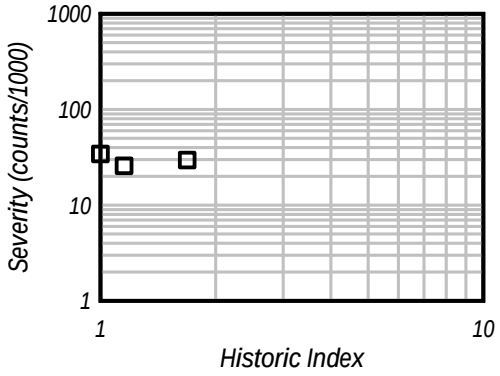

B_P service load level tests channel 5

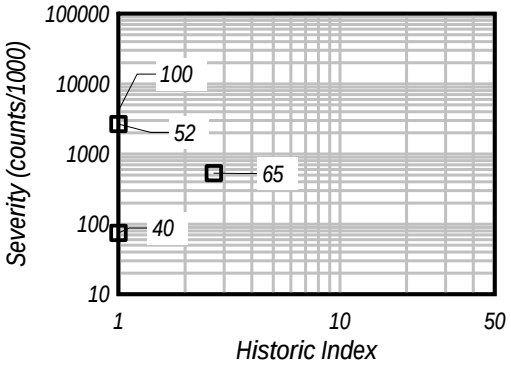

B_P ultimate load level tests channel 5

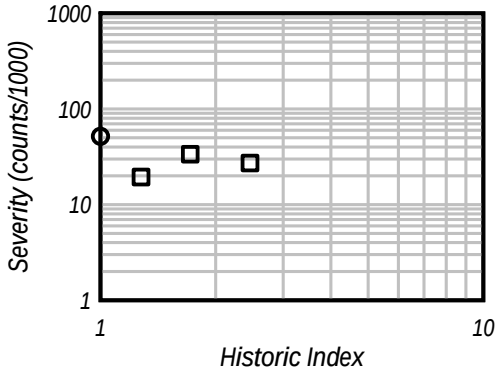

B_P service load level tests channel 6

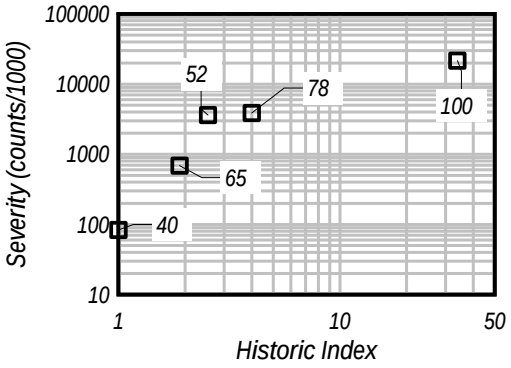

B_P ultimate load level tests channel 6

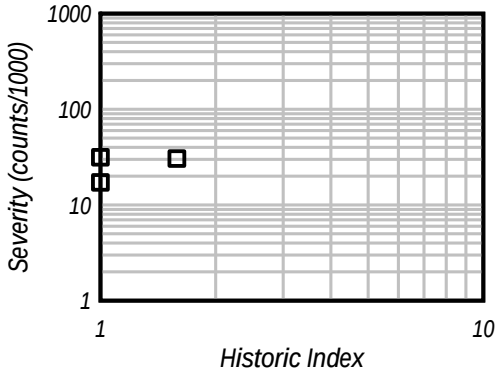

B_P service load level tests channel 7

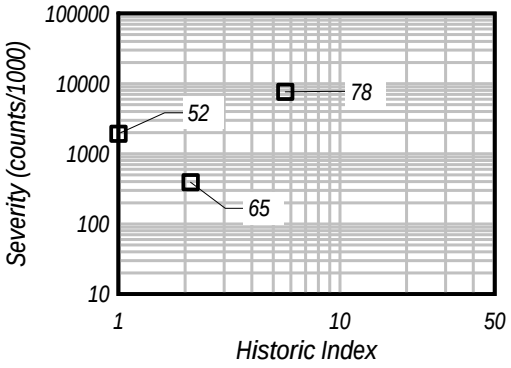

B_P ultimate load level tests channel 7

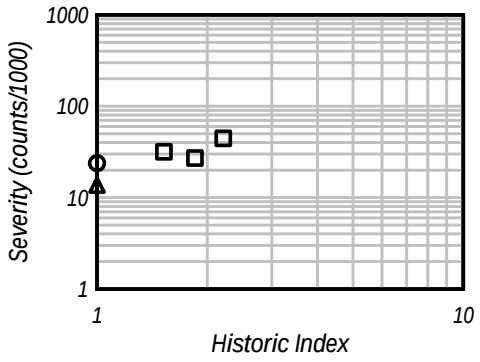

B_P service load level tests channel 8

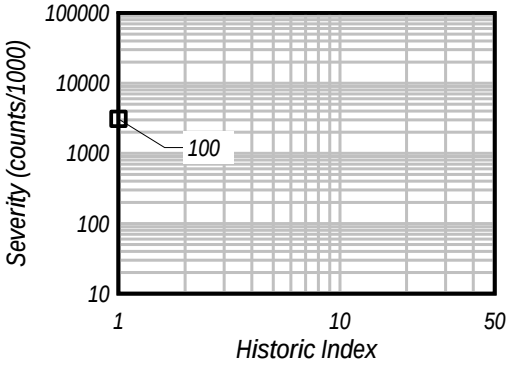

B_P ultimate load level tests channel 8

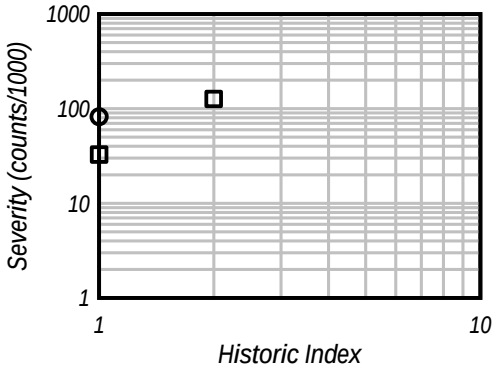

B_N service load level tests channel 1

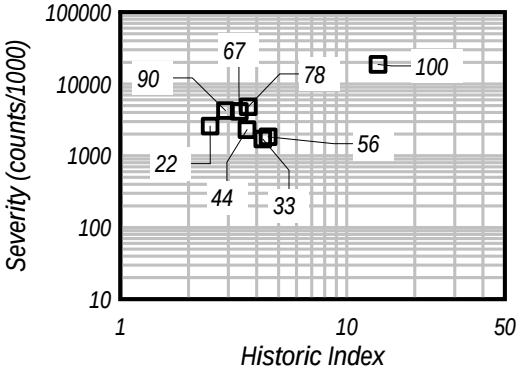

B_N ultimate load level tests channel 1

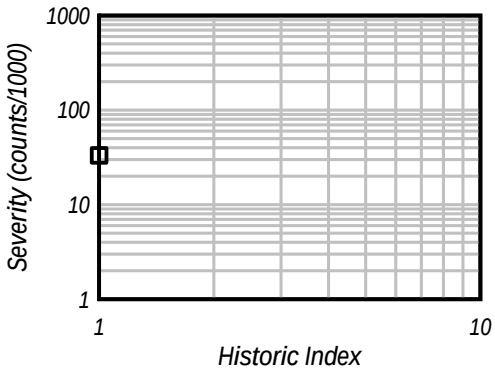

B_N service load level tests channel 2

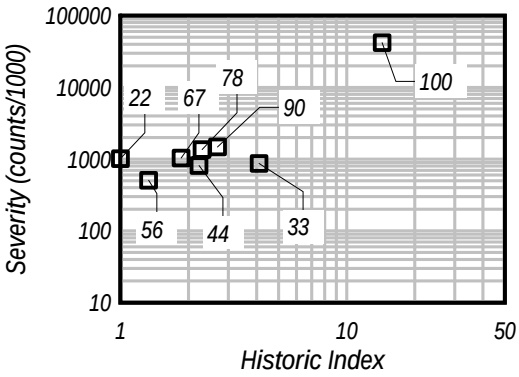

B_N ultimate load level tests channel 1

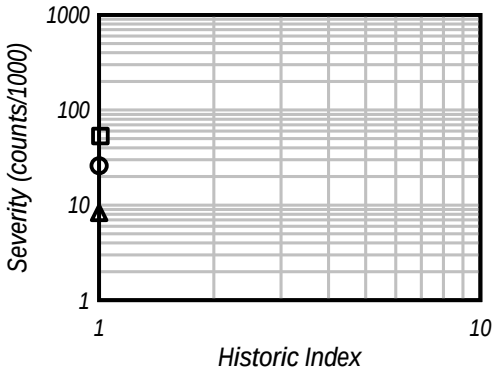

B_N service load level tests channel 3

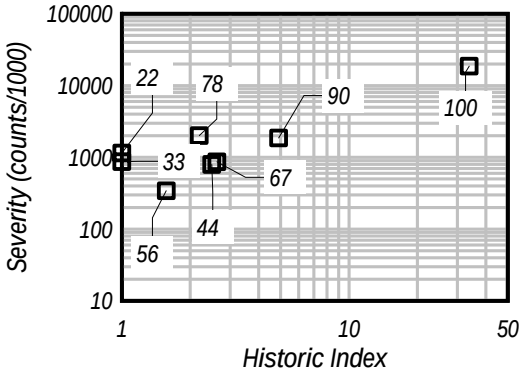

B_N ultimate load level tests channel 3

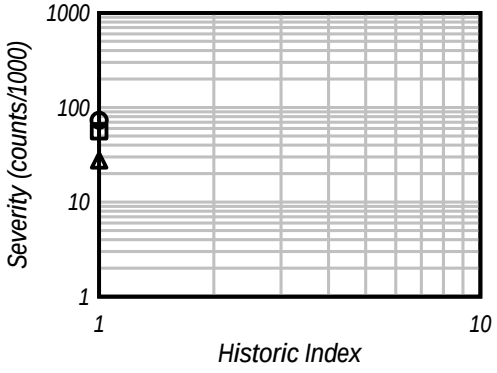

B_N service load level tests channel 4

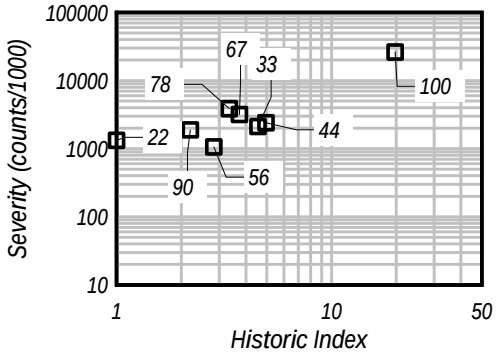

B_N ultimate load level tests channel 4

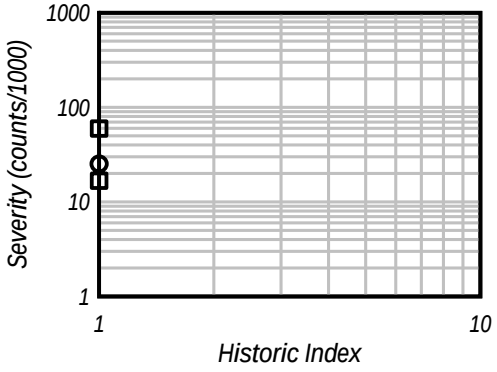

B_N service load level tests channel 5

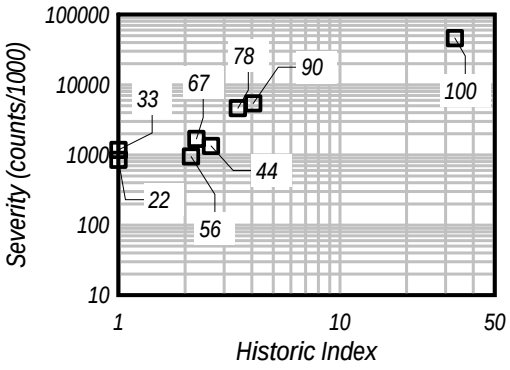

B_N ultimate load level tests channel 5

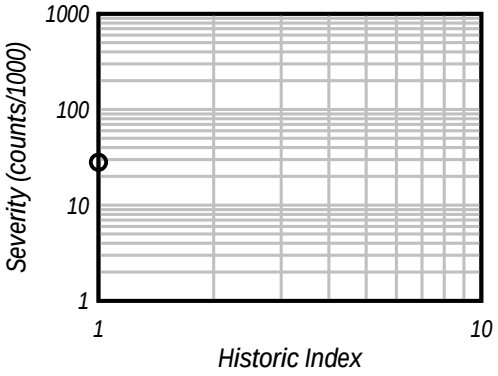

B_N service load level tests channel 6

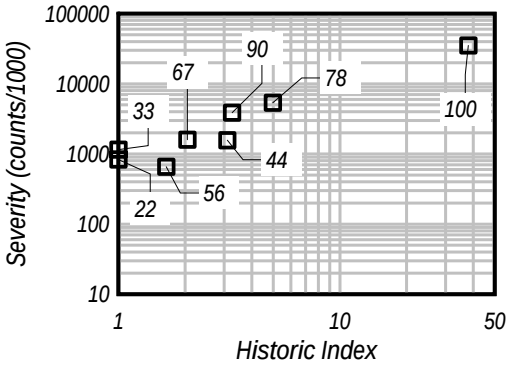

B_N ultimate load level tests channel 6

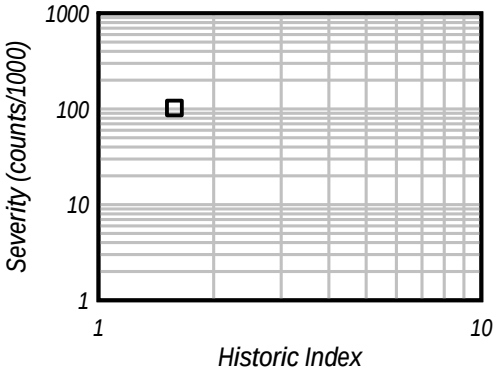

B_N service load level tests channel 7

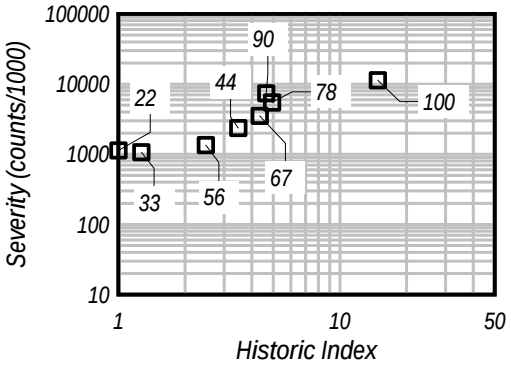

B_N ultimate load level tests channel 7

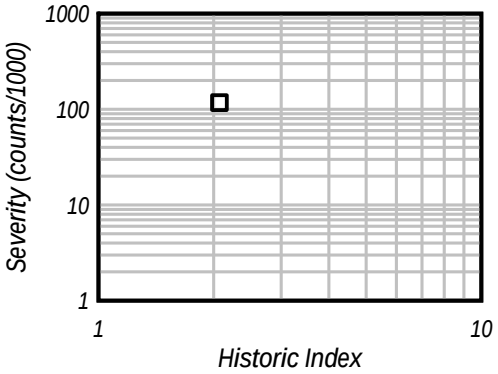

B_N service load level tests channel 8

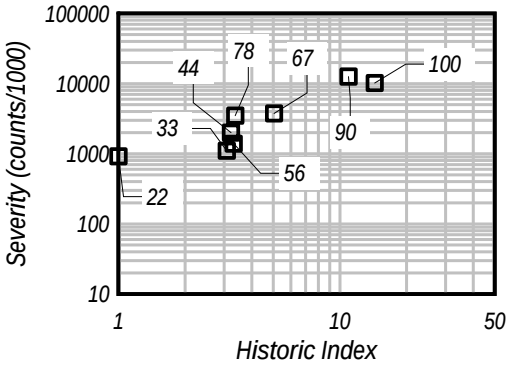

B_N ultimate load level tests channel 8

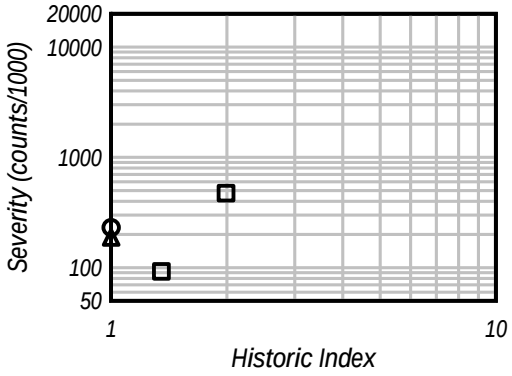

C_P service load level tests channel 1

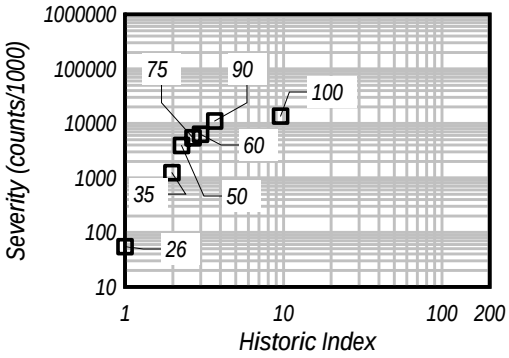

C_P ultimate load level tests channel 1

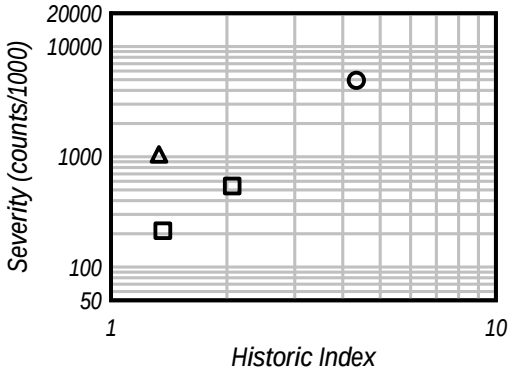

C_P service load level tests channel 2

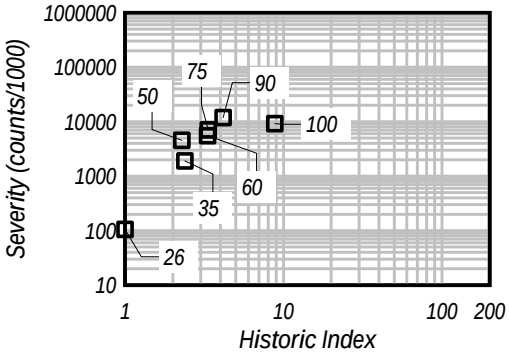

C_P ultimate load level tests channel 2

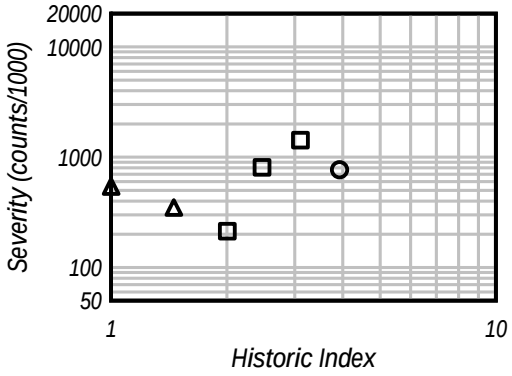

C_P service load level tests channel 3

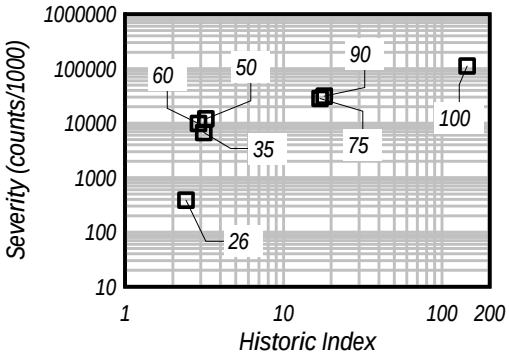

C_P ultimate load level tests channel 3

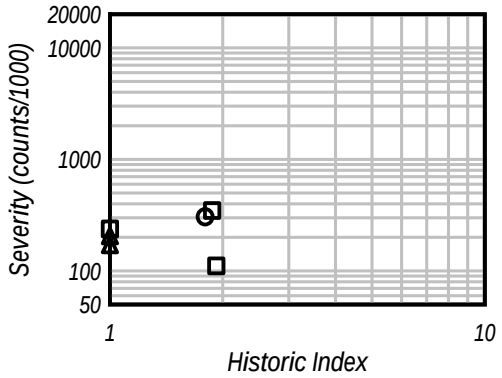

C_P service load level tests channel 4

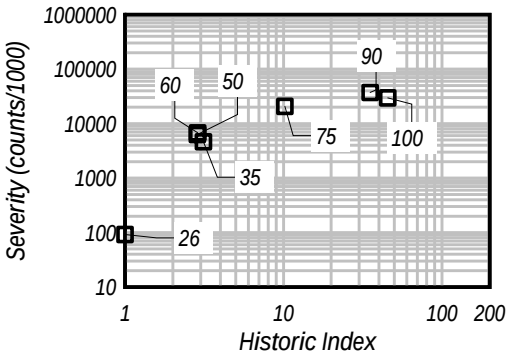

C_P ultimate load level tests channel 4

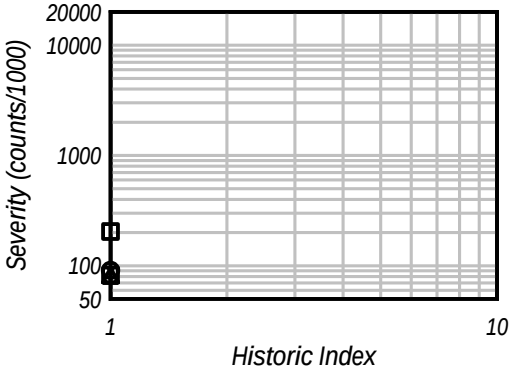

C_P service load level tests channel 5

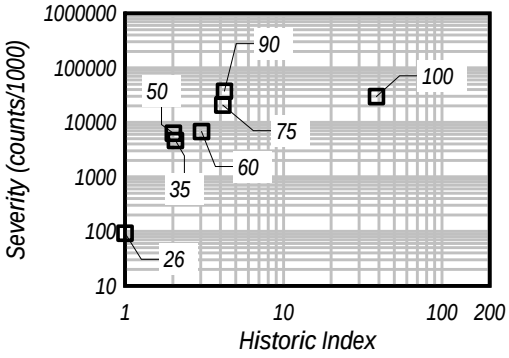

C_P ultimate load level tests channel 5

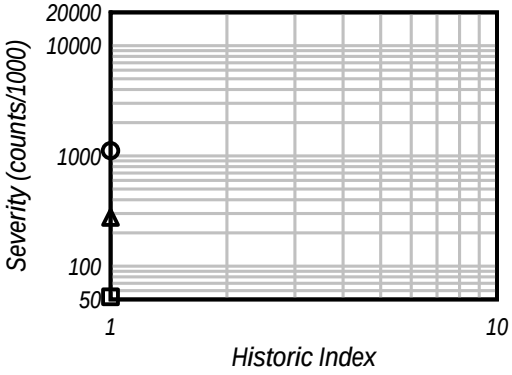

C_P service load level tests channel 6

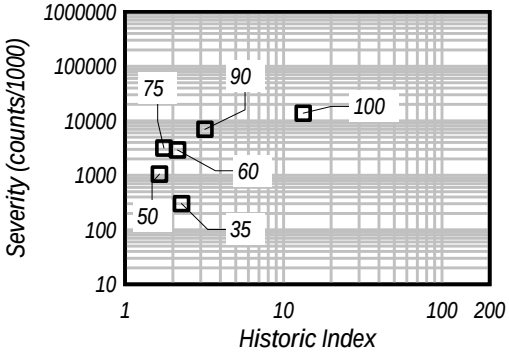

C_P ultimate load level tests channel 6

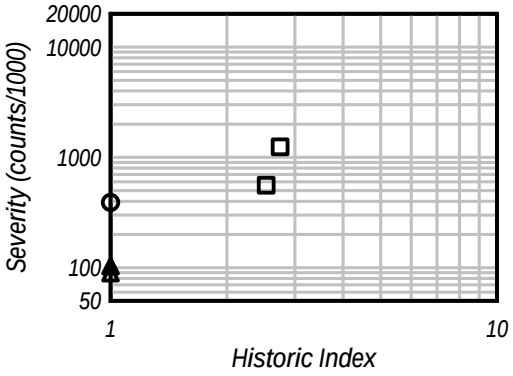

C_P service load level tests channel 7

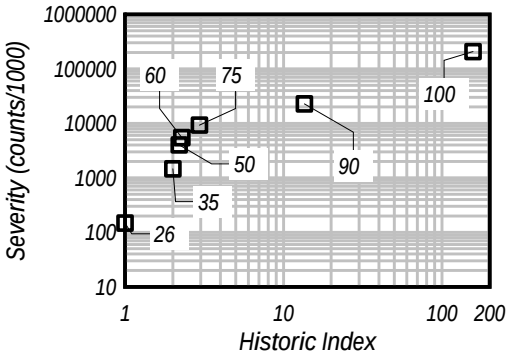

C_P ultimate load level tests channel 7

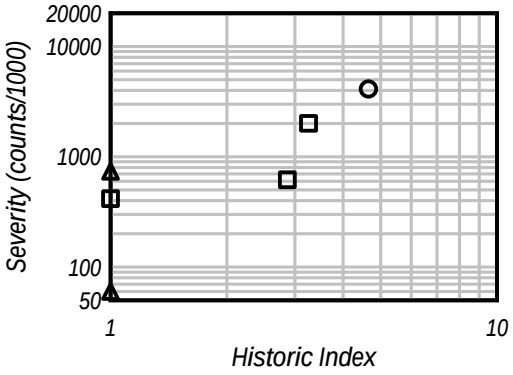

C_P service load level tests channel 8

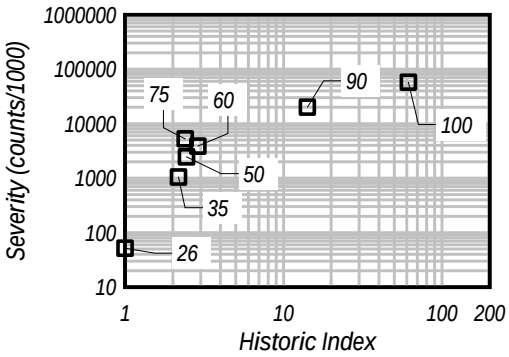

C_P ultimate load level tests channel 8

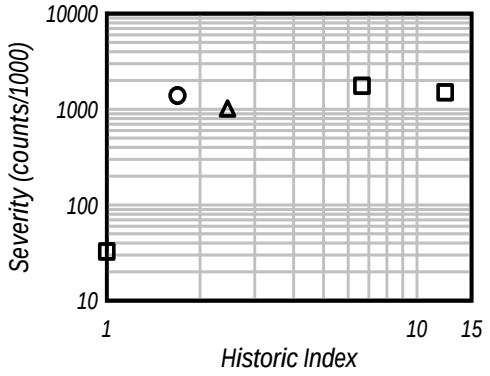

C_N service load level tests channel 1

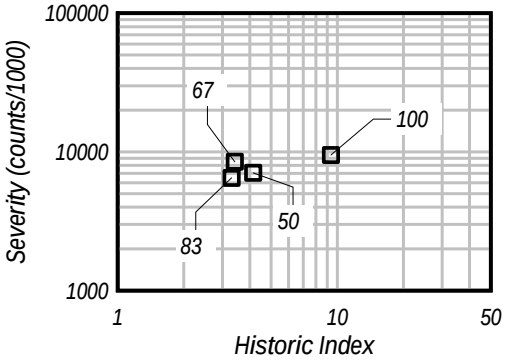

C_N ultimate load level tests channel 1

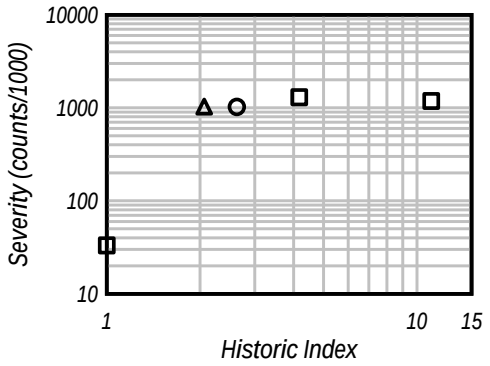

C_N service load level tests channel 2

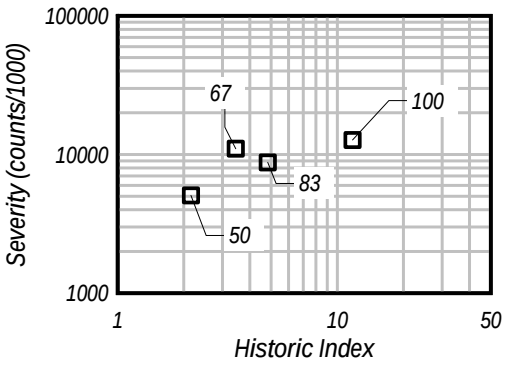

C_N ultimate load level tests channel 2

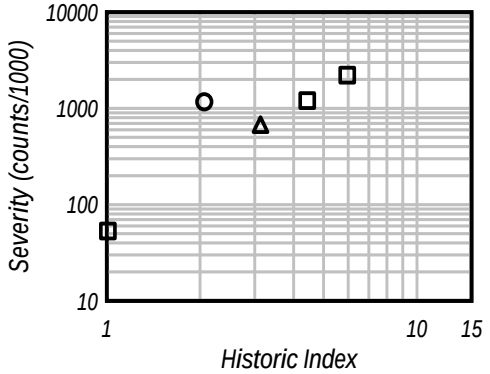

C_N service load level tests channel 3

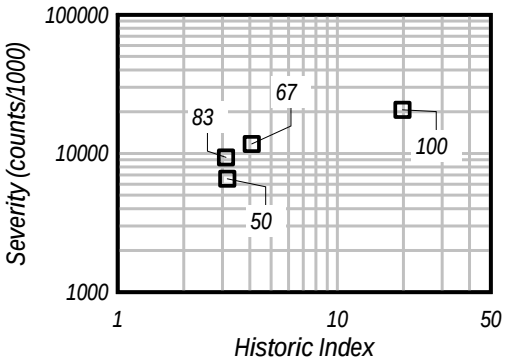

C_N ultimate load level tests channel 3

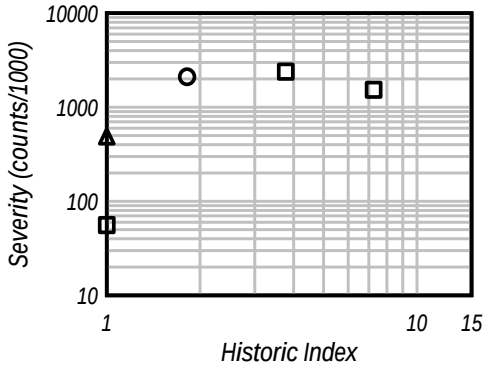

C_N service load level tests channel 4

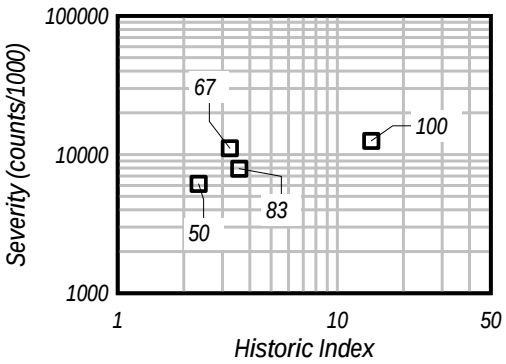

C_N ultimate load level tests channel 4

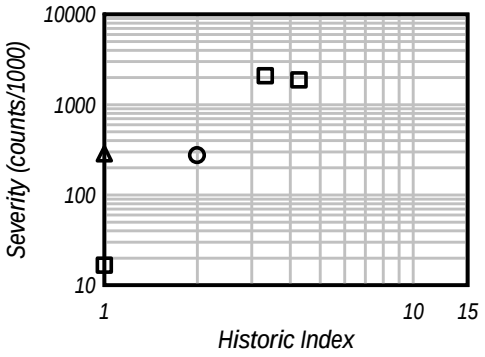

C_N service load level tests channel 5

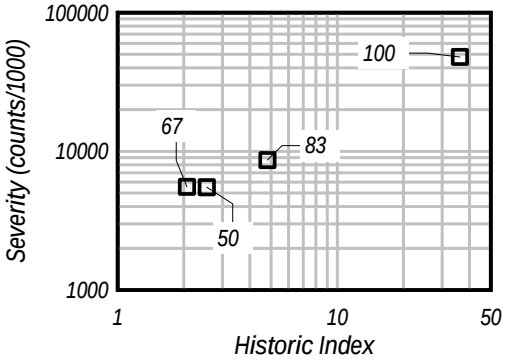

C_N ultimate load level tests channel 5

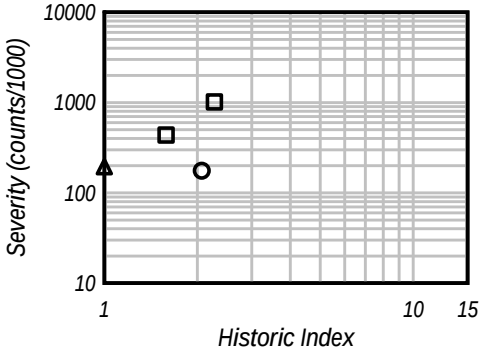

C_N service load level tests channel 6

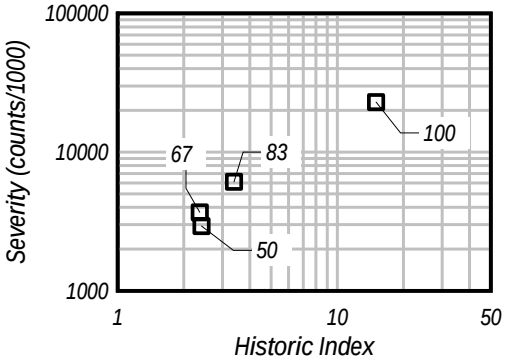

C_N ultimate load level tests channel 6

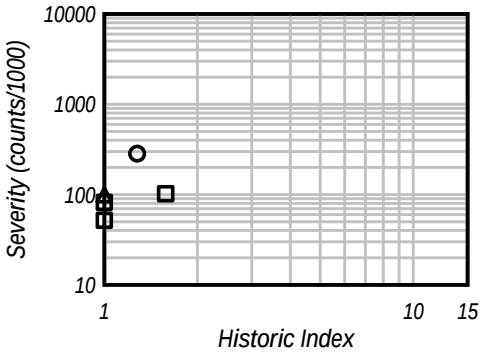

C_N service load level tests channel 7

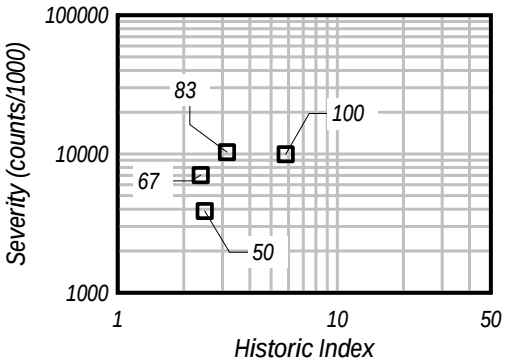

C_N ultimate load level tests channel 7

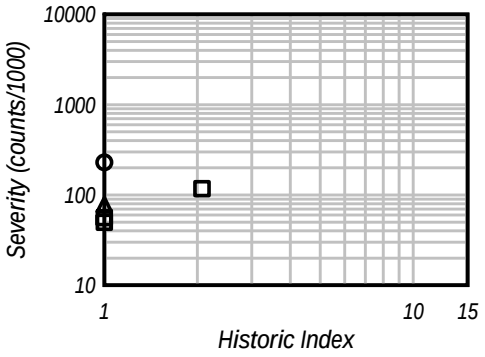

C_N service load level tests channel 8

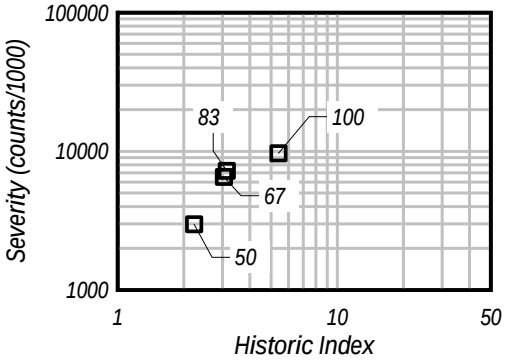

C_N ultimate load level tests channel 8

Part II – Infrared Thermography

1 Introduction

The purpose of this research project is to investigate infrared thermography (IRT) as a potential nondestructive evaluation tool to assess the performance of glass fiber reinforced polymer (GFRP) bridge decks. The specific objective is to develop IRT inspection parameters, deployment strategies, and data analysis guidelines that will serve as a foundation for future research and/or deployment on in-service GFRP bridge decks.

Infrared thermography is a relatively well-established NDE tool with existing ASTM standards for detecting delaminations in traditional reinforced concrete bridge decks[(1)] and detecting defects in FRP composites used in aerospace structures[(2)]. The general concept behind IRT as an NDE technique is as follows:

- The surface of an object is heated by an external source.
- An infrared camera is positioned to record thermal images of the surface during heating and cooling.
- Subsurface defects will result in a non-uniform temperature distribution on the surface. These temperature irregularities (i.e. the defect's signal) may be detected with the infrared camera.
- The characteristics of the defect signal may be used to draw conclusions about the characteristics of the defect (e.g. planar area, depth, and material composition).

In general, large defects located close to the surface are more likely to be detected than small defects located deep beneath the surface. The definition of "large" vs. "small" and "shallow" vs. "deep" varies depending on the material under consideration, and most of the research involving IRT to detect defects includes determining the detection limits for a specific material/defect configuration.

Potential applications for IRT and defect detection in GFRP bridge decks include:

1. Delamination between the bottom panel and internal structural elements due to fatigue or overloading.
2. Moisture, blistering. or fatigue-induced delamination in the bottom panel of the GFRP deck.
3. Delamination between the wearing surface and the top of the GFRP deck.

The primary focus of the current research is detecting damage in GFRP bridge decks caused by overloading. Figure 1 provides an example of major structural damage to a deck panel

that was loaded to failure under laboratory conditions. The resulting delamination between the pultruded flanges and bottom GFRP plate would not be visible from either the top or bottom of the deck. By heating the soffit (bottom surface) of the GFRP deck with halogen lamps and monitoring the resulting temperature response with an IR camera (Figure 2), it may be possible to not only detect this damage but also gain insight into the overall severity and need for repair.

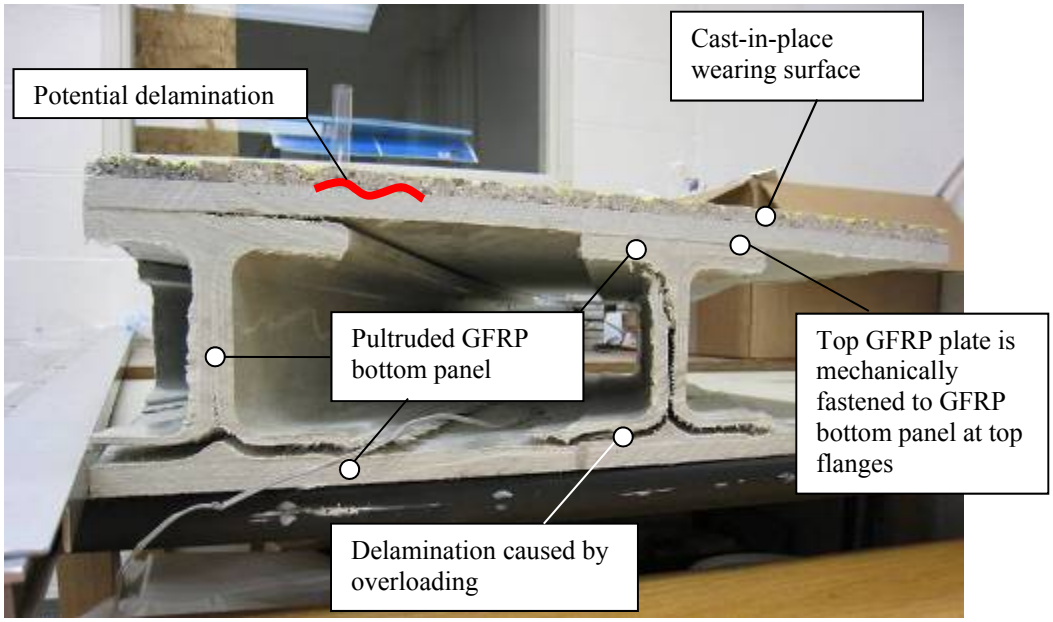

Figure 1-Section view of damaged GFRP bridge deck. Sample provided by UF/FDOT.

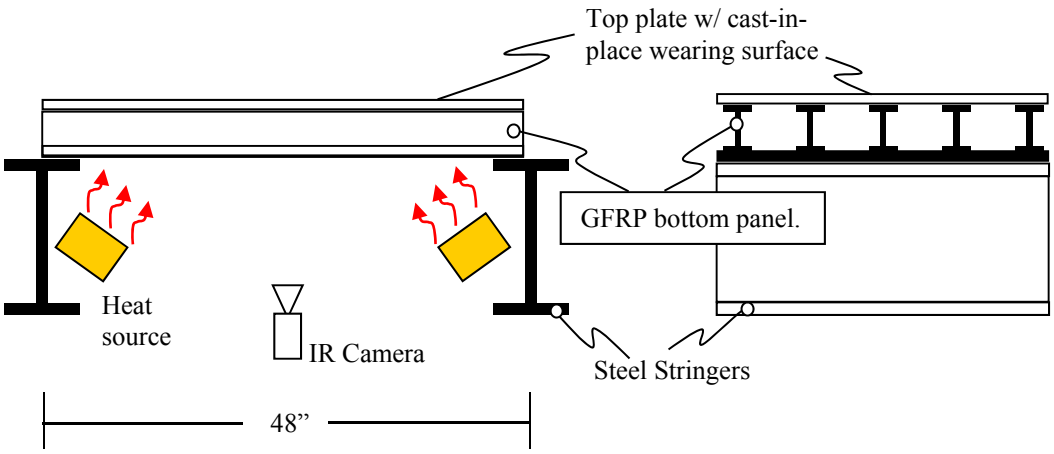

Figure 2-Conceptual design for IRT inspection to detect damage in GFRP bottom panel

Section 2 of this part of the report provides additional background and literature review for IRT as a NDE tool. A general overview of quantitative IRT as it is currently applied to

defect detection and materials evaluation is provided along with a discussion on general strategies for data collection and post-processing. Section 3 describes the specific research objectives and methodology used in the current study. Section 4 provides results from a parametric study that was conducted using finite element software (ANSYS) to simulate the heat transfer processes expected to occur during an IRT inspection for a specific GFRP bridge deck geometry. Section 4 also includes finite element results for generic defects in GFRP composite plates that can be used to differentiate subsurface defects caused by manufacturing errors or other damage mechanisms not directly related to overloading. Section 5 describes the experimental program that was conducted using damaged and undamaged samples of GFRP bridge decks. The highlight of the experimental program was a series of tests conducted at the FDOT M. H. Ansley Structures Research Center in Tallahassee, Florida, in which full-size deck panels were loaded to failure and IRT inspections were performed at various stages of loading. Section 6 describes additional experimental work that was conducted to enhance detectability of load-induced damage and address some of the shortcomings encountered during the load testing experiments described in Section 5. Finally, Section 7 includes a general discussion of the results and makes recommendations for future research and field deployment of the method for in-service GFRP bridge decks.

2 Background and Literature Review

Infrared thermography (IRT) is an established NDE technique that may be used to identify subsurface defects in a variety of materials. Early research applications of IRT for defect detection in GFRP composite materials originated in the aerospace industry [e.g. 3,4]. Work in this sector is ongoing by researchers at NASA who routinely use infrared thermography to inspect reinforced carbon-carbon components of the space shuttle orbiters as part of the flight recertification process [e.g. 5,6].

There have also been numerous applications of IRT for composites in civil structures. This work is divided into two basic areas: (1) NDE of GFRP bridge decks and (2) FRP applied to strengthen existing reinforced concrete structures. These topics will be discussed in Sections 2.2.1 and 2.2.2, respectively. The following section highlights some of the general advances in IRT as a tool for NDE and serves as a starting point for the design and implementation of the inspection protocol used in the current study.

2.1 IR Thermography for NDE and Materials Characterization

2.1.1 General Considerations

Infrared thermography inspections are typically divided into two basic categories: active and passive. Passive inspections are conducted by positioning an IR camera to view an object or given scene and measuring the variations in surface temperature that exist naturally due to ambient conditions. Active thermography inspections include a supplementary heat source that is used to provide a direct thermal stimulus to the object under consideration. Nondestructive evaluation applications using IRT for composite materials typically rely on the active approach. Some examples of heat sources used in published studies include:

- Photography flash systems with power outputs ranging from 6 to 10 kJ[5,6]
- Halogen lamps[7]
- IR heat lamps[8]
- High velocity hot air for convective heating[9]

The primary criteria for evaluating the suitability of a heat source for a given application include the following:

- Maximum power density (W/m^2) of the generated heat flux
- Spatial variation of power density across the surface being heated (uniformity)
- Ability to control intensity and/or duration of heating

Photography flash systems are ideally suited to most aerospace composite applications and commercial systems are available which combine the flash lamps, IR camera, data acquisition and imaging processing equipment into a standalone system [10]. The field of view for a typical integrated system is on the order of 14.5 in. x 10.5 in. (~ $1ft^2$), which translates into the need to perform multiple inspections at different locations over the entire surface of the object under consideration. The time required for each inspection is related to the thickness and thermal diffusivity of the material. A general observation from recent literature on NDE of aerospace composites using IRT suggests that the observation time required for inspecting these systems is on the order of 10 to 30 s [5,6,11]. This allows for the inspection of relatively large areas in a reasonable period of time (approximately 1 ft^2/min).

Preliminary investigation into the GFRP materials and bridge deck geometry under consideration for the current study suggested that time scales for observing the temperature response of the heated surface would be on the order of 400 to 900 s (see Section 3.1). This observation eliminated the feasibility of deploying a flash based system due to the limited power density that can be generated over a large area. In order to keep the overall inspection time within reasonable limits (< 10 min/ft^2), focus shifted towards deploying an array of halogen lamps capable of illuminating approximately 9 ft^2 for each inspection (Figure 3).

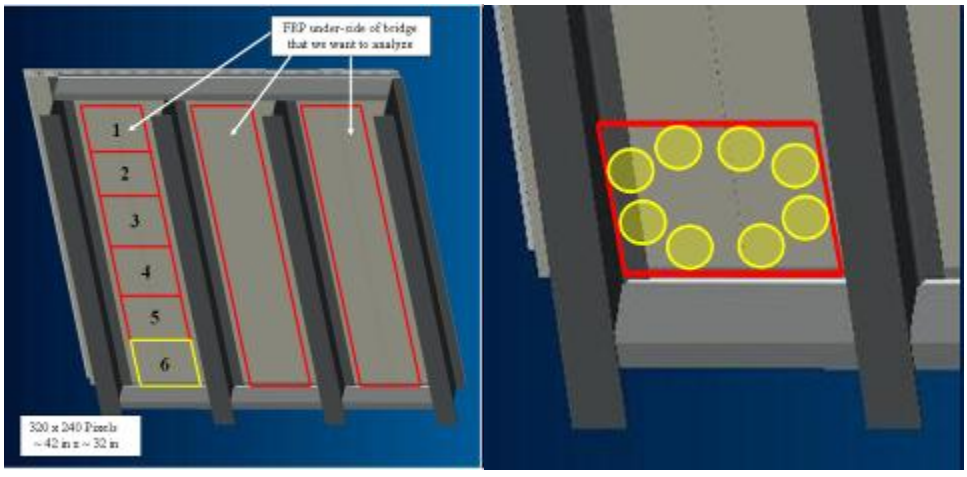

Figure 3-Conceptual design for IRT inspection of GFRP bridge decks for steel stringer bridge.

2.1.2 Strategies for Deployment and Data Acquisition

The fundamental parameters for data acquisition that must be defined for an active IRT inspection are:

1. Heating intensity and duration
2. Image acquisition frequency and duration

There are three general categories of IRT inspections based on the heating intensity and duration: pulse heating, step heating, and sinusoidal heating (lock-in). Pulse heating involves depositing high intensity (~ 15 MW/m^2), short bursts (~ 5 to 15 ms) of energy on the surface with photography flash lamps. Step heating relies on lower intensity (~ 1.5 kW/m^2), longer duration (~ 1 s to 30 min) square heat pulses. Sinusoidal heating typically uses the same maximum intensities as step heating, but the heat source is modulated at a specific sinusoidal frequency.

The required image acquisition frequency and duration depends on the material being inspected, the depth of the defects encountered, and the required sensitivity for resolving defects at different depths. Typical IRT systems for inspecting aerospace composites employ image capture rates between 50 and 200 Hz, but capture rates as low as .0083 Hz (1 image every 2 minutes) have been reported for inspecting GFRP composite bridge decks[9]. Ultimately, the decision on image capture rates is based on hardware limitations imposed by the IR camera, the temporal resolution needed to resolve the depth of encountered defects, and the time required for post-processing a given set of thermal images from each inspection.

The required image acquisition duration is also a function of material composition and defect depth. From the perspective of deployment, it is important to determine whether images will be acquired during heating, after heating (cooling), or both. If image acquisition is required during heating, the heat sources must be positioned such that the inspected surface is still visible by the camera. Pulse heating applications rely almost exclusively on images obtained after the surface has been heated. Step heating uses images collected either during heating or during cooling, and sinusoidal heating requires that images are collected throughout the heating process.

2.1.3 Data Processing

The final consideration in the development of an IRT inspection program relates to data processing and management. The output from the data acquisition phase consists of a series of thermal images collected over a specified duration at a specific frequency. A major focus of on-

going IRT/NDE research involves manipulating the collected data set in an effort to (1) improve the likelihood that a defect or damage will be detected (enhancement) and (2) obtaining additional information about the nature of a defect such as depth, thickness, planar area, and material composition (characterization). The following sections describe available techniques for processing IRT data using the step heating and sinusoidal heating scenarios discussed in Section 2.1.2.

The primary disadvantages associated with step heating are non-uniform heating and apparent temperatures due to reflections of the heat source. It is possible to minimize the effects of non-uniform heating and heat source reflections by considering the entire temperature vs. time response for each pixel in a series of thermal images (single pixel analysis). The theoretical surface temperature response for a one-dimensional solid composed of a homogeneous layer of finite thickness, L, and subjected to a constant heat flux (Figure 3A) is given by[12]:

$$\Delta T(t) = C\cdot\sqrt{t}\cdot\left[1 + \sum_{n=1}^{\infty}\left[2\cdot\left(-\Gamma^{n}\right)\cdot\left(exp\left(\frac{-n^2\cdot L^2}{\alpha_0\cdot t}\right) - \frac{n\cdot L\cdot\sqrt{\pi}}{\sqrt{\alpha_0\cdot t}}\cdot erfc\left(\frac{n\cdot L}{\sqrt{\alpha_0\cdot t}}\right)\right)\right]\right] \qquad \text{Equation 1}$$

$$C = \frac{2\cdot q'_0}{k_0}\cdot\sqrt{\frac{\alpha_0}{\pi}} \qquad \text{Equation 2}$$

$$\Gamma = \frac{e_1 - e_0}{e_1 + e_0} \qquad \text{Equation 3}$$

$$\alpha_0 = \frac{k_0}{\rho_0\cdot c_0} \qquad \text{Equation 4}$$

$$e_i = \sqrt{k_i\cdot\rho_i\cdot c_i} \qquad \text{Equation 5}$$

where: $q`_0$ is the heat flux intensity applied to the surface (W/m^2), L is the thickness of the GFRP layer, k_i is the thermal conductivity, ρ_i is the density, c_i is the specific heat, α_i is the thermal diffusivity, e is the thermal effusivity, and Γ is the thermal mismatch factor between the layer of finite thickness and air. The subscript '0' indicates specific material properties for the bonded layer of finite thickness and the subscript '1' indicates material properties for air. Equation 1 does not include the effects of convection and assumes the air on the reverse side of the heated surface to be a semi-infinite substrate material.

Another interesting feature of Equation 1 is that the intensity of the applied heat flux is confined to the constant, C. This constant can be determined for each pixel by measuring the slope of the initial temperature response plotted against $t^{1/2}$ before the effects of the plate's thickness influences the temperature response. Once value for C is obtained for each pixel, the temperature response can be normalized with the following relationship[12]:

$$\Delta T_{norm}(t) = \frac{\Delta T(t)}{C \cdot \sqrt{t}} - 1 \qquad \text{Equation 6}$$

The advantages of computing the normalized temperature response are illustrated in Figure 4 for a case involving carbon FRP composites applied to concrete[13]. The raw thermal image was collected after 15 s of heating with four 500 W halogen lamps. The total area of the specimens is 3 ft^2. The artificial defects that were implanted below the surface of the FRP are clearly visible, but there are also large areas near the perimeter of the specimens that are influenced by non-uniform heating. Equation 6 was used to normalize the temperature response for each pixel in the series of thermal images and the resulting normalized images were not significantly influenced by non-uniform heating (Figure 5).

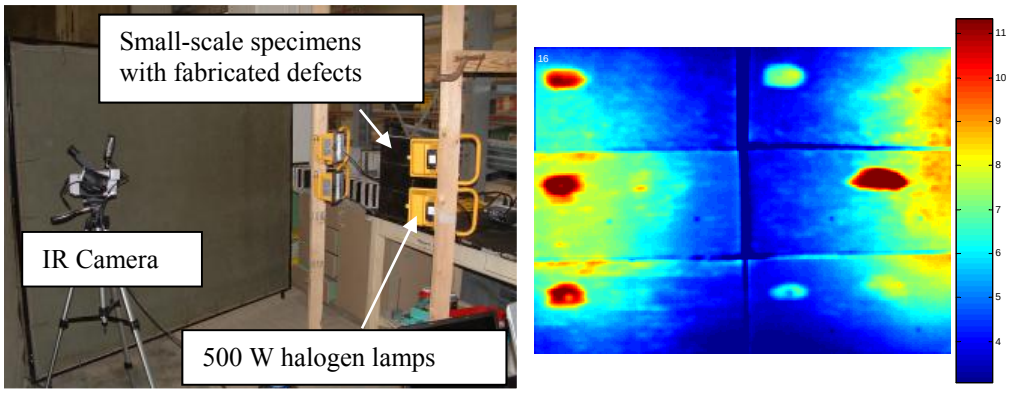

(a) (b)

Figure 4-Laboratory setup for step heating experiments. (a) IR Camera and four 500W halogen lamps used to heat 3 ft^2 area. (b) Thermal image of small-scale specimens with fabricated defects after 15 s heating.

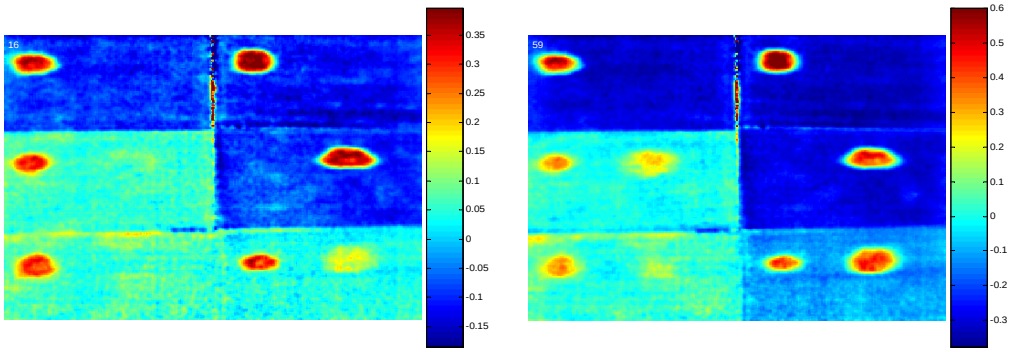

(a) (b)

Figure 5-Normalized temperature response for properly saturated carbon FRP specimens with fabricated defects. Thickness of FRP composite is provided for each specimen. (a) t = 15 s. (b) t = 60 s.

Sinusoidal heating also results in surface temperature variations, both real and apparent, due to heat lamp proximity and reflections from the heat source. Figure 6 provides a thermal image for an GFRP bridge deck sample heated with four 500W halogen lamps using a sinusoidal intensity with a period of 900 s for 1800 s. The three points identified in the figure experience a different surface temperature response because the array of halogen lamps is positioned very closely to the perimeter of the sample.

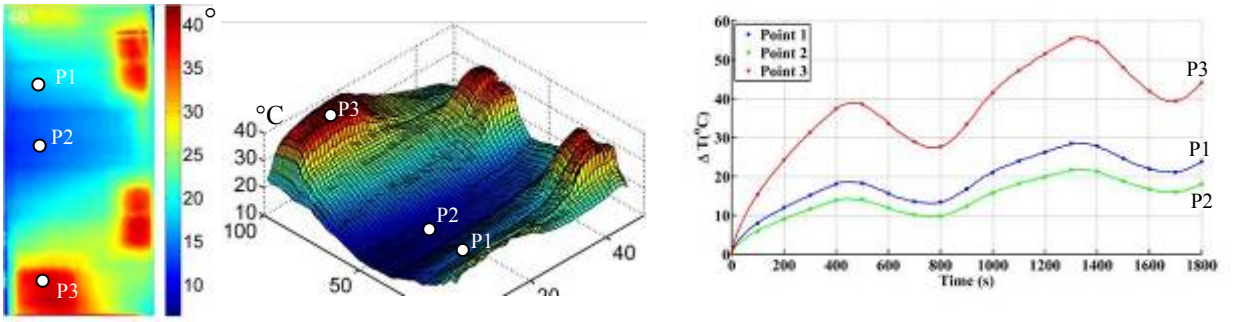

Figure 6-Raw ΔT image and surface plot for undamaged sample at t = 460s (T = 15 min) and ΔT vs. time plot for three points of interest.

The effects of this non-uniform heating can be minimized by applying a least-squares sinusoidal curve fit to the temperature vs. time response for each pixel in the series of thermal images. The general form of the curve fit used is as follows:

$$\Delta T(t) = a_0 + a_1 \cos\left(\frac{2\pi t}{T}\right) + a_2 \sin\left(\frac{2\pi t}{T}\right) \qquad \text{Equation 7}$$

where a_0, a_1, and a_2, and are unknown constants. Once these values have been obtained using least squares regression, the corresponding phase angle, Φ, may be determined for each pixel with the following:

$$\Phi = \arctan\left(\frac{a_2}{a_1}\right) \qquad \text{Equation 8}$$

Phase angle is influenced by defects or other anomalies below the surface but is relatively independent of the magnitude of the temperature response [14]. The resulting phase image for this series of thermal images is provided in Figure 7. Additional details on interpreting this image are provided in Section 4.1.3.

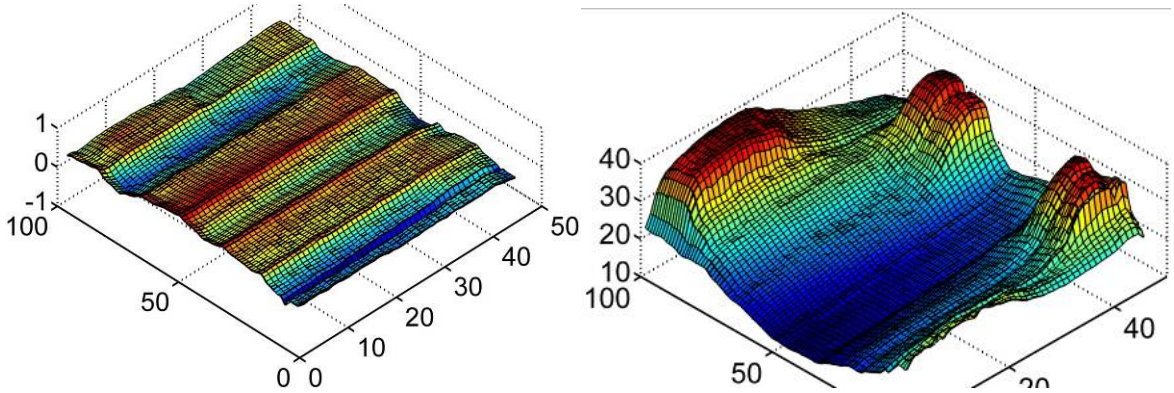

(a) (b)

Figure 7-Phase image (a) and raw thermal image (b) for GFRP composite bridge deck sample.

2.2 IR Thermography Applied to Civil Infrastructure

2.2.1 GFRP Bridge Decks

Previous work by Miceli et al.[9] investigated IR thermography as a NDE tool for GFRP bridge decks. The heating strategy employed in this study involved forcing hot air through internal ducts that passed through the GFRP deck panels. While this particular heating method is not necessarily applicable to the deck panels in the current study, their findings regarding the time scales involved in heating and viewing the deck with the IR camera are relevant.

Results are presented for 10 test series that involved heating times ranging from 4 minutes to 45 minutes. The image collection interval used for all tests was 1 image every 2 minutes. The "final" image selected for analysis was reported as having been collected after 45

minutes of cooling. This results in a time period ranging from 49 to 90 minutes for each inspection.

2.2.2 FRP-Strengthened Reinforced Concrete

Previous work by Brown and Hamilton[7,13] investigated IRT as a tool for evaluating bond in FRP strengthening systems applied to reinforced concrete. A study sponsored by the FDOT[15] included inspection of full-scale AASHTO girders in both laboratory and field settings. The FDOT study demonstrated that IRT is an effective means for detecting near-surface defects in typical carbon/epoxy and glass/epoxy FRP systems. The study also highlighted the importance of properly calibrating the IRT inspection parameters based on as-built FRP system properties, which can vary significantly for wet lay-up FRP systems.

(a) (b)

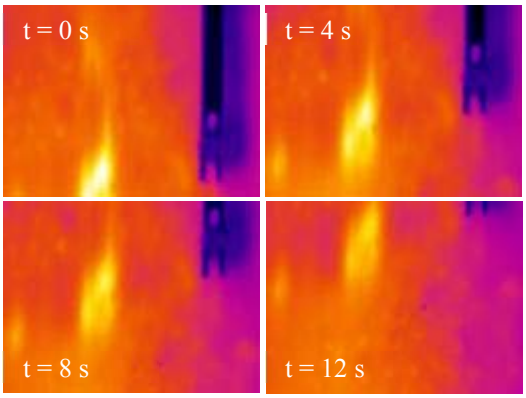

(c)

Figure 8-Data collection for full-scale AASHTO girders. (a) Scanning cart configuration for Girder 3. (b) Girders 4 to 6. (c) Typical thermal images

3 Finite Element Modeling

In an effort to establish general boundaries for the heating and image acquisition requirements that are unique to this problem, several FE models were developed in ANSYS to simulate the heat transfer behavior of the GFRP bottom panel for Deck A. The geometry of the GFRP bottom panel provides some interesting opportunities from an IRT/NDT perspective. When heat is applied to the soffit of the GFRP bottom panel, a thermal front will develop and travel towards the backside of the plate. When the thermal front reaches the backside of the plate it is effectively stopped by the convection controlled boundary condition. This will ultimately manifest on the heated surface as an increase in the rate of change in ΔT. The thermal front is allowed to continue undisturbed through the web and will not experience the relative increase in ΔT. This should result in a "cool-spot" above the web. From an NDT perspective, identifying this cool spot in the region of web would indicate that the web is mechanically connected to the GFRP bottom panel and no delamination has occurred.

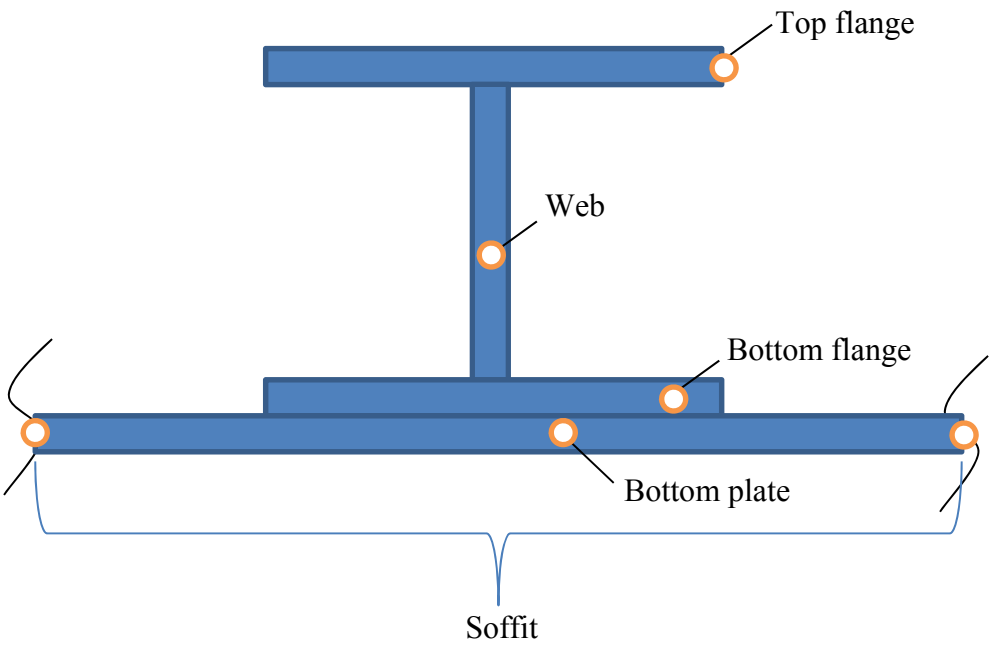

Figure 9-Components of monolithic GFRP bottom panel

3.1 One-Dimensional Heat Transfer

Three 1-D heat transfer models were developed to simulate the response to constant heating of three areas on the GFRP soffit for Deck A (Figure 10). Area A is located on the exterior surface of the 1.3 cm thick GFRP bottom plate, Area B is located on the surface of the 1.7 cm thick GFRP plate and flange, and Area C is located on the surface directly below the web. A constant heat flux of 1550 W/m^2 was applied to the surface node of each model and the temperature response was monitored over a period of 1000 s. These models indicate that divergence between Area A and Area C begins at approximately t = 400 s ($t^{1/2}$ = 20 $s^{1/2}$).

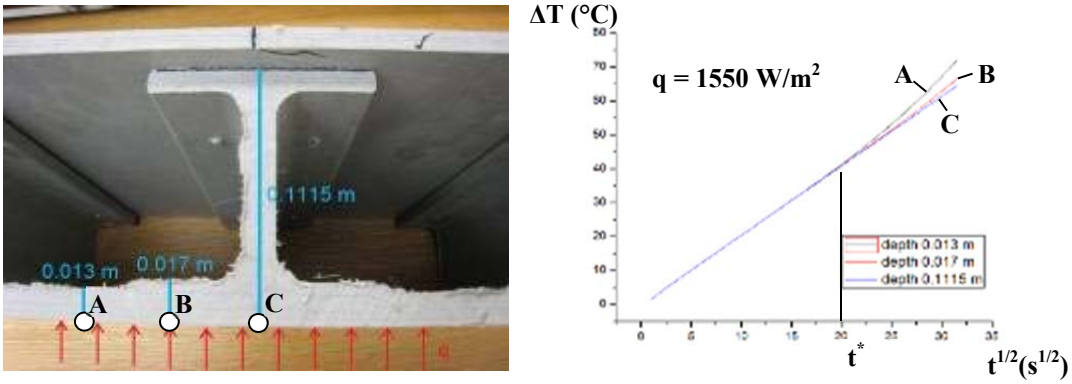

Figure 10-One-D FE model results for constant heat flux applied to soffit of GFRP plate.

3.2 Two-Dimensional Heat Transfer

A 2-D model was also developed in ANSYS to better characterize the geometry of the GFRP bottom panel as well as to provide a platform for simulating defects in the GFRP bottom plate. Another feature that was added to the model was sinusoidal heating. One of the challenges associated with deploying IRT in the field is that uniform heating of a surface is almost impossible to obtain. If the required heating durations are long and the temperature differences are small, the temperature gradients that result from non-uniform heating can overwhelm a particular thermal image and make it difficult to detect any desired features. If the applied heat flux is sinusoidal, a least-squares sinusoidal curve fit can be used to obtain the phase response for each point on the surface. The phase is independent of the amplitude of the applied heat flux. Short periods of heat flux modulation (high frequencies) reveal anomalies close to the surface while longer periods (low frequencies) reveal anomalies deeper beneath the surface. This principal can also be used to identify the web in the GFRP bottom panel.

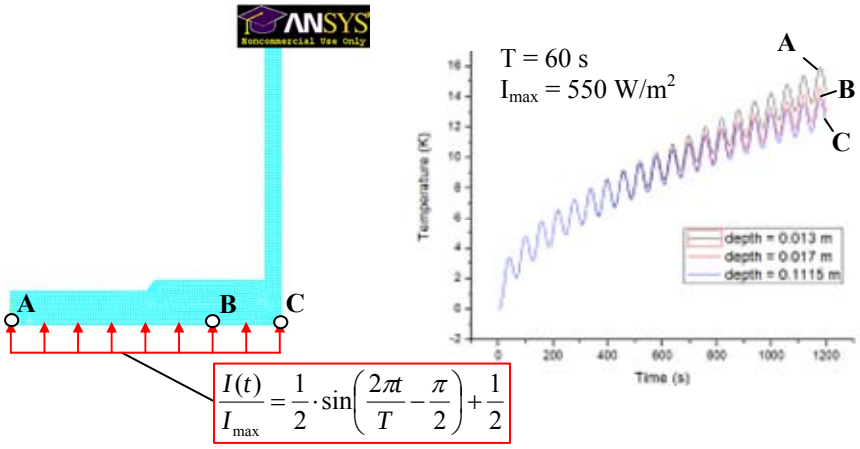

Figure 11-Two-dimensional FE model results for sinusoidal heating.

The results of the FE modeling are presented in terms of a phase profile across the soffit of the GFRP bottom panel. A unique phase profile is generated for each period that was investigated (T = 60 s, 120 s, 240 s, 480 s, and 960 s). Each period was investigated for a total of 2 cycles. The phase responses across the surface for the two shortest periods (60 s and 100 s) are essentially straight lines because the thermal front that is propagating towards the back surface has not yet been affected by the air space present at Point A and Point B. The phase profile for the 240 s period does begin to diverge around the location of the bottom flanges, but the largest divergence ($\Delta\Phi$ = 0.05 rad) occurs for the T = 960 s period.

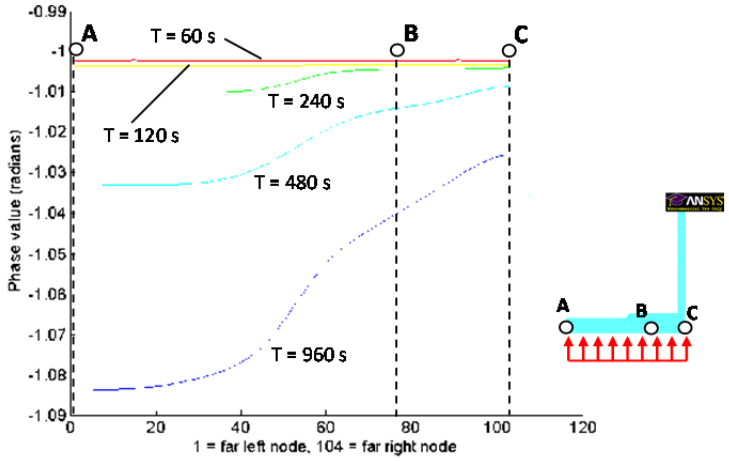

Figure 12-Phase profile results for different heating modulation periods

3.2.1 Generic Defects in GFRP Plates

Additional FE modeling was conducted to simulate defects in the 13-mm thick GFRP bottom plate. An axisymmetric model was developed for transient heat transfer analysis (thickness = 13 mm, radius = 100 mm). Defects were simulated by changing the material properties of specific elements from glass GFRP to air. The "thickness" of each defect was held constant at 1 mm and the radius and depth of the defect in each FE model were varied as shown in Table 1. This resulted in a total of 32 permutations based on defect geometry (four radii at eight depths).

Table 1-Defect radii and depths for axisymmetric FE models

Defect radius (mm)	Defect depth (mm)
5	1
10	2
15	3
25	4
	5
	7
	9
	11

Each of the 32 FE models with different defect configurations was analyzed for the case of a sinusoidally varying heat flux applied to the soffit of the GFRP plate. A total of eight different sinusoid periods, T, were investigated (Table 2) resulting in a total of 256 FE model runs.

Table 2-Sinusoid periods

Sinusoidal heating period, T (s)
7.5
15
30
60
120
240
480
960

Each model was subjected to the sinusoidally varying heat flux for a total of two periods (2T). The temperature vs. time response was extracted for all nodes along the soffit of the GFRP

plate at each time step. The complete temperature vs. time response for each node was then used as input into a least-squares sinusoidal curve fit routine and the corresponding phase angle was computed. This resulted in a single "phase profile" along the soffit of the GFRP plate for each FE model run that was completed (Figure 13).

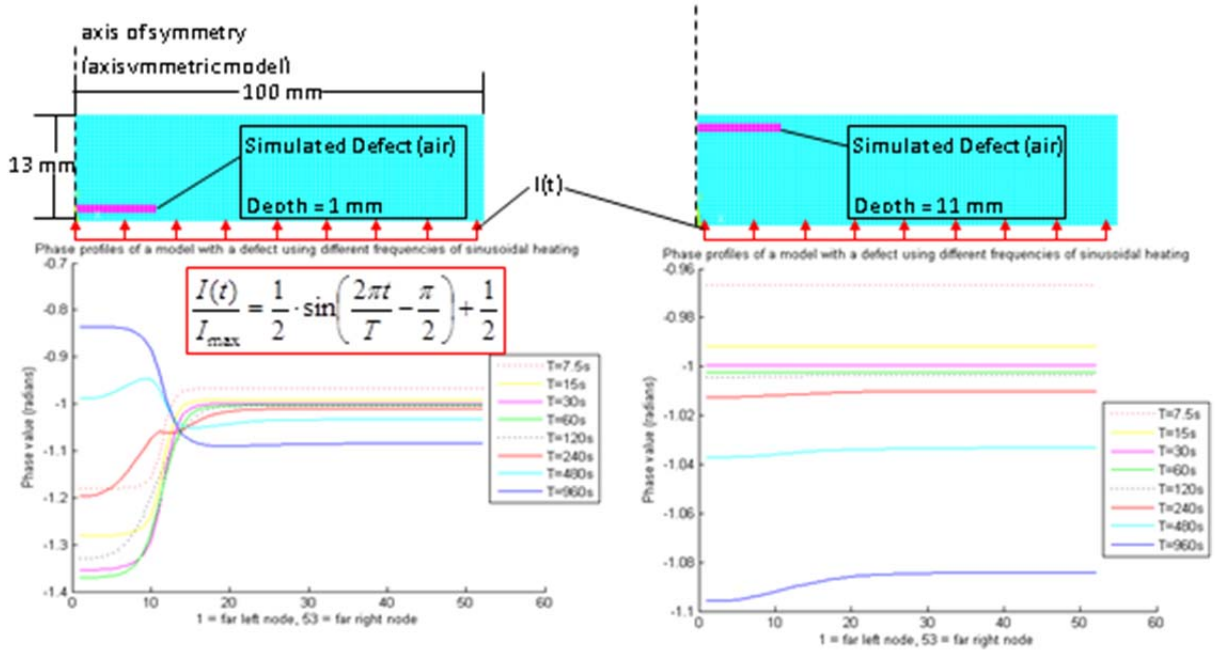

(a) (b)

Figure 13-Sample phase profile results for defect radius = 10 mm and (a) defect depth = 1mm and (b) defect depth = 11 mm.

The results from each phase profile can be reduced into a single value for the phase difference between the node above the center of the defect and the adjacent defect-free region (Figure 14). These results can be used to design the heating protocol for the in-field inspections as well as characterize the relative depth of any detected defect. Figure 14 provides a summary of the FE model results with defects of the same radius plotted on the same curve. Figure 15 provides the same results but with the defect depth variable held constant for each graph.

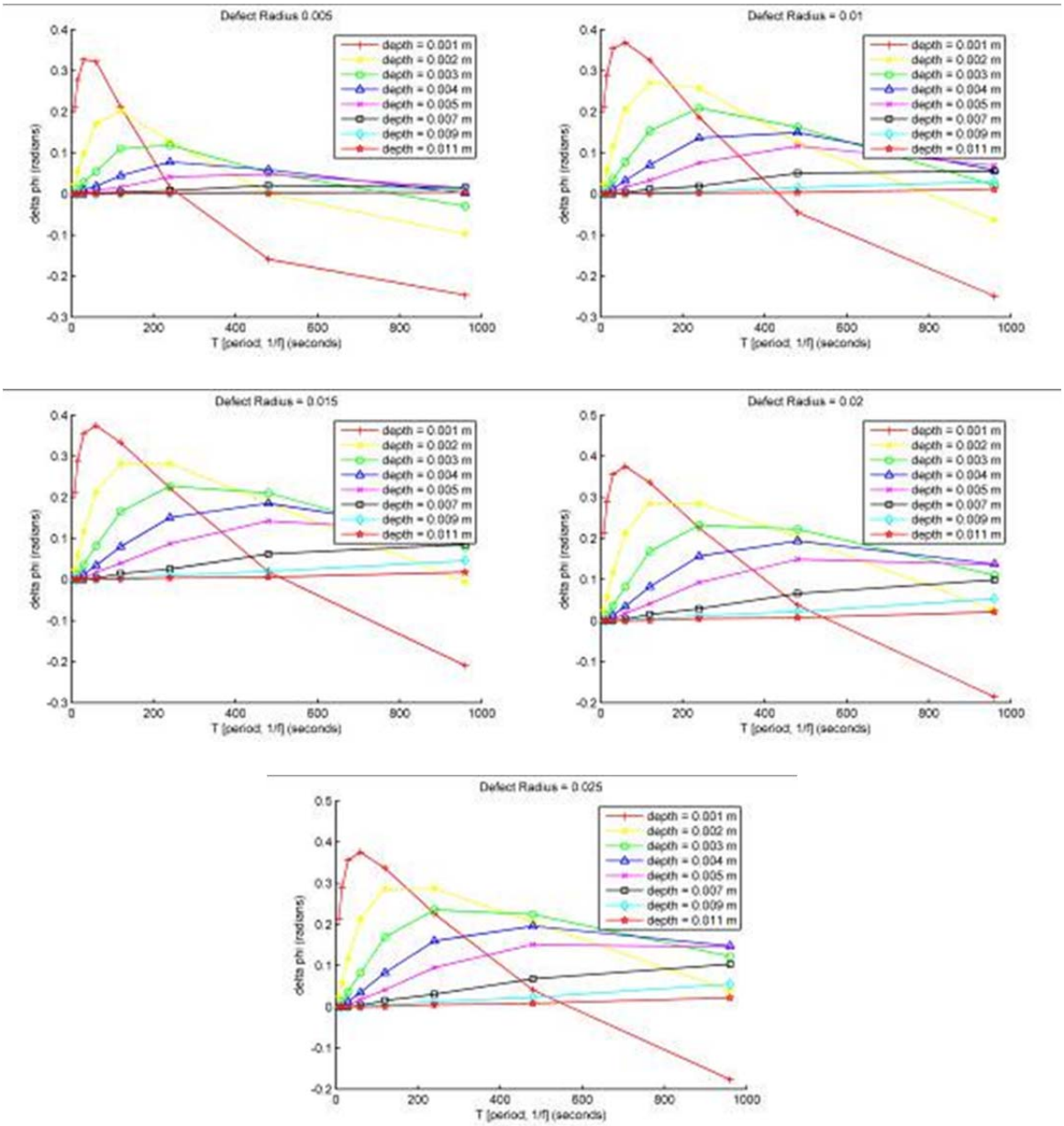

Figure 14-Defect signal strength (ΔΦ) vs. period (T) results for fixed radii values.

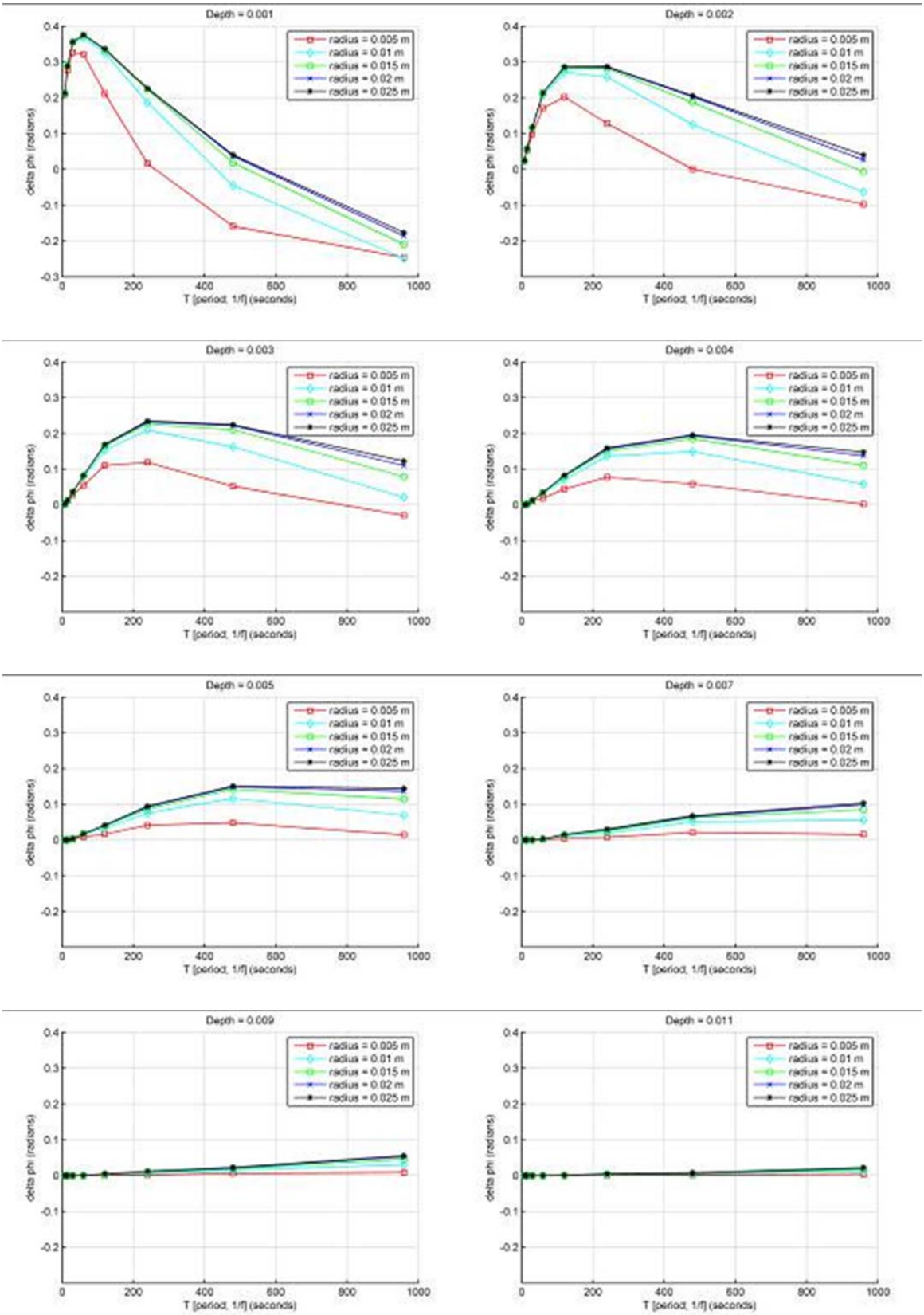

Figure 15-Defect signal strength (ΔΦ) vs. period (T) results for fixed depth values.

4 Experimental Program

4.1 Proof of Concept Testing – Sinusoidal Heating

Two GFRP bridge deck samples were provided by the FDOT. One sample (25 cm x 71 cm) was cut from a full-size panel that had been loaded to failure in a laboratory load test. The second sample (31 cm x 89 cm) was also cut from a full-size panel and was undamaged (Figure 16). The orientation of the webs for each sample is provided in Figure7.

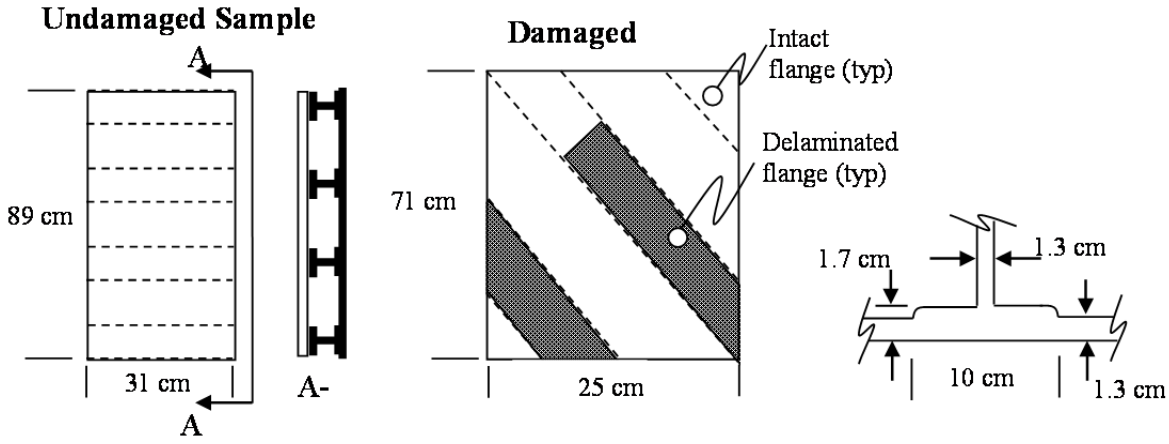

Figure 16-Specimen details and web orientation for experimental study

4.1.1 Thermal Imaging

Eight 500 W halogen lamps were attached to a frame as shown in Figure 17. The perpendicular distance from the face of the lights to the plane of the GFRP deck samples was 36 cm and the total heated area was approximately 1m x 0.75m. A FLIR A325 IR camera (8-12µm uncooled 320x240 microbolometer array) with a 45° wide angle lens was positioned 1.3 m from the GFRP deck samples such that the entire 1m x 0.75m area could be observed. The GFRP deck samples were roughly centered in the field of view with the damaged sample on the left and the undamaged sample on the right. One laptop computer was used to control an analog output DAQ card that was responsible for supplying the proportional output signal for the desired heat flux modulation. All eight lights were connected directly to a 4-channel analog dimmer with an output capacity of 1200 W per channel. The IR camera was connected to a second PC and synchronization/triggering of the camera was achieved through a serial port.

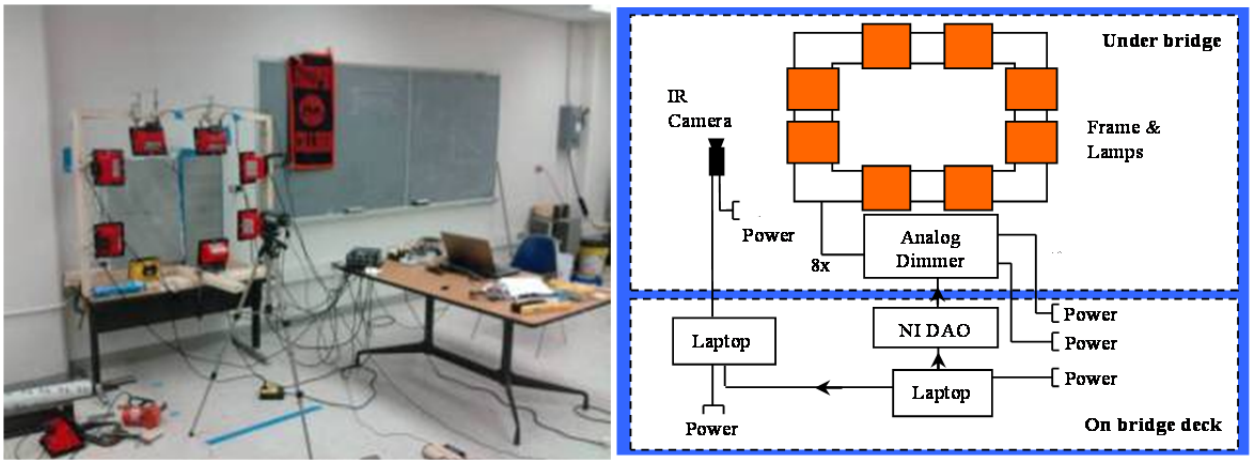

Figure 17-Laboratory setup and general schematic for IRT inspection

4.1.2 Data Collection and Raw Thermal Images

Three modulation periods were investigated in the preliminary study: T = 15 min, T = 25 min. and T = 35 min. Two complete cycles of heating were provided during each experiment and thermal images were collected at a rate of 1 frame per 5 seconds (0.2 Hz). The modulated heating differed slightly from that used in the numerical modeling. Rather than beginning an experiment with the heat flux intensity equal to zero (a phase shift of $-\pi/2$), each experiment began with the lamps at 50% of their maximum output. The heat flux intensity, I, generated for duration 2T during each experiment was as follows:

$$\frac{I(t)}{I_{max}} = \frac{1}{2}\sin\left(\frac{2\pi t}{T}\right) + \frac{1}{2} \quad \text{for t = 0…2T} \qquad \text{Equation 9}$$

After the series of thermal images were collected for each period under consideration, the images were cropped into independent series for the damaged and undamaged specimens. Image subtraction was performed for each of the cropped images using the first image in the sequence collected at t = 0s. The cropped and subtracted thermal images represent the raw temperature change measured by the IR camera.

4.1.3 Deck A Results – Undamaged

Under ideal circumstances, the bottom flanges and webs should result in relative cool spots in the thermal images and the GFRP bottom plate should appear as a warm area or hot-spot. The raw images shown in Figure 6 (Section 2.1.3) clearly demonstrate the challenges associated with any type of active heating for extended periods. The most dominate features in

the thermal image are reflections from the halogen lamps and the overall temperature variation across the sample, even away from the reflections, approaches 20 °C. While it is possible to discern some of the features of interest (the flanges and webs) very little useful information can be gleaned from these data.

The least squares sinusoidal curve fit processing technique (Section 2.1.3) greatly improves the quality of the image and is effective at removing non-uniformities due to lamp proximity and reflections. It is also possible to perform the curve fitting operation over any desired portion of the ΔT vs. time history. The results provided in Figure 18 indicate that there is very little advantage to collecting data for the second heating cycle that was provided for each modulation frequency.

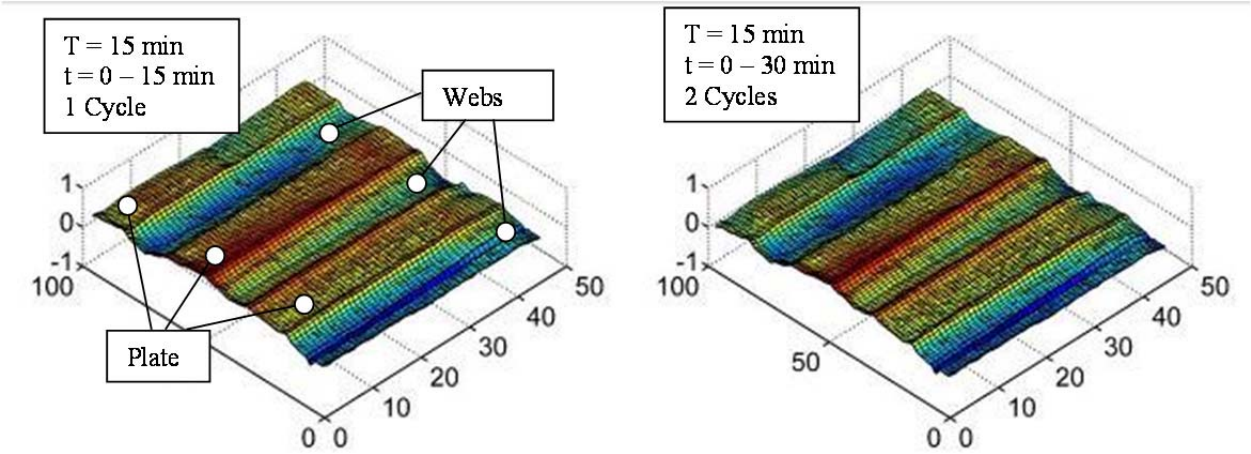

Figure 18-Phase image surface plots for undamaged sample. T = 15 min. Plot on the left obtained after 15 min of heating. Plot on the right obtained for 30 min heating.

Increasing the period of the heat flux modulation to T=25 min or T=35 min also appears to provide little advantage with regards to enhanced feature detection. The phase profile plots generated through the center of the undamaged sample (Figure 19) show very little variation as a function of modulation frequency other than an overall shift. This shift also varies as a function of the number of cycles, N, used to generate the phase value for each pixel. The higher period images actually appear to degrade around the exterior edge of the sample, but the reason for this is not entirely clear. Considering the long time period required even for the 15 min modulation period and no discernable advantage by including more than one cycle for each experiment, it

would appear that the surface plots provided in Figure 18 and the profile plot for T=15min, N=1 in Figure 19 is the best result one might expect for this particular GFRP deck system.

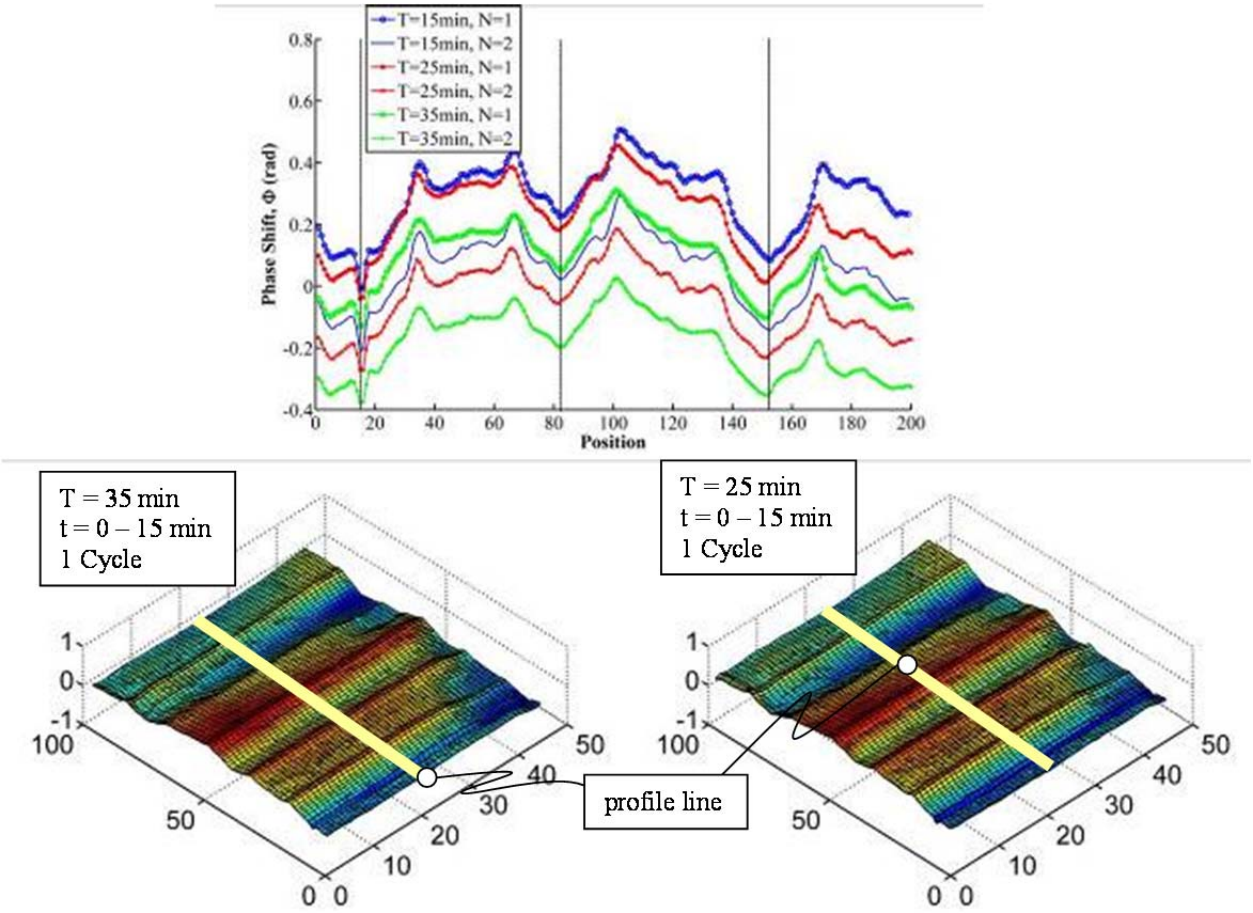

Figure 19-Phase profiles and surface plots for undamaged sample. Vertical lines in profile plot represent the locations of the webs.

In addition to being able to distinguish the webs from the GFRP bottom late, which provides an indication that no delamination has occurred, additional features can also be distinguished in the area near the GFRP bottom plate and flange interface. The peaks in this region could indicate localized variability in matrix saturation of the composite or other manufacturing features. Without additional destructive testing it is not possible to state this with any degree of certainty. Variations in surface absorptivity/reflectivity were also apparent in these regions, which may have led to these apparent anomalies.

4.1.4 Deck A Results – Damaged

Results for the damaged sample are presented in Figure 20. Areas where the flanges had delaminated from the GFRP bottom plate are distinguishable in the surface plots and the difference between the damaged and undamaged specimens appears to be significant. Once again, there was no apparent advantage to including the T=25min and T=35min modulation periods.

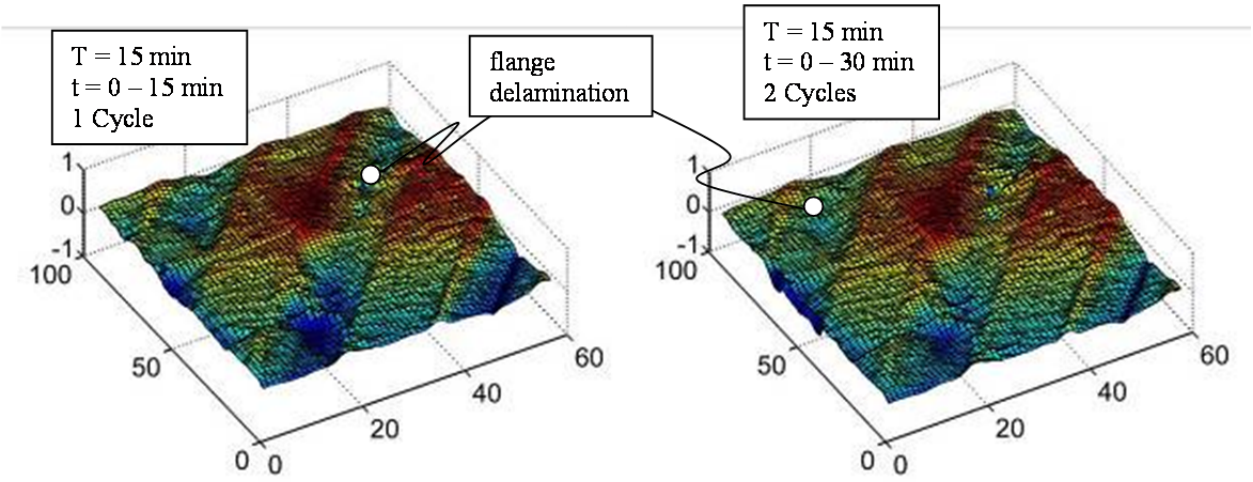

Figure 20-Phase image surface plots for damaged sample. T = 15 min. Plot on the left obtained after 15 min of heating. Plot on the right obtained for 30 min heating.

4.1.5 Conclusions from Preliminary Study

These results confirmed the general findings from the finite element study and suggest that IR thermography is a potentially useful tool in detecting severe damage in GFRP bridge decks. Specifically, we have demonstrated that it is possible to identify flange delamination and web separation that occurs at a depth of up to 1.7 cm below the surface. It should be noted, however, that these results are limited to this specific type of GFRP bridge deck system (Deck A). A minimum heating/image acquisition time of 15 minutes was required to reveal this damage. A least-squares sinusoidal curve fit was also necessary to remove the heating non-uniformities due to lamp proximity and reflections. Additional research is necessary to validate the performance of this method under actual field conditions and there are a number of practical barriers to deployment in the field that must be addressed.

4.2 IRT Inspections of Deck Panels Loaded to Failure

A second set of experiments were performed in August 2010. Three GFRP deck types were investigated in this study (Deck A, Deck B, and Deck C described in Part 1 of this report), and the general strategy was as follows:

- Perform preliminary inspections on undamaged specimens to establish baseline characteristics
- Load the specimens to failure and perform IR thermography inspections at various stages of loading in order to determine at what point in the load history it becomes possible to identify damage.
- Perform a final IR thermography inspection of the failed specimens

4.2.1 Experimental Setup

A custom-made fixture system for eight 500W halogen lamps and the IR camera (FLIR A325) was used to collect IRT inspection data from the soffit of each GFRP deck (Figure 21). The camera was controlled by proprietary software (ThermaCAM Researcher) and triggered remotely by an integrated Labview program. The Labview program also controlled the intensity of the lamps through an analog dimmer.

A total clearance of 60 in. was provided between the soffit of the deck and the floor. The clear span between supports for loading was 48 in., but the field of view in the direction parallel to the span length was limited to 36 in. by the steel I-beam supports.

Figure 21-Test setup with lamp and camera fixtures positioned below soffit of the GFRP deck.

A time-varying sinusoidal heating profile was used in order to minimize the effects of non-uniform heating due to lamp proximity on the soffit of the GFRP deck. A series of thermal images were collected during each inspection and a least-squares sinusoidal curve fit was applied to the resulting temperature vs. time response for each pixel. The resulting phase angle was computed for each pixel and used to reconstruct a single phase image.

A standardized data collection procedure was deployed for each of the three GFRP deck types. This involved sinusoidal heating at six different periods (T = 30s, 60s, 120s, 240s, 480s, and 960s) for two heating cycles (Figure 22).

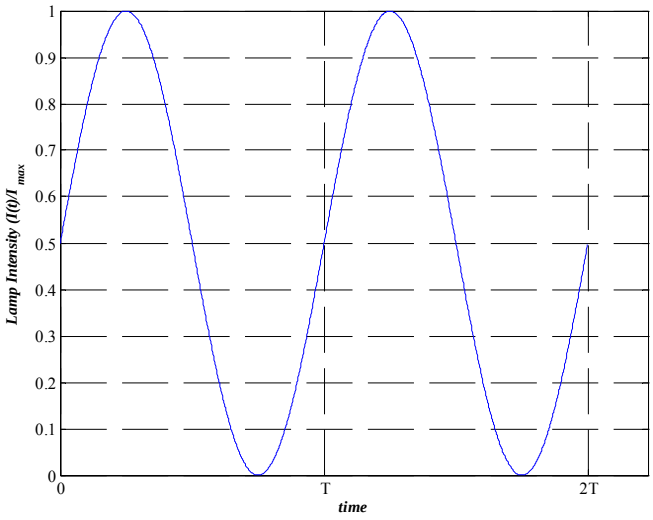

Period T(min)	# of cycles	Image save rate (Hz)	# of Images
0.5	2	2	121
1	2	1	121
2	2	1	241
4	2	1	481
8	2	1	961
16	2	0.5	961

Figure 22-IRT inspection parameters for undamaged GFRP bridge deck specimens

Data processing for the undamaged specimens was completed in 4 steps:

1. Convert images from FLIR proprietary format to Matlab format
2. Trim unwanted images from the beginning and end of each image sequence
3. Crop GFRP deck area to remove unwanted pixels from the perimeter of each remaining image
4. Perform least-squares sinusoidal curve fit for each sequence to obtain a single phase image

4.2.2 Results Deck A

The lower periods (T = 30s and T = 60s) are intended to identify defects or abnormalities in material composition close to the surface. An interesting finding for Deck A is that for periods as low as 60s a series of ridges begin to appear in the phase images. These localized peaks correspond to strips on the surface that appear darker than the surrounding area and also correspond to the locations where the edges of the bottom flanges connect to the GFRP bottom plate.

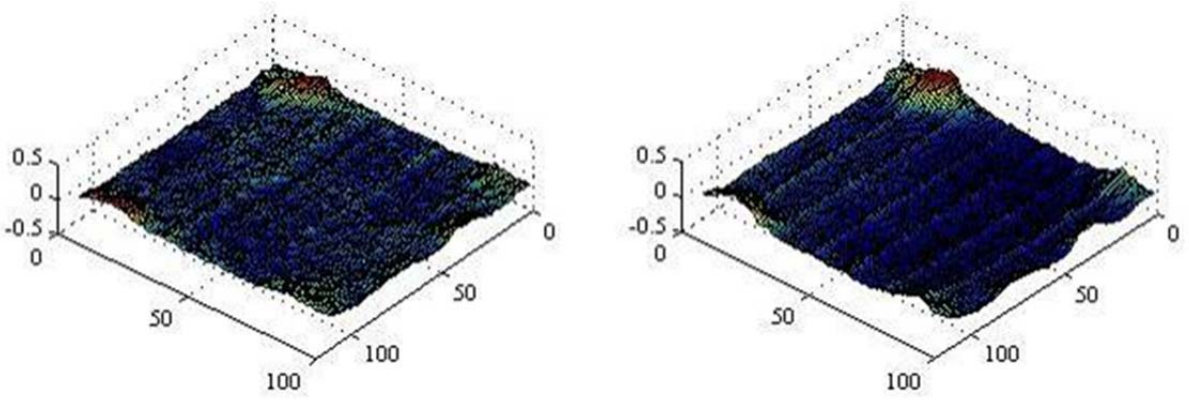

T = 30 s

T = 60 s

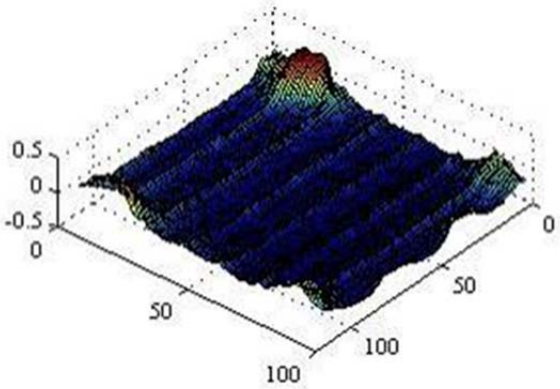

T = 120 s

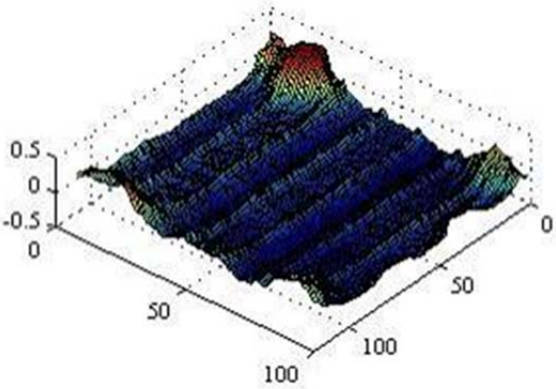

T = 240 s

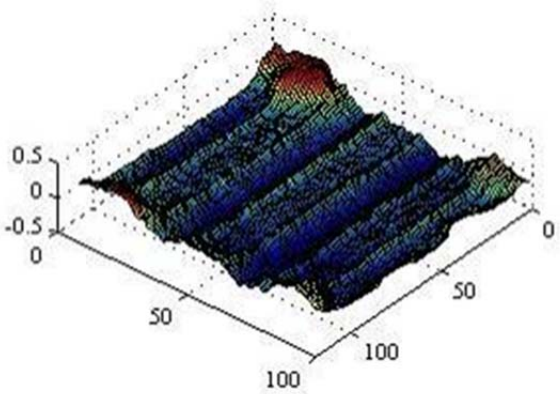

T = 480 s

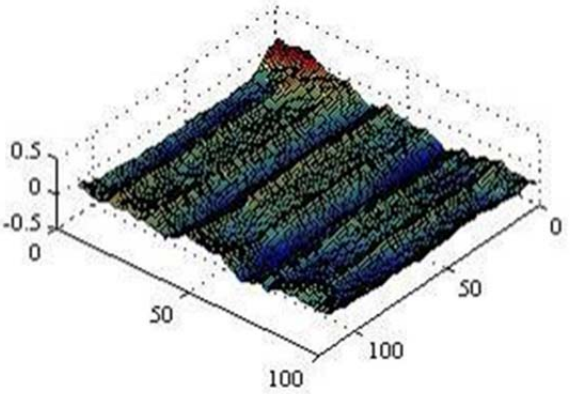

T = 960 s

Figure 23-Surface profiles (phase angle) for Deck A at six different heating periods.

The webs do not become prominent in the phase profiles until the heating period reaches 240 s. Increasing the period to 480 s and 960 s does little to enhance the difference between the GFRP bottom plate and the webs. This may be an indication that the pultruded GFRP deck contains some other material variability where the flanges connect to the bottom panel. This is

consistent with findings from the damaged specimens where the bottom panel had delaminated but the web still appeared in the phase image.

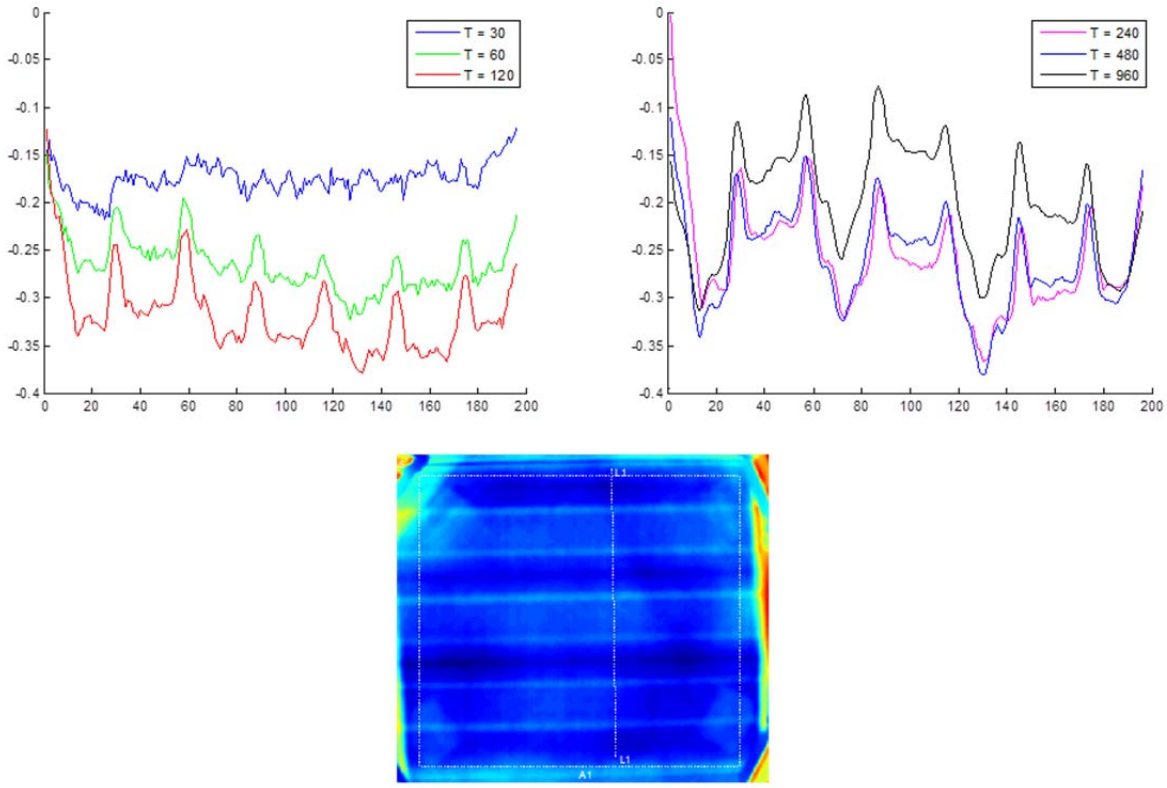

Figure 24-Line profiles along L1 (phase angle) for Deck A at six different heating periods.

4.2.3 Results Deck B

The 30s and 60s periods also showed some minor variations in the phase profile corresponding to surface irregularities. The corrugated core material begins to appear in the 60s period data but is easily distinguished in the 120s period data. The line profiles indicate that the maximum difference between the corrugated core and the bottom panel occurs at a period of 480s (Figure 25).

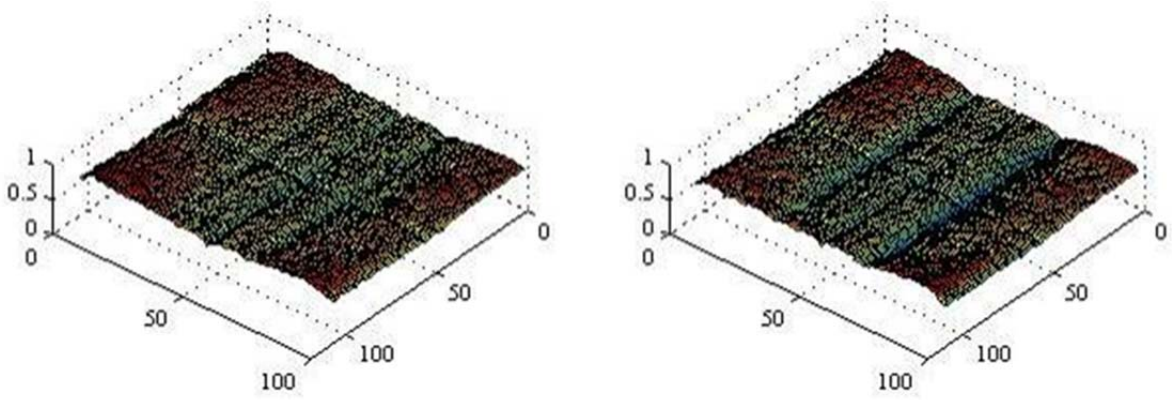

T = 30 s

T = 60 s

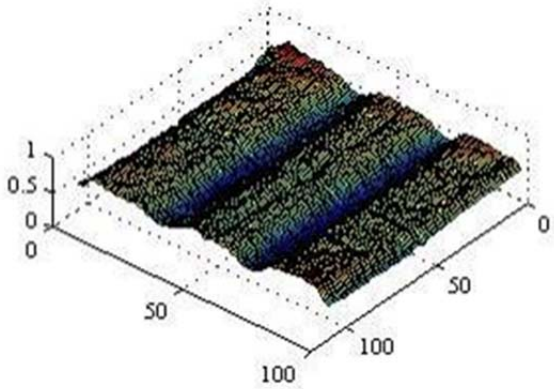

T = 120 s

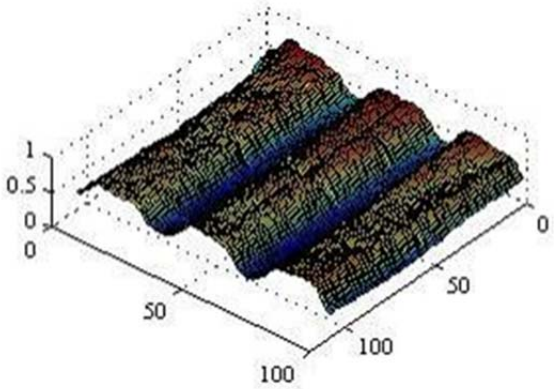

T = 240 s

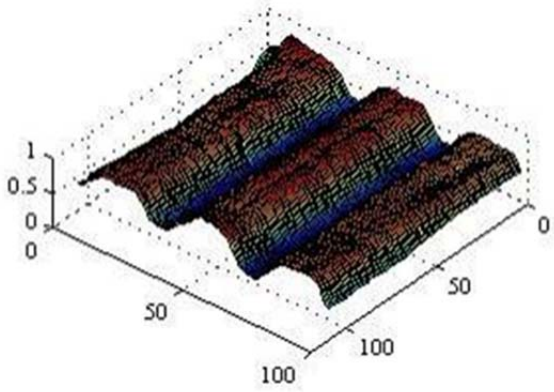

T = 480 s

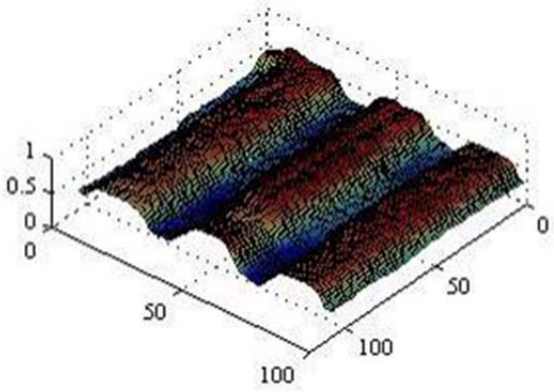

T = 960 s

Figure 25-Surface profiles (phase angle) for Type B deck at six different heating periods.

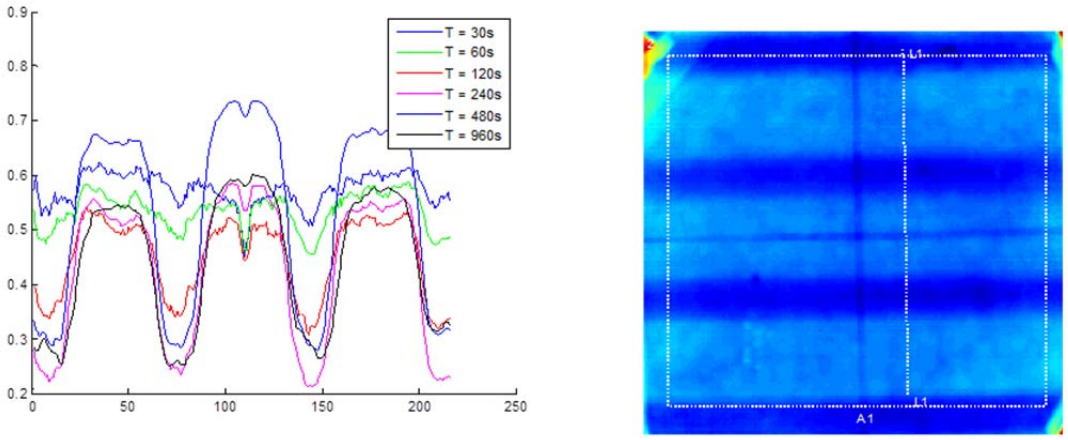

Figure 26-Line profiles along L1 (phase angle) for Deck B at six different heating periods.

4.2.4 Results Deck C

The honeycomb core material was not distinguishable at any of the heating periods investigated. There was one interesting finding regarding the large number of apparent defects that were identified at all periods investigated. These defects were identified as surface imperfections and variations in roughness and overall degrees of sanding. These surface defects appear with similar amplitude variations at all of the heating periods that were investigated. These results confirm the general principle that lower periods only reveal defects closer to the surface, but they also suggest that collecting data for more than one period can be beneficial in distinguishing surface imperfections from subsurface defects.

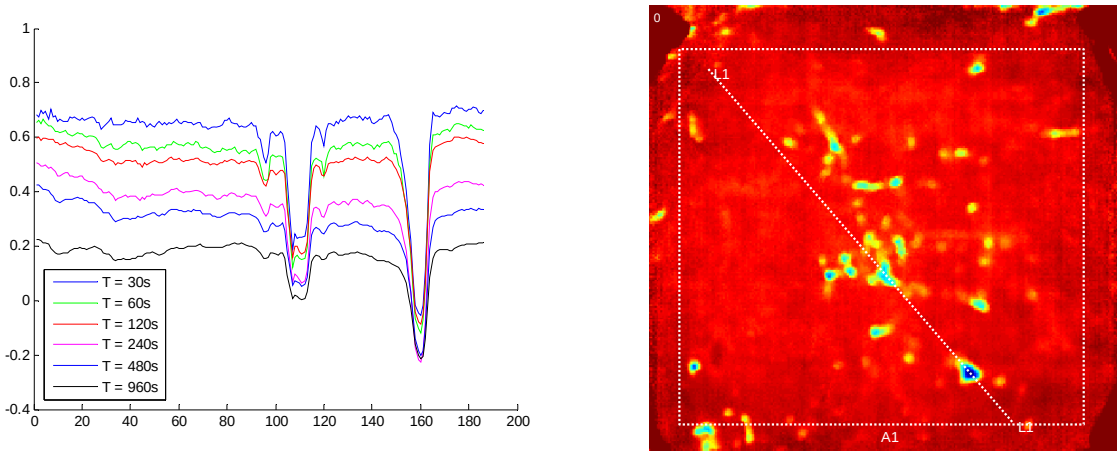

Figure 27-Line profiles along L1 (phase angle) for Deck C at six different heating periods.

4.2.5 Damaged Specimens

Two of the Deck A panels were selected for additional testing during loading and after failure. Damaged Specimen 1 (DS1) was configured with two GFRP top plates. The joint for these panels was located at midspan of the deck and oriented perpendicular to the primary span direction. Damaged Specimen 2 (DS2) was configured with a single GFRP top plate. A complete breakdown of IRT inspections performed on these panels is provided in Table 1.

DS1 experienced web-buckling failure near the top flange while DS2 experienced a delamination failure between the bottom flange and the GFRP bottom plate (Figure 28). From a thermal imaging perspective, preliminary results obtained from a damaged specimen with a failure mode similar to DS2 suggested that bottom flange delamination can be detected. The damage incurred as a result of web-buckling near the top of the web is very far from the surface that is heated during the inspection and, therefore, is not considered to be a practical application for IRT.

Table 3-IRT Inspection Matrix for Damaged Deck A

Specimen ID	Load Level (kip)	Period, T (min)	# of cycles	Image save rate (Hz)	# of Images
DS1	0	15	1	1	901
	12	15	1	1	901
	30	15	1	1	901
	45	15	1	1	901
	60	15	1	1	901
	70	15	1	1	901
	PF*	15	1	1	901
	PF w/ 12	15	1	1	901
DS2	PF	15	1	1	901
	PF	15	2	0.5	901
	PF	25	1	1	1501
	PFS**	15	1	1	901
	PF + 60 w/ 12***	15	2	0.5	901
	PFS + 60	15	2	0.5	901
	PFS + 60	25	1	0.5	751

*PF = post-failure or after failure due to loading
**PFS = post-failure w/ specimen shifted such that all of delaminated area was in camera FOV
***w/12k = IRT inspection performed while specimen was subjected to 12 k load

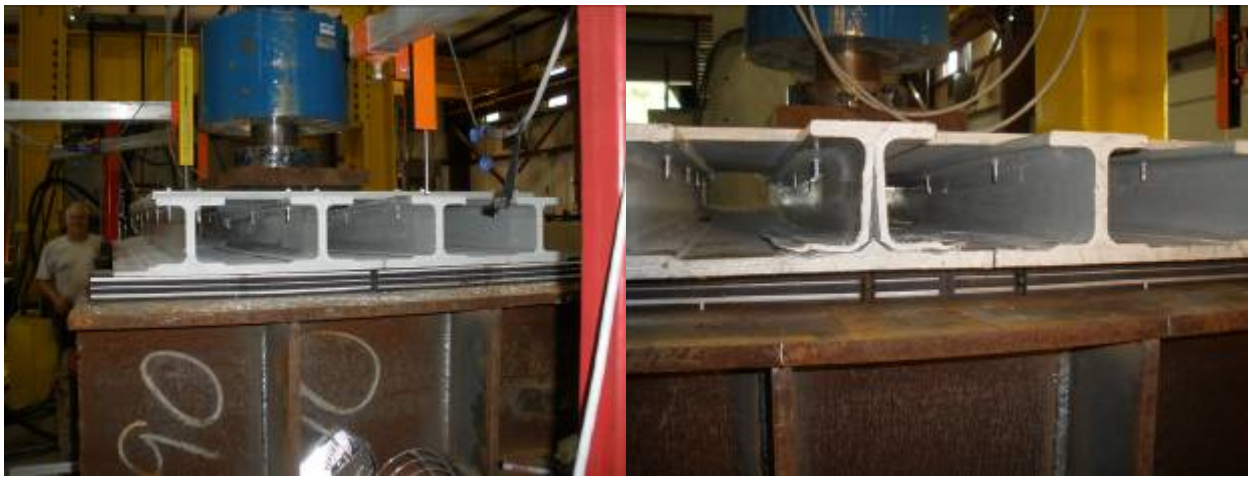

(a) (b)

Figure 28-(a) DS1 with web-buckling near top of web and (b) DS2 with flange/bottom-plate delamination.

Results for Deck A in its damaged state do not appear as promising as the initial work completed on a previously damaged specimen. For DS2, the delamination that occurred between the bottom flange and the GFRP bottom plate was severe (Figure 29). The delamination was expected to interrupt the heat transfer into the web resulting in a difference between the flange and the GFRP bottom plate. The IRT results for this specimen, however, do not provide any obvious indication that such a failure has occurred.

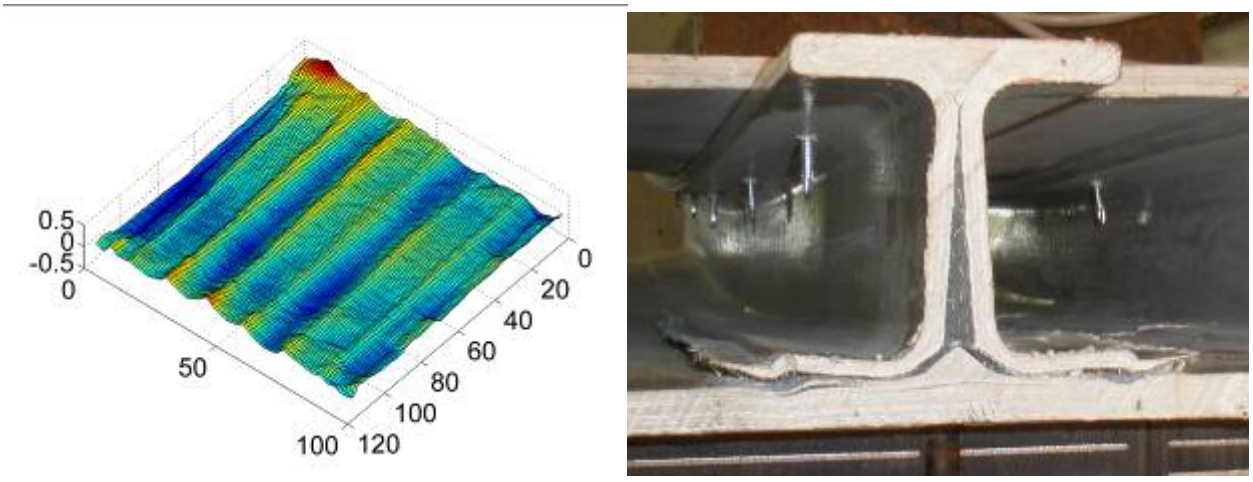

Figure 29-Phase image results for Deck A, specimen DS1 with severe bottom flange delamination.

5 Discussion and Recommendations for Future Research

The original objective of this research was to investigate the feasibility of using infrared thermography (IRT) as a nondestructive evaluation tool for detecting severe damage in GFRP bridge decks caused by overloading. A series of finite element analyses were conducted to simulate the heat transfer process for GFRP Deck A when a constant heat flux was applied to the soffit of the deck. These analyses demonstrated that a measurable temperature difference would develop across the soffit due to the webs that allow heat to continue to flow upwards towards the GFRP top plate. In addition to measuring the temperature differences that develop across the soffit, the finite element results were also post-processed with a least-squares sinusoidal curve fit in order to determine a single value for phase shift. The post-processed finite element results also indicated that phase shift provides an accurate means to detect areas where a web is present.

The preliminary experiments performed on two sample sections of GFRP Deck A (one undamaged and one damaged) demonstrated the potential for IRT to detect this type of damage. The phase image that was generated for the undamaged specimen displayed a regular pattern and it was possible to differentiate the webs from the GFRP bottom plate. The phase image for the damaged section displayed considerable variation across the surface and areas where the web had separated from the bottom plate appeared to be distinguishable from the phase response generated by the undamaged specimen (Figure 30).

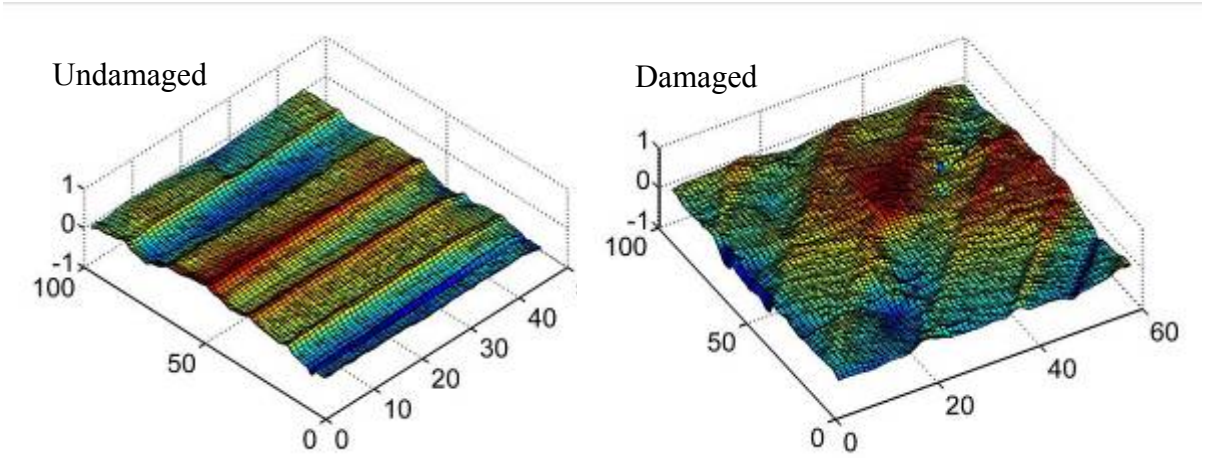

Figure 30-Phase image results for undamaged and damaged GFRP Deck A

When the same procedure was applied to damaged and undamaged Deck A specimens during the full-scale load testing, there were no clearly recognizable differences in the phase response for the damaged specimen (Figure 31).

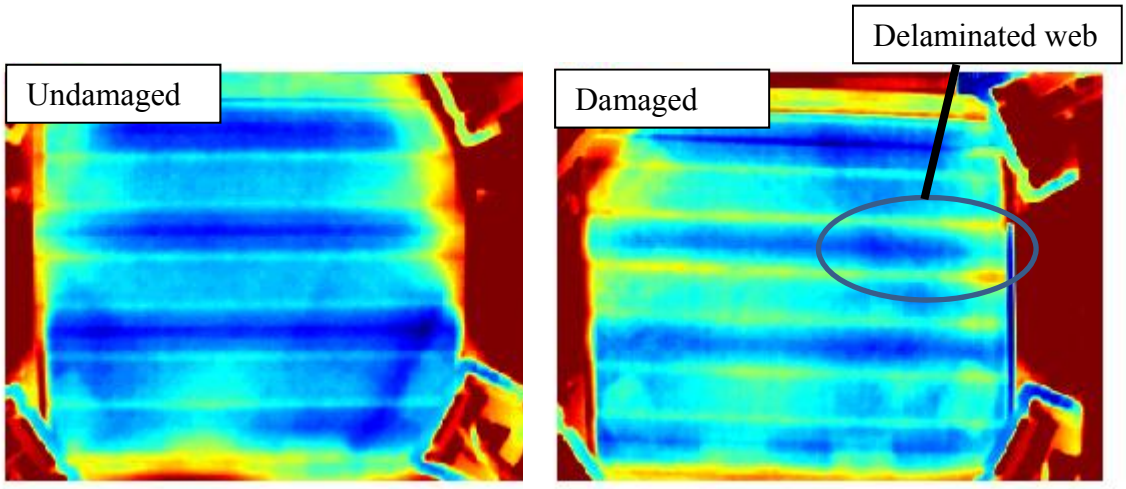

Figure 31-Comparison of damaged and undamaged Deck A specimens from full-scale load testing.

There are two possible explanations for the apparent inability of IRT to identify the web delamination that occurred in Specimen 2 for Deck A during the full-scale load test. The first explanation relates to the relative severity of the delamination encountered during the full-scale load test compared to the sample that was used in the preliminary study. During the full-scale load test, the bottom flanges and web separated from the GFRP bottom plate for a distance of approximately 18 in. over a single beam (Figure 32). The delaminated area in the preliminary study specimen was much larger and included two of the three adjacent beams. Furthermore, even though the bottom flanges of the full-scale test specimen were clearly delaminated over the entire 18 in. length, it was not clear as to whether or not this damage extended through to the web across the entire damaged area. Additional destructive testing of the specimen would be needed to verify the extent to which the web had separated from the GFRP bottom plate.

The second explanation relates to the location of the damage in the full-scale specimen and, specifically, its proximity to the edge of the specimen and the heating lamps. During the full-scale testing, the eight halogen lamps were oriented as shown in Figure 33. Ideally, all eight lamps would have been equally spaced around the perimeter of the panel (see setup for preliminary tests) in order to minimize non-uniform heating of the specimen. The modified

configuration was required due to the load supports used during the full-scale load testing. This configuration resulted in relatively weak heating of the specimen near the vertical edges, and this shadow effect tended to cause the resulting phase shift to drift upwards around the vertical edges of the panel (lensing). This upward drift occurred for Deck A in both the damaged and undamaged states (Figure 34). In this specific case, it is almost impossible to discern the difference between phase shift that may be caused by damage in the specimen and phase shift resulting from non-uniform heating.

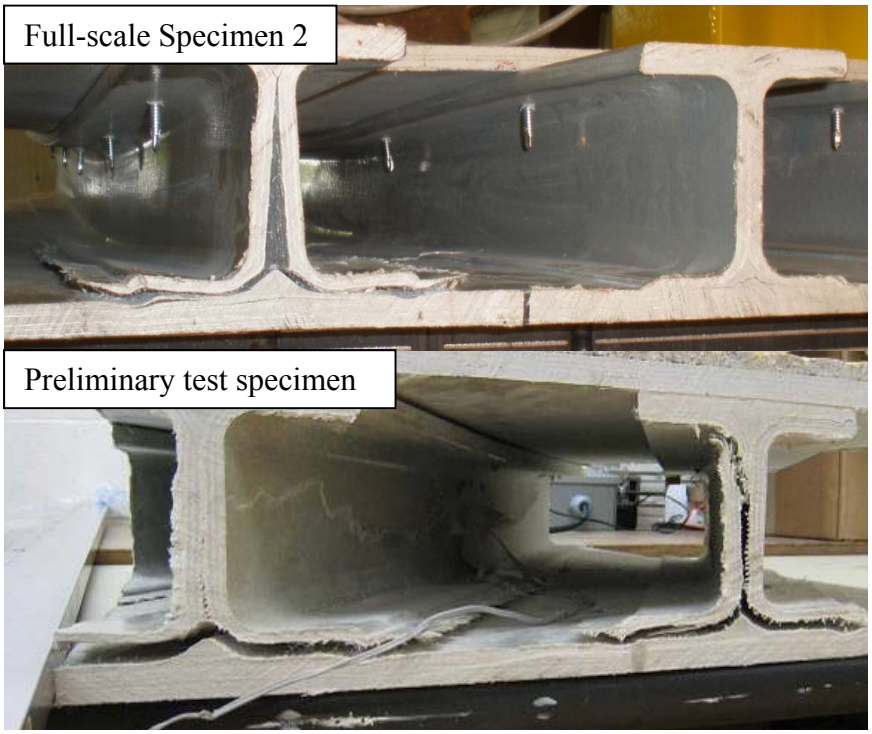

Figure 32-Comparison of web delamination levels between preliminary and full-scale test specimens.

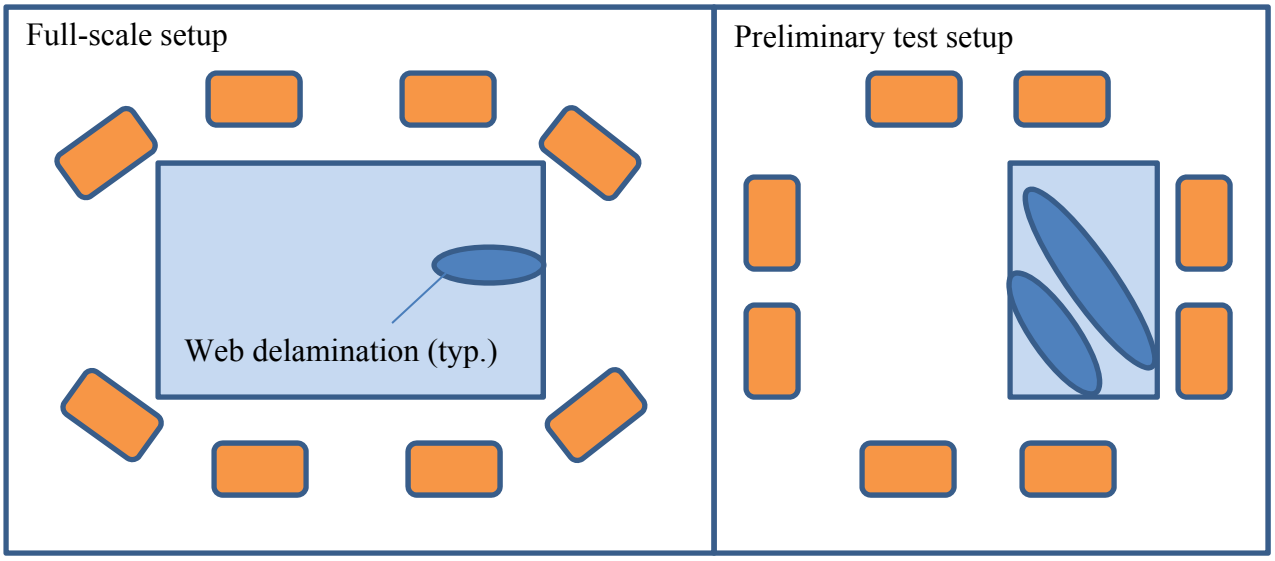

Figure 33-Halogen lamp configuration for full-scale and preliminary test setups.

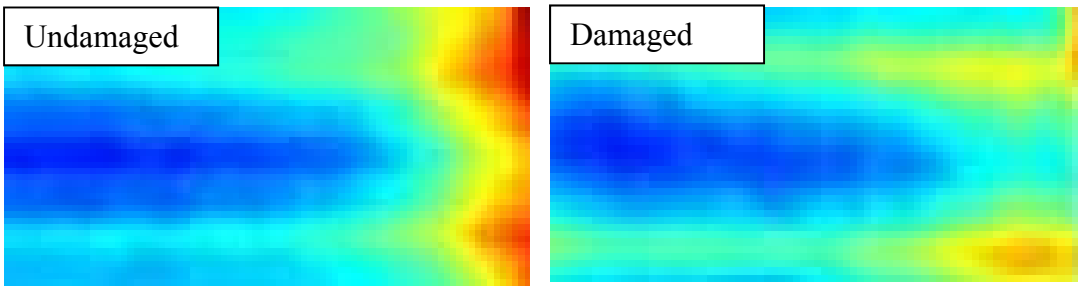

Figure 34-Undesired phase shift near edge of specimen due to non-uniform heating. These enlarged areas correspond to the "delaminated web" area identified in Figure 31.

A natural solution to the non-uniform heating problem would involve dividing the GFRP deck into four or more smaller inspection areas and focusing the lamps and camera on this smaller area for a series of inspections. The downside of this approach is the increased time required to inspect the entire panel. The minimum time of 15 minutes per inspection may become prohibitive if the entire operation is scaled up for field deployment. Furthermore, even if the non-uniform heating issue was eliminated entirely, it still is not clear whether or not the level of damage experienced by Deck A, Specimen 2, during the full-scale load testing can be detected using the methods developed for the current study.

In spite of the apparent shortcomings of the phase thermography method described in this report, it is still worth noting the significant improvements that can be realized with this method compared to simply observing a raw thermal image (Figure 35). Performing a series of

inspections for the same area with different sinusoidal frequencies can also provide insight regarding the relative depth of any defects or anomalies that are detected. This was illustrated clearly in the case of Deck C where variations in surface roughness resulted in apparent defects across the specimen (Figure 27). The fact that these apparent defects were present and equally pronounced in all of the phase images for periods ranging from 30 s to 960 s indicated that they were caused by something close to the surface.

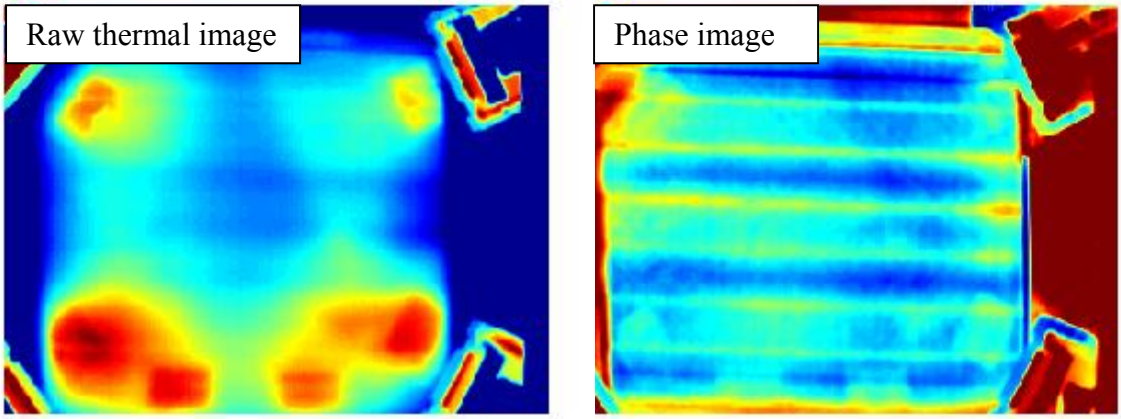

Figure 35-Comparison of raw thermal image and phase image for Deck A.

It may also be concluded from this study that IRT is only suitable for detecting certain types of load-induced damage in GFRP bridge decks. For Deck A, the only type of damage that was even considered "detectable" with IRT involved delamination of the webs and bottom flanges. Deck A only exhibited this failure mode when the GFRP top panel consisted of a single plate that was fastened to the GFRP deck and the composite section was subjected to three-point bending (Specimen 2). When the top panel consisted of two plates that formed a joint at the centerline of loading, the resulting failure mode was web buckling near the top flanges (Specimen 1). The failure modes exhibited by Deck B and Deck C (See Volume I of report) were also not conducive to NDE using IRT.

Infrared thermography may still prove useful in detecting other types of damage or defects that were not considered in the current study. Examples of this potential damage include blistering and delamination within the GFRP bottom plate that may develop during the service life of the GFRP deck. The presence or absence of such defects may serve as an overall indicator of the health of the deck. Another area where IRT may be useful is in relation to quality control during manufacturing and certification of a specific bridge deck before

installation. Infrared thermography may not be capable of evaluating the integrity of all the material used to form a specific deck panel, but it can ensure the uniformity of the material within approximately 0.25 – 0.5 in. of the surface. Additional research is needed to investigate how IRT might be incorporated into a quality assurance/quality control program to ensure that GFRP decks are fabricated properly and are capable of providing the required service-life.

Prior to deploying the IRT methods described in the current study on in-service GFRP bridge decks, additional research is recommended to address the issues encountered with non-uniform heating and heat source reflections. Specifically, it will be important to characterize the influence these non-uniformities have on the phase response that is computed for each pixel. Through additional post-processing of the existing data set it may be possible to minimize the effects that non-uniform heating has on phase response and thereby increase the overall sensitivity of the method. Additional work might also include a comprehensive study in which the lamp orientation is varied systematically and the resulting variation in phase response is characterized over the entire 2-D field of view of the IR camera. These results may lead to additional optimization of the lamp configuration that minimizes the variation in phase shift across the resulting phase image.

Additional investigation into alternative heat sources may also provide better results in confronting the issues surrounding non-uniform heating. Halogen lamps are inexpensive, easy to replace when damaged, and provide a sufficient heat flux to inspect the GFRP panels encountered in the current study. A significant deficiency, however, is their tendency to concentrate heat in isolated areas on the surface being inspected. Other devices, such as industrial IR heaters, may provide more uniform heating within the IR camera's field of view.

Another challenge that was made apparent in the current study is the length of time required to inspect each GFRP deck panel using IRT. If multiple periods are desired for each inspection and even a modest cooling time is provided between each period, the total time required to inspect a 9 ft^2 area could easily exceed 60 - 90 minutes. In a field deployment situation, the inspection team may also require significant time to reposition the lamps and camera for each section of the GFRP deck that requires inspection. Depending on the level of access that one has to the soffit of the GFRP deck and the sophistication of the fixtures that are deployed to hold the lamps and camera, the total time required to inspect a small bridge deck may be prohibitive using the method described in this study.

One potential solution to this problem would involve shifting from a fixed lamp/fixed camera inspection mode to a conventional line scanning inspection mode. Line scanning would require a moving heat source with the camera positioned such that the leading edge of the camera FOV remains fixed on the trailing edge of the heat source (Figure 36). Additional research is needed to calibrate the inspection parameters for specific GFRP deck types as well as to establish the reasonable limits for damage and defect detection.

Additional modifications could also be made to the traditional line scanning procedure in which the camera could move independently of the heat source and collect data while the surface is cooling over a larger area for a longer duration. This would require additional image processing after each test to reconstruct the cooling curve for each point on the soffit of the GFRP deck.

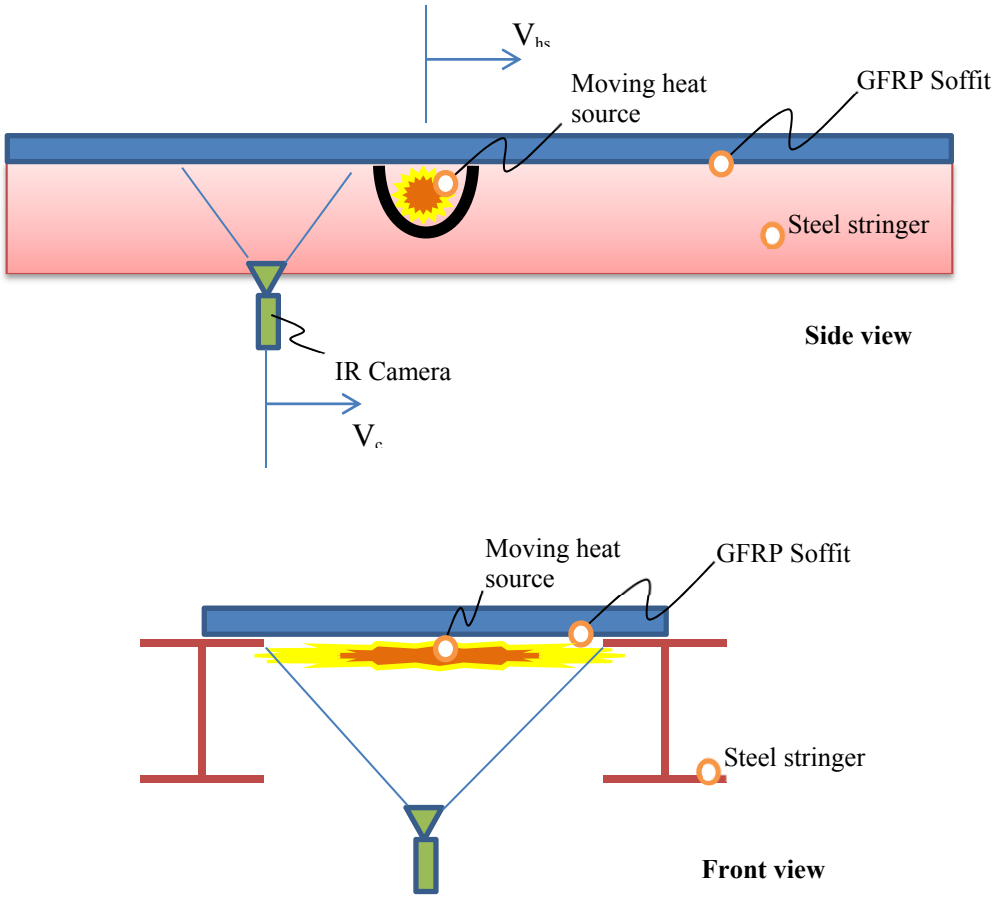

Figure 36-Line scanning alternative for field deployment.

6 References for Part II

1. ASTM Standard D4788, 2007, "Standard Test Method for Detecting Delaminations in Bridge Decks Using Infrared Thermography," ASTM International, West Conshohocken, PA, 2007, 10.1520/D4788-03R07, www.astm.org.
2. ASTM Standard E2582, 2007, "Standard Practice for Infrared Flash Thermography of Composite Panels and Repair Patches Used in Aerospace Applications," ASTM International, West Conshohocken, PA, 2007, DOI: 10.1520/E2582-07, www.astm.org.
3. Balageas, Daniel L., Alain A. Déom, and Daniel M. Boscher. "Characterization and Nondestructive Testing of Carbon-Epoxy Composites by a Pulsed Photothermal Method." *Materials Evaluation* 45.4 (1987): 461-65.
4. Kulowitch, P. J., I. M. Perez, and D. Granata. "Flash Infrared Thermography for Nondestructive Testing (NDT) I/E of Naval Aircraft." *Proceedings of SPIE*. Thermosense XVI. Vol. 2473. 1995. 252-62. Print.
5. Cramer, Elliott, and William P. Winfree. "Fixed Eigenvector Analysis of Thermographic NDE Data." *Proceedings of SPIE*. Thermosense XXXIII. Vol. 8013. 2011. Print.
6. Winfree, William P., Joseph N. Zalameda, and Patricia A. Howell. "Improved Flaw Detection and and Characterization with Difference Thermography." *Proceedings of SPIE*. Thermosense XXXIII. Vol. 8013. 2011. Print.
7. Brown, Jeff R., and H.R. Hamilton. "Investigation of Heating Methods and Detection Limits for Infrared Thermography Inspection of FRP Composites Used to Strengthen Reinforced Concrete." *ACI Materials Journal* 104.5 (2007): 481-90. Print.
8. Starnes, Monica A., Nicholas J. Carino, and Eduardo A. Kausel. "Preliminary Thermography Studies for Quality Control of Concrete Structures Strengthened with Fiber-Reinforced Polymer Composites." *Journal of Materials in Civil Engineering* 15.3 (2003): 266. Print.
9. Miceli, Marybeth, John C. Duke, and Mike Horne. "Health Monitoring of Fiber Reinforced Polymer Bridge Decks with Infrared Thermography." *Materials Evaluation* 60.10 (2002): 1245-252. Print.
10. "TWI - EchoTherm." *Thermal Wave Imaging Inc. - Home*. Web. 28 June 2011. <http://thermalwave.com/echotherm.htm>.

11. Balageas, Daniel L. "Defense and Illustration of Time-Resolved Pulsed Thermography for NDE." *Proceedings of SPIE*. Thermosense XXXIII. Vol. 8013. 2011. Print.
12. Osiander, R. J., W. M. Spicer, and J. C. Murphy. "Analysis Methods for Full-field Time-resolved Infrared Radiometry." *Proceedings of SPIE*. Thermosense XVI. Vol. 2766. 1996. 218-27. Print.
13. Brown, Jeff R., and H.R. Hamilton. "Quantitative Infrared Thermography Inspection for FRP Applied to Concrete Using Single Pixel Analysis." *Construction & Building Materials.* ACI Committee 228 25th Anniversary Special Edition (In Press).
14. Bai, W., and B. S. Wong. "Photothermal Models for Lock-in Thermographic Evaluation of Plates with Finite Thickness under Convection Conditions." *Journal of Applied Physics* 89.6 (2001): 3275. Print.
15. Hamilton III, H.R. and Brown, J. (2004). "CFRP Repair of Impact-Damaged Bridge Girders Volume II - Infrared Thermographic Inspection of FRP Composite Repairs," FDOT Report BC354 RPWO #55, Florida Department of Transportation.